

A Search for Lightly Ionizing Particles in the LUX Detector  
and Research and Development For Future Liquid Xenon  
Time Projection Chambers

by

Katayun Kamdin

A dissertation submitted in partial satisfaction of the  
requirements for the degree of

Doctor of Philosophy

in

Physics

in the

Graduate Division

of the

University of California, Berkeley

Committee in charge:

Professor Daniel McKinsey, Chair

Professor Marjorie Shapiro

Doctor Peter Sorensen

Professor Kai Vetter

Fall 2018

## ABSTRACT

---

A Search for Lightly Ionizing Particles in the LUX Detector and  
Research and Development For Future Liquid Xenon Time Projection  
Chambers

by

Katayun Kamdin

Doctor of Philosophy  
University of California, Berkeley  
Professor Daniel McKinsey, Chair

The nature of dark matter is one of the most compelling mysteries of modern physics. Liquid xenon detectors have been at the forefront of the attempt to directly detect dark matter particles for the last decade. The Large Underground Xenon (LUX) experiment recently concluded its operations at the Sanford Underground Research Facility in Lead, South Dakota. During its tenure, LUX set world-leading limits on WIMP dark matter, and paved the way for novel calibration techniques. Due in part to experiments like LUX, the available WIMP parameter space has been dwindling, making experimentalists look to other dark matter candidates. While new technologies will no doubt be needed in the hunt for dark matter, the well-understood detector technology of liquid xenon can be leveraged to search for non-WIMP dark matter. One such candidate, from the general class of dark sector theories, is the Lightly Ionizing Particle (LIP). LIPs interact with regular matter with an effective fractional charge, and the LUX detector is capable of detecting such interactions. New analysis techniques were developed to search for cosmogenic LIPs in the LUX detector, the first such analysis of its kind in liquid xenon.

Larger, more sensitive successors to the LUX experiment are already in planning and construction phases. As detectors become more sensitive, previously subdominant effects become more important. Under the umbrella of detector R&D for LUX's more sensitive successor, LZ, a test bed was built to investigate issues that may threaten the sensitivity of future xenon dark matter detectors. Radon backgrounds and the phenomenon

of delayed electron noise were studied, revealing new behavior that may help control backgrounds. Delayed electron noise is of special interest, as this phenomenon is the main background for the LIP search.

To my mom, for always making me feel like I could do this. To my friends, for being there when I was sure I couldn't.

## ACKNOWLEDGMENTS

---

I would like extend extreme gratitude to Bob, Dan, and Peter for taking in a stray grad student. Thank you to Bob for helping me transition research paths. Thank you to Dan for guidance through my very weird LUX analysis. Thank you to Peter for turning me into scientist who knows her way around a lab bench. And for teaching me a suite of skills with a razor blade, which I'm sure will raise no questions from future employers.

Thank you to my fellow LUX/LZ grad students for being wonderful people to work with. Elizabeth, thank you for the impromptu coffee breaks. Evan, thank you for knowing the answer to literally every question of the form “What was X in Run03?” Kelsey, thank you for being an awesome officemate. Brian, thank you for all the dad jokes and Mickelson trail runs. Thank you to Ethan, Scott Hertel, Scott Kravitz, and Quentin for being so generous with your engineerly and postdoctorly time. You are all amazing teachers, and I have been lucky to work with you.

Thank you to my mom for always supporting me in my endeavor to become a physicist, and instilling me with the confidence to pursue this path in the first place.

It’s difficult to express how important support from my friends has been throughout all the years of graduate school. Jackie, Carolyn, and Michael, I could not even without you. How do? Hoodoo? Tova, I feel like you’ve been there through this entire test of endurance despite living in Geneva for half of it. Thank you for being my problem set buddy, for desert yoga, and for slowly realizing it was me in that wavy-arm-man costume. Heather, thank you for moving from New York into an apartment in Berkeley that was one block down the street. I am extremely lucky to call you a friend; I would not have made it though the last several years or our 10 Year Anniversary Ultramarathon without you.

And Bradley, thank you for your unwavering support, cheerleading, and not blinking an eye despite having a front row seat to the Katayun anxiety show. You are incredible; words cannot describe.

# CONTENTS

---

1	INTRODUCTION	1
I	THEORETICAL CONTEXT AND EXPERIMENTAL STRATEGIES	2
2	THEORETICAL BACKGROUND	3
2.1	A Brief History of Dark Matter . . . . .	3
2.2	Evidence for Dark Matter . . . . .	5
2.2.1	Galaxies and Clusters . . . . .	6
2.2.2	Cosmic Microwave Background . . . . .	9
2.3	Standard Models . . . . .	14
2.3.1	The Standard Cosmology . . . . .	14
2.3.2	The Standard Model of Particle Physics . . . . .	18
2.4	Dark Matter Candidates Motivated by Particle Physics . . . . .	19
2.4.1	WIMPs and the Hierarchy Problem . . . . .	19
2.4.2	Axions and the Strong CP Problem . . . . .	21
2.5	The Dark Sector and Lightly Ionizing Particles . . . . .	23
2.5.1	Dark Sector . . . . .	23
2.5.2	Lightly Ionizing Particles . . . . .	24
2.5.3	WIMPless Miracle and the New Physics Flavor Problem . . . . .	27
2.5.4	Charge Quantization . . . . .	29
2.6	Experimental Strategies for Detecting Dark Matter . . . . .	29
2.6.1	Production . . . . .	29
2.6.2	Indirect Detection . . . . .	30
2.6.3	Direct Detection . . . . .	31
3	PARTICLE DETECTION WITH LIQUID XENON	35
3.1	Liquid Xenon as a Detector Medium . . . . .	35
3.1.1	Properties of Liquid Xenon . . . . .	35
3.1.2	Scintillation and Ionization Signal Generation	37
3.2	Types of Xe Detectors . . . . .	38
3.2.1	XMASS: A Single Phase LXe Detector . . . . .	38
3.2.2	EXO-200: A Single Phase LXe TPC . . . . .	39
3.2.3	LUX: A Dual Phase LXe TPC . . . . .	40
3.3	Energy Reconstruction in Dual Phase LXeTPCs . . . . .	42
3.4	Dual Phase Xenon TPCs for Dark Matter Detection . . . . .	47
3.4.1	WIMP Searches with LXe TPCs . . . . .	47
3.4.2	Other Dark Matter Searches with LXe TPCs . . . . .	53
II	BIG SCIENCE	58
4	THE LUX DETECTOR	59

4.1	LUX Overview . . . . .	59
4.2	Internal Components . . . . .	59
4.3	External Components . . . . .	61
4.4	Trigger and Data Acquisition . . . . .	63
4.5	Data Processing . . . . .	66
4.6	Calibrations . . . . .	68
4.6.1	Energy Reconstruction . . . . .	68
4.6.2	Metastable Krypton-83 ( $^{83m}\text{Kr}$ ): A Multifunction Calibration . . . . .	70
4.6.3	Tritium Beta Decay: Calibration of the ER Band and Yields . . . . .	76
4.6.4	Deuterium-Deuterium (DD) Neutrons: Calibration of the NR Band and Yields . . . . .	78
4.6.5	Energy Resolution and Signal Yields Outside the WIMP Search Range . . . . .	81
4.6.6	Significance of LUX Calibrations . . . . .	84
5	LIGHTLY IONIZING PARTICLE SEARCH	85
5.1	LIP Search with LUX . . . . .	85
5.2	Modeling LIP Interaction . . . . .	86
5.2.1	Collision Cross Section . . . . .	86
5.2.2	Photo Absorption Ionization Model for Charged Particle Energy Loss . . . . .	87
5.2.3	Straggling Monte Carlo for Energy Deposition	90
5.2.4	Downsampling for 3D Distribution . . . . .	94
5.2.5	Generating PMT Waveforms . . . . .	96
5.2.6	PMT Waveform Processing . . . . .	98
5.3	LIP Filter . . . . .	101
5.3.1	Track Reconstruction and RQs . . . . .	102
5.3.2	Energy Consistency RQs . . . . .	104
5.4	LIP Backgrounds . . . . .	108
5.5	LIP Search Analysis . . . . .	114
5.5.1	Run03 Dataset . . . . .	114
5.5.2	LIP Signal Region . . . . .	115
5.5.3	Systematic Errors . . . . .	126
5.6	Result: Vertical Flux Limit . . . . .	129
5.7	Discussion . . . . .	129
III	LITTLE SCIENCE	131
6	RESEARCH AND DEVELOPMENT TESTBED FOR FUTURE LIQUID XENON TPCs	132
6.1	Test Bed Apparatus Overview . . . . .	132
6.2	Circulation System . . . . .	133
6.3	Slow Control . . . . .	133

6.4	PMT . . . . .	135
6.5	Charge Amplifiers . . . . .	136
6.5.1	Charge Amplifier Noise Behavior . . . . .	138
6.6	Data Acquisition and Processing . . . . .	141
6.6.1	Estimating Picoscope Dead Time . . . . .	141
6.6.2	PMT Signal Processing . . . . .	141
6.6.3	Charge Amplifier Signal Processing . . . . .	143
6.7	High Voltage Feedthrough Design . . . . .	145
6.7.1	Off The Shelf Feedthroughs . . . . .	148
6.7.2	Custom Feedthroughs . . . . .	154
6.7.3	Final Feedthrough Design . . . . .	158
6.8	Electric Fields in Test Bed . . . . .	160
7	SOLUBILITY OF RADON DAUGHTERS IN LIQUID XENON	162
7.1	Motivation . . . . .	162
7.1.1	Plate Out . . . . .	164
7.2	Experimental Configuration and Method . . . . .	165
7.2.1	Plate Out of $^{220}\text{Rn}$ Daughters . . . . .	167
7.2.2	Data Collection . . . . .	169
7.2.3	Calibration . . . . .	169
7.2.4	Position Reconstruction . . . . .	170
7.2.5	Fiducial Volume . . . . .	170
7.3	Analysis . . . . .	170
7.3.1	Number of $^{220}\text{Rn}$ daughters in the TPC . . . . .	170
7.3.2	Data Selection . . . . .	171
7.4	Results . . . . .	178
7.5	Discussion . . . . .	179
8	STUDIES OF DELAYED SINGLE ELECTRON SIGNALS	183
8.1	Motivation for Studying Delayed Single Electron Signals	183
8.2	Origin of Delayed Single Electron Signals . . . . .	185
8.2.1	Photoionization on Grids . . . . .	185
8.2.2	Photoionization of Impurities . . . . .	186
8.2.3	Delayed Extraction of Trapped Electrons . . . . .	186
8.3	Test Bed Studies Of Electron Trains . . . . .	189
8.3.1	Radon Source and “Full TPC Configuration” .	190
8.3.2	Polonium Source and “Extraction Region Only” Configuration . . . . .	196
8.4	Electron Train Study Summary . . . . .	200
8.5	Discussion . . . . .	205
IV	CONCLUSIONS	207
9	SUMMARY AND OUTLOOK	208

V	APPENDIX	210
A	PAI CROSS SECTION AND OPTICAL CONSTANTS	211
	A.1 Sources for Optical Constants . . . . .	211
	A.2 PAI Cross Section . . . . .	212
B	LIP FILTER RQS	213
	BIBLIOGRAPHY	222

## LIST OF FIGURES

---

Figure 1	Superposition of 21 rotation curves from galaxies with a large range of radii and luminosities. All of these galaxies have a distinctive flat rotation curve at large radii. Figure from [4]. . . . .	4
Figure 2	CfA Redshift Survey result showing the distribution of galaxies in a strip on the sky about 6 degrees wide and 130 degrees long. The radial coordinate is redshift, in km/sec, calculated with a Hubble constant of 20km/sec/million ly. Figure from [9]. . . . .	5
Figure 3	Galactic rotation curve from [10] fit with two different dark matter halo models. The Figure (left) is closer to the rotation curve produced by dark matter with an NFW profile (see [11]), and our understanding of the ratio of dark matter to visible matter in most spiral galaxies. . . . .	6
Figure 4	Galactocentric speed distributions for SDSS stars within 4 kpc of the Sun and distances of $7 < r < 10$ kpc. The distributions are shown for $[Fe/H]$ in $[-2.2, -2]$ (solid purple) and $[Fe/H] < -2.2$ (solid orange). The Standard Halo Model with mean $v_0 = 220$ km/s is shown for comparison (dashed gray). The inset shows the expected background-free 95% C.L. limit on the DM spin-independent scattering cross section, assuming the exposure and energy threshold of the LUX experiment different velocity distributions. Figure from [16]. . .	7
Figure 5	(left) The visible light image from the Magellan telescope of the merging Bullet Cluster overlaid with the weak lensing measurement contours in green, and white 68.3%, 95.5%, and 99.7% confidence levels for the weak lensing peaks. (right) The Chandra x-ray image overlaid with the same weak lensing measurement. Figure from [21]. .	9

Figure 6	(top) The FIRAS instrument on the COBE satellite mission measured the <a href="#">CMB</a> temperature to be $2.7377 \pm 0.0038$ K. (bottom) The FIRAS instrument also confirmed the perfect Planck black body spectral shape of the <a href="#">CMB</a> radiation. Figures from [22]. . . . .	10
Figure 7	(top) The relative spatial resolution of COBE, WMAP, and Planck. Figure courtesy of NASA. (bottom) The Mollweide projection of the Planck 2013 CMB temperature map. The color scale represents fluctuations of $\pm 30 \mu\text{K}$ around a central value of 2.7377 K. Figure courtesy of ESA and the Planck Collaboration. . . . .	11
Figure 8	The angular power spectrum from Plank 2018 results [24]. . . . .	13
Figure 9	The effect of baryons (left) and total matter (right) on the magnitude and location of <a href="#">CMB</a> angular power spectrum peaks. [23] . . . . .	13
Figure 10	The effect of curvature (left), dark energy (center), and equation of state (right) on the magnitude and location of <a href="#">CMB</a> angular power spectrum peaks. [23] . . . . .	16
Figure 11	The particles that comprise the standard model of particle physics, including names, spins, masses, and charges. It is also indicated which fermions interact with which bosons, e.g. gluons interact with the quarks but not with the leptons. . . . .	18
Figure 12	(left) The co-moving number density $Y$ (left y-axis) resulting in the thermal relic density $\Omega_\chi$ (right y-axis) for a dark matter particle of mass $m_\chi = 100$ GeV. The solid black line is the annihilation cross section which yields the correct relic density and bands indicate cross sections that differ by successive factors of 10 from the “correct” annihilation cross section. (right) A band of natural values for a thermal relic $\chi$ that composes different percentages of the observed dark matter content. The width of the band is set by the deviation of $g$ from $g_{\text{weak}}$ in Equation 12. Figures from [33]. . . . .	22

Figure 13	A Feynman diagram of a dark sector particle $h$ interacting with atomic electrons. $g'$ is the gauge coupling to $A'$ in the dark sector, $\theta$ the kinetic mixing angle between $A'$ and $A$ , and $g$ is the usual electromagnetic gauge coupling, $g = e$ . . . . .	26
Figure 14	Regions of mass-charge space ruled out for LIPs from several different sources. The dashed line limits apply in the case of a dark sector photon (our case of interest), and the dotted line is the limit without dark photons. Abbreviations: AC, accelerator experiments; Op, search for the invisible decay of ortho-positronium; SLAC, the SLAC millicharged particle search; L, the Lamb shift; BBN, big bang nucleosynthesis; RG, plasmon decay in red giants; WD, plasmon decay in white dwarfs; DM, dark matter searches; SN, Supernova 1987A. Figure from [40]. . . . .	26
Figure 15	Recent limits on the flux of LIPs with charge $e/f$ where $f$ is the x-axis. Figure reproduced from [41]. . . . .	27
Figure 16	Contours in the $(m_\chi, g_\chi)$ -plane for two different temperature conditions for the hidden sector. The upper line is for a hidden sector that achieves 80% of the visible sector temperature after reheating, the lower line is for 30%. For this plot, the hidden sector is assumed to be a 1-generation flavor-free version of the minimal supersymmetric standard model. Figure adapted from [33]. . . . .	28
Figure 17	Summary of DM detection schemes with illustrative Feynman diagrams. In all cases, the arrow of time is from left to right. (left) SM particles can be collided at high energy facilities, which may produce DM particles, $\chi$ . (center) $\chi$ may scatter with SM particles, leaving behind a characteristic signal. (right) $\chi$ particles in the galaxy may annihilate and produce SM particles, which produces an SM signal in excess of expectations from standard astrophysical processes. . . . .	30
Figure 18	Diagram summarizing the generation of the scintillation and ionization signal generation in dual-phase xenon time projection chambers. . . . .	38

Figure 19	Diagram of the XMASS detector and water tank. Figure from [63]. . . . .	39
Figure 20	Diagram of the EXO-200 detector and systems. Figure from [65]. . . . .	40
Figure 21	Diagram of a dual-phase xenon time projection chamber. The time difference between S1 and S2 gives the depth ( $z$ ) of the interaction, and $(x, y)$ is reconstructed from the S2 signal. . . . .	41
Figure 22	(top) Plot illustrating the effect of recombination and detector effects on a line source ( $^{127}\text{Xe}$ ), courtesy of E. Pease. (bottom) Field dependence of scintillation and ionization yield in LXe for 122 keV electron recoils (ER), 56.5 keV nuclear recoils (NR) and 5.5 MeV alphas, relative to the yield with no drift field from [73]. . . . .	44
Figure 23	Plots showing combined energy contours in two common sets of axis units, for an example set of $g_1$ and $g_2$ . . . . .	46
Figure 24	Plot showing ER and NR bands from LUX. Solid lines are the ER and NR Gaussian means, $\mu$ ; dotted lines are $\mu \pm 1\sigma$ . Figure from [68]. . . . .	48
Figure 25	Plot showing spin-independent WIMP rates in common detector target materials, dots indicate typical thresholds for the targets. Xenon gains in favored SUSY parameter space ( $M_\chi \gtrsim 100$ GeV) due to a kinematic enhancement ( $M_\chi \sim M_{Xe}$ ) and a cross-section enhancement ( $\sigma_{SI} \propto A^2$ ). Figure from [63]. . . . .	51

Figure 26	A summary of the excluded <b>WIMP</b> parameter space by all experiments (green). Solid lines indicate previous results and dashed lines indicate projections for future experiments. Although next generation xenon experiments (LZ, black dashed) perform better for <b>SUSY WIMP</b> parameter space (gray region labelled pMSSM), germanium and silicon (SuperCDMS SNOLAB, pink dashed) can access other light dark matter parameter space below 10 GeV. The signal regions are from the DAMA collaboration, which has a long standing claim of detection with an annular modulation search; however, no other experiments have been able to reproduce such an observation. Plot courtesy of L. Tvrznikova, regenerated from [79]. . . . .	52
Figure 27	Xenon10 low-mass <b>WIMP</b> limit (black line) extended the range of the standard <b>WIMP</b> result (yellow dashed lines). Figure from [86]. . . . .	54
Figure 28	(left) Top: Expected 1,2,3-electron signal rates for Sub-GeV DM with $\sigma_e = 10^{-36} \text{ cm}^2$ and Bottom: exclusion limit set with Xenon10 few-electron signals. (right) Exclusion limits for dark matter scattering through an electric-dipole moment (red) and through a very light ( $\ll \text{keV}$ ) mediator (blue). Figures from [87]. . . . .	55
Figure 29	(top) Recent limits on solar axion coupling and mass (bottom) recent limits on galactic axion coupling and mass. Figure taken from [89]. . . . .	57
Figure 30	Major components and dimensions of the <b>LUX</b> detector. Figure from [90]. . . . .	60
Figure 31	Field-shaping rings detail. Figure from [90]. . . . .	61
Figure 32	A simplified diagram of the <b>LUX</b> cryogenic system. Figure from [92]. . . . .	62
Figure 33	A photo of the <b>LUX</b> detector installed inside the water tank. Photo credit Mark Kapust. . . . .	64

Figure 34	Backgrounds distributions in squared radius and height for expected (right) and measured (left) backgrounds in the energy range 0.9–5.3 keV <sub>ee</sub> (2–30 phe S1) for the 85.3 live-day Run03 WIMP exposure. Black lines show the 118 kg fiducial mass. Units are log <sub>10</sub> DRU <sub>ee</sub> , electron equivalent differential rate units, i.e. keV <sub>ee</sub> <sup>-1</sup> kg <sup>-1</sup> day <sup>-1</sup> . Figure from [94]. . . . .	64
Figure 35	Overview of the LUX trigger system. Figure from [95]. . . . .	65
Figure 36	An example recorded event. Channels that do not pass the POD threshold are not recorded. The waveforms are summed over all channels to produce the S1 and S2. Figure from [95]. . .	65
Figure 37	An example of LUX pulse classification from a multiscatter event showing detail of individual pulses of types S1, S2, SPHE, and SE. In addition to the pulse classes illustrated here, there is an Else class, for pulses that do not fit any of the definitions shown. . . . .	67
Figure 38	Plot showing calibration sources used for determination of the detector gains, $g_1$ and $g_2$ . The axis label subscript $c$ denotes corrected variables with calibration for geometrical effects and electron lifetime; these corrections are discussed in Section 4.6.2. Figure from [67]. . . . .	69
Figure 39	Doke plot used to fit for $g_1$ and $g_2$ in LUX Run03. Figure from [67]. . . . .	70
Figure 40	Decay scheme of <sup>83m</sup> Kr. The width of each column is proportional to the branching fraction of that decay mode, the vertical divisions are proportional to energy partitioning among internal conversion electrons (blue), Auger electrons (yellow), x rays (green), and gamma rays (red). In the LUX detector, the S1s of the 32.1 keV $\beta$ and the 9.4 keV $\beta$ were sometimes separable, the S2s were always merged. If the S1s were separate they were referred to as S1a and S1b. Figure from [99]. . . . .	71
Figure 41	Spatial dependence of pulse area corrections for S1 (left) and S2 (right) from an example <sup>83m</sup> Kr calibration. The red circle indicates normalization point. Figure from [99]. . . . .	73

Figure 42	(left) A simplified 2D COMSOL model showing electric field lines and equipotentials for the <b>LUX</b> detector in Run03. A radially inward component is seen. (right) The resulting edge S2 coordinates of a uniform distribution of electrons drifted under the electric field model is shown in solid blue. The edge S2 coordinates of from $^{83m}\text{Kr}$ data is in dashed red; it is consistent with the field model prediction. Figure from [99]. . .	74
Figure 43	The effect of radial position mapping between S2 coordinates (left) and real coordinates (right). The top panels show a thin horizontal slice of the detector and the bottom panels show a thin vertical slice. The red and blue colors are to make the effect of the mapping visible. Note that squared radius in the bottom panels exaggerates the scale of the effect. Figure from [99].	75
Figure 44	Field map of Run03 produced by $^{83m}\text{Kr}$ S1a:S1b ratio. Because only a fraction of $^{83m}\text{Kr}$ produce separate S1a and S1b, the bins are large to accommodate reduced statistics. Figure from [99] . . .	76
Figure 45	(left) Plot showing the theoretical tritium beta spectrum with the spectrum obtained from data, and residuals. (right) The ratio of data to theory convoluted with the detector energy resolution. Figure from [71]. . . . .	77
Figure 46	(left) The measured quanta yields shown with lines of equal energy. (right) A plot depicting the expected initial quanta yields, $N_{ion}$ and $N_{ex}$ , compared with the measured yield of photons and electrons. The difference is caused by the energy dependence of recombination. Figure from [71]. . . . .	77
Figure 47	(left) The <b>ER</b> band for in <b>WIMP</b> search energy range obtained from the tritium calibration. (right) Leakage fraction of <b>ER</b> events below the <b>NR</b> mean in the <b>WIMP</b> search energy range. Knowledge of the <b>NR</b> band comes from the <b>DD</b> calibration detailed in Section 4.6.4. Figure from [71]. . . . .	78

Figure 48	(left) Photo of the water tank interior showing the neutron conduit, which is raised during <b>DD</b> calibration. (right) Diagram of the <b>DD</b> generator and water tank neutron conduit during <b>DD</b> operation. Figure courtesy of E. Pease. . . . .	79
Figure 49	Calibration showing the <b>NR</b> band mean and width from the <b>DD</b> calibration. The x-axis is $S1_{spike}$ , for which candidate single photons (“spikes”) are identified and tallied in sparse waveforms. This can be a more accurate photon count for low energies and is preferred here to the usual integrated waveform method (see [102] for more information). The black data points are the Gaussian fit centroid values for each $S1_{spike}$ bin. The red data points are corresponding Gaussian fit mean value for the simulated nuclear recoil band produced using the model described in Sec. VII. The black and red dot-dashed lines indicate the 90% one-sided limits from data and simulation, respectively. The magenta dashed lines indicate the lower and upper $S2$ thresholds applied to the <b>WIMP</b> search. Error bars are statistical only. Figure from [76]. . . . .	80
Figure 50	Single-scatter events identified in the <b>LUX</b> 2013 <b>WIMP</b> -search data. The labels indicate the source isotopes and their energies. In addition to single scatters, some of these isotopes have other decay modes that can produce multiple scatters. Figure from [68]. . . . .	81
Figure 51	The measured energy resolution at known energy peaks in the <b>LUX</b> ER backgrounds. The detector is optimized for low-energy sensitivity, and variable amounts of PMT saturation and single-electron contributions affect $S2$ pulses and hamper the energy resolution at high energy. An empirical fit $a/\sqrt{E}$ is applied. Figure from [68]. . . . .	83
Figure 52	Improved spin-independent <b>WIMP</b> limit of the Run03 exposure following the <b>DD</b> calibration of <b>LUX</b> . The first Run03 limit is the gray line labelled LUX 2014, the improved Run03 observed limit is the black line labelled This Result. Figure from [102]. . . . .	84

Figure 53	(left) Plot showing the deviations of the PAI cross section from the Rutherford cross section for Si. Deviations occur at energies corresponding the M,L, and K electron shells. The result for Si is compared to [109] to check for agreement. (right) PAI cross section compared to the Rutherford cross section for xenon. In both plots, the y-axes are labeled with $\sigma$ as a short-hand for $d\sigma/dE$ . . . . .	89
Figure 54	Solid line is the “true” straggling for particles of $\beta\gamma = 3.6$ traversing 1.2 cm of Ar gas. $\Delta_p$ denotes the most probable energy deposition, and $\langle \Delta \rangle$ is the average energy deposition. Note that the average energy deposition is skewed to the high tail. The dotted line shows the Landau function approximation to straggling, which is offset from the true straggling. The physical origin of the high energy tail are the rare, “hard” scatters with electrons. Figure from [109]. . . .	91
Figure 55	(left) Plot showing $\Phi(E; \beta\gamma)$ , the integrated single collision spectrum for xenon. (right) Plot showing the inverted integrated single collision spectrum for xenon, $\Phi^{-1}(E; \beta\gamma)$ . In order to assure unbiased sampling of the distribution, the x-axis must be equally spaced. This can be accomplished by interpolating $\Phi^{-1}$ over an x-axis of equally spaced points from $[0, 1]$ . Interpolating with e.g. 10 points will result in a coarse sampling of the PDF and interpolating with e.g. 10000 points will result in a smooth sampling. Drawing a random number $r$ gives the associated $E_{loss}(r)$ . . . . .	92
Figure 56	A diagrammatic representation of the output of the Monte Carlo. The output for one event is a collection of $dE_i$ (blue circles) and the space between them $dx_i$ . The Monte Carlo is run many times, resulting in an accumulation of segments like these. Results of this type are referred to as the “base 1D” Monte Carlo. . . . .	92

Figure 57	(left) Plot showing the straggling for different charge fractions $f$ in 10 cm of <a href="#">LXe</a> . To generate these straggling PDFs, the Monte Carlo described above was carried out 1000 times. (right) Plot showing the number of collisions for each charge fraction $f$ . . . . .	93
Figure 58	(left) The most probable energy deposition for a given charge fraction traveling though a path length of <a href="#">LXe</a> . The plot was generated by carrying out the Monte Carlo described above, histogramming the results, and finding the peak of the distribution. (right) The average number of interactions for a <a href="#">LIP</a> of charge fraction $f$ traveling though a path length of <a href="#">LXe</a> . . . . .	94
Figure 59	Plot showing the peak (triangle) and the average (circle) of energy deposition in different path lengths. At high charge fraction, interactions are less likely, and so are greatly affected by statistical deviations. The line is $f^{-2}3.1 \text{ MeV/cm}$ , as energy deposition for <a href="#">LIPs</a> falls off as $f^{-2}$ . The value expected at $f = 1$ ( $\langle dE/dx \rangle$ for a muon) is $3.6 \text{ MeV/cm}$ [106] (red line); our result is 13% lower than this. Reference [106] gives the energy loss in units of $\text{MeV g}^{-1} \text{ cm}^2$ , a Liquid Xenon ( <a href="#">LXe</a> ) density of $2.94 \text{ g/cm}^3$ is used to translate to $\text{MeV/cm}$ . This is the same value for <a href="#">LXe</a> density used in the straggling Monte Carlo. . . . .	95
Figure 60	Diagram illustrating the downsampling method for <a href="#">LIPs</a> . Geantinos were generated with uniform random position and momentum on a hemisphere. If a geantino entered the <a href="#">LXe</a> volume of the detector, the position where it entered the <a href="#">LXe</a> was saved along with its momentum. The base 1D Monte Carlo was then “injected” into the <a href="#">LXe</a> with this position and momentum and propagated until it left the <a href="#">LXe</a> volume. . . . .	95
Figure 61	A 2D histogram of the initial positions for geantinos that entered the xenon space of <a href="#">LUX</a> . Polar angle indicates deviation from the vertical. . . . .	96

Figure 62	The simulated detector response to a LIP of charge fraction $f = 100$ . The hexagonal maps filled with circles represent the top and bottom PMT arrays. The color scale indicates how many photons were observed in each PMT. The top graph shows each PMT voltage trace in a different color, and the bottom graph shows the summed PMT waveforms. . . . .	98
Figure 63	The result of the LUX DPF on a LIP of charge fraction $f = 100$ . The pink dashed lines highlight energy depositions that were merged by the pulse finder. The “x” markers on the PMT map indicate the Mercury reconstructed positions, which have position corrections applied.	99
Figure 64	The result of the LUX DPF on a LIP of charge fraction $f = 10$ . The pulse finding capability was seen to fall dramatically with decreasing $f$ . This event traversed the detector starting near PMTs 53 and 52, and proceeded across to PMTs 23 and 24. . . . .	99
Figure 65	The result of the LUX DPF on a LIP of charge fraction $f = 10$ . The pulse finding capability was seen to fall dramatically with decreasing $f$ . The pulse finder was sometimes able to isolate individual S2s for low $f$ events, but the Mercury reconstruction of these events often failed. There are no positions marked on the PMT hit map for this event, indicating that position reconstruction failed. . . . .	100

Figure 66	The reconstructed $dE/dx$ for several charge fractions. The plot was generated by reconstructing the energies $E$ and track lengths $L$ from LIP waveforms that were processed with the LUX DPF. The $E/L$ from each event was added to a histogram, and the averages of the histograms for each simulated $f$ were found. The detector response matches expectations from the PAI cross section in the charge range $f = [50, 200]$ (compare to Figure 59). Below this range, the pulse finder yields a “loss” of any non-S2 area. Above the range, only the highest energy fluctuations are detected; and the detector response levels off due to low statistics (most events are in the first bin, but there are many events which did not deposit enough energy to be “measured”, i.e. to make it into the histogram). . . . .	101
Figure 67	A diagram of the $\chi^2$ minimization variable for track reconstruction. The figure shows the example of one point, e.g. the corrected reconstructed position of one S2 pulse. A minimum of three points was required by the LIP Filter for track reconstruction, so that a $\chi^2$ may be defined. . . . .	103
Figure 68	The result of track reconstruction for $f = 100$ LIPs using the $\chi^2$ in Equation 53 as the minimization variable. Each color represents a different LIP event. The panels show the full 3D view (top left), the top-down view in $(x, y)$ (top right), and two side views $(x, z)$ and $(y, z)$ (bottom left and right, respectively.) . . . . .	105
Figure 69	The binned phd/sample straggling histograms for several events displayed on the same axes. Each color represents a different event; the top shows the straggling of background events and the bottom shows the straggling of $f = 10$ and $f = 100$ events. The two background panels show the same events, but the top right plot is a zoomed-in and re-binned version of the top left plot. . . . .	107

Figure 70	The Moyal and normal distributions shown for the same $\mu$ and $s$ variable. For the normal distribution $s$ is usually called $\sigma$ . The Anderson-Darling test was employed for LIPs with the Moyal as the test distribution. . . . .	108
Figure 71	An example of an electron train following a large S2. In this particular example, there is no S1 found before the large S2. S1s are required to provide a drift time for S2 pulses, and events with no drift time have no pulse area or position corrections applied. If only the corrected pulse areas were used, they would appear to be approximately uniform and could be confused for a LIP. In this case, the corrected positions (displayed as “x” markers on the PMT array) are not aligned in a track, so a track cut could reject this particular event. Sometimes, electron trains do happen to lie along a track, and RQs using raw S2 areas and positions must be employed. . . . .	110
Figure 72	An example of an electron burp, which happens to straddle two event windows. The S2s in electron burps are often similarly sized, and though there is no true S1, the pulse finder sometimes identifies an S1 in the midst of the electron burp. A robust method to cut these events is to limit the amount of area appearing before the S1. . .	111
Figure 73	An example of a few electron train events that led to reconstructed tracks. Different colors indicate different events. All of the 2D plots are displayed with the marker sizes scaled as pulse area. All of these events had a $\chi^2$ between 1.2 and 2.0. An eventual cut was applied that required $0 < \chi^2 < 1$ , so these particular events would not have made the track reconstruction cut. . . . .	112

Figure 74	An example of a few electron train events that led to reconstructed tracks. Different colors indicate different events. All of the 2D plots are displayed with the marker sizes scaled as pulse area. All of these events had a $\chi^2 < 1.0$ . An eventual cut was applied that required $0 < \chi^2 < 1$ , so these particular events would pass the track reconstruction cut. However, they do not subtend the entire detector, which we require of LIPs. . . . .	113
Figure 75	Acquisitions from Run03 that were reprocessed, allowing 100 pulses to be found instead of the usual 10. The livetime of each acquisition is indicated in red, while the cumulative percentage of the available livetime is in blue. . . . .	115
Figure 76	A plot of the expected rate of number of S2 pulses as a function of charge fraction. The flux for all charge fractions is assumed to be $\Phi = 1/\text{Large Underground Xenon (LUX)}/\text{day}$ . As the charge fraction increases, the expected rate of events (black) decreases because only some events will deposit enough energy to be above threshold to trigger the detector. The fall-off is more severe when a certain number of well-reconstructed S2 pulses is required. . . . .	116
Figure 77	A 2D histogram of number of corrected S2 pulses versus the sum of all pulse area in the event. A cut is placed requiring the number of S2 pulses to be greater than 4. Only the first acquisition, lux10_20130515T0811_cp26812, is plotted for the demonstration. . . . .	118
Figure 78	A 2D histogram of the standard deviation of the corrected S2 pulse area versus the $\chi^2/\text{dof}$ from the track fit. A cut is placed requiring $0 < \chi^2/\text{dof} < 1$ . The top plots are shown with no cuts, the bottom plots are shown with the previous cut applied, the counts in red indicate how many events will be left after this cut. Only the first acquisition is plotted for the demonstration, all LIP charge fractions are shown. . . . .	118

Figure 79	A 2D histogram of the standard deviation of the corrected S2 pulse area versus the fit length divided by the “data length”. The fit length $L_{fit}$ is the reconstructed track length. The data length $L_{data}$ is defined as the distance between the first and last (corrected) S2 positions. The factor $L_{fit}/L_{data}$ is a measure of whether the event subtends the detector. A cut is placed requiring $0.9 < L_{fit}/L_{data} < 1.5$ . In general $L_{fit}$ is expected to be larger than $L_{data}$ , as the <a href="#">LIP</a> may travel some distance into the <a href="#">LXe</a> before depositing energy. The top plots are shown with no cuts, the bottom plots are shown with the previous cut applied, the counts in red indicate how many events will be left after this cut. Only the first acquisition is plotted for the demonstration, all <a href="#">LIP</a> charge fractions are shown. . . . .	119
Figure 80	A 2D histogram of the standard deviation of the corrected S2 pulse area versus the corrected S2 energy divided by $L_{fit}$ . The S2 energy is reconstructed using $E_{S2} = W(S2/g2)$ . The top plots are shown with no cuts, the bottom plots are shown with the previous cut applied, the counts in red indicate how many events will be left after this cut. Only the first acquisition is plotted for the demonstration, all <a href="#">LIP</a> charge fractions are shown. . . . .	120
Figure 81	A 2D histogram of the standard deviation of the corrected S2 pulse area versus the ratio of the first 2 to the last 2 area corrected S2 pulses. A cut using the ellipse shown is applied. The top plots are shown with no cuts, the bottom plots are shown with the previous cut applied, the counts in red indicate how many events will be left after this cut. Only the first acquisition is plotted for the demonstration, all <a href="#">LIP</a> charge fractions are shown. . . . .	121

Figure 82	A 2D histogram of the standard deviation of the corrected S2 pulse area versus the reconstructed polar angle of the track. A cut requiring $\theta > 20$ deg is placed because a disproportionate number of the background electron train events appear as vertical-going LIPs. The true acceptance for LIPs is very limited at small polar angles, so a cut on the entry angle does not result on a large loss of signal efficiency (see Figure 61). The top plots are shown with no cuts, the bottom plots are shown with the previous cut applied, the counts in red indicate how many events will be left after this cut. Only the first acquisition is plotted for the demonstration, all LIP charge fractions are shown. . . . .	122
Figure 83	A 2D histogram of the raw S2 pulse area normalized to the first S1 area versus corrected S2 pulse area normalized to the first S1 area. A cut requiring events to be inside the indicated ellipse is applied. This is essentially an “S1-normalized” bad area cut, requiring that the pulse area in the event mostly goes into S2 area that has successful position reconstruction. The area that is being cut in the LIP plot is loss in lower $f$ , where some area is partitioned into raw S2. The top plots are shown with no cuts, the bottom plots are shown with the previous cut applied, the counts in red indicate how many events will be left after this cut. Only the first acquisition is plotted for the demonstration, all LIP charge fractions are shown. . . . .	123

Figure 84	A 2D histogram of the standard deviation of distances between the raw positions of S2s in an event versus the $\chi^2/dof$ . A cut requiring the standard deviation between points to be less than 8 cm is applied. The top plots are shown with no cuts, the bottom plots are shown with the previous cut applied, the counts in red indicate how many events will be left after this cut. The top data plot shows only the first acquisition. The bottom data plot shows the remaining events in the first 13 acquisitions after previous cuts were applied. All LIP charge fractions are shown.	124
Figure 85	A 2D histogram of the Anderson-Darling test statistic versus the sum of the area before the first S1. A cut is placed requiring the Anderson-Darling test statistic to be less than 2 and the area before the first S1 to fall between 0 phd and 10 phd, inclusive. The x-axis actually shows $\log_{10}$ of the pre-S1 area, so all events with zero area before the S1 are not shown on the plot; however, these events are retained in the cut. The top plots are shown with no cuts, the bottom plots are shown with the previous cut applied, the counts in red indicate how many events will be left after this cut. The top data plot shows only the first acquisition. The bottom data plot shows the remaining events in the first 13 acquisitions after previous cuts were applied. All LIP charge fractions are shown.	125
Figure 86	The efficiencies for each subsequent cut as a function of charge fraction. The detection efficiency is taken to be the logical and of all the cuts.	126
Figure 87	Two examples of the $\chi^2/dof$ dependence on $dE/dx$ . The plots show the $\chi^2/dof$ versus the reconstructed $E/L$ for two different charge fractions.	127
Figure 88	Examples of the 5% bins used in the sampling procedure to asses the systematic error are overlaid (gray dotted lines) on histograms of $\chi^2/dof$ versus the reconstructed $E/L$ for two different charge fractions.	128

Figure 89	(left) $\chi^2/dof$ versus $E/L$ for $f = 100$ . (right) The resampled $\chi^2/dof$ distribution versus $E/L$ after shifting the original $E/L$ by a factor of 1.13. 128	
Figure 90	The systematic efficiencies of each subsequent fit. 129	
Figure 91	The vertical flux limit from 278.47 hours of live- time during LUX Run03 compared to other re- cent flux limits. The result of this analysis is shown in black, with grey bands indicating the combined statistical and systematic error on de- tection efficiency. . . . . 130	
Figure 92	Large scale view of the experimental apparatus showing key parts. The CF tower extent is in- dicated with a dotted line; this whole tower is also part of the inner xenon space. . . . . 133	
Figure 93	Diagrams of two often used internal arrange- ments. The configuration (left) has both a drift and extraction region. The configuration (right) is “extraction region only”. The blue region with the wavy line indicates the liquid level. . . . . 134	
Figure 94	Pumping and instrumentation diagram of the test bed. Special symbols are labelled in the di- agram, see key for other symbols. For readabil- ity, all gauges are not shown. . . . . 134	
Figure 95	A diagram showing components of the slow con- trol. . . . . 135	
Figure 96	(left) Segmented anode showing the xenon-facing anode segments. The innermost segment is re- ferred to as the “bullseye”, the next is called the “inner ring” and the last is called the “outer ring”. The largest segment on the anode was not in- strumented with charge amplifiers and was held at ground. (right) The wires on the top of the anode which lead to the charge amplifiers. . . . 136	
Figure 97	A picture of the CR-110 charge amplifier from the manufacturer’s data sheet, shown with an equivalent circuit diagram. . . . . 137	
Figure 98	A raw (cyan) and shaped (yellow) charge amp signal taken in -100C gaseous xenon, with the radon source plumbed in. The PMT signal is vis- ible in blue and the NIM trigger signal is in ma- genta. . . . . 137	

Figure 99	(left) original mounting of CR-110 charge amplifiers inside the experimental vessel. (right) Mounting in the outer vacuum reduced heat load on the <b>TPC</b> . In the outer vessel, the charge amplifiers were surrounded by a Faraday cage constructed from copper mesh to reduce noise. . . . .	138
Figure 100	Different lengths of BNC cable attached to a CR-110 test board to show the RMS noise relationship to input capacitance. Two equal length segments (calculated to be 33.3 pF) were observed to have slightly different properties. . . . .	139
Figure 101	(left) Event showing charge amp with detector -100 C, 1.5 bar, gas only (time scale 1.00 ms/div). (middle) Effect of circulation pump on charge amp is to cause 500 Hz oscillation noise (-100 C, 1.5 bar, gas only (time scale 1.00 ms/div)). (right) Same event as (middle), but zoomed-in time scale (10.0 $\mu$ s/div). In all figures, cyan is the raw charge signal (1 mV/div), yellow is the shaped charge (100 mV/div), blue is the <b>PMT</b> (10 mV/div) and magenta is the <b>NIM</b> trigger (100 mV/div). . . . .	140
Figure 102	An event with the detector at -100 C, 1.5 bar, with liquid condensed to a level between extraction grid and anode. In both figures, cyan is the raw charge signal (1 mV/div), yellow is the shaped charge (100 mV/div), blue is the <b>PMT</b> (10 mV/div) and magenta is the <b>NIM</b> trigger (100 mV/-div). (left) Scope trace showing a long time view the raw and shaped charge amplifier signals (time scale 1.0 ms/div). (right) Scope trace showing the same event, but zoomed in (10.0 $\mu$ s/div). The baseline restorer on the shaped charge signal allowed it to be used as a trigger. . . . .	140
Figure 103	(left) 50 kHz periodic noise from the Glassman 20 kV negative polarity voltage supply. (right) Partial breakdown in coaxial High Voltage ( <b>HV</b> ) cable as picked up by charge amplifiers. In both figures, the time scale is 10.0 $\mu$ s/div and the voltage scale is 2.00 mV/div. . . . .	140
Figure 104	(top) Laboratory method to find the maximum <b>DAQ</b> record time time. (bottom) Calculating dead time from maximum record rate. . . . .	142

Figure 105	Fitting the charge traces with a piece-wise defined linear rise and exponential fall. 1 sample is 8 ns. . . . .	144
Figure 106	The step-finding algorithm shown with a choice of 20 samples averaged (left) and with 50 samples averaged (right). If $n_s$ is chosen to be the rise time of the pulse, the height of the output waveform is the height of the step. These step algorithms actually include an offset, $n_o = 1000$ , so the averages are taken from $[i + n_o + n_s, i + n_o + 2n_s]$ and $[i + n_o, i + n_o + n_s]$ . Alternatively, a smaller number can be chosen for $n_s$ , and the location of the maximum of the output waveform can be used to find the location of the top of the step (shown in Figure 107). 1 sample is 8 ns. . . . .	145
Figure 107	The location of the top of the step can be robustly found from the location of maximum of the step-finding algorithm. Some number of samples at the top of the step can be averaged to give the step height. 1 sample is 8 ns. This particular example uses $n_s = 20$ . The step-finding algorithm is calculated with an offset, $n_o = 1000$ , so the averages are taken from $[i + n_o + n_s, i + n_o + 2n_s]$ and $[i + n_o, i + n_o + n_s]$ . If the peak location (red peak) is $n_p$ , then the approximate location of the step is $n_p + n_o + 2n_s$ , and some number of samples of the original trace (50 samples shown in green) can be averaged to give the step height. . . . .	146
Figure 108	An alpha event showing the Shockley-Ramo effect on the inner and outer ring segments of the anode. The top plot shows the PMT trace and the bottom plot shows the shaped response of the anode segments. The Shockley-Ramo effect is the rise (around 4700 samples) and subsequent dip (around 5500 samples) of the inner and outer ring traces. The event happened under the bullseye segment, but the other traces see the field line density increase and then disappear, producing both an increase and decrease in the shaped anode signal. . . . .	147

Figure 109	A 12kV SHV weldable connector from vacuum supplier Kurt Lesker. . . . .	148
Figure 110	(left) The copper tape in this picture is sitting on top of a 1/2 inch swage connector (indicated by the arrow). The swage connector captures a 1/2 in pipe, which has the 12 kV SHV feedthrough welded to the end. (right) 12 kV SHV weldable connector, inverted, clipped, and attached with a machined copper connector. The connector uses a screw to capture the SHV feed though, and the same screw to capture a stranded wire, visible in this picture as the silver strands on the copper tip, which is then fed through a hole drilled in the PTFE to connect to the wire grid frames. The wire was wrapped around the grid frame. . . . .	149
Figure 111	(left) The same 12 kV SHV feedthrough as in Figure 110, now with a modified spring connection connecting the feedthrough to the grid frame. (right) A close-up of the cathode grid showing the spring connection. . . . .	150
Figure 112	Oscilloscope showing baseline rate of single photons (left) compared to a high rate of single photons (right) caused by the high voltage feedthrough. . . . .	150
Figure 113	(left) Full xenon breakdown as visible on the PMT trace. The large, saturated pulse is caused by the high intensity of light. This type of breakdown was often accompanied by an audible buzz, and a rise in current that would initiate a trip of the high voltage supply. (right) a close up of the xenon-facing side of the feedthrough. The arrows indicate visible gaps where xenon gas is exposed to high fields. These areas are particularly problematic for breakdowns. . . . .	151
Figure 114	Design of high voltage delivery system based on an SHV-20 feedthrough. (top left) cathode connection side (top right) SHV-20 connection side. (bottom left) an example showing how the cable was attached to the stock SHV-20 feed though end (bottom right) a custom cap fit over the connection, smoothing out triple points. The cap had a hole at the tip to allow the cable to pass through. . . . .	152

Figure 115	Effect of holding the feedthrough in place with PEEK zip ties was explored. The voltage properties were not found to improve, but neither did they degrade. . . . .	152
Figure 116	The black line shows the aging observed in the course of normal operations. The red line shows breakdown tests of the SHV-20 feed though in gas, illustrating that the aging observed during operation was due to aging of the feed though. .	153
Figure 117	First attempt at a custom feedthrough built out of Swagelock parts combined with basic materials like PTFE and stainless steel rods. The orientation shown (left) was later inverted due to concerns of temperature stress and pressure stress on the PTFE ferrules. The feedthrough as assembled (center) was functional, but higher voltage capability was desired. The effect of adding a grounding braid (right) was found to decrease the voltage capability instead of increasing it. .	154
Figure 118	(top) Input to a COMSOL model simulating gaps between the grounding braid and dielectric of a high voltage feedthrough. (bottom) COMSOL output of the model, showing that peak fields arise when gaps exist between dielectric and grounding braid. Both images provided by W. Waldron.	155
Figure 119	Top: (left) Close up showing the PTFE ferrules and notch. (right) Close-up of the sealed top connection. Although the PTFE ferrules and some epoxy where the rod exited the PTFE tube kept an acceptable vacuum and pressure seal, more epoxy was added during installation on the experimental vessel inside the swage nut near the ferrules. Bottom: (left) Threaded U-bend cathode connector (right) Feedthrough assembled and installed. . . . .	157

Figure 120	Top: (left) Sealed top connection with liberal epoxy use. A male Bendix pin was soldered to the cable conductor. (middle) SHV connector with female Bendix to mate with feedthrough (right) Grounded safety housing with SHV connector. Bottom: (left) Ends of the feedthrough were held in the Teflon stack. (middle) Close up showing cable conductor, PTFE dielectric, and grounding sheath pulled back. The calipers are measuring the length of exposed conductor. (right) Grounding scheme for feedthrough cables at the top of the CF tower. . . . .	159
Figure 121	(left) COMSOL model with specific cathode voltage and liquid level. The peak fields of $\sim 130$ kV/cm occur on the wires, and the gas fields are $\sim 20$ kV/cm. These two values are both dark red on the color scale, which can be misleading. (right) Analytic calculation following the McDonald notes [121], which shows how the peak fields vary with change in liquid level and cathode voltage. The voltages in the legend refer to the cathode voltage; the anode is held at ground. . . . .	160
Figure 122	Ranges for the electric fields in gas and liquid for different cathode voltages and liquid levels. .	161
Figure 123	The $^{222}\text{Rn}$ decay scheme. The fast and slow chains are indicated. Data from [127], image provided by K. Lesko and modified for this thesis. . . . .	163
Figure 124	Pathways to radon and radon daughter contamination. . . . .	164
Figure 125	Diagram of the test bed. For this study, the cathode is held at -6.0 kV, and the grid is held at -4.0 kV. $E_1^{\text{liq}} \approx 5.0$ kV/cm, $E_1^{\text{gas}} \approx 10.0$ kV/cm $E_2 = 1.0$ kV/cm. $E_3 = 2.7$ kV/cm. The large gray regions represent the structural rings of PTFE. The line between the grid and anode represents the liquid xenon level. The xenon inlet pipes incoming gas directly into the liquid region, and the liquid outlet pulls from the level of the active region. A gas outlet (not pictured) also draws xenon gas into the circulation system to be purified. . . . .	166

Figure 126	An example a circulation path used for plate out is shown on the pumping and instrumentation diagram. During data-taking the radon source was bypassed. The typical liquid level is indicated on the diagram to show that the outlet drew from the liquid via a capillary, ensuring purification of the liquid xenon. A gas purge also purified the gas column in the detector. . .	167
Figure 127	The $^{220}\text{Rn}$ decay scheme. The fast and slow chains are indicated. Events in the plate out data sets are from the slow chain. Data from [127], image provided by K. Lesko and modified for this thesis. . . . .	168
Figure 128	(a) and (b) and (c) show the plate out conditions of datasets A, B, and C, respectively. The gray bands indicate time when data was being acquired. Dataset D (calibration) was taken following dataset A and consisted of a few hours. .	172
Figure 130	Monte Carlo study to find the maximum distance a $^{212}\text{Bi}$ beta (2.2 MeV) on the cathode could penetrate into the drift region. The projected range (red) is the relevant curve for this analysis; it shows a beta is not expected to travel more than 1.2mm from the cathode. The plot inset describes the difference between the two ranges: the CDSA range is a measure of the entire path length travelled, the projected range is the one-dimensional maximum range. . . . .	175
Figure 131	For datasets A and B: (left) Distribution of events in z. (right) The same events distributed in the S1-S2 plane, showing selection criteria for candidate $^{212}\text{Bi}$ alpha events in the bulk liquid xenon.	176
Figure 132	For datasets C and D: (left) Distribution of events in z. (right) The same events distributed in the S1-S2 plane, showing selection criteria for candidate $^{212}\text{Bi}$ alpha events in the bulk liquid xenon. The calibration cut shown for dataset D (bottom right) selected events within the region indicated at 98% efficiency. That is, all the gray points passed the [topology] cuts to identify a bulk $^{220}\text{Rn}$ alpha decay, and the circle restricts the signal region further, keeping 98% of the gray points. . . . .	177

Figure 133	An electron train spanning several ms. Pre-trigger and electron train regions are indicated along with the <a href="#">LUX</a> event that originated the electron train. The inset shows the shorter time structure of e-burps. The y-axis is a proxy for phd/sample. Figure courtesy of J. Xu. . . . .	<a href="#">184</a>
Figure 134	A histogram of the small electron signals in the Xenon10 low-mass dark matter search. The significance of the plot is that single/few-electron pluses immediately following an S2 can be positively identified as belonging to an electron train. In subsequent event windows, single electrons can appear alone or in coincidence as a small S2, which can be mistaken for the S2 produced by a low-mass dark matter interaction. Figure adapted from [86]. . . . .	<a href="#">184</a>
Figure 135	The average of many high energy S2s from <a href="#">LUX</a> , plotted with logarithmic y-scale, showing a prominent photoionization feature. After the photoionization, an instrumental effect is visible: for the highest-energy events, one to a few <a href="#">PMT</a> s often do not return to baseline quickly, which gives the single electrons in the following train artificially higher areas. Figure from J. Xu. . .	<a href="#">186</a>
Figure 136	(left) The per-event rate of single electron signals 20 to 150 $\mu$ s after the main S2 of a single-scatter type event as a function of the main S2 size. The fit line and residuals show a good proportionality in the relation. (right) The per-event rate of single electron signals, for events with the main S2 between 5000 and 10000 phe, as a function of the O2-equivalent concentration of impurities in liquid xenon. Figures from [139]. .	<a href="#">187</a>
Figure 137	(left) The absolute <a href="#">EEE</a> measured by Gushchin from [140]. The <a href="#">LXe</a> points were re-colored red. (right) Two relative <a href="#">EEE</a> measurements from modern experiments, Xenon100 and PIXEY, compared to Gushchin. The plot is from the PIXEY result [141], where the authors fit their result with a quadratic function ( $y = ax^2 + bx + c$ ). The fit to the PIXEY data (black dashed line) is scaled by a constant and applied to the Xenon100 data (blue dotted line). . . . .	<a href="#">188</a>

Figure 138	(left) Effect of anode saturation measured as deviation from signal linearity as a function of the peak anode current. (right) Effect of capacitor depletion on the voltage trace in the R8778. The blue trace shows the largest S2-like pulse that can be generated with a LUX voltage divider base (generated with a $1 \mu\text{s}$ square pulse on a blue LED); the 2% and 5% deviations from linearity are shown. The fall-off indicates the capacitor is depleted and the photomultiplication process is temporarily turned off. The black trace shows the effect of adding an extra capacitor between dynodes Dy9-Dy10. Figures are from [91], which also contains more information about the LUX PMTs and bases. . . . .	192
Figure 139	A series of PMT masks made from CF blanks which reduced the light collection area of the PMT to approximately 2%, 5%, 15%, and 10% (clock-wise from top left). The masks were installed in place of the PMT shield grid, and similarly to the PMT grid, they were kept at the same bias voltage of the PMT. . . . .	193
Figure 140	The single phe spectrum from the PMT with a bias voltage of 1300 V. The spectrum was obtained by using a variable gain amplifier to 100x amplify the PMT signal (at room temperature, in vacuum). A NIM quad discriminator was used to externally trigger the picoscope. The waveforms were summed in a fixed window, and the results were histogrammed. The single photo-electron peak is appears around 80 mV/ns, and the double photoelectron peak is visible around 160 mV/ns. (See [72] for more detail on the double photoelectron emission in VUV-sensitive PMTs.)	194

Figure 141	Bunemann's condition for grid transparency for a grid voltage of -4.0 kV. The cathode voltage must be between -7.24 kV and -4 kV to achieve grid transparency. A cathode voltage greater than -4 kV would result in a "reverse field", with the electrons drifting downward to the PMT instead of the upward to the gas gap. For cathode voltages below -7.24 kV (more negative), field lines terminate on the grid and the charge is deposited there instead of proceeding upward to be extracted. . . . .	195
Figure 142	Ionization charge vs. drift time presented in both S2 (left) and charge amplifier voltage from the central anode segment (right). The events are $^{220}\text{Rn}$ and $^{216}\text{Po}$ alpha decays from the radon source. A ~50% drop in signal is visible between events occurring above the grid and events occurring below the grid. The effect of purity is also visible in the fall off of the charge signal with drift time. The points under the obvious line in the charge amplifier plot are from events which share charge with other anode segments. The charge amplifier approaches its threshold at the cathode, indicated by the sharp cut-off at 0.1 V. . . . .	196
Figure 143	The testbed configuration used in [146]. There is only a cathode grid and anode, with no separate drift region. The TPC can be thought of as "extraction region only". . . . .	197
Figure 144	(left) Method for depositing $^{210}\text{Po}$ on the cathode was to use a dropper to submerge a section of wire in polonium chloride and allowing the liquid to evaporate. (right) This method was robust for depositing $^{210}\text{Po}$ on the cathode, as evidenced by an alpha population with drift consistent with the cathode. . . . .	198
Figure 145	$^{210}\text{Po}$ decay scheme. Data from [127]. . . . .	198
Figure 146	Decays on grid wires experience different field strength depending on particle trajectory, this results in different recombination. Adapted from [151]. . . . .	198

Figure 147	(top) Recoiling $^{206}\text{Pb}$ nucleus. (bottom) $^{210}\text{Po}$ alpha decay. Capacitor depletion is visible in the S2 shape, and $\sim 20 \mu\text{s}$ dead time between the S2 and start of the electron train. Insets on both (top) and (bottom) show detail of the event S1 and S2, and electron train segments. Figure from [146]. . . . .	199
Figure 148	Stacked waveforms and fits from a dataset with cathode voltage at -4 kV. Figure from [146]. . .	200
Figure 149	Examples of the charge amplifier mirror effect on one anode segment. The example (left) is an event where charge is collected on the anode segment, and so the charge amplifier signal trace shows a step. The example (right) shows the charge trace mirroring the PMT, but with no charge collected on the anode segment. . . . .	201
Figure 150	Histogram of charge amplifier step height for a cathode voltage of -3 kV. The histogram is skewed by wire position-dependent recombination; the same effect is visible in Figure 144 (right). This mean of the fit was converted to electrons using the manufacturer's specification of charge amplifier gain, 1.4 V/pC. 5.5mV converts to 24500 electrons. . . . .	202
Figure 151	Single electron and photoelectron peaks obtained in liquid conditions for a PMT bias voltage of 1500 V. . . . .	203
Figure 152	$\kappa$ is the extraction efficiency as in Equation 61, so unextracted electrons should scale as $(1 - \kappa)$ . In this thesis, (a) is reference [140], an absolute measurement of EEE; (b) is reference [141], a relative measurement of EEE. The methods use different methods and assumptions; they are shown to illustrate that the fast component follows the behavior trend of what is expected from unextracted electrons. . . . .	203



## LIST OF TABLES

---

Table 1	A summary of the fit parameters and derived quantities from Planck's 2018 results [24]. . . . .	17
Table 2	Possible dark sector portals, related dark matter candidates, and operators that connect the dark sector to the SM. Table from [37]. . . . .	24
Table 3	Dimensions of the of the anode segments. 1 refers to the inner-most segment or “bullseye”, 2 refers to the inner ring, 3 to the outer ring and full to the entire anode, which includes inactive area that is not instrumented with charge amplifiers. . . . .	136
Table 4	Summary of plate out and data-taking conditions. Data sets A and B were taken after circulating radon gas and data set C, background, had no radon circulation. Data set D was taken following dataset A, and radon was circulated in a liquid xenon environment, purposefully introducing radon into the detector bulk to calibrate the detector response. The errors in live-time come from the fact that it is not recorded when datasets ended, only when they started. The error accounts for a new data set not beginning promptly after another dataset finishes.	169
Table 5	Calculations of fiducial volume. The liquid level is taken to be $14 \pm 1$ mm. The density of LXe near its boiling point is taken to be 2.9 g/mL . . .	171
Table 6	Number of detected alpha particle events whose energy determination was consistent with $^{212}\text{Bi}$ decay to $^{208}\text{Tl}$ . Live times are quoted in Table 4	178
Table 7	Using observations from Table 6, proceed through solubility calculation. . . . .	182

## ACRONYMS

---

- SM Standard Model  
BSM Beyond the Standard Model  
SUSY Supersymmetry  
MSSM Minimal Supersymmetric Model  
LSP Lightest Supersymmetric Particle  
WIMP Weakly Interacting Massive Particle  
LIP Lightly Ionizing Particle  
CDM Cold Dark Matter  
DM Dark Matter  
MOND Modified Newtonian Dynamics  
NFW Navarro-Frenk-White  
CMB Cosmic Microwave Background  
 $\Lambda$ CDM “Lambda” CDM  
LHS Left Hand Side  
RHS Right Hand Side  
GUT Grand Unified Theory  
LSP Lightest Super Partner  
BBN Big Bang Nucleosynthesis  
GMSB Gauge-Mediated Supersymmetry Breaking  
ALP Axion-like Particle  
QED Quantum Electrodynamics  
LHC Large Hadron Collider  
CDMS Cryogenic Dark Matter Search

MJD	Majorana Demonstrator
LUX	Large Underground Xenon
LZ	LUX-Zeplin
LXe	Liquid Xenon
LAr	Liquid Argon
TPC	Time Projection Chamber
SURF	Sanford Underground Research Facility
ER	Electron Recoil
NR	Nuclear Recoil
UV	Ultra Violet
VUV	Vacuum Ultra Violet
DPF	Data Processing Framework
LUG	LUX Electronic Log
DAQ	Data Acquisition
FPGA	Field Programmable Gate Array
POD	Pulse Only Digitization
ADC	Analog-to-Digital Converter
SE	Single Electron
SPHE	Single Photoelectron
LRF	Light Response Function
RQ	Reduced Quantity
DD	Deuterium-Deuterium
PVC	Polyvinylchloride
MFC	Mass Flow Controller
NEST	Noble Element Simulation Technique
HV	High Voltage
SHV	Safe High Voltage

SS Stainless Steel  
CF Conflat  
PMT Photomultiplier Tube  
QE Quantum Efficiency  
EEE Electron Extraction Efficiency  
LBNL Lawrence Berkeley National Laboratory  
NIM Nuclear Instrumentation Module  
IV Inner Vessel  
OV Outer Vessel  
RTD Resistance Temperature Detector  
LN Liquid Nitrogen  
PTFE Polytetrafluoroethylene  
PEEK Polyether ether ketone  
RMS root mean square  
CCS Collisional Cross Section  
PAI Photo Absorption Ionization  
FVP Fermi Virtual Photon  
PDF probability distribution function  
CDF cumulative probability distribution function  
LBECA Low Background Electron Counting Apparatus

# 1

## INTRODUCTION

---

*I was dreamin' when I wrote this, forgive me if it goes astray.*

— Prince, 1999, 1989

This thesis is laid out in four main sections.

Part I, Theoretical Context and Experimental Strategies, deals with the evidence for dark matter and theoretical background for different dark matter candidates. An overview of experimental strategies to detect dark matter is then given, going into detail for one particular detection strategy, the dual-phase [LXe](#) Time Projection Chamber ([TPC](#)).

Part II, Big Science, delves into details about the [LUX](#) detector, a dual-phase [LXe TPC](#), and presents a search for the Lightly Ionizing Particle ([LIP](#)) dark matter candidate carried out with [LUX](#) data.

Part III, Little Science, describes an R&D test bed that was built at Lawrence Berkeley National Laboratory ([LBNL](#)) over the course of this PhD and describes two studies completed with the test bed.

Part IV, Conclusions, summarizes the work presented in this thesis and provides outlook for future experiments.

## PART I

# THEORETICAL CONTEXT AND EXPERIMENTAL STRATEGIES

This section describes the theoretical foundation for the analysis presented in [Part II](#). It includes a summary of the evidence for dark matter, and an overview of the Standard Cosmology and Standard Model of Particle Physics. Theoretical dark matter candidates are motivated and detection schemes for detecting these theoretical particles are presented. Particle detection in liquid xenon and the dual phase [LXe TPC](#) detector technology are discussed in detail.

# 2

## THEORETICAL BACKGROUND

---

### 2.1 A BRIEF HISTORY OF DARK MATTER

Our understanding of the universe develops in a leap-frog of theory and observation, one catching up to and surpassing the other as technology improves, to be passed in turn by a new idea or new observation. The picture of dark matter commonly accepted today is much different than what Zwicky anticipated in 1933 when he found that the velocity dispersion of the galaxies in the Coma Cluster was much larger than expected from the Virial Theorem [1]. This observation is typically cited as popularizing the term “dark matter”, and starting the hunt for the mysterious invisible substance. Zwicky postulated that the faster rotation was caused by dark matter consisting of cold gas or stars and both macro- and micro-scopic solid bodies, and estimated that there was about 400 times more dark matter than visible matter. Smith, a contemporary of Zwicky’s, did a similar analysis with the Virgo Cluster and his results yielded a much smaller dark matter to visible matter ratio [2]. Meanwhile, many in the astrophysics community disagreed with an underlying assumption of these analyses and argued that galaxy clusters are not at equilibrium so the Virial Theorem does not apply [2]. At the time, the only consensus reached was that more information was needed to understand the dynamics of galaxy clusters.

In the 1970’s, a new technology called the image tube spectrograph allowed Vera Rubin and Kent Ford, the developer of the spectrograph, to measure the rotational velocity of the Andromeda Galaxy at different points along its radius (called a galactic rotation curve) [3]. The new data were of higher quality than previous attempts at measuring galactic rotation curves, and the result, that the galaxy was rotating faster than expected at large radius, indicating “hidden mass,” was soon replicated by others [2]. Over the next decade, a significant number of galactic rotation curves were obtained, all showing essentially the same result: galaxies were rotating faster than expected at high radii, indicating that the masses of galaxies continued to grow past where their lights dimmed. A figure showing this characteristic behavior in 21 galaxies from a 1980 review paper [4] is shown in Figure 1. Another argument in favor of dark

matter came from contemporary numerical simulations of galactic gravitational dynamics. At first, many simulations showed that disk galaxies were unstable, in contradiction with many observations [2]. However, Ostriker and Peebles demonstrated that if the galactic disk was embedded in a massive (i.e. gravitationally interactive) spherical halo, the disk was stable [5].

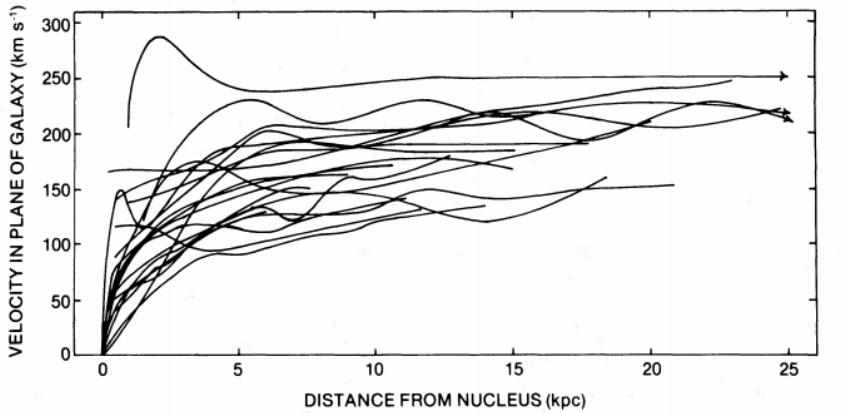


Figure 1: Superposition of 21 rotation curves from galaxies with a large range of radii and luminosities. All of these galaxies have a distinctive flat rotation curve at large radii. Figure from [4].

In order to explain the behavior of galactic rotation curves without dark matter, Milgrom proposed Modified Newtonian Dynamics (**MOND**) in a trio of 1983 papers, [6], [7], [8]. Milgrom showed that if Newtonian dynamics was modified from  $F = ma$  to  $F = ma/a_0$ , for a  $\ll a_0 \approx 1.2 \times 10^{-10} m/s^2$  the observed galactic rotation curves could be accounted for without requiring any hidden or dark matter. Milgrom's goal in these first papers describing **MOND** was to present an approximate limit of some as-yet unknown full theory, which he and others went on to develop in the following decades [2]. However, theoretical and technological advancements in the fields of cosmology and astronomy have made **MOND** an unsatisfying theory, unable to explain several observed phenomena. Of these phenomena, gravitational lensing and the Cosmic Microwave Background (**CMB**) are discussed further below.

Big-Bang cosmology had a large success in 1965 with Penzias and Wilsons' observation of the **CMB**. It was in the 1980's however, that cosmology, particle physics, and astronomy became tied together as they are understood today, and dark matter came to refer to an as yet undiscovered particle species and not the cold gas and stars of Zwicky's day [2]. The root of this paradigm shift was in the new theory of cosmological inflation [2]. Inflation refers to a period of exponential expansion  $10^{-36}$  to  $10^{-33}$  seconds after Big Bang. Without an inflationary period, fluctuations would

be washed out as the universe expanded, leading to a universe devoid of structure. Inflation, however, provides a mechanism for quantum fluctuations to be ‘blown up’ and seed the structure observed by the 1982 CfA redshift survey (Figure 2). Numerical simulations to reproduce the structure seen by the CfA redshift survey benefited from new improvements in processing speed and numerical techniques, and also from the new theory of inflation, which provided a physical reason for initial density perturbations [2]. The structure was reproduced only in the presence of gravitationally-interacting dark matter. It is interesting to note here that these cosmological simulations were largely insensitive to any additional, non-gravitational interactions the dark matter had, as long they were sufficiently weak. However, the simulations did require the dark matter to be non-relativistic or “cold”. Such dark matter is referred to as Cold Dark Matter ([CDM](#)), and plays a prominent part in the standard cosmology to describe the structure and evolution of our universe.

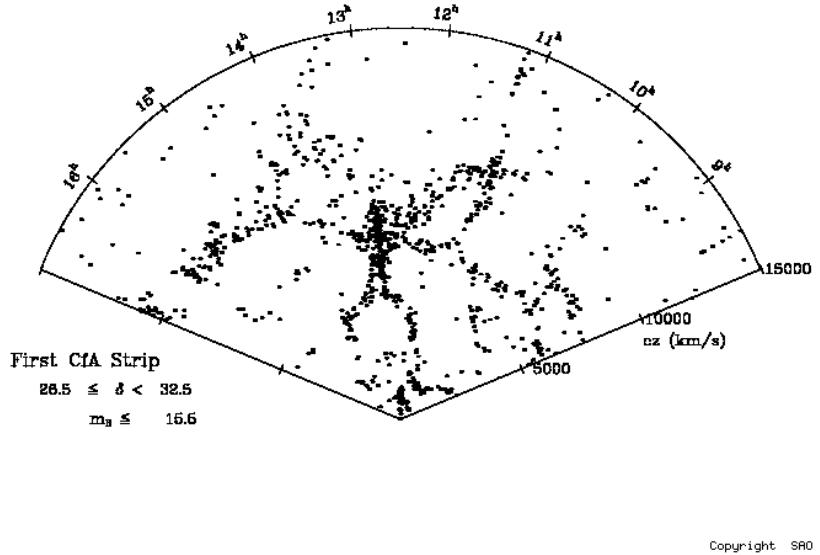


Figure 2: CfA Redshift Survey result showing the distribution of galaxies in a strip on the sky about 6 degrees wide and 130 degrees long. The radial coordinate is redshift, in km/sec, calculated with a Hubble constant of 20km/sec/million ly. Figure from [9].

## 2.2 EVIDENCE FOR DARK MATTER

The previous section gave an overview of why [CDM](#) has become, over the last century, the leading paradigm to explain the small and large-scale

structure observed in our universe. The following subsections deal with particular pieces of evidence, discussed in detail.

## 2.2.1 GALAXIES AND CLUSTERS

Galactic rotation curves were discussed above as evidence for dark matter halos. Here we further discuss the properties of dark matter halos. An example of a galactic rotation curve of a spiral galaxy showing the presence of an inferred dark matter halo is shown below in Figure 3. Each side of Figure 3 shows the same galaxy, NGC 3198, but fit with a different disk and halo model. In this particular example from 1985, the authors note their uncertainty about which halo model is the correct one: “Should one seriously consider the case where the amount of visible matter is negligible with respect to the amount of dark matter [Figure 3 (left)]? Or is the maximum disk case [Figure 3 (right)] closer to the truth?” [10]. A decade later, in 1996, Navarro, Frenk and White published a paper describing high-resolution simulations of CDM, which could all be fit with a universal dark matter halo profile [11]. This formula became known as the Navarro-Frenk-White (NFW) profile; it is still widely used today, and is the basis for many direct detection experiments, including LUX. The NFW profile showed that Figure 3 (left) is the preferred model, where the amount of dark matter far outweighs the amount of visible matter.

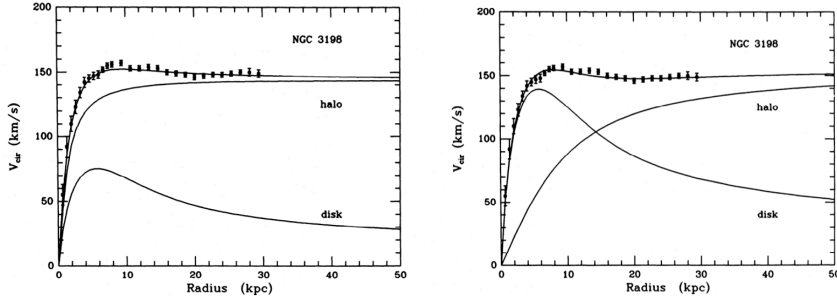


Figure 3: Galactic rotation curve from [10] fit with two different dark matter halo models. The Figure (left) is closer to the rotation curve produced by dark matter with an NFW profile (see [11]), and our understanding of the ratio of dark matter to visible matter in most spiral galaxies.

The astrophysics community is nearly unanimous in agreement that galaxies have a dark matter component. Today, research continues into the particular shape of the dark matter profile. While NFW is in common use and agrees with many observations, it is not consistent with observations of low surface brightness and dwarf galaxies [12], [13]. This known as the core-cusp problem: NFW galaxies have an over-density of dark matter at small radius (cuspy), while dwarf galaxies favor flatter density pro-

files (core). Some argue that such behavior may be a consequence of the nature of dark matter, or that current simulations are not sufficient to properly understand dwarf galaxies [14]. Others argue that a cusp can be changed to a core via baryonic feedback that arises in simulations of active galactic nuclei [15].

Other current research into dark matter halos centers on the globular clusters and stars that orbit the Milky Way. These researchers look for evidence of halo substructure and streams of dark matter from the movements of stars orbiting the Milky Way. Data from the Gaia satellite, launched in 2013, calls into question whether dark matter halos are truly in equilibrium, which has consequences for direct detection experiments, as it would change the expected dark matter recoil spectrum [16] [17]. In particular, [16] measures the velocity distribution of the Milky Way from populations of stars with different metallicities, and finds that the empirical velocity distribution is shifted toward lower velocities and has a slightly different shape when compared with the standard halo model. See Figure 4 for the velocity distributions and the inset for the effect on the resulting zero background limits.

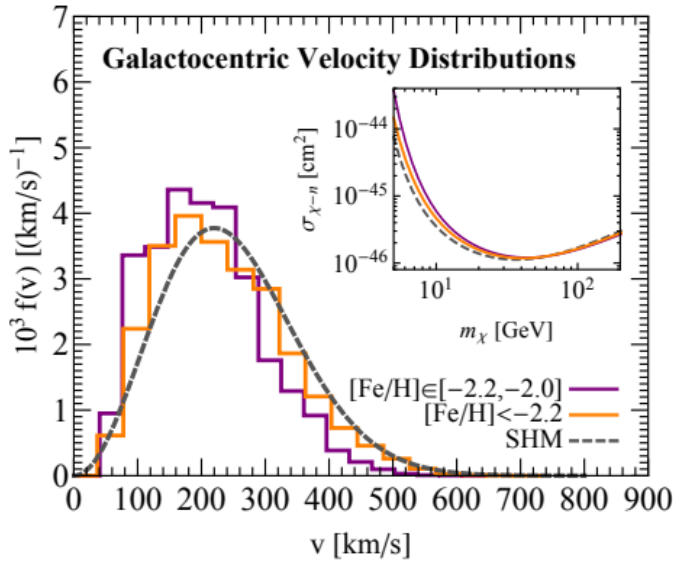


Figure 4: Galactocentric speed distributions for SDSS stars within 4 kpc of the Sun and distances of  $7 < r < 10$  kpc. The distributions are shown for  $[Fe/H]$  in  $[-2.2, -2]$  (solid purple) and  $[Fe/H] < -2.2$  (solid orange). The Standard Halo Model with mean  $v_0 = 220$  km/s is shown for comparison (dashed gray). The inset shows the expected background-free 95% C.L. limit on the DM spin-independent scattering cross section, assuming the exposure and energy threshold of the LUX experiment different velocity distributions. Figure from [16].

In addition to the stars and globular clusters orbiting the Milky Way, there could be clusters of dark matter more dense than the surrounding halo. Telescope data shows evidence for dark matter halo substructure in the Milky Way [18], and simulations expect upcoming data from LSST to further contribute to the understanding of Milky Way halo substructure and rule out or confirm certain dark matter halo models [19].

Galaxy clusters make up some of the strongest direct evidence for dark matter though the method of gravitational lensing. A gravitational lens is created when a massive object is located between a light source and an observer. General relativity requires photons to propagate on the null geodesics of spacetime, meaning the path the light takes from the source will be bent by the distorted space-time of the the massive object. Thus images of background galaxies are distorted by invisible mass along the line of sight from the observer. Being dependent on general relativity, and therefore Newtonian dynamics, the numerous observations of gravitational lensing in large structures strongly disfavor MOND.

There are three types of gravitational lensing: strong, weak, and microlensing. Weak lensing has been used to observe dark matter in large scale structures (galaxy clusters); the other types of lensing are not treated here. In weak lensing, the light sources are far away from the foreground mass (or the mass is small). Several light sources are required, and the location of the mass is statistically reconstructed. The Bullet Cluster (1E0657-558) is one of the most dramatic weak lensing measurements to date: it is actually the collision of the galaxy cluster 1E0657-56 and smaller cluster (the “bullet”) [20]. The x-ray image of the collision, by the Chandra x-ray observatory, shows the location of the baryonic matter. The baryonic matter suddenly slowed down upon the collision, emitting shock x-rays [20]. The authors of [20] call it “a textbook example of a bow shock”, indicating the x-ray behavior is well understood. A few years later, Clowe et al. also call the Bullet Cluster “a direct empirical proof of the existence of dark matter” [21]. Their weak lensing observations show the location of the total mass centers of the two clusters to be offset from the location of the baryonic matter at a significance of  $8\sigma$  [21]. In the collision, the dark matter halos of the two clusters pass through each other without slowing down, while the baryonic matter in the two clusters interacts, slowing down dramatically and producing x-rays. The weak lensing measurement is shown overlaid with the visible and x-ray images in Figure 5. Such a dramatic offset cannot be explained by modifications to gravity. It is important to note that there are many lensing measurements that show a statistically significant offset between baryonic matter and total matter; the Bullet Cluster is just one example, albeit particularly dramatic.

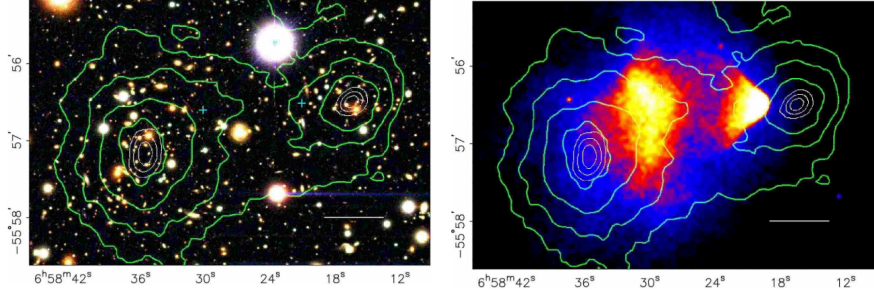


Figure 5: (left) The visible light image from the Magellan telescope of the merging Bullet Cluster overlaid with the weak lensing measurement contours in green, and white 68.3%, 95.5%, and 99.7% confidence levels for the weak lensing peaks. (right) The Chandra x-ray image overlaid with the same weak lensing measurement. Figure from [21].

## 2.2.2 COSMIC MICROWAVE BACKGROUND

In the thermal history of our universe, the term recombination refers to the epoch when temperatures had cooled enough to allow electrons and protons to combine into hydrogen, leaving photons to propagate freely through the universe. The photons should have decoupled from the matter as a black body peaked at the temperature of recombination,  $\approx 3000$  K. The relic radiation from this epoch is visible today as the [CMB](#), where the continuing expansion of the universe has redshifted the peak of the black body spectrum to  $\approx 2.7$  K. The [CMB](#) photons are also referred to as the light of last scattering, referring to the interaction the photons had with free electrons before the electrons became bound to protons in hydrogen. The temperature of the [CMB](#) was precisely measured to be  $2.7377 \pm 0.0038$  K by the COBE mission, which also confirmed its perfect adherence to a black body spectrum [22] (Figure 6).

While the COBE satellite mission's measurements of the [CMB](#) provided strong support for the Big Bang model of cosmology, it was COBE's discovery of anisotropies in the [CMB](#) that eventually led to powerful evidence for [CDM](#). Since COBE, two more [CMB](#) satellite missions, WMAP and Planck, have launched and gathered data, each with successively higher spatial and energy resolution. The relative resolutions of COBE, WMAP, and Planck are shown in Figure 7 along with the full Planck [CMB](#) anisotropy map. The scale of the anisotropy fluctuations represent a scale of  $\pm 30 \mu\text{K}$ ; the [CMB](#) power spectrum remains the most perfect black body spectrum observed in nature.

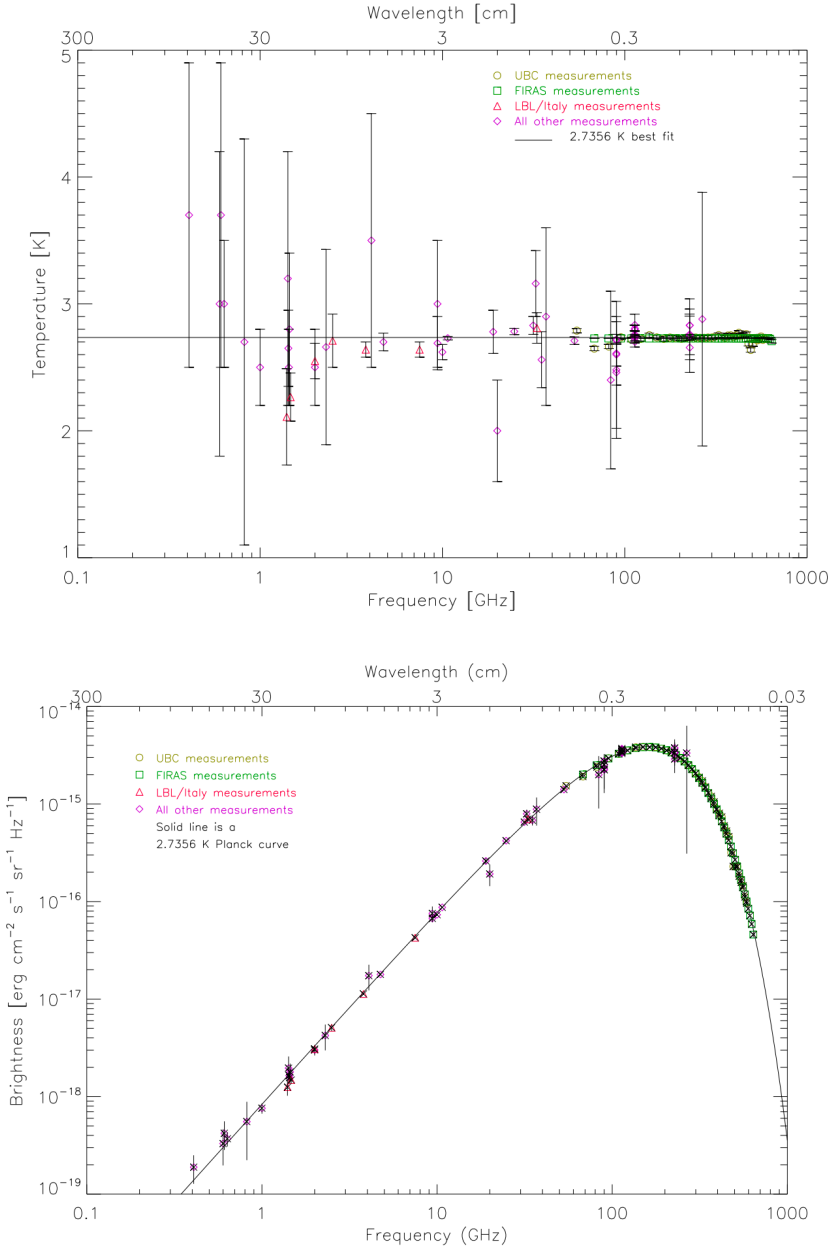


Figure 6: (top) The FIRAS instrument on the COBE satellite mission measured the CMB temperature to be  $2.7377 \pm 0.0038$  K. (bottom) The FIRAS instrument also confirmed the perfect Planck black body spectral shape of the CMB radiation. Figures from [22].

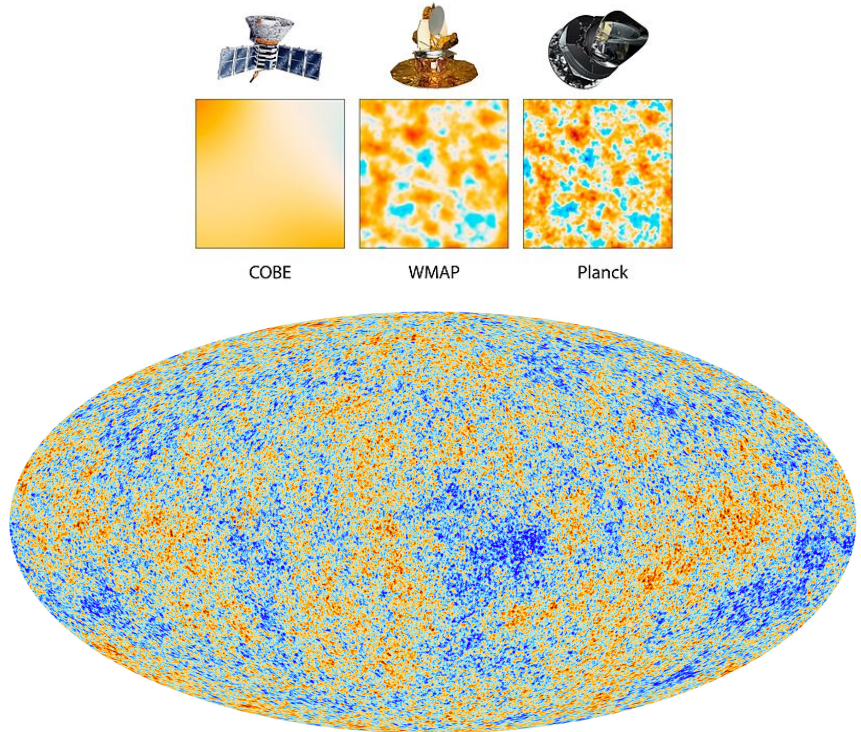


Figure 7: (top) The relative spatial resolution of COBE, WMAP, and Planck. Figure courtesy of NASA. (bottom) The Mollweide projection of the Planck 2013 CMB temperature map. The color scale represents fluctuations of  $\pm 30 \mu\text{K}$  around a central value of 2.7377 K. Figure courtesy of ESA and the Planck Collaboration.

The fluctuations  $\Delta T(\theta, \phi)$  of the CMB map shown in Figure 7 can be decomposed into its basis components via Fourier analysis, where each expansion component is represented by the spherical harmonics,  $Y_{lm}$ :

$$\Delta T(\theta, \phi) = \sum_{l=2}^{\infty} \sum_{m=-l}^l b_{lm} Y_{lm}(\theta, \phi) \quad (1)$$

The sum leaves out the  $l = 0$  (mean) and  $l = 1$  (dipole Doppler shift caused by movement of the earth with respect to the CMB) components, which were subtracted from the CMB temperature map, leaving only the fluctuations as in Figure 7. The power spectrum of the temperature fluctuations, which is calculated by squaring Equation 1, averaging it over all points that have the same angular separation  $\theta$ , and performing an integral over all  $m$  (because the temperature anisotropies have no preferred direction), encodes all the statistical variation in the CMB sky (see, e.g. [23] for a derivation). The angular correlations of the different multipole moment  $l$  are typically extracted from this power spectrum and plotted as function of  $l$  and the coefficients  $C_l$  from the power spectrum. This quantity is referred to as the angular power spectrum and takes the form:

$$D_l^{TT} = \frac{l(l+1)}{2\pi} C_l \quad (2)$$

where the  $TT$  superscript denotes temperature anisotropies (polarization anisotropies, not discussed here, can be parameterized similarly). The latest angular power spectrum from Planck is shown in Figure 8.

The location and magnitude of peaks in the angular power spectrum (Figure 8), constrain the curvature, content, and evolution of our universe. The physical interpretation of the CMB fluctuations is as follows: photons from the time of last scattering, newly free to propagate through the universe, carry information about the density fluctuations in the plasma from which they decoupled. The plasma, which was then composed of photons, baryons, and dark matter, behaved as an oscillator driven by gravitational attraction, with a restoring force from the fluid pressure of the plasma. The maxima of the angular power spectrum indicate extrema, overdensities or underdensities, in the plasma. The presence of baryons increases the magnitude of odd peaks relative to even peaks. The physical interpretation of this is that baryons add inertia to the oscillator system, causing an increase in compression (odd) compared to expansion (even) [23]. The angular power spectrum peaks are sometimes referred to acoustic peaks, as the oscillations that produced them were longitudinal and depended on density, much like sound waves. The presence of dark matter is apparent in the relative heights of the second and third peak in the spectrum. The

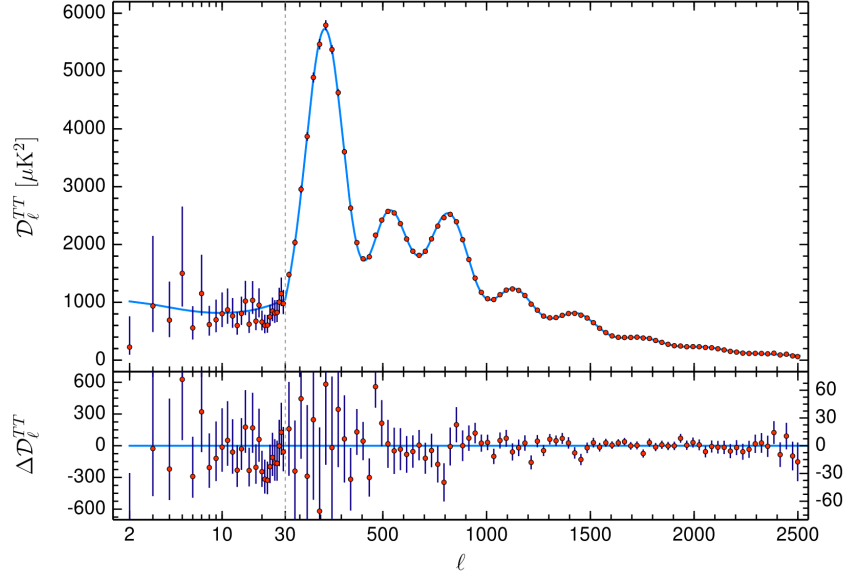


Figure 8: The angular power spectrum from Plank 2018 results [24].

driving force of the oscillator is the total matter content (baryons + dark matter,) which contributes to odd peaks, while baryons contribute characteristically to the even peaks. A third peak that is similar or larger than a second peak indicates that the matter content at the time of recombination was dominated by dark matter. A useful demonstration of the effect of baryons and total matter on the angular power spectrum is shown in Figure 9.

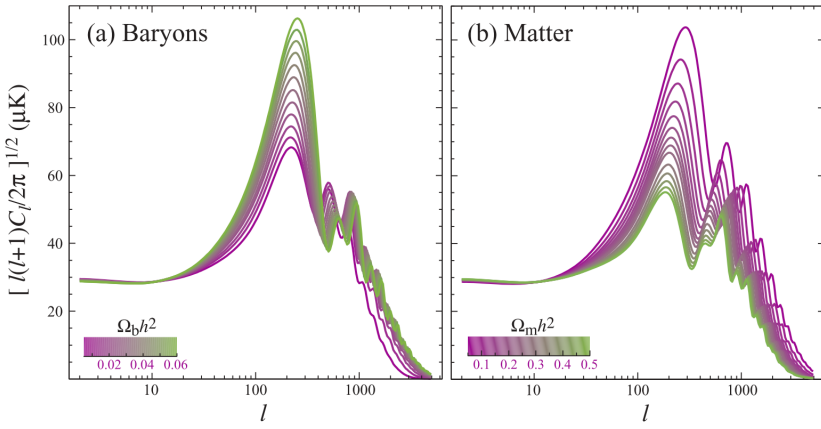


Figure 9: The effect of baryons (left) and total matter (right) on the magnitude and location of CMB angular power spectrum peaks. [23]

The measure of the dark matter content and baryon content of today's universe can be extrapolated from fitting the CMB angular power spectrum as in Figure 9. The results from the Planck 2018 angular power spectrum ([24]) are:

$$\Omega_{cdm} = 0.2696 \pm 0.0047 \quad (3)$$

$$\Omega_b = 0.0495 \pm 0.0005 \quad (4)$$

where the subscript  $b$  refers to baryon and the subscript  $cdm$  refers to cold dark matter. Each  $\Omega_x$ , defined in more detail below, represents the fraction of today's mass-energy density comprised by constituent  $x$ . These values do not add to one because a large fraction of the mass-energy density of the universe is comprised of dark energy, which we have left discussion of until the next section. However, note that these two values alone measure dark matter to comprise 84% of the matter in our universe.

## 2.3 STANDARD MODELS

Thus far we have focused only on the astrophysical and cosmological evidence for particle CDM. CDM plays a central role in the standard model of cosmology, known as “Lambda” CDM ( $\Lambda$ CDM). In this section, we briefly summarize the standard models of cosmology and particle physics.

### 2.3.1 THE STANDARD COSMOLOGY

The standard  $\Lambda$ CDM cosmology is based on the Einstein field equations:

$$R_{\mu\nu} - \frac{1}{2}g_{\mu\nu}R = \frac{8\pi G}{c^4}T_{\mu\nu} + \Lambda g_{\mu\nu} \quad (5)$$

where  $R_{\mu\nu}$  is the Ricci tensor,  $R$  is the Ricci scalar, and  $g_{\mu\nu}$  is the metric tensor.  $T_{\mu\nu}$  is the stress-energy tensor,  $G$  is Newton's gravitational constant,  $c$  is the speed of light in vacuum, and  $\Lambda$  is the cosmological constant. The equation relates the geometry of space-time (on the left hand side) to the energy content of the universe (on the right hand side).

Einstein originally introduced the cosmological constant  $\Lambda$  to counteract gravity and produce a steady-state universe. Today, however, we know that the universe is expanding, and that the rate of expansion is accelerating. The second fact, first evidenced by supernova Type Ia measurements [25] [26], is what led to the modern interpretation of  $\Lambda$  as dark

energy. Today, we understand  $\Lambda$  to represent a “vacuum energy” associated with space-time itself, rather than its matter content. It is the source of the accelerating expansion of the universe, sometimes referred to as “negative pressure” or “gravitational repulsion”, and it is the dominant component of mass-energy density in our universe (see Table 1).

The Einstein field equations are solved with the Friedman-Lemaitre-Robertson-Walker metric (not shown here, see e.g. [27], [28]), which describes the symmetries we observe in our universe and therefore require of our model: isotropy and homogeneity. The solution yields the Friedman equation (Equation 6), which details how the addition of different energy sources (matter, radiation, dark energy) change the expansion rate of the universe. The rate of expansion is given by the Hubble constant  $H(t)$  (a slight misnomer because it can change over time scales  $\sim$  history of our universe). It is defined as  $H(t)^2 \equiv \frac{\dot{a}(t)}{a(t)}$ , where  $a$  is the so-called scale factor, which is a dimensionless factor that parametrizes the size of the universe. The Friedman equation, given below, delineates how the Hubble constant changes with the energy content  $\rho_{tot}$  and curvature  $k$  of our universe.

$$H(t)^2 \equiv \left( \frac{\dot{a}(t)}{a(t)} \right) = \frac{8\pi G}{3} \rho_{tot}(t) - \frac{k}{a(t)^2} \quad (6)$$

The Friedman equation yields a quantity known as the critical density  $\rho_c$ , which is the density for a flat universe ( $k = 0$ ).

$$\rho_c(t) = \frac{3H(t)^2}{8\pi G} \quad (7)$$

A species  $x$  is defined as having a fraction of the mass-energy density  $\Omega_x(t) = \rho_i(t)/\rho_c(t)$ . The individual  $\Omega_x$  have different time evolutions according to their equation of state (see e.g. [27], [28], for a complete, pedagogical treatment). After treating equations of state, the Friedman equation can be re-written in a more convenient form:

$$\frac{H^2}{H_0^2} = \frac{\Omega_{r,0}}{a^4} + \frac{\Omega_{m,0}}{a^3} + \Omega_{\Lambda,0} + \frac{(1 - \Omega_{tot,0})}{a^2} \quad (8)$$

where the 0 subscript denotes today’s value,  $r$  denotes radiation,  $m$  denotes matter, and  $\Lambda$  denotes dark energy. Note that the last term disappears when  $\rho_0 = \rho_c$ , that is, if our universe is flat. Equation 8 makes a powerful statement: by measuring the energy content of the universe, we can tell the history and fate of the Universe. This is the core of  $\Lambda$ CDM – it is essentially a system of equations, which, when solved, can describe the

history and predict the future of the universe in terms of a few measurable parameters (e.g  $\Omega_x$ ).

The Planck collaboration fits for a standard, 6 parameter  $\Lambda\text{CDM}$  of the CMB. This fit includes some parameters specific to the intricacies CMB measurements, as well as the familiar  $\Omega_x$  density parameters from Equation 8. The 6 fit parameters<sup>1</sup> are:  $\Omega_b h^2$ ,  $\Omega_{cdm} h^2$ ,  $\tau$ ,  $\ln(10^{10} A_s)$ ,  $n_s$ , and  $100\theta_{MC}$ . Other quantities are derived from these parameters. A summary of the parameters, derived quantities, and their values is given in Table 1. Note that the parameter  $A_s$  is the amplitude of curvature fluctuations in the CMB angular power spectrum (Figure 8). The effect of baryons and dark matter on the angular power spectrum were discussed in Section 2.2.2. Similarly, dark energy content, curvature, and equation of state of the universe also produce visible effects (see examples in Figure 10). Namely, dark energy and curvature determine the magnitude of the first peak, and curvature determines peak locations.

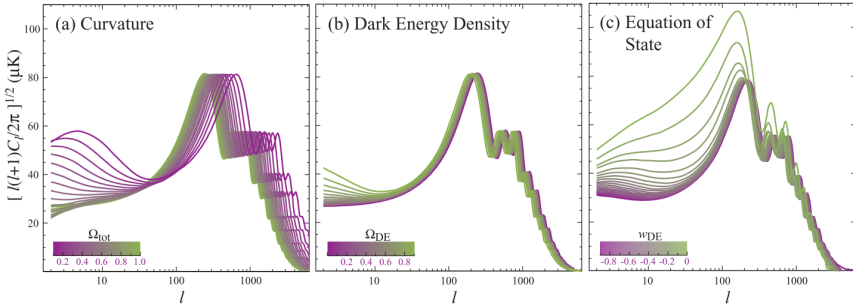


Figure 10: The effect of curvature (left), dark energy (center), and equation of state (right) on the magnitude and location of CMB angular power spectrum peaks. [23]

---

<sup>1</sup> The density parameters are often reported as  $\Omega_x h^2$  since the main source of error in their measurement comes from the Hubble constant  $H_0$ .  $h$  is a dimensionless parameter defined as:  $h = H_0/(100 \text{ km s}^{-1} \text{ Mpc}^{-1})$

Table 1: A summary of the fit parameters and derived quantities from Planck's 2018 results [24].

Fit Parameter	Definition	Planck TT spectrum
$\Omega_b h^2$	baryon density	$0.02212 \pm 0.00022$
$\Omega_{cdm} h^2$	CDM density	$0.1206 \pm 0.0021$
$100\theta_{MC}$	angular acoustic scale	$1.04077 \pm 0.00047$
$\tau$	optical depth	$0.0522 \pm 0.0080$
$\ln(10^{10} A_s)$	curvature fluctuations	$3.040 \pm 0.016$
$n_s$	spectral index	$0.9626 \pm 0.0057$
Derived Quantity	Definition	Planck TT spectrum
$\Omega_b$	baryon content	$0.0495 \pm 0.0005$
$\Omega_{cdm}$	CDM content	$0.2696 \pm 0.0047$
$\Omega_m$	matter content	$0.321 \pm 0.013$
$\Omega_\Lambda$	dark energy content	$0.679 \pm 0.013$
$H_0$ [km s <sup>-1</sup> Mpc <sup>-1</sup> ]	Hubble constant	$66.88 \pm 0.92$
Age [Gyr]	age of the universe	$13.830 \pm 0.037$
$k$	curvature	consistent w/ $k = 0$

### 2.3.2 THE STANDARD MODEL OF PARTICLE PHYSICS

The Standard Model (SM) of particle physics describes all the currently known matter particles and force carrier particles, which can also have mass, and which dictate interactions between the matter particles. As of 2012, it also includes a mass generation mechanism from the Higgs boson. The SM is formulated using the principles of Quantum Field Theory, where symmetries in the Lagrangian give rise to conserved physical quantities and thereby determine the rules for interactions.

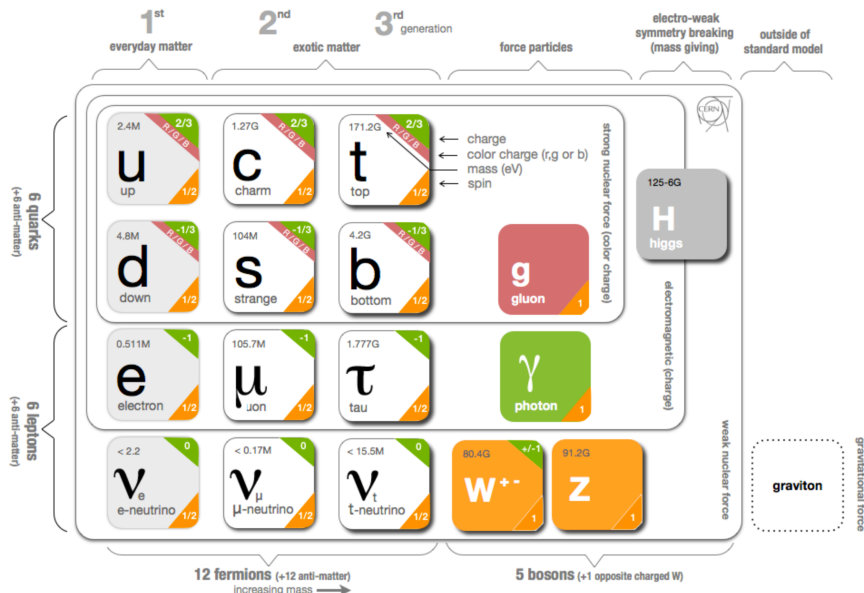


Figure 11: The particles that comprise the standard model of particle physics, including names, spins, masses, and charges. It is also indicated which fermions interact with which bosons, e.g. gluons interact with the quarks but not with the leptons.

The known particles of the SM are shown in Figure 11, along with a theoretical force carrier for gravity, the graviton. These particles are typically grouped into categories: fermions and bosons. Fermions comprise all the known matter particles and are spin- $\frac{1}{2}$  particles. Each of the fermions in Figure 11 has an anti-particle, although it is an open question whether the neutrino is its own anti-particle. The integer-spin bosons, excepting the Higgs boson, which provides a mechanism for giving mass to all the other particles, are the force carriers of the standard model. The spin-1 bosons: the gluon, photon, and W and Z boson, describe three of the four forces known to physics. The gluon mediates the strong force, which governs interactions between quarks, binding them in hadrons (three quark states which make up e.g. protons and neutrons) and mesons (two-

quark states such as pions). The photon mediates electromagnetism, governing interactions between particles with electric charge. The  $W^+$ ,  $W^-$ , and  $Z$  bosons mediate the weak force, which includes phenomena such as beta-decay and neutrino-electron scattering.

It was once proposed that the  $Z$  boson could mediate the interaction between Dark Matter ([DM](#)) and [SM](#), because a [DM](#) particle that interacts via the weak force fits the Weakly Interacting Massive Particle ([WIMP](#)) paradigm discussed below. Direct detection experiments have long excluded the scattering cross section, of  $10^{-39} \text{ cm}^2$ , which is the cross section for an  $O(1)$  coupling to the  $Z$ . It should be noted that some extensions to the [SM](#) allow for  $< O(1)$  coupling to the  $Z$  via, e.g., a mixing angle [29]. Naively, it is possible for neutrinos, which interact weakly and have mass, to be [CDM](#). However, neutrinos were relativistic during structure formation so could not perform the role of necessary of [CDM](#). Estimates of the density of today's relic neutrinos show that  $\Omega_v \approx (1.2 - 2.2) \times 10^{-3} << \Omega_{cdm}$  [30], [31]. The standard model, as it is known today, contains no particles that could be [CDM](#).

## 2.4 DARK MATTER CANDIDATES MOTIVATED BY PARTICLE PHYSICS

Cosmology, while providing very precise measurements of the dark matter content of the universe, essentially requires only three things of dark matter candidates: (1) the candidate must account for the observed  $\Omega_{cdm}$ , (2) at least 95% of it is non-relativistic or “cold” [32], (3) it is not strongly self-interacting (“collisionless”) or strongly interacting with baryons. Requirement (1) is fairly loose, as it is possible for multiple different dark matter particles to comprise together  $\Omega_{cdm}$ , but note that it implies the dark matter candidate(s) must be stable on the timescale of the universe, or there must be a production mechanism to create the necessary abundance seen today. This section briefly summarizes two very different dark matter candidates, which have additional motivation due to open questions from the standard model.

### 2.4.1 WIMPS AND THE HIERARCHY PROBLEM

Any system that describes particle interactions today at “low energy”, should also scale to describe particle interactions at different times (and therefore energies) in the history of our universe, namely in the first  $10^{-43}$  seconds after the Big Bang in a time known as the Planck epoch. During the Planck epoch, energies were at the Planck scale of  $10^{19} \text{ GeV}$ , and gravitational interactions become as large as the other forces. Any sound

quantum theory should be able to account for interactions at this energy scale. However, the largest masses for **SM** particles are  $O(100)$  GeV; this scale is known as the weak scale and is 17 orders of magnitude less than the Planck scale. The hierarchy problem is essentially a question of why the Higgs mass is so much lighter than the Planck mass. If one tries to calculate the Higgs mass the usual way, by summing all the loop contributions to the two point function, the sum diverges. This is in contrast to the measured mass, which is about 125 GeV.

In order to solve the Hierarchy Problem, a framework known as Supersymmetry (**SUSY**) was developed. In **SUSY** each **SM** particle has a “superpartner.” In general, the superpartners have a spectrum of masses higher than **SM** particles and a symmetry called  $R$ -parity partitions and limits interactions between **SM** and **SUSY**. The superpartners add additional diagrams to the radiative corrections for the Higgs mass. These new contributions stabilize the calculation, cancelling the divergence and resulting in a finite value for the Higgs mass. The connection between **SUSY** and **DM** is that some of these new particles could be dark matter candidates. The lightest of the **SUSY** particles, called the Lightest Super Partner (**LSP**), can be stable. If the **LSP** is neutrally charged, then it is a **WIMP** dark matter candidate.

The **WIMP** paradigm has its roots in the mathematical coincidence called the “**WIMP** Miracle”. If one assumes a weak-scale coupling and mass for dark matter, it naturally produces the entire  $\Omega_{cdm}$  observed today via thermal freezeout. When the universe was small and dense with particles, a **WIMP**,  $\chi$ , would meet its antiparticle  $\bar{\chi}$  and annihilate into lighter particles:  $\chi\bar{\chi} \rightarrow l\bar{l}$ . The reverse reaction to produce the heavier **WIMP** ( $l\bar{l} \rightarrow \chi\bar{\chi}$ ) proceeds as long as the energies of the particle is sufficiently high, i.e.  $T > m_\chi$ . When this condition is met, the number density  $n$  of **WIMPs** is at its thermal equilibrium value  $n_{eq}$ . As the universe expands, the reaction falls out of thermal equilibrium. Both directions of the reaction ( $\chi\bar{\chi} \rightleftharpoons l\bar{l}$ ) are affected: the reverse reaction cannot produce more  $\chi$  due to cooling, and the forward reaction stalls because annihilation rate  $\Gamma_A$  relies on a sufficiently high number density  $n$ , such that the probability of  $\chi$  to meet  $\bar{\chi}$  is large. The number density of **WIMPs** become frozen into a relic density that we can observe today when the Hubble expansion rate overcame the annihilation rate:

$$\begin{aligned} H(t) &> \Gamma_A \\ &> n_\chi \langle \sigma_A v \rangle \end{aligned} \tag{9}$$

where  $\langle \sigma_A v \rangle$  is the thermally averaged annihilation cross section. The time when  $H(t) = \Gamma_A$  is referred to as freezeout. Following [33], the time evolution of the number density is described by the Boltzmann equation

(see Figure 12 (left) for number density evolution before and after freeze-out):

$$\frac{dn}{dt} = -3Hn - \langle\sigma_A v\rangle(n^2 - n_{eq}^2) \quad (10)$$

This equation must be solved numerically (a more complete analysis can be found in e.g. [34]), but making a few assumptions, [33] finds:

$$\begin{aligned} \Omega_\chi &\sim \frac{m_\chi T_0^3}{\rho_c} \frac{n_f}{T_f} \\ &\propto [\text{constants}] \langle\sigma_A v\rangle^{-1} \end{aligned} \quad (11)$$

where  $\rho_c$  is the critical density,  $f$  subscripts refer to freezeout and 0 subscripts refer to today's values.  $\Omega_\chi$  then depends only on the particular annihilation cross section, which is set by the mass scale  $m_\chi$ :

$$\sigma_A v = k \frac{g_{weak}^4}{16\pi^2 m_\chi^2} (1 \text{ or } v^2) \quad (12)$$

where  $v^2$  is present or absent for S- or P-wave annihilation and  $k \sim \frac{1}{2} - 2$  parameterizes the deviation of  $g$  from  $g_{weak} \approx 0.065$ . If the mass of the dark matter particle is in the range  $m_\chi \sim 100 \text{ GeV}-1 \text{ TeV}$ , then  $\Omega_\chi$  accounts for 100% of today's observed  $\Omega_{cdm}$ . This is the **WIMP** miracle: weak-scale particles can account for *all* the dark matter content. Even if the **WIMP** mass  $m_\chi$  deviates from this perfect situation, the particle can still make up a substantial percentage of dark matter (see Figure 12 (right)),

A particle with the exact mass and weak-scale coupling, i.e scattering mediation via O(1) coupling with the Z-boson, has been ruled out by direct detection experiments, but various **SUSY** parameter regions remain. The **LSP** can be a **WIMP**, and thereby it could solve two mysteries of physics: the hierarchy problem, and dark matter.

#### 2.4.2 AXIONS AND THE STRONG CP PROBLEM

The **SM** includes a term in the quark sector that should contribute to CP-violating, flavor-conserving observables that scale with a mixing angle  $\theta_3$ :

$$\mathcal{L} = \theta_3 \frac{g_3^2}{32\pi^2} G_a^{\mu\nu} \tilde{G}_{a\mu\nu} \quad (13)$$

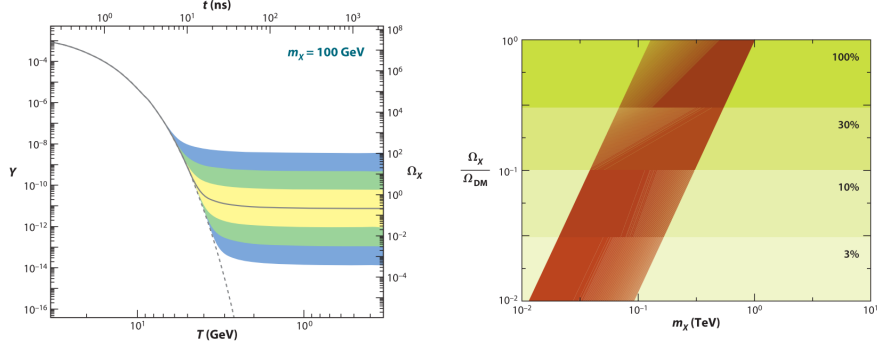


Figure 12: (left) The co-moving number density  $Y$  (left y-axis) resulting in the thermal relic density  $\Omega_\chi$  (right y-axis) for a dark matter particle of mass  $m_\chi=100$  GeV. The solid black line is the annihilation cross section which yields the correct relic density and bands indicate cross sections that differ by successive factors of 10 from the “correct” annihilation cross section. (right) A band of natural values for a thermal relic  $\chi$  that composes different percentages of the observed dark matter content. The width of the band is set by the deviation of  $g$  from  $g_{\text{weak}}$  in Equation 12. Figures from [33]

where  $g_3$  is the gluon coupling constant,  $G_a^{\mu\nu}$  is the gluon field strength, and  $\theta_3$  is a dimensionless constant.

This term should produce, for example, an electric dipole moment of the neutron,  $d_e$ . For natural values of  $\theta_3 \sim 1$ , one would expect  $d_e \sim 10^{-16}$  e cm. However, such a dipole moment has never been observed and current experimental limits constrain  $d_e < 2.9 \times 10^{-26}$  e cm [33]. To account for this,  $\theta_3$  must be ‘fine tuned’ to  $\theta_3 \rightarrow \theta_3 10^{-10}$ . This is known as the Strong-CP Problem: we expect CP-violating observables from the SM, but instead we find that CP is strongly conserved.

In 1977 Peccei and Quinn proposed a mechanism that solves the strong CP problem: a new hidden and spontaneously broken global symmetry allows  $\theta_3$  to be a dynamical value which goes to zero when the symmetry is broken. A spontaneously broken global symmetry generates a Goldstone boson, so there is a new particle with non-zero mass called the axion (or QCD axion). Although they are predicted to be light ( $\sim \mu\text{eV}$  to  $\text{meV}$ ), axion production is possible in the early Universe in such a way that they can be CDM. Depending on whether the Peccei-Quinn symmetry is broken before or after cosmological inflation, different constraints apply. In either case it is possible for an axion with the appropriate mass to make up all of the  $\Omega_{cdm}$  observed today [35].

## 2.5 THE DARK SECTOR AND LIGHTLY IONIZING PARTICLES

Chapter 5 of this thesis details a search for LIPs, in this section the theoretical underpinning of such a particle is discussed.

### 2.5.1 DARK SECTOR

Our universe is dominated by non-baryonic dark matter. A simple way of explaining dark matter without modifying the existing SM is to require the existence of a dark sector (also called hidden sector), which interacts with the visible sector primarily through gravity [36]. In general, there may be multiple dark sectors, each with structure rich enough to rival that of the SM. The dark sector and visible sector may have different thermal histories, but the size of the dark sector (counted in degrees of freedom) is still constrained by the cosmological history we observe in the visible sector. If the hidden sector and visible sector have equal temperatures at the time of Big Bang Nucleosynthesis (BBN)<sup>2</sup>, an exact copy of the SM is excluded. If the hidden sector and visible sector do not have the same temperature at BBN, either because they are not in thermal contact or they cool independently after inflation, hundreds of degrees of freedom, equivalent to several copies of the SM are allowed [33].

Dark sectors arise in many extensions to the SM to provide viable dark matter candidates, such as (pseudo-)scalars that appear naturally when symmetries are broken at high energy scales. If that sounds familiar, it is because an example of such a dark matter candidate, the QCD axion, was discussed above. Aside from gravity, symmetry requirements restrict the interactions the dark sector particles may have with the SM to a few interactions. These interactions provide what is known as a “portal” to the SM. In general, a dark sector may be completely hidden with no interactions other than gravity with the SM, but some portals are well-motivated by theoretical concerns [37] [33]. In some cases a portal is even required in order to explain galactic structure formation [36]. Four portals that are discussed often with respect to dark sectors are shown in Table 2 [37].

Higgs portal and neutrino portal searches are best suited to high-energy collider searches and neutrino facilities, respectively. Axion and vector portal searches can also be accomplished with these technologies, but direct detection offers low cost alternatives that are also model-independent. Such detection schemes are discussed more below, in Section 2.6. The

---

<sup>2</sup> BBN is the time when the the universe has cooled enough to allow the nuclei of the light elements to form ( $t_{BBN} \sim 1\text{-}1000$  s). For more in-depth and pedagogical discussion of BBN and what constraints it places see e.g. [27], [28].

Table 2: Possible dark sector portals, related dark matter candidates, and operators that connect the dark sector to the [SM](#). Table from [37].

Portal Name	Dark Matter Candidates	Operator(s)
Vector	Dark Photons or LIPs	$\frac{\theta}{2} F^{\mu\nu} F'^{\mu\nu}$
Axion	Pseudoscalars	$\frac{a}{f_a} F_{\mu\nu} \tilde{F}^{\mu\nu},$ $\frac{a}{f_a} G_{i\mu\nu} \tilde{G}_i^{\mu\nu},$ $\frac{\partial_\mu a}{f_a} \bar{\psi} \gamma^\mu \gamma^5 \psi$
Higgs	Dark Scalars	$(\mu S + \lambda S^2) H^\dagger H$
Neutrino	Sterile Neutrinos	$y_N LHN$

axion described in Section 2.4.2 is referred to as the QCD axion, it has a specific combination of axion mass and axion-[SM](#) coupling. More general axion models, called Axion-like Particle ([ALP](#))s, are less constrained and can make up some percentage of [DM](#) [37]. The vector portal is characterized by a dark photon (“paraphoton” in older texts),  $A'$ , that kinetically mixes with the [SM](#) photon,  $A$ . The mixing strength is parametrized by a factor  $\theta$ . Dark photon dark sectors are broken up into two cases:  $m_{A'} = 0$ , and  $m_{A'} > 0$ . For the massive dark photon case ( $m_{A'} > 0$ ), the dark photon itself can be dark matter. In the simplest case for the vector portal, the dark sector only consists of a massive dark photon and no other particles. Models exist for  $m_{A'} \sim \text{MeV-GeV}$  range as well as the sub-eV range [37].

In the case where the dark photon is massless ( $m_{A'} = 0$ ), other hidden sector particles  $h$  can be stable and massive. This case yields [LIPs](#), discussed in the next section.

## 2.5.2 LIGHTLY IONIZING PARTICLES

Lightly ionizing particles, also known as milli- or fractionally-charged particles, stem from massless dark photon models. The kinetic Lagrangian includes the terms [38] [39]:

$$\mathcal{L} \supset -\frac{1}{4g^2} F_{\mu\nu} F^{\mu\nu} - \frac{1}{4g'^2} F'_{\mu\nu} F'^{\mu\nu} + \frac{\theta}{2gg'} F_{\mu\nu} F'^{\mu\nu} \quad (14)$$

where  $F_{\mu\nu} = \partial_\mu A_\nu - \partial_\nu A_\mu$  is the usual electromagnetic field tensor, and  $F'_{\mu\nu}$  is similarly the field tensor for the dark photon. The last term is called the kinetic mixing term, as it mixes the gauge kinetic terms for each sector.

Let  $h$  be a hidden sector fermion field that has a bare coupling to the hidden photon  $A'$ , such that

$$\mathcal{L} \supset \bar{h} \not{A}' h \quad (15)$$

where we use the Feynman slash notation ( $\not{X} \equiv \gamma^\mu X_\mu$ ). The kinetic mixing term in Equation 14 can be diagonalized by the shift:

$$A'_{\mu u} \longrightarrow \tilde{A}'_{\mu u} + \theta A_\mu \quad (16)$$

With the shift, the hidden sector fermion  $h$  now couples to the photon:

$$\mathcal{L} \supset \bar{h} \not{A}' h \longrightarrow \bar{h} \not{\tilde{A}'} + \theta \bar{h} \not{A} h \quad (17)$$

The last term in the equation above corresponds to an effective coupling  $q$  of the hidden sector particle  $h$  with the visible photon  $A$ :

$$q = \theta g' \equiv \epsilon \quad (18)$$

In general,  $g'$  can be large, but  $\theta$  is constrained to be small (otherwise the sector would not be hidden). An example diagram of  $h$  interacting with electrons is shown in Figure 13. The electrons only “see”  $h$  through the  $A'$  coupling with  $A$ , and thus  $h$  appears with a small, non-integer charge with respect to the visible sector. The magnitude of the diagram goes as the three couplings:

$$|M| \sim \theta g' g = \theta g' e \equiv \epsilon e \quad (19)$$

where we substituted the known low-energy Quantum Electrodynamics (QED) gauge coupling  $e$  for  $g$ . The particle  $h$  is known as a LIP, and can be treated as having  $\epsilon e$  charge in encounters with SM electrons. There are many constraints on LIPs from various sources summarized in Figure 14, taken from a 2009 review article on fractionally charged particles [40].

Unlike many of the constraints in Figure 14, a search for fractionally charged cosmic rays is model independent. That is, it does not depend on the particular production mechanism of the LIP, nor on its mass. A tacit assumption is made that the cosmic ray is high energy, and indeed such high energy LIPs may be produced in the present era in violent astrophysical processes or between interaction of ordinary cosmic rays in the atmosphere [40]. The analysis in Chapter 5 concerns the search for LIP cosmic rays. The search sensitivity for LIP cosmic ray searches is given in terms of flux,  $\Phi$ , with units  $\text{cm}^{-2} \text{sr}^{-1} \text{s}^{-1}$  as a function of the “charge fraction”  $f$ , where  $f$  is defined as the denominator of the LIP fractional charge,  $e/f$ . See Figure 15 for recent LIP flux limits.

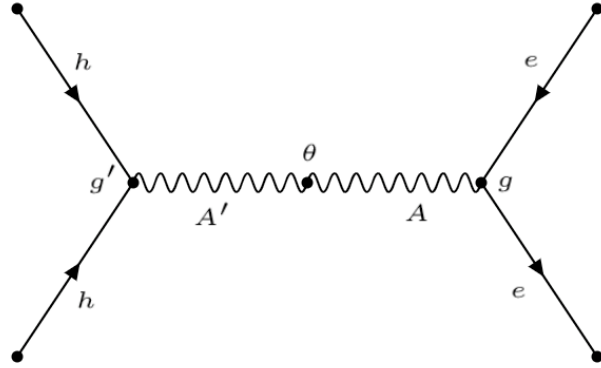


Figure 13: A Feynman diagram of a dark sector particle  $h$  interacting with atomic electrons.  $g'$  is the gauge coupling to  $A'$  in the dark sector,  $\theta$  the kinetic mixing angle between  $A'$  and  $A$ , and  $g$  is the usual electromagnetic gauge coupling,  $g = e$ .

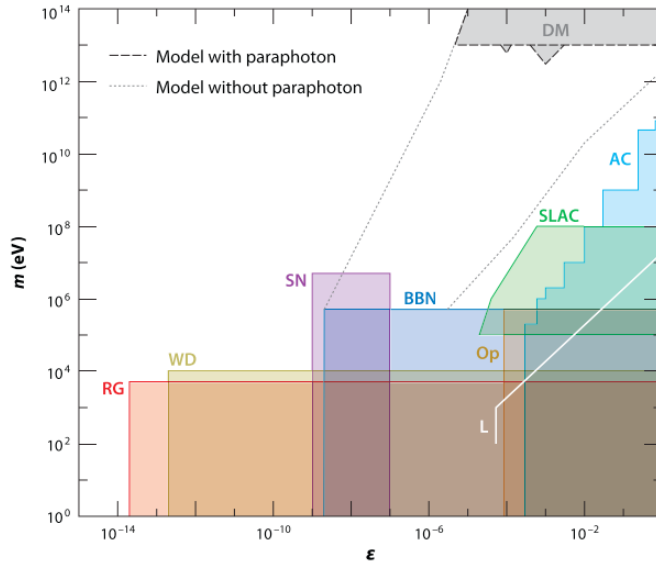


Figure 14: Regions of mass-charge space ruled out for LIPs from several different sources. The dashed line limits apply in the case of a dark sector photon (our case of interest), and the dotted line is the limit without dark photons. Abbreviations: AC, accelerator experiments; Op, search for the invisible decay of ortho-positronium; SLAC, the SLAC millicharged particle search; L, the Lamb shift; BBN, big bang nucleosynthesis; RG, plasmon decay in red giants; WD, plasmon decay in white dwarfs; DM, dark matter searches; SN, Supernova 1987A. Figure from [40].

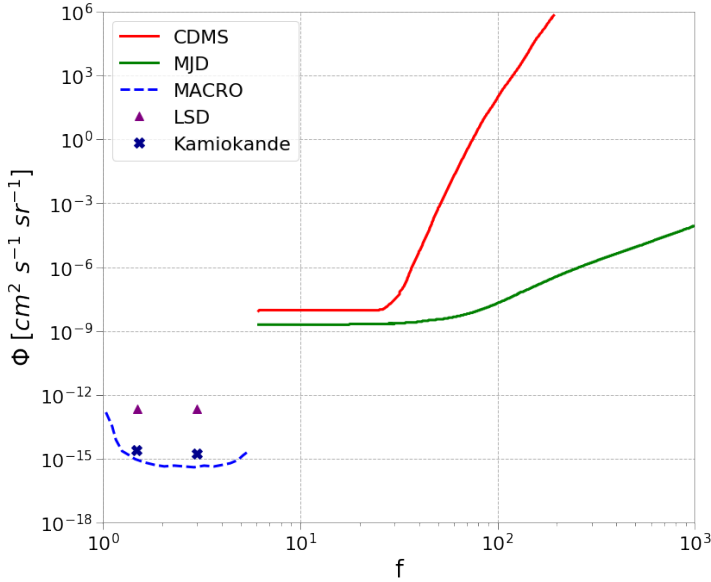


Figure 15: Recent limits on the flux of LIPs with charge  $e/f$  where  $f$  is the x-axis.

Figure reproduced from [41].

### 2.5.3 WIMPLESS MIRACLE AND THE NEW PHYSICS FLAVOR PROBLEM

As with any dark matter candidate, it is desirable for hidden sector dark matter to have the correct relic density. In Section 2.4.1, we discussed the **WIMP** miracle: how a particle with a weak scale mass and coupling undergoes thermal freezeout to naturally produce the correct relic abundance. There is a similar situation for the hidden sector dubbed the “**WIMPless** miracle”, which is much more general. Recall that for a stable thermal relic particle  $\chi$ , the relic density  $\Omega_\chi$  goes as:

$$\Omega_\chi \sim \langle \sigma_A v \rangle^{-1} \sim \frac{m_\chi^2}{g_\chi^4} \quad (20)$$

The **WIMP** miracle says that for  $m_\chi \sim m_{weak}$  and  $g_\chi \sim g_{weak}$ ,  $\Omega_\chi \approx \Omega_{cdm}$ . For a particle that interacts via a known **SM** force, the weak force is the only reasonable choice, so  $g_\chi \sim g_{weak}$ . Hidden sector dark matter, however, has its own matter content and gauge forces, so many combinations of  $(m_\chi, g_\chi)$  are possible. This generalizes the **WIMP** miracle to the **WIMPless** miracle: hidden sector dark matter can produce the correct relic density, but need not have weak scale mass nor interact via the weak force (Figure 16). In the case of hidden sector mediated **SUSY** breaking<sup>3</sup>,

<sup>3</sup> **SUSY** is a symmetry that must be broken, otherwise a host of problems would be present. For example, without a broken **SUSY**, the electron and selectron would have the same

it's not merely a coincidence that  $(m_\chi, g_\chi)$  can be constrained to a line, but rather that a fixed ratio of  $m_\chi/g_\chi^2$  is well-motivated [42].

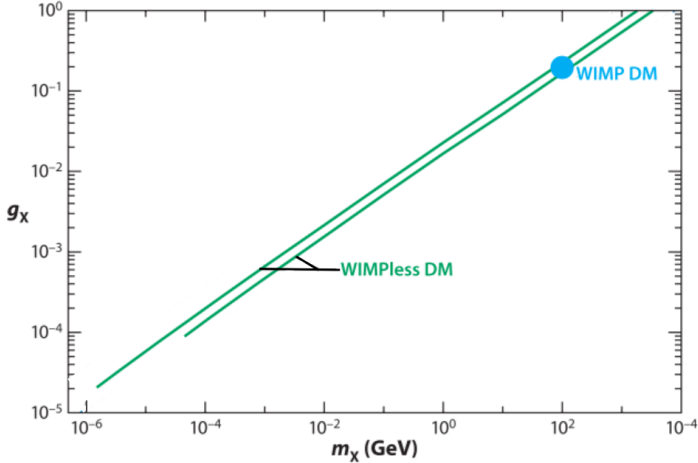


Figure 16: Contours in the  $(m_\chi, g_\chi)$ -plane for two different temperature conditions for the hidden sector. The upper line is for a hidden sector that achieves 80% of the visible sector temperature after reheating, the lower line is for 30%. For this plot, the hidden sector is assumed to be a 1-generation flavor-free version of the minimal supersymmetric standard model. Figure adapted from [33].

Recall also from Section 2.4.1, that in addition to it producing the correct relic abundance, the **WIMP** is a favored dark matter candidate because it is related to **SUSY**, which is introduced to solve the hierarchy problem of the **SM**. In attempting to solve the gauge hierarchy problem, **SUSY** gives rise to another problem called the “new physics flavor problem” [33]. **SUSY** particles may violate baryon number, lepton number, flavor, or CP. At the same time, we observe these symmetries to be extremely well preserved in the **SM**. The new physics flavor problem, in a nutshell, is that not all **SUSY** models are capable of elegantly conserving these symmetries. Creating models that solve the new physics flavor problem is a “prime driver in the field of supersymmetric model building” [33]. A particularly elegant subset of **SUSY** models that do solve the new physics flavor problems are known as Gauge-Mediated Supersymmetry Breaking (**GMSB**). In these models, a hidden sector mediates **SUSY** breaking. In **WIMPless** scenarios, one asks why the hidden sector dark matter should be stable. For **GMSB** models, which solve the new physics flavor problem, an elegant way to stabilize the hidden sector dark matter is through the hidden U(1) charge

---

mass. Furthermore, selectrons are bosons. If we lived in a world where both electrons and selectrons were common, we would not have atomic structure because orbital fermionic electrons are a higher energy state than infinite ground state selectrons.

conservation, which necessitates a massless gauge boson in the hidden sector. This is precisely the situation we have with LIPs. To quote [33]: “In summary, hidden sector dark matter models may in fact be motivated by leading problems in particle physics, and may even have naturally the correct relic density, through a generalization of the WIMP miracle to the WIMPless miracle.”

#### 2.5.4 CHARGE QUANTIZATION

It is known experimentally that all charged particles in the SM have charge  $\pm \frac{1}{3}e$ ,  $\pm \frac{2}{3}e$ , or  $\pm e$ . However, there is no theoretical motivation behind this quantization of electric charge. Holdom suggested a new, U(1) with a “paraphoton” gauge boson could produce quantized charge in the SM and transfer fractional shifts to fermions that interact with the paraphoton [38], which is the LIP paradigm. Others, [43], [44], [45], [46], and [47], have proposed various extensions to the SM that would produce charge quantization. Some of these theories yield fractionally charged particles, and all of them require new physics beyond the SM. It is useful to note that even outside of the hidden sector, there are theoretical motivations for fractionally charged particles.

## 2.6 EXPERIMENTAL STRATEGIES FOR DETECTING DARK MATTER

Experiments designed to detect dark matter, be it WIMP, axion, dark sector, or other candidates, fall into three main categories: production, indirect detection, and direct detection (see Figure 17). Detection schemes and examples are discussed in the following subsections. All three methods are in use to provide a diverse, multipronged DM detection program.

### 2.6.1 PRODUCTION

Colliders like the Large Hadron Collider (LHC) are capable of accelerating SM particles to high energies. The SM particles, typically protons, antiprotons, electrons, and/or positrons, can be collided with each other or with a fixed target. In general, dark matter produced in these collisions appears as “missing energy” when the event is reconstructed. A classic signal of a new, non-interacting particle is missing missing momentum transverse to the beam line, indicating the particle escaped without interacting in the detector. A recent overview of collider searches for several different dark matter candidates can be found in [48].

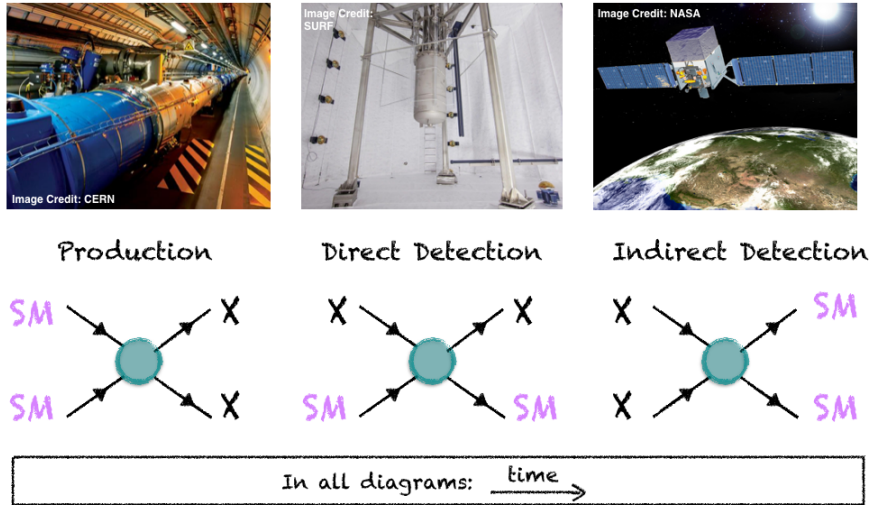


Figure 17: Summary of **DM** detection schemes with illustrative Feynman diagrams. In all cases, the arrow of time is from left to right. (left) **SM** particles can be collided at high energy facilities, which may produce **DM** particles,  $\chi$ . (center)  $\chi$  may scatter with **SM** particles, leaving behind a characteristic signal. (right)  $\chi$  particles in the galaxy may annihilate and produce **SM** particles, which produces an **SM** signal in excess of expectations from standard astrophysical processes.

### 2.6.1 LIP PRODUCTION

It is noted in [40] that “high-energy electron-positron colliders provide the most definitive search method among accelerator and collider searches for fractionally charge particles [in the range  $\pm \frac{1}{3}e - \pm \frac{4}{3}e$ ].” This is due to the production cross section being large and known to high accuracy. Another successful collider method to search for fractionally charged particles with charge  $\ll 1$  is called a “beam dump”. In beam dump experiments, the collider accelerates e.g. an electron into a fixed target, producing secondary particles. A large mass of shielding is between the target and the detector. Only secondary particles with a small charge can make it through the shielding to reach the detector. The limit in Figure 14 titled SLAC is from a beam dump type experiment; see [49] for details about the SLAC millicharged particle search. Hadron colliders can also look for such particles, albeit with more restrictions [40].

### 2.6.2 INDIRECT DETECTION

The signal of dark matter annihilation can appear in both ground-based and satellite detectors. Dark matter may decay or annihilate into **SM** particles, which can be detected by conventional detectors. Positive identifi-

cation of an indirect dark matter signal is difficult due to large potential backgrounds from astrophysical sources, which are not perfectly understood. However, indirect detection can probe questions collider and direct searches cannot, such as whether **DM** is perfectly stable and what the annihilation cross sections are.

### 2.6.2.1 LIP INDIRECT DETECTION

Indirect limits for fractionally charged particles come from stellar evolution and supernovae (see limits titled WD, RG, and SN in Figure 14). Essentially, new low-mass particles can be produced in the hot and dense medium of stars, and eventually escape, carrying away energy [50]. The additional energy-loss channel modifies stellar evolution, and observations of brightness, etc. can set a limit on the **LIP** mass and interaction strength. For Supernova 1987A, the number of neutrinos detected at Earth roughly agrees with theoretical expectations. If fractionally charged particles contribute to cooling, the neutrino flux would decrease; the SN limit in Figure 14 is from such an analysis [40] [50].

### 2.6.3 DIRECT DETECTION

In direct detection, experimentalists seek to observe **DM** interactions in a detector composed of **SM** materials. Detectors are designed with a **DM** candidate in mind, and aspects of the detector are optimized at the design stage to search for one type of **DM**. Because direct detection searches are built with a particular **DM** candidate in mind, backgrounds can be controlled and minimized much more than in indirect or production searches. Experimental conditions can even be improved by designing for lower backgrounds for the candidate of interest; such changes cannot be applied to indirect searches. Of course, a given detector can search for **DM** candidate even if it was not initially designed/optimized to do so, and in this case, the search still benefits from the detailed understanding of backgrounds in the detector. Most current direct detection experiments fall into one of two categories: **WIMP** detector or axion detector. In the case of **WIMP** detectors, the detector target material is some homogenous material like solid Ge or liquid Xe, and experimentalists seek to detect energy deposition consistent with that of a **WIMP** causing a nuclear recoil in the target. This type of detector must be composed of radiopure materials and located deep underground to be capable of detecting rare **WIMP** interactions. In the case of axions, the detector is a resonator cavity or circuit with a strong magnetic field, which couples with the axion field. Cosmic rays and radioactivity are not backgrounds for axion detection, so these detectors need not be placed underground or built of radiopure

materials; however, their electronic noise must be strictly managed. Axion detectors take advantage of a resonance amplification of their signal that would occur at a specific axion mass and coupling. To observe the resonance signal, detector background noise must be kept sufficiently low.

### 2.6.3.1 LIP DIRECT DETECTION

Direct detection searches for fractionally charged particles include schemes like the Millikan drop experiment, which modern methods have improved upon (see [40] for more detail). Table-top style experiments searching for anomalous decay of ortho-positronium, or changes in the Lamb shift, would indicate additional couplings to a hidden sector [40]; these are marked Op and L in Figure 14, respectively. Searches for cosmogenic LIPs can also be accomplished by a variety of detectors and detector technologies. These types of searches set limits on the flux LIPs as a function of charge fraction. Limits from previous cosmogenic LIP searches, each described below, can be found Figure 15.

Kamiokande II, a large water Cherenkov detector, carried out a search for LIPs of charge  $e/3$  and  $2e/3$  [51]. Kamiokande II had a diverse neutrino science program, and made significant contributions to the current understanding of solar, atmospheric, and supernova neutrinos. The detector was fortuitously operational during Supernova 1987A and observed 11 neutrino events from the supernova [52], garnering a Nobel Prize. The detector consisted of a cylindrical steel tank containing 2400 tons of water viewed by 948 20-inch Photomultiplier Tube (PMT)s. This inner detector was surrounded by a  $4\pi$  steradian water veto at least 1.2 m thick, viewed by 123 20-inch PMTs. The LIP search utilized the number of Cherenkov photons detected to distinguish the fractional charges from the integer charge of the muon. The number of Cherenkov photons emitted per unit path length and unit wavelength is proportional to  $(1/f)^2$ , where  $f$  is the denominator of the fractional charge. The fractional charges were simulated by taking real muon events and multiplying the photon yield by  $(1/f)^2$ . Parameter spaces such as total photoelectron yield versus number of hit PMT identified a LIP region that was distinct from the muon region, providing a detection efficiency. PMT hit maps from the simulations were used to distinguish, by-eye, the LIPs from stopped muons and other complicated muon behavior in the detector that could reduce the photon yield. A limit was set on the flux of LIPs.

LSD, large scintillator detector, also carried out a search for LIPs of charge  $e/3$  and  $2e/3$  [53]. LSD, also known as the Mont Blanc Neutrino Scintillation Detector, was mainly concerned with detecting low energy neutrinos from cosmic sources. The LSD detector was composed of a modular array of 72 ( $1 \times 1 \times 1.5$ ) m<sup>3</sup> independent counter tanks arranged in 3 layers, with a total mass of 90 tons of C<sub>n</sub>H<sub>2n+2</sub> liquid scintillator.

Each tank was seen by three PMTs in a 3-fold coincidence. To reduce external radioactive backgrounds, the whole detector was shielded by iron, lead, and borex parafine. For the LIP search, the approach was to simulate the expected energy loss of the fractional charges in the detector, which show behavior distinct from a muon. Selection cuts were placed to reject muons and select LIPs by comparing, e.g. the energy loss in the upper plane to the energy loss in the middle plane. Some background events from muons remained in the signal region due to the muon only passing through 2 tanks, and an accompanying  $\gamma$  triggering the third tank. Signals such as these had energy deposition lower than a muon, and they could mimic a LIP. Background events such as the muon with  $\gamma$  signature were added to the simulation to assess the expected background rate in the LIP signal region. The number of LIP candidates from the real data were then compared to the expected background number, and a limit was set.

MACRO, another large scintillator detector, carried out a search for LIPs down to a charge of  $e/5$  [54] [55]. The main goal of MACRO was to search for magnetic monopoles, but it also made measurements relevant to high energy muon and neutrino astronomy [56]. The MACRO detector was divided into six modules, each of dimension  $(12.6 \times 12 \times 9.3) \text{ m}^3$ ; the global dimensions were  $(76.5 \times 12 \times 9.3) \text{ m}^3$  [56]. Each module contained a combination of scintillation counters, streamer tubes, and nuclear track detectors for a total mass of  $\sim 5300$  tons (see [56] for more detail). For the LIP search, timing information from the streamer tube modules was used to reconstruct a track. LIP candidates were required to have a reconstructed track and pass through the entire detector. Based on the track length, LIP candidates were further processed to determine the rate of energy loss in the scintillator. This energy deposition was used to distinguish LIPs from muons, as the energy deposited by a LIP scales with  $(1/f^2)$  compared to the muon energy deposition. The trigger efficiency of the modules to low energy events was determined with muons that “clipped” individual detectors, and the energy resolution was calibrated with low energy  $\gamma$  rays from natural radioactivity. Further data cleaning cuts are made to eliminate tracks that passed too close to the edge of a scintillator counter and those where timing information from the streamer tubes and scintillator modules disagree. Four remaining events were investigated by eye and determined to arise from complicated muon behavior, and a limit was set on the LIP flux.

Cryogenic Dark Matter Search (CDMS), a cryogenic germanium and silicon detector, carried out the first search for cosmogenic LIPs of charge  $\leq e/6$  [57]. CDMS was primarily a WIMP dark matter search experiment. The CDMS detector was composed of alternating Si and Ge modules arranged in stacks of six modules each (“towers”). For the LIP search, the probability distribution of energy deposition of LIPs of different charge fraction

in each tower module was determined. [LIP](#) candidates were required to pass through each module in a tower and deposit energy consistent with these probability distributions. Tracks were reconstructed based on the  $(x, y)$  positions of the energy depositions in each module, and a good track reconstruction was required. The dominant background was from  $\gamma$  scattering, which resulted in inconsistent energy depositions and poor tracks. Together, the tracking condition and the energy consistency requirements determined a [LIP](#) signal region, and simulation determined the efficiency for selecting [LIP](#) events from gamma events. In the search, all events were found to lie outside the signal region and a limit was set on the [LIP](#) flux.

Majorana Demonstrator ([MJD](#)), also a cryogenic germanium detector, carried out a search in the charge range  $\leq e/6$ , accessing more [LIP](#) parameter space than the [CDMS](#) result [41]. [MJD](#) is primarily a neutrinoless double beta decay experiment, seeking to understand if the neutrino is its own antiparticle. The [MJD](#) detector is composed of several towers of Ge modules, similar to the [CDMS](#) detector, but with many more towers. For the [LIP](#) search, the energy deposition of [LIPs](#) was simulated in order to assess the detection efficiency. A simple tracking algorithm compared the vectors between pairs of triggered modules; for straight tracks, the vectors all “point” to the same direction. The backgrounds such as gammas and electrical noise that fit the energy deposition criteria were eliminated with the tracking algorithm and a limit was set on the [LIP](#) flux.

A search for cosmic ray [LIPs](#) is carried out in Chapter 5 with the [LUX](#) experiment, which is also a canonical [WIMP](#) detector, but uses [LXe](#) for its target material. More details about [LXe](#) as a detector medium are found in Chapter 3. Details about the [LUX](#) detector can be found in Chapter 4.

# 3

## PARTICLE DETECTION WITH LIQUID XENON

---

Liquid xenon detectors are powerful tools for rare event searches. In particular, the dual phase [LXe TPC](#) has been very successful in accessing [WIMP](#) parameter space and currently holds the worlds most sensitive limits on [WIMPs](#). This chapter covers particle interactions in liquid xenon and explains the operating principles of [LXe TPCs](#). The features of these detectors that make them especially useful for [WIMP](#) searches are discussed, and some methods by which their function can be adapted to search for other dark matter candidates are given.

### 3.1 LIQUID XENON AS A DETECTOR MEDIUM

This section first describes the properties of [LXe](#) and the microphysics of signal generation in xenon. A few examples of xenon detector programs are given, and the basic principles of [TPCs](#) are described.

#### 3.1.1 PROPERTIES OF LIQUID XENON

Liquid xenon has many properties relevant to particle detection, particle identification, and also many properties related to the ease of detector operation:

- The density of [LXe](#) is  $2.9 \text{ g/cm}^3$  at  $170 \text{ K}$ , which is higher than other noble elements (Liquid Argon ([LAr](#)) has density  $1.4 \text{ g/cm}^3$  at  $87 \text{ K}$ ). The advantage of this two-fold: (1) large target mass gives a large exposure, increasing the sensitivity of the dark matter search; (2) self-shielding: high density targets are capable of stopping external radiation, producing an ultra-low-background volume in the center of the detector where rare-event searches can be performed (this region is called the “fiducial volume”).
- Xenon gas is easily liquefied with liquid nitrogen ( $77 \text{ K}$ ) or commercially available pulse tube refrigerators.
- Xenon has very few long-lived radioisotopes that cause troublesome backgrounds. The isotopes are the  $2\nu\beta\beta$  decays of  $^{136}\text{Xe}$  (nat-

ural abundance 8.875%) with measured half-life of  $T_{1/2}^{2\nu\beta\beta} = 2.1 \times 10^{21}$  years and  $^{134}\text{Xe}$  (natural abundance 10.4%) with half-life  $T_{1/2}^{2\nu\beta\beta} > 8.7 \times 10^{20}$  years. These long half-lives and relatively low abundances together result in a very low count rate, and the isotopes can be used to search for neutrino-less double beta decay ( $0\nu\beta\beta$ ).

- Particles interacting in [LXe](#) create excitons and electron ion-pairs, producing detectable quanta: scintillation photons and ionization electrons (described in Section 3.1.2).
- Xenon is transparent to its own scintillation light (described in Section 3.1.2). The scintillation light is of wavelength  $\lambda = 178$  nm and can be directly detected with current [PMT](#) technology, and doesn't require the use of e.g wavelength shifter.
- Xenon has high light and charge yields, and therefore a low threshold for producing detectable quanta. A useful quantity is the so-called “W-value” of [LXe](#):  $W = 13.7 \pm 0.2$  eV [58]. The W-value, analogous to a work-function, is a measure of the average energy expenditure to produce one quantum (scintillation photon or an ionization electron) from liquid xenon.
- Ionization electrons produced in particle interactions can be drifted away from the interaction site and detected independently of the scintillation signal. This is the basic principle of [TPCs](#), which provides measurement of both light and charge (see Section 3.2).
- Xenon, as a noble element, is easily purified with a heated getter to rid electronegative impurities. Some of these impurities absorb xenon scintillation light, e.g.  $\text{N}_2$ , and others can absorb electrons, interfering with the ionization signal in [TPCs](#), e.g.  $\text{O}_2$ .
- [LXe TPCs](#) are easily scalable: creating a large homogenous volume is straightforward. In contrast, solid state detectors, such as cryogenic Ge, are more difficult to scale up directly and require instead the production of multiple small modules ( $O(10)$  cm) which each must be instrumented separately.
- The comparatively large mass of xenon allows it to be purified of other noble gasses via gas chromatography [59] and cryogenic distillation [60]. As other noble gasses cannot be removed via getter, this feature is extremely useful in removing the troublesome background of  $^{85}\text{Kr}$  decay.  $^{85}\text{Kr}$  decays via beta emission to stable  $^{85}\text{Rb}$  with a half-life of 10.8 years and  $Q_\beta = 687$  keV. The decay proceeds directly to the  $^{85}\text{Rb}$  ground state with a branching ratio of 99.6%.

Since no de-excitation of  $^{85}\text{Rb}$  follows, this beta decay cannot be rejected as background by coincidence with a gamma, and relies purely on the ability to discriminate between WIMP-like Nuclear Recoil ([NR](#)) and beta- or gamma- produced Electron Recoil ([ER](#)). While ER/NR discrimination is one of the features of [LXe TPCs](#) (described further in Section 3.4.1.1), leakage of [ER](#) events in to the [NR](#) signal region can occur and the best mitigation is to remove as much of the  $^{85}\text{Kr}$  as possible. Single-phase [LXe](#) detectors, with no ER/NR discrimination, benefit greatly from the ability to remove  $^{85}\text{Kr}$ .

### 3.1.2 SCINTILLATION AND IONIZATION SIGNAL GENERATION

Signal generation in xenon is summarized in Figure 18. A particle can interact with a xenon atom through interaction with an orbiting electron, creating an [ER](#), or though an interaction with the xenon nucleus [NR](#), where the nucleus is imparted with momentum and recoils. The recoiling electron or nucleus loses energy via interaction with neighboring xenon atoms, creating more excited atoms and electron-ion pairs. The excited xenon atoms,  $\text{Xe}^*$ , combine with other atoms to form an excited dimer (also called excitons or excimers),  $\text{Xe}_2^*$ . The excited dimer forms one of two states: a triplet or a singlet, which de-excites with the emission of a 178 nm photon. The lifetimes of the triplet and singlet are measured to be 24 ns and 3 ns, respectively [61]. Since the scintillation light is produced by the excimer, which has a different electronic structure than atomic xenon, the light is free to propagate through the detector and will not be absorbed by the atomic xenon. The energy of the scintillation photons is in fact much less than the energy needed to excite  $\text{Xe}$  atoms. The  $\text{Xe}^+$  ions of the electron-ion pairs combine with other  $\text{Xe}$  atoms to form dimers  $\text{Xe}_2^+$ , and these dimers can combine with electrons (from the electron-ion pairs) to form excitons,  $\text{Xe}_2^*$ , which then decay and produce additional 178 nm scintillation photons. This process is called recombination. If no electric field is applied, all electron-ion pairs recombine to produce additional scintillation photons. If an external electric field is present, some electrons can be drifted away from the interaction site to be detected with other methods.

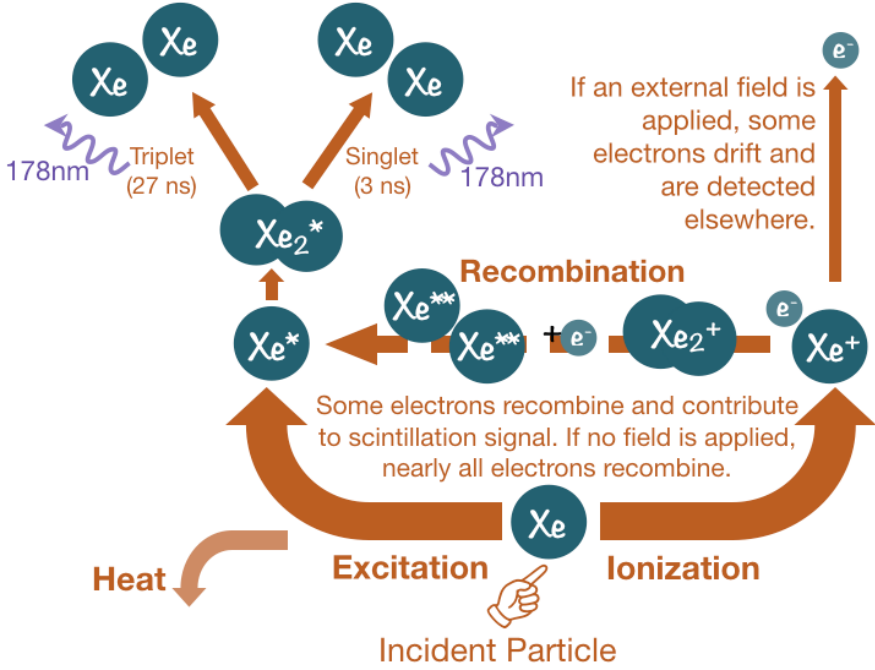


Figure 18: Diagram summarizing the generation of the scintillation and ionization signal generation in dual-phase xenon time projection chambers.

## 3.2 TYPES OF XE DETECTORS

There are a variety of detectors that use xenon as their target material. Xenon is utilized in single phase detectors which can be comprised of liquid or gas. Xenon is also utilized in dual-phase detectors which have both liquid and gas regions. This section gives examples of a few types of Xe detector programs, commenting on the challenges that affect their sensitivities.

### 3.2.1 XMASS: A SINGLE PHASE LXE DETECTOR

XMASS is a single phase liquid xenon detector shown in Figure 19; it measures a scintillation-only signal [62]. There is no electric field, so no separate ionization signal can be detected. It is useful to note that even the case of zero field, all ionization electrons may not recombine. If  $kT$  is large, an ionized electron may not “find” a  $Xe^+$  ion. XMASS is a multipurpose experiment, which aims to study solar neutrinos, double beta decay, and WIMPs [63].

The sensitivity of liquid xenon detectors to low energy recoils depends on their ability to detect the 178 nm scintillation photons with high-efficiency.

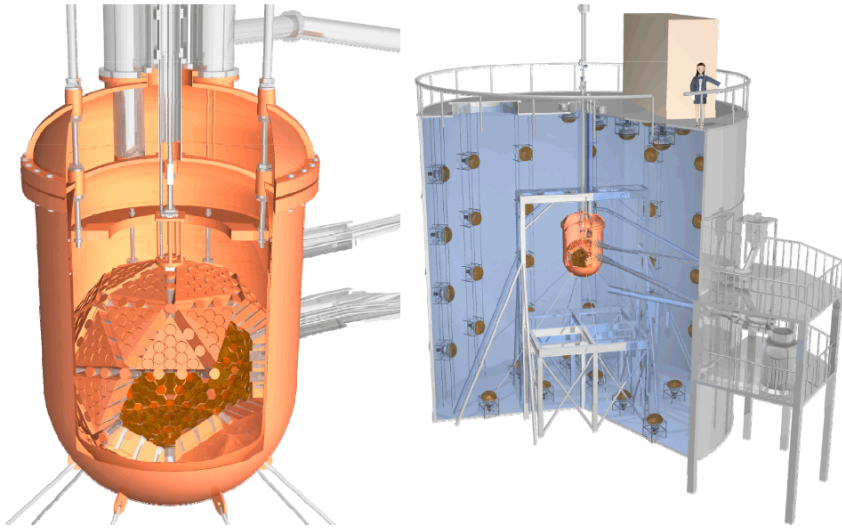


Figure 19: Diagram of the XMASS detector and water tank. Figure from [63].

High Quantum Efficiency (QE) PMTs constructed with ultra-low radioactivity materials are the go-to instrument for this purpose. In addition to high-efficiency photon-detectors, liquid xenon detectors must also have high geometrical light collection efficiency to optimize sensitivity. Single-phase liquid xenon detectors such as XMASS aim to maximize light-collection with a spherical geometry, endeavoring to cover  $4\pi$  steradians surrounding the LXe. The XMASS detector geometry accomplishes photocathode coverage of 62%. Two types of Hamamatsu PMTs are used (R10789-11 and R10789-11MOD), which have QE of 28%. Putting this together, XMASS quotes a final signal collection efficiency of 20% [62], [64].

### 3.2.2 EXO-200: A SINGLE PHASE LXE TPC

The EXO-200 experiment is a single phase liquid xenon TPC shown in Figure 20. TPCs detect the scintillation photons and ionization electrons separately. The scintillation photons are detected promptly, while the ionization electrons are drifted away from the interaction site to be detected elsewhere. EXO-200 uses avalanche photodiodes to collect the scintillation photons and crossed-wire planes to collect the ionization electrons [65].

In addition to light-collection efficiency, the sensitivity of TPC xenon detectors also depends on their ability to collect signal from the ionization electrons. There are challenges in delivering HV to liquid xenon in order to set up the electric field which drifts the ionization electrons (some of these challenges are illustrated in Chapter 6). Additionally, electroneg-

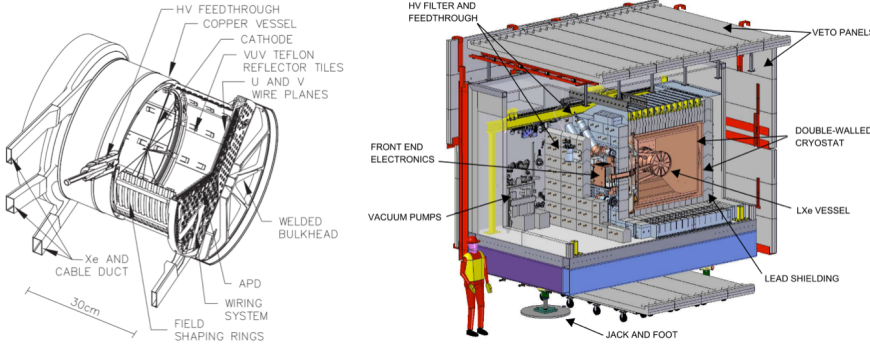


Figure 20: Diagram of the EXO-200 detector and systems. Figure from [65].

ative impurities such as oxygen ( $O_2$ ) present in the detector attract and capture ionization electrons as they drift, eating away the ionization signal. These non-noble impurities are removed by constantly circulating the xenon through a heated zirconium getter and returning it to the detection volume. Purification through a getter must be done in gaseous phase, so liquid xenon removed from the detection volume is evaporated, passed through the getter via a circulation system, and re-condensed into the detection volume.

### 3.2.3 LUX: A DUAL PHASE LXe TPC

The [LUX](#) experiment is a dual phase [LXe TPC](#) shown diagrammatically in Figure 21; much more detail about the [LUX](#) detector and components can be found in Chapter 4. A dual phase liquid xenon [TPC](#) is a type of [TPC](#) with a large liquid target volume and a small region of xenon vapor above the liquid volume, instrumented with light sensors (typically [PMTs](#)). [LUX](#) uses high [QE PMTs](#) (Hamamatsu R8778) to detect the prompt scintillation photons; this primary signal is called S1. The ionization electrons are drifted upward to the gas region by an applied electric field, and extracted across the liquid-gas boundary by a higher electric field, where they undergo proportional scintillation and produce a second signal called S2, which is also detected by the [PMTs](#). Separating an energy deposition into two separate signals, S1 and S2, allows for powerful background rejection in dark matter searches, discussed further in Section 3.4.1.1.

The electric fields are supplied by a series of electrodes, composed of wire planes, grids, or chemically etched meshes, held at constant voltages. The bottom-most field-producing electrode is called the cathode. At the top of the liquid region is the gate or extraction electrode, followed by the anode in the gas. The liquid region is often referred to as the “drift region” and region between the gate and anode is referred to

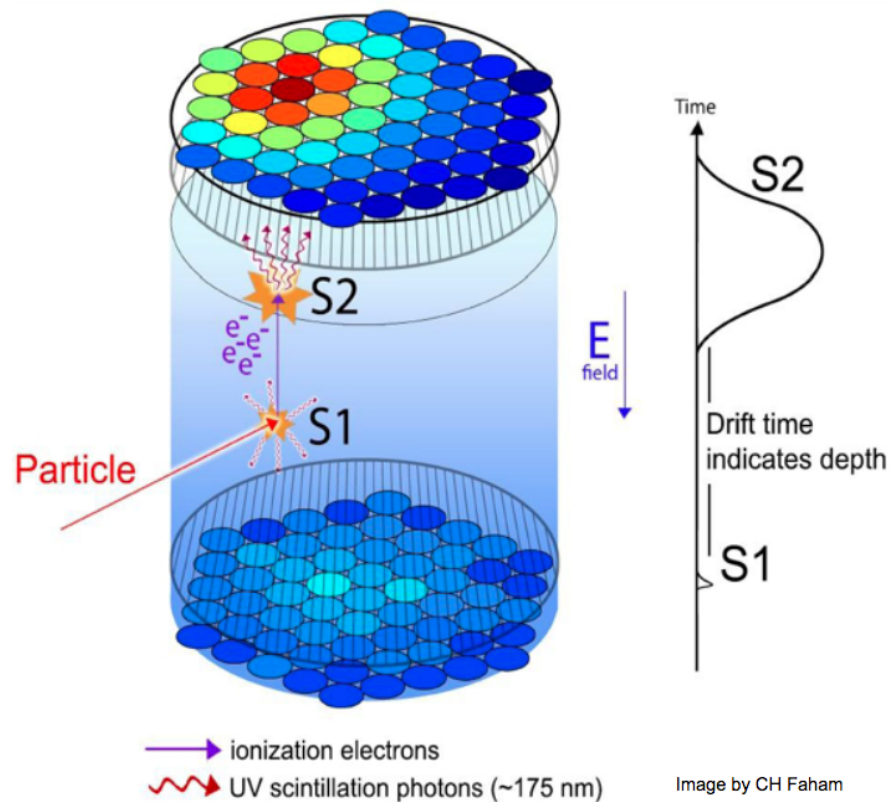


Figure 21: Diagram of a dual-phase xenon time projection chamber. The time difference between S1 and S2 gives the depth ( $z$ ) of the interaction, and  $(x, y)$  is reconstructed from the S2 signal.

as the “extraction region”. The electrons are extracted from liquid to gas with some efficiency, called the Electron Extraction Efficiency ([EEE](#)). In addition to the challenges of light-collection, [HV](#) delivery, and xenon purification, [EEE](#) plays an important role in the operation of dual phase [LXe TPCs](#), and is discussed further in Chapter 8.

[LUX](#) is lined with Polytetrafluoroethylene ([PTFE](#)) to take advantage of its extremely high (~99%) reflectivity for 178 nm light in [LXe](#) [66]. The [LUX](#) detector uses a cylindrical geometry, with all non-light-collecting surfaces lined with [PTFE](#). The Hamamatsu R8778 [PMTs](#) ([QE](#) of 33%) are installed only on the top and bottom of the detector, but the reflective [PTFE](#) allows [LUX](#) to accomplish an S1 light detection efficiency of 11% [67].

The S2 in a dual phase [TPC](#) plays two important roles: (i) internal amplification of the signal, whereby a few electrons are transformed into O(10) times as many photons (ii)  $(x, y)$  localization via [PMT](#) hit pattern. The time spacing of the S1 and S2 signals (called “drift time”) can be converted to depth ( $z$ ) of the interaction, providing full  $(x, y, z)$ -reconstruction of the interaction position. The full position reconstruction capability allows [LXe TPCs](#) to select a fiducial volume in the center of the detector that has ultra low background, as the xenon medium self-shields from radioactive backgrounds located in and on detector components.

The remainder of this chapter focuses on the dual phase [LXe TPC](#) technology for dark matter detection.

### 3.3 ENERGY RECONSTRUCTION IN DUAL PHASE LXETPCS

Energy reconstruction in dual phase xenon [TPCs](#) comes from the measurable quantities, S1 and S2, but begins with the number of excitons  $n_{ex}$  and electron-ions pairs  $n_i$  generated at the interaction site.

$$E = fW(n_{ex} + n_i) \quad (21)$$

where  $E$  is the deposited energy.  $W$  is the average energy needed to produce a single excited or ionized atom,  $W = 13.7 \pm 0.2$  eV [61]. The quenching factor,  $f$ , is 1 for electronic recoils but  $f \neq 1$  for nuclear recoils. For now, take the case of electronic recoils and set  $f = 1$ . This equation can be rewritten:

$$E_{ER} = W\left(1 + \frac{n_{ex}}{n_i}\right)n_i \quad (22)$$

The ratio of excitons to ions is constant for electron recoils  $n_{ex}/n_i = 0.2$  [68]. It should be noted that this value of 0.2 is an experimental result,

but it disagrees with the calculated value of 0.06; see [69], [70], and [71] and references therein for more detail. As discussed in Section 3.1.2, each exciton deexcites, emitting a 178 nm photon, some fraction  $r$  of the initial electron-ion pairs recombine and form additional excitons. The total number of prompt scintillation photons created by the interaction is then:

$$n_\gamma = \left( r + \frac{n_{ex}}{n_i} \right) n_i \quad (23)$$

And the total number of electrons escaping recombination is:

$$n_e = (1 - r) n_i \quad (24)$$

Thus, the effect of recombination is to “trade-out” electrons for photons, but the total number of quanta is conserved (Figure 22 (top)). The amount of recombination depends on applied electric field, LXe density, and particle energy [68]. In the case of the 122 keV electron recoils in Figure 22 (bottom): at low fields, most of the electron-ion pairs recombine, which results in more scintillation photons. As the applied electric field increases, more electrons are pulled away from the interaction site resulting in fewer scintillation photons and more ionization electrons. These amounts of photons and electrons are referred to as the scintillation and ionization yields. The two quantities,  $n_\gamma$  and  $n_e$  relate directly to the observable S1 and S2 signals, so we can rewrite Equation 25 as follows:

$$\begin{aligned} E_{ER} &= W(n_\gamma + n_e) \\ &= W\left(\frac{S1}{g_1} + \frac{S2}{g_2}\right) \end{aligned} \quad (25)$$

where S1 and S2 are in units of detected photons (phd) or photoelectrons (phe), and  $g_1$  and  $g_2$  are detector gains in units of phd/quanta or phe/quanta<sup>1</sup>.  $g_1$  is the detection efficiency for the prompt scintillation photons: it is a product of the average geometrical light collection efficiency and the average PMT QE. Typical values for  $g_1$  are in the range of 0.1-0.2.  $g_2$  is the analogous quantity for S2 proportional scintillation light: it is a product of the EEE and the average number of detected photons produced by one extracted electron. Typical values for  $g_2$  are in the range 10-60.

---

<sup>1</sup> An distinction should be made between the traditional units of phe and the units of phd which are used in many LUX publications. The Hamamatsu R8778 PMTs used in LUX emit two photoelectrons for a single VUV photon ~20% of the time [72], but the PMT gain calibration photons (from blue LEDs) do not. LUX performed additional calibration with VUV photons to account for the difference, and report detected photons instead of photoelectrons [67]

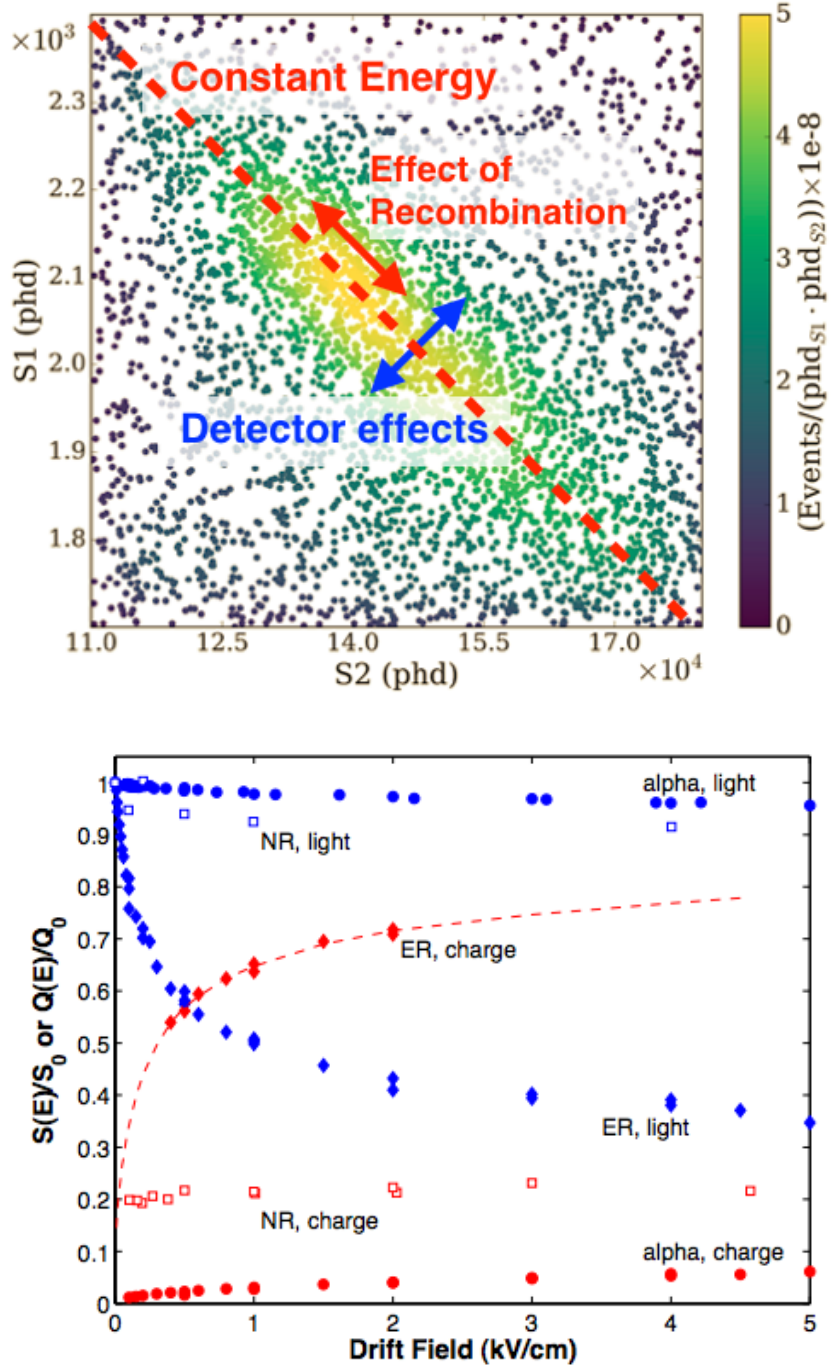


Figure 22: (top) Plot illustrating the effect of recombination and detector effects on a line source ( $^{127}\text{Xe}$ ), courtesy of E. Pease. (bottom) Field dependence of scintillation and ionization yield in LXe for 122 keV electron recoils (ER), 56.5 keV nuclear recoils (NR) and 5.5 MeV alphas, relative to the yield with no drift field from [73].

To properly reconstruct the energy of nuclear recoils, we must revisit the quenching factor factor  $f$ . Equation 25 then becomes:

$$\begin{aligned} E_{NR} &= fW(n_\gamma + n_e) \\ &= fW\left(\frac{S1}{g_1} + \frac{S2}{g_2}\right) \end{aligned} \quad (26)$$

This equation can be rewritten:

$$E_{NR} = fE_{ER} = \frac{E_{ER}}{\mathcal{L}} \quad (27)$$

where  $\mathcal{L}$  is Lindhard's factor. Lindhard's factor accounts for the fraction of energy lost to atomic motion (heat) in nuclear recoils [74]. Recall that a recoiling Xe nucleus loses energy in interactions with neighboring Xe atoms to produce S1 and S2; it is the energy partitioning in this cascade with neighboring atoms that results in different energy scales for ER and NR. Lindhard showed that the energy partitioned in nuclear interactions and electron interactions (as opposed to heat) from a recoiling xenon nucleus is:

$$\mathcal{L} = \frac{kg(\epsilon)}{1 + kg(\epsilon)} \quad (28)$$

where  $k = 0.133Z^{2/3}A^{-1/2}$  is a proportionality constant that relates electronic stopping power and the velocity of the recoiling xenon atom, and  $\epsilon = 11.5(E_{NR}/keV)Z^{-7/3}$  [74]. Lindhard's calculation yields  $k = 0.166$ , which is the commonly accepted value. Measurements of nuclear recoils in LXe are used to fit for  $k$ . Several experiments were compared by Sorensen and Dahl to determine that nuclear recoil energy is well described by  $0.110 < k < 0.166$  [75]. Results from LUX yielded  $k = 0.1735 \pm 0.0060$  [76].

If it is not known *a priori* whether an interaction is a nuclear recoil or electron recoil, the “electron equivalent” energy is given in units keV<sub>ee</sub>. If it is known that the recoil is a nuclear recoil, Lindhard’s factor is applied and the units can be given in keV<sub>nr</sub>. Lindhard’s factor allows us to combine nuclear recoils and electronic recoils on one energy scale by labelling contours of constant reconstructed energy with both keV<sub>ee</sub> and keV<sub>nr</sub> (examples in Figure 23).

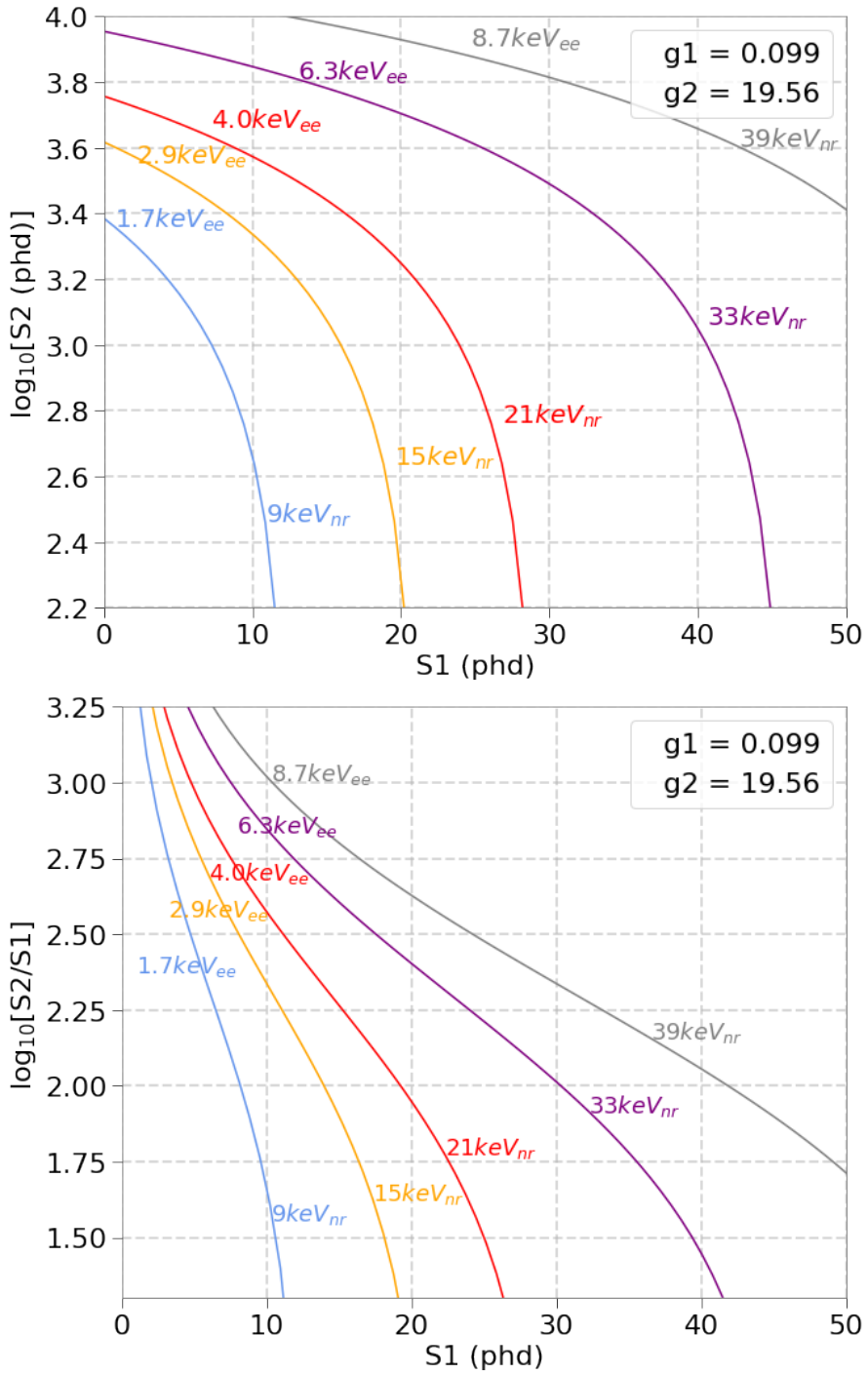


Figure 23: Plots showing combined energy contours in two common sets of axis units, for an example set of  $g_1$  and  $g_2$ .

## 3.4 DUAL PHASE XENON TPCS FOR DARK MATTER DETECTION

Dual phase Xe TPCs have been at the forefront of the hunt for dark matter in the last several decades. As described above, the xenon medium and detector technology make excellent low-background, rare-event searches with high signal yields. Dual phase Xe TPCs also provide a few enhancements to WIMP dark matter searches, but other dark matter or rare event searches are also possible with the same detector. This section describes the basic principle of WIMP searches with LXe TPCs, then goes on to discuss how other types of dark matter searches are carried out with these detectors.

### 3.4.1 WIMP SEARCHES WITH LXE TPCS

Dual-phase LXe TPCs are designed with WIMP searches in mind. They have been very successful in reaching large areas of WIMP parameter space. This section describes how WIMP searches are carried out with this detector technology.

#### 3.4.1.1 ER, NR DISCRIMINATION

One of the most powerful features of LXe TPCs, which has made the technology especially useful in the hunt for WIMP dark matter, is the ability to discriminate between electron recoils and nuclear recoils. WIMP interactions are expected to be nuclear recoils, but most natural radioactivity ( $\beta, \gamma$ ) are electron recoils. The ratio of initial excitons to ions ( $n_{ex}/n_i$ ) and the amount of recombination for equal energy ER and NR is different, so for events with the same reconstructed energy  $E$  (keV $_{ee}$ ), the ratio of S2/S1 is characteristically different. A useful discrimination space is  $\log_{10}(S2/S1)$  vs S1, as the distributions of  $\log_{10}(S2/S1)$  for ER and NR events of the same S1 are approximately Gaussian. Different calibration sources are used to develop a population of events known to be ER and a population of events known to be NR, these calibration sources reveal what is known as the ER and NR bands. Figure 24 shows the ER and NR bands from LUX; the details of these calibrations are discussed further in Chapter 4.

In the course of a WIMP search, the experimentalists are tasked with keeping a stable detector operating for months or years. In this time, the detector will see events of natural radioactivity and perhaps WIMPs. The more prevalent natural radioactivity from  $\beta$  and  $\gamma$  appears in the ER band (location of bands is known from calibration), and nuclear recoil events (due to background neutrons or WIMPs) appear in the NR band. Due to

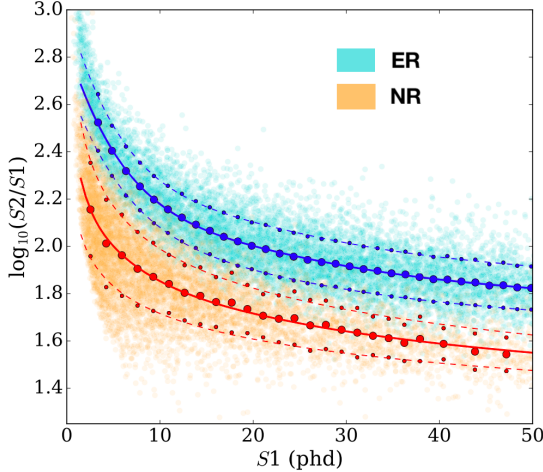


Figure 24: Plot showing **ER** and **NR** bands from **LUX**. Solid lines are the **ER** and **NR** Gaussian means,  $\mu$ ; dotted lines are  $\mu \pm 1\sigma$ . Figure from [68].

band overlap, only events appearing below the **NR** mean are considered **WIMP** candidates. This restriction cuts signal acceptance to 50%, but allows dual-phase **TPCs** to reject background electronic recoils at  $\gtrsim 99\%$ . The background acceptance rate is known as **ER** leakage. It is the fraction of events appearing below the **NR** mean from the **ER** calibration source. For a background rejection rate of 99.99%, the **ER** leakage is 0.01%, this number, combined with the background rate and exposure, determines the sensitivity of the detector.

#### 3.4.1.2 WIMP RATES AND CROSS SECTION

The choice of direct detection for **WIMP** searches was touched on in Section 2.6. Here, we go through the specifics of **WIMP** rates and their cross section in **LXe**. Although a multi-pronged approach including collider searches and indirect detection is ultimately necessary to understand dark matter, the **LXe TPC** technology profits from a few enhancements that make it especially suited for **WIMP** searches. These enhancements are revealed below, as the **WIMP** rates and cross section are outlined.

**WIMPs** scattering in the **TPC** produce measurable nuclear recoils. The observed nuclear recoil spectrum eventually determines the number of **WIMP** events observed, and it depends on both **WIMP** properties and detector properties. The energy imparted to the nucleus depends on the **WIMP** mass  $M_\chi$  and velocity distribution, as well as the mass of the target nucleus  $M_T$  and the cross section  $\sigma$  that governs how effectively energy is transferred to the nucleus. Each of these pieces is described below, indicated with a **bold note** to aid the reader.

**Local Number Density and Velocity Distribution:** Assuming a spherical dark matter halo, estimates for the local density of dark matter  $\rho\chi$  can be made from astrophysical observations. The velocity distribution  $f(v)$  is assumed to be isotropic and Maxwellian, with a cut-off at the escape velocity  $v_{esc}$  of the Milky Way. If we account for the velocity of the Earth through the galactic plane  $v_E$ , the velocity distribution is shifted:  $f(v) = f(v, v_E)$ . Following Lewin and Smith [77], we can write the local number density:

$$\begin{aligned} dn &= \frac{n_0}{k} f(v, v_E) d^3v \\ &= \frac{n_0}{k} \exp\left(-\frac{(v + v_E)^2}{v_0^2}\right) d^3v \end{aligned} \quad (29)$$

where  $n_0 = \rho_\chi/M_\chi$  is the average local number density of dark matter particles,  $v_0 \approx 230$  km/s [77] is the mean of the dark matter velocity distribution, and  $k$  is a normalization constant such that  $\int_0^{v_{esc}} dn \equiv n_0$ . If the escape velocity is infinite, the normalization integral is easily evaluated:

$$k = \int_0^{2\pi} \int_{-1}^{1i} d(\cos\theta) \int_0^\infty f(v, v_E) v^2 dv = (\pi v_0^2)^{3/2} \equiv k_0 \quad (30)$$

However,  $v_{esc}$  is not infinite ( $v_{esc} \approx 544$  km/s [78]), and so the normalization integral evaluates to:

$$k = k_0 \left[ \operatorname{erf}\left(\frac{v_{esc}}{v_0}\right) - \frac{2}{\pi^{1/2}} \frac{v_{esc}}{v_0} \exp(-v_{esc}^2/v_0^2) \right] \equiv k_1 \quad (31)$$

Although this is a more complicated expression, it should be noted the difference between  $k_0$  and  $k_1$  is less than 0.5%.

**Scattering Rate:** We now have a full picture of the local number density of dark matter, and we focus on the scattering rate in the detector. If we let  $\sigma$  be the scattering cross-section per nucleus (the details of  $\sigma$  are discussed later), the event rate per unit mass detector with target mass  $M_T$  is:

$$dR = \frac{1}{M_T} \sigma v dn \quad (32)$$

The experimentalist is concerned with the observable recoil energy spectrum produced by such a dark matter rate. A WIMP of mass  $M_\chi$  and initial energy  $E_\chi = \frac{1}{2} M_\chi v^2$  scattering at angle  $\theta$  (in the center-of-mass frame) will impart a recoil energy  $E_R$  to a target nucleus of  $M_T$

$$E_R = r E_\chi \frac{1 - \cos\theta}{2} \quad (33)$$

where  $r$  is the kinematic factor:

$$r = \frac{4M_\chi M_T}{(M_\chi + M_T)^2} \quad (34)$$

Note that the kinematic factor indicates that recoil energies are greatest for  $M_\chi \approx M_T$ . SUSY models favor WIMP masses in the range 100 GeV–1000 GeV (Figure 26), which provides xenon ( $M_{Xe} \approx 123$  GeV) with an enhancement for WIMPs when compared with other dark matter candidates. WIMP scatters are assumed to be isotropic, so recoil energies are distributed uniformly in the range  $0 < E_R < rE_\chi$  (i.e. Equation 33 for  $0 < \cos\theta < 1$ ). We can put this together with Equation 32 to arrive at an differential rate per recoil energy in the detector – i.e. the observable recoil spectrum for WIMP-nucleus scattering. Note that equation Equation 32 is in terms of the WIMP velocity  $v$  and Equation 33 is in terms of WIMP energy  $E_\chi = \frac{1}{2}M_\chi v^2$ , so a change of variables is required. After the variable change, we can write:

$$\frac{dR}{dE_R} = \frac{\rho_\chi}{M_\chi} \frac{\sigma}{k} \left( \frac{M_T + M_\chi}{M_T M_\chi} \right)^2 \int_{v_{min}}^{v_{max}} \frac{1}{v} f(v, v_E) d^3v \quad (35)$$

**WIMP-Xe Cross Section:** Until now, we have left off discussion of the WIMP-nucleus cross section  $\sigma$ . Equation 35, as it stands, is the WIMP spectrum in the limit of billiard-ball coherent scattering. In reality, the nucleus has structure which must be accounted for; this is accomplished with a nuclear form factor  $F = F(q)$ . In addition, the cross-section is split into spin-independent ( $\sigma_{SI}$ ) and spin-dependent ( $\sigma_{SD}$ ) components:

$$\sigma = \sigma_{SI} F_{SI}^2(q) + \sigma_{SD} F_{SD}^2(q) \quad (36)$$

The nuclear form factor,  $F(q)_{SI,SD}$ , decreases the cross section at higher momentum transfer; it is not discussed further. The two coherent terms  $\sigma_{SI}$  and  $\sigma_{SD}$  (i.e. the cross sections in the limit of zero momentum transfer) are parametrized as follows:

$$\begin{aligned} \sigma_{SI} &= \frac{4\mu^2}{\pi} [(A - Z)f_n + Zf_p]^2 \\ &\approx \frac{4\mu^2 A^2}{\pi} f_n^2 \end{aligned} \quad (37)$$

where  $\mu$  is the usual reduced mass, and the second line takes into account that for SUSY WIMP models, the couplings to neutrons and protons are approximately equal ( $f_n \approx f_p$ ).

$$\sigma_{SD} = \frac{32G_F\mu^2}{\pi} \frac{J+1}{J} [\langle s_n \rangle a_n + \langle s_p \rangle a_p]^2 \quad (38)$$

where  $G_F$  is the Fermi constant,  $J$  is the total nuclear spin of the target, and  $\langle s_{n,p} \rangle$  and  $a_{n,p}$  represent values for neutron and proton spins and couplings, respectively. Note that  $\sigma_{SI}$  scales as  $A^2$ , which indicates a larger cross-section for larger targets; this is the second enhancement from which xenon WIMP detectors profit.  $\sigma_{SD}$  lacks the  $A^2$  scaling, and is smaller than  $\sigma_{SI}$ . This indicates that recoil-rates are dominated by spin-independent interactions. The two cases are treated separately, with collaborations releasing both spin-independent and spin-dependent WIMP limits. In liquid xenon detectors, the odd-numbered nuclei  $^{129}\text{Xe}$  and  $^{131}\text{Xe}$  contribute to the spin-dependent rate. The enhancements for the WIMP recoil rate in Xe, which come from the kinematic enhancement in rate and the  $A^2$  cross section enhancement, are illustrated in Figure 25 [63]. For low-mass WIMPs ( $M_\chi \lesssim 5 \text{ GeV}$ ), xenon detectors quickly lose sensitivity when compared with cryogenic germanium and silicon detectors (Figure 26), and new analysis techniques are needed to search for these candidates in xenon. The next section discusses some analysis techniques that stretch the capabilities of LXe TPCs to search in new dark matter parameter spaces.

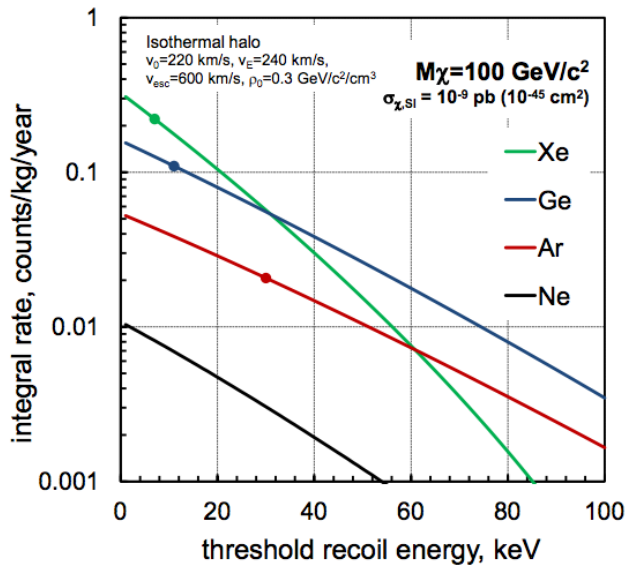


Figure 25: Plot showing spin-independent WIMP rates in common detector target materials, dots indicate typical thresholds for the targets. Xenon gains in favored SUSY parameter space ( $M_\chi \gtrsim 100 \text{ GeV}$ ) due to a kinematic enhancement ( $M_\chi \sim M_{Xe}$ ) and a cross-section enhancement ( $\sigma_{SI} \propto A^2$ ). Figure from [63].

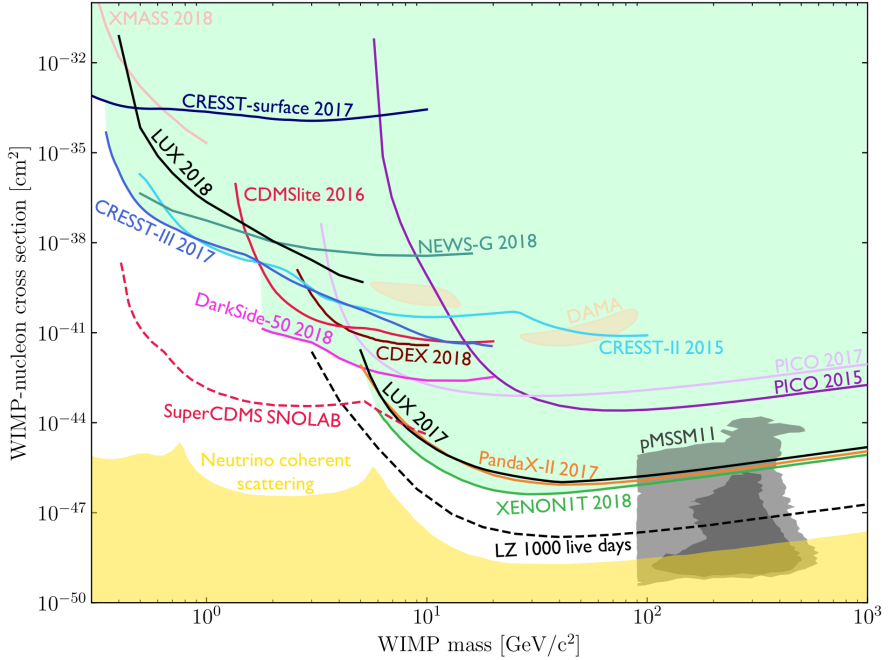


Figure 26: A summary of the excluded WIMP parameter space by all experiments (green). Solid lines indicate previous results and dashed lines indicate projections for future experiments. Although next generation xenon experiments (LZ, black dashed) perform better for SUSY WIMP parameter space (gray region labelled pMSSM), germanium and silicon (SuperCDMS SNOLAB, pink dashed) can access other light dark matter parameter space below 10 GeV. The signal regions are from the DAMA collaboration, which has a long standing claim of detection with an annular modulation search; however, no other experiments have been able to reproduce such an observation. Plot courtesy of L. Tvrznikova, regenerated from [79].

### 3.4.2 OTHER DARK MATTER SEARCHES WITH LXe TPCs

For the simplest models,<sup>3</sup> available SUSY parameter space has dwindled greatly in the last few decades, due in large part to the success of LXe detector technology. Coupled with no observation of SUSY at the LHC, experimentalists are beginning to look to other models and parameter spaces for dark matter. New technologies are being developed and refined for new dark matter candidates, but already existing, well-understood detector technologies such as dual phase TPCs can also be employed in the search for non-WIMP dark matter. New analysis techniques can stretch the standard WIMP analysis to lower masses, and to completely different dark matter candidates as well. This section briefly summarizes a few key analysis techniques that have been utilized by LXe TPCs to stretch the detector technology and access new parameter spaces.

To understand how to expand a typical WIMP analysis, we must first understand the thresholds that affect the current searches. Due to internal amplification of the S2 signal, LXe TPCs are capable of detecting events that produce a single electron. However, these detectors typically employ analysis thresholds much higher than their bare detection threshold for WIMP searches. In their first WIMP search results, the Xenon10 collaboration imposed an analysis threshold of  $4.5 \text{ keV}_{nr}$  [80]. The first LUX results set an analysis threshold of  $4.3 \text{ keV}_{nr}$  (with  $2 < S1(\text{phd}) < 30$  and  $S2(\text{phd}) > 200$ ;  $S2(\text{electrons}) \gtrsim 8$ ) [81]. The first Xenon100 results set an analysis threshold of  $8.7 \text{ keV}_{nr}$  ( $4 < S1(\text{phe}) < 20$  and  $S2(\text{phe}) > 300$ ;  $S2(\text{electrons}) \gtrsim 10$ ) [82]. Such thresholds are determined by the S1 light-collection efficiency of the detector; the analysis thresholds just described ensure the presence of an S1 in the event (S1 light collection efficiency is responsible for the steep rise in the xenon TPC limits at low WIMP mass). Without both an S1 and S2 in the event, the full  $(x, y, z)$  position cannot be reconstructed, and so a fiducial volume cut cannot be applied. Sorensen showed that the Xenon10 S2 pulse width carries a mild  $z$ -dependence [83], and so larger detectors with a long drift time may gain reliable  $z$ -position reconstruction via S2 pulse width [84]. A Xenon100 “S2-only” analysis sets limits on low mass WIMPs, using the same detector conditions as the canonical WIMP search [85] (an S2 pulse with  $z$ -correlation is not employed).

In 2011 the Xenon10 collaboration presented a search for low-mass (5 - 20 GeV) dark matter [86]. They used both new analysis techniques and modified detector conditions for an S2-only search. The detector conditions were distinct from the Xenon10 WIMP search in [80]: the secondary scintillation gain was about 12% higher, and the S2-sensitive trigger threshold was set at the level of a single electron. With this, the collaboration carried out a standard WIMP analysis (i.e one based on the pro-

cedure presented in 3.4.1.2), with a lowered S2 analysis threshold of 4 electrons ( $1.4 \text{ keV}_{nr}$ ). Since Xenon10 is a small detector, they were not able to take advantage of S2-width z-correlations, but they employed a radial fiducial cut and other analysis techniques to produce the result in Figure 27, which also shows the Xenon10 standard WIMP analysis for comparison. The reason this analysis did not proceed down to the detection threshold of 1 electron is very interesting and has to do with a detector effect known as delayed electron noise or “electron trains”; this phenomenon is discussed further in Chapter 8.

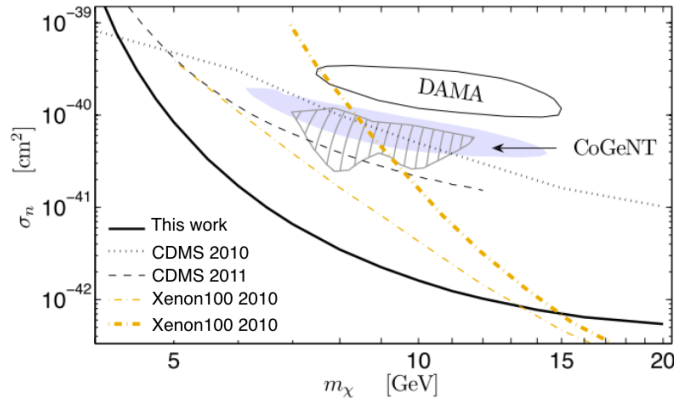


Figure 27: Xenon10 low-mass WIMP limit (black line) extended the range of the standard WIMP result (yellow dashed lines). Figure from [86].

A few years later, Essig et al. used the information reported in [86] and other Xenon10 publications to produce the first direct detection limits of sub-Gev dark matter [87]. The detection threshold for WIMPs in LXe decreases sharply for  $M_{WIMP} \lesssim 10 \text{ GeV}$ ; however, this detection threshold is based on the assumption that the dark matter is interacting only with the xenon nucleus. If sub-GeV dark matter scatters with atomic *electrons*, as opposed to nuclei, then it can produce observable signals of a few electrons. In LXe TPCs, the few electron signals are observable as S2s but the S1 signal is lost due to the difficultly of light collection for low energy events. The approach in the paper is to follow approximately the same procedure as in Section 3.4.1.2, with a few but significant substitutions. The recoil energy ( $E_R$  in Equation 33) must now account for the binding energy of the electron, and take a different form to refer to the recoil of the electron and not the nucleus. The cross section of interest is now  $\sigma_e$ , the sum over all of the differential ionization cross sections for electrons in the  $(n, l)$ -th shell. For a dark photon with mass  $O(\text{MeV-GeV})$  coupled to the visible sector via kinetic mixing (a very generic class of standard model extensions discussed previously in Chapter 2.5), Essig et al. set the exclusion limit in the  $m_{DM} - \sigma_e$  plane in Figure 28 (left). If there is

some momentum-transfer enhancement due to e.g. scattering through an electric-dipole moment,  $\sigma_e \rightarrow \sigma_e F_{DM}(q) \equiv \bar{\sigma}_e$ . Essig set exclusion limits for such dark matter candidates in Figure 28 (right).

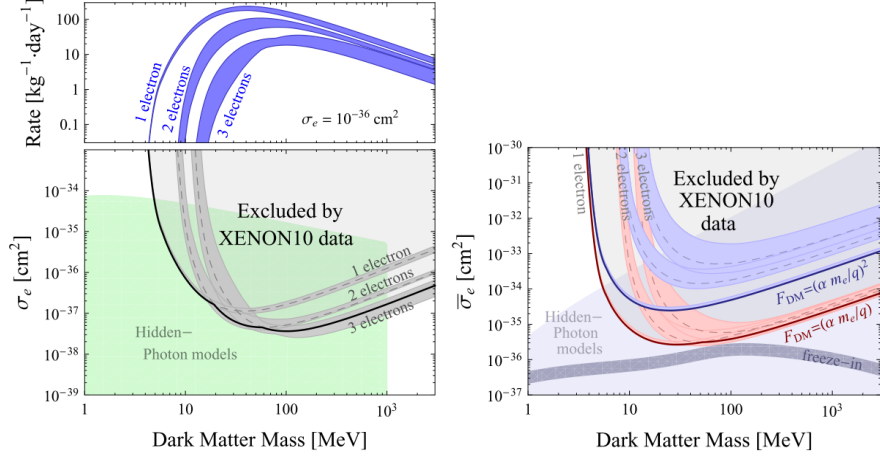


Figure 28: (left) Top: Expected 1,2,3-electron signal rates for Sub-GeV DM with  $\sigma_e = 10^{-36} \text{ cm}^2$  and Bottom: exclusion limit set with Xenon10 few-electron signals. (right) Exclusion limits for dark matter scattering through an electric-dipole moment (red) and through a very light ( $\ll$  keV) mediator (blue). Figures from [87].

In addition to the hidden photon searches just described, dual phase LXe TPCs can search for other dark matter signals from scattering on electrons. Annual modulation searches (in ER or NR) can provide clues to dark matter. Such searches take advantage of the fact that  $v_E$  varies with the rotation of the earth around the sun, reaching a maximum in June and minimum in December. The modulation in  $v_E$  leads to a modulation in the recoil rate observed in the detector. Searches for dark matter-induced rate modulations can offer a generic approach to identify dark matter interactions, complementary to the model-driven dark matter searches. The LUX experiment carried out such a search, looking at ER modulations in an energy range of interest (2-6 keV<sub>ee</sub>). This energy range was chosen to overlap with the DAMA/LIBRA Collaboration's long-standing and controversial claim of dark matter modulation on a target of NaI(Tl), which appears strongest around a recoil energy of 3 keV<sub>ee</sub> (their signal region is shown in Figure 26). LUX found no significant indication of rate modulation [88]. If future large dual phase TPCs like XENONnT and LZ observe an NR WIMP signal, the additional positive identification of a modulation signal of the NR signal would be a smoking-gun for WIMP discovery.

Another dark matter candidate that could produce an electron recoil signal in xenon is the axion (or more generally, axion-like-particles). For

searches such as these, a signal model is produced from the spectrum of axions from different sources, such as galactic axions or solar axions. The resulting signal model is an [ER](#) spectrum that accounts for finite detector energy resolution and threshold. The signal model spectrum is compared to the observed [ER](#) spectrum in the appropriate energy ranges, resulting in a confidence statement mass of the axion  $m_A$  and the axio-electric coupling  $g_{Ae}$ . The results of searches for solar axion and galactic axion signals are shown in Figure 29.

Finally, a model-independent search for [LIPs](#) is possible in dual phase xenon [TPCs](#). As discussed in Chapter 2.5, [LIPs](#) appear in dark sector models with a massless dark photon, where another dark sector particle couples to the standard model electron via kinetic mixing of the dark photon and standard model photon. [LIPs](#) deposit energies that can be described with particles of effective fractional charge. Chapter 5 describes the signal model and analysis method to search for [LIPs](#) in [LUX](#).

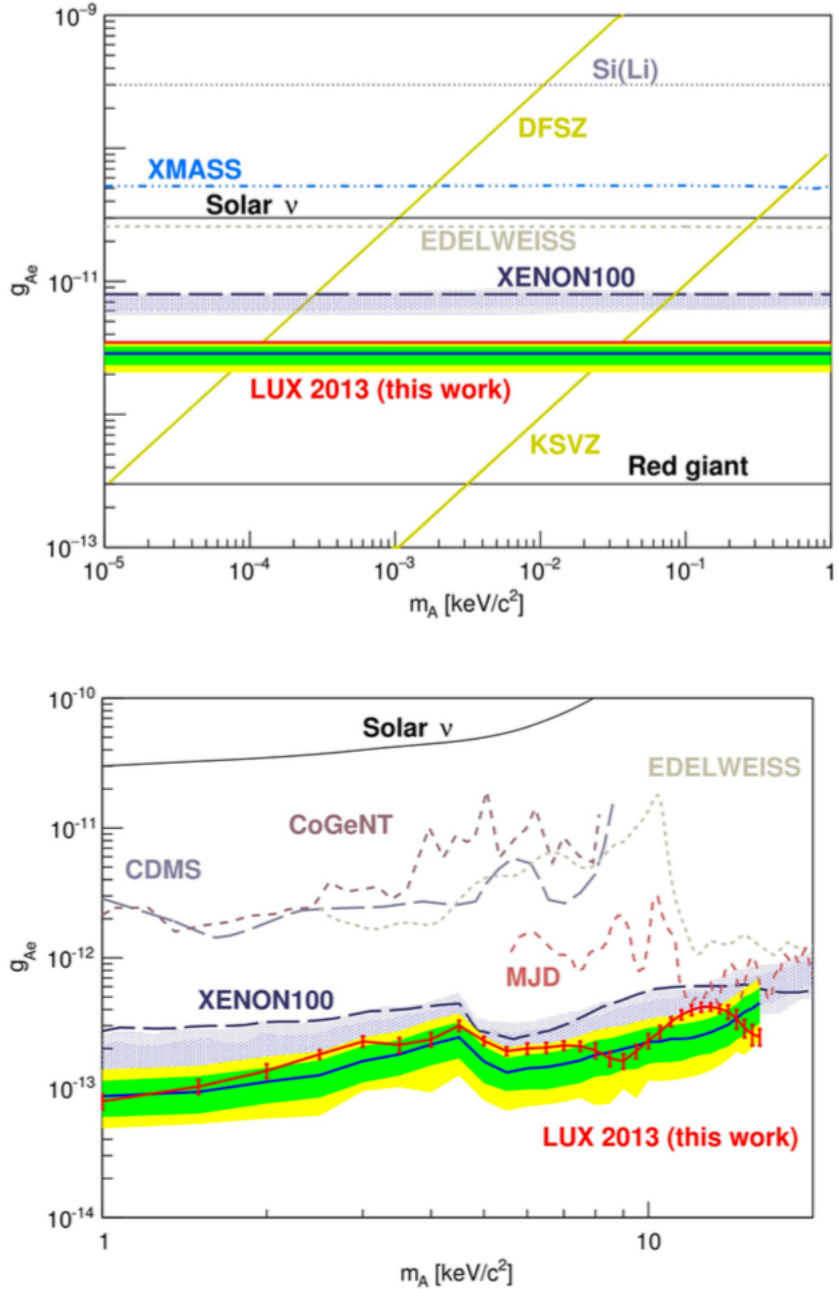


Figure 29: (top) Recent limits on solar axion coupling and mass (bottom) recent limits on galactic axion coupling and mass. Figure taken from [89].

## PART II

### BIG SCIENCE

This section describes research done with the [LUX](#) Detector. The [LUX](#) program is discussed in detail, including key detector components and calibrations. This is followed by a search for cosmogenic [LIPs](#).

# 4

## THE LUX DETECTOR

---

### 4.1 LUX OVERVIEW

The [LUX](#) detector was an ultra-low background dual phase liquid xenon [TPC](#) that set world-leading limits on [WIMP](#) interactions.

[LUX](#) began underground commissioning in July 2012, moving to the 4850 level (4300 m.w.e) of Sanford Underground Research Facility ([SURF](#)) in Lead, South Dakota. The [LUX](#) Collaboration’s first [WIMP](#) search exposure was for a period of 85.3 live-days, acquired between April 2013 and August 2013. This period of time is referred to as Run03, and the [WIMP](#) result is referred to as WS2013. The detector then underwent a grid conditioning campaign to improve voltage capabilities, followed by a series of extensive calibrations to characterize the new operating conditions. The detector then ran for a period of 332 live-days from September 2014 to May 2016 (Run04, WS2014-2016), ending with decommissioning in September 2016. Run03 and Run04 had distinct operating conditions and calibrations. The [LIP](#) search in Chapter 5 was carried out using Run03 data, and the calibrations in the latter half of this chapter describe the detector conditions as they were in Run03.

### 4.2 INTERNAL COMPONENTS

The major internal components of [LUX](#) are shown in Figure 30. The active volume of [LUX](#) was composed of 250 kg of liquid xenon, instrumented with two arrays of Hamamatsu R8778 Vacuum Ultra Violet ([VUV](#))-sensitive [PMTs](#) viewing the liquid region from the top and bottom. Both arrays were composed of 61 [PMTs](#) that detected S1 and S2 photons from particle interactions in the active liquid volume, and were held in place by copper mounting blocks. The [PMTs](#) were tightly packed in a hexagonal formation to maximize light collection. The xenon-facing surfaces of copper [PMT](#) mounting blocks were covered with [PTFE](#) tri-foils to reflect the 178 nm light, since copper is a poor reflector of [VUV](#) light.

The active region was defined by a series of strung wire or mesh grids: the cathode grid was at the bottom of the detector, and the gate grid was

48.3 cm above the cathode when cold. These two grids formed the drift field, which was 180 kV/cm during Run03. The region between the cathode and gate grids is known as the drift region; it is where detectable particle interactions take place. The anode mesh plane was 1 cm above the gate grid, and the xenon liquid level was held constant between these two electrodes by a spillover weir. The anode and gate form the extraction region of the experiment, where electrons are extracted across the liquid-gas boundary and undergo proportional scintillation to form S2 pulses. There are two additional grids, the top and bottom grids, which are placed 2 cm from the top and bottom PMT arrays to insulate the PMTs from the high fields produced by the other grids. The top and bottom grids were held at approximately the same voltage applied to the PMTs. All electrodes were 88%-99% optically transparent at normal incidence, and made of stainless steel 316.

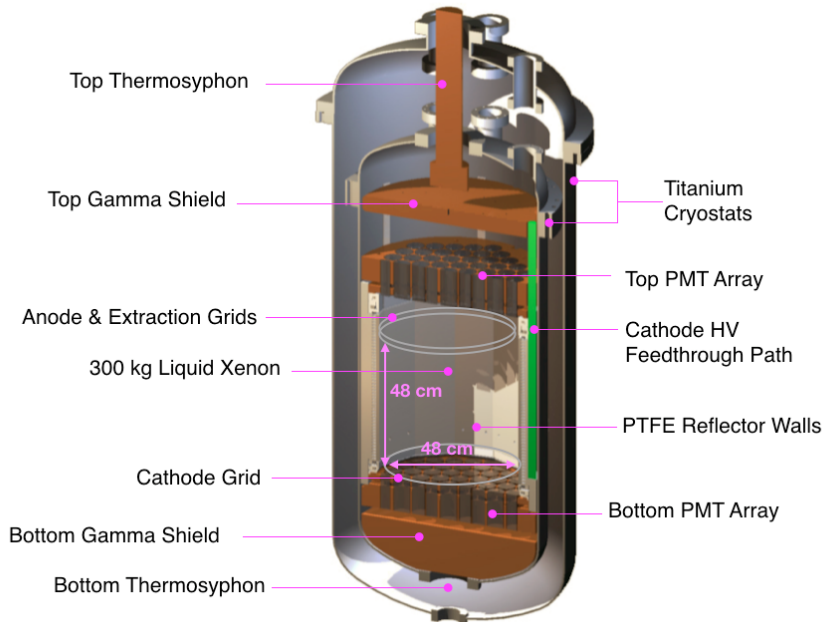


Figure 30: Major components and dimensions of the [LUX](#) detector. Figure from [90].

The insides of the detector walls were lined with 12 PTFE panels, which made the exact detector geometry a dodecagonal prism with flat faces, instead of a perfect cylinder with one rounded face. Immediately behind the PTFE were 48 copper field-shaping “rings” (dodecagons). The rings were vertically separated by 1 cm, and the gate-to-cathode voltage was graded evenly over the rings by a resistor chain connecting the rings.

Below and above the PMT mounting blocks were two large solid copper domes which acted as gamma ray shields and also functioned as thermal

mass that aided in keeping the detector temperature stable. The bottom dome also acted as a heat exchanger to quickly re-thermalize incoming xenon gas (from the circulation system) as it entered the liquid region. The bottom dome also minimized the volume filled with non-active liquid xenon. See Figure 31 for details about the field-shaping rings and copper shields.

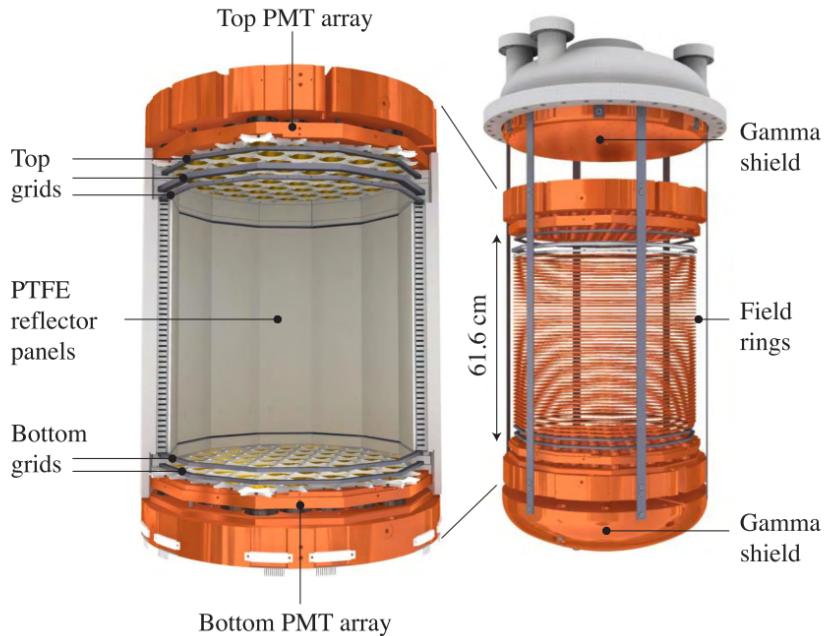


Figure 31: Field-shaping rings detail. Figure from [90].

More details about the internal components, including extensive characterization of the PMTs, can be found in C. Faham's PhD thesis [91].

### 4.3 EXTERNAL COMPONENTS

The [LUX](#) cryogenic system was based on thermosyphons, which deliver “cooling power” to solid copper cold heads, which are in thermal contact with the liquid xenon space. A simplified diagram is shown in Figure 32. A thermosyphon is a closed-loop cooling device containing a thermal messenger gas; N<sub>2</sub> was used in the [LUX](#) thermosyphons. The top of the thermosyphon is immersed in a bath of liquid nitrogen, and the bottom is in thermal contact with the liquid xenon space. The internal messenger gas condenses at the top and drips down to the cold head, where it absorbs heat from the xenon space, evaporates, and returns to the top of the thermosyphon to condense and repeat the cycle. In this manner, heat from the liquid xenon space is transferred to the external nitrogen bath, which

boils off and must be periodically replenished. The pressure of the internal nitrogen messenger gas can be adjusted, providing more or less cooling power as desired. The LUX thermosyphons were also instrumented with resistive heaters, for further fine control. Four thermosyphons were used to operate the LUX detector stably at 175 K with a xenon vapor pressure of 2 bar.

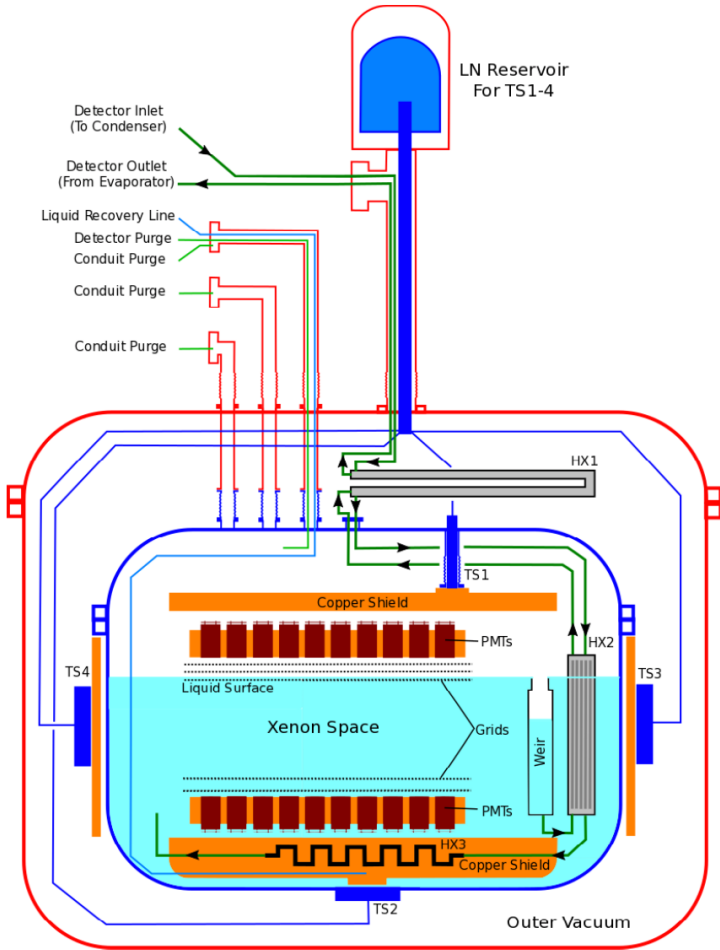


Figure 32: A simplified diagram of the LUX cryogenic system. Figure from [92].

The spillover liquid xenon from the liquid-level-setting weir mentioned above was directed into a circulation system through a series of heat exchangers that helped cool clean, incoming xenon gas. The xenon circulation was driven by one twin-head KNF double-diaphragm pump, which pushed liquid xenon from the spillover weir through a SAES MonoTorr heated zirconium getter to remove non-noble impurities before returning the clean xenon gas into the detector. A sampling system was able to pull xenon gas samples from different parts of the circulation system and

measure impurity content, as well as test for the presence of  $^{85}\text{Kr}$  [93], a troublesome beta emitter which must be removed from the xenon prior to carrying out a successful **WIMP** search.

The circulation pump was installed in parallel with a backup pump, which could be switched on immediately in case of a pump outage. Flow was regulated to the system by two high-flow Mass Flow Controller (**MFC**)s. Additional low-flow **MFCs** controlled purge flow through the cabling conduits in Figure 32 to ensure gas flow was away from the detector and prevent any contaminants from diffusing into the active xenon space.

Internal calibration sources were plumbed into alternate flow paths of the circulation system. Xenon gas could be directed through a substrate source, such as the  $^{83m}\text{Kr}$  source described below, to pull  $^{83m}\text{Kr}$  into the detector volume. A bottle containing a source such as the  $\text{CH}_3\text{T}$  source described below could be used to deposit the gaseous source in an evacuated section of pipe. Xenon could then be directed through the section of pipe containing the source, sweeping it into the detector volume.

Lastly, **LUX** was placed in a 7.6 m diameter, 6.1 m high water tank (Figure 33). The shielding provided by the water tank attenuated the  $\gamma$  background from the cavern walls and thermalized neutrons from cavern background radioactivity and muon spallation. The water tank provided superior shielding from cavern radioactivity such that the detector backgrounds were dominated by the radioactivity of internal detector components, which in turn were controlled through a strict campaign of cleanliness and choice of detector materials [90], [94]. Vertical tubes visible in Figure 33 were used to deploy external calibration sources at different heights, such as  $^{137}\text{Cs}$ , which were directed into the detector via a collimating source assembly.

The **LUX** detector water tank and material screening achieved a very low background ( $\ll 1 \text{ keV}_{ee}^{-1}\text{kg}^{-1}\text{day}^{-1}$ ) in the **WIMP** search energy range as shown in Figure 34. Figure 34 also illustrates the fiducial volume chosen for the Run03 **WIMP** search.

## 4.4 TRIGGER AND DATA ACQUISITION

Cabling for **PMTs** and other monitoring instrumentation were routed from the inner detector volume to the outside via conduits illustrated in Figure 32. A flow chart illustrating the signal path is shown in Figure 35.

The **PMT** signals were shaped and amplified by two sets of amplifiers. These analog voltage waveforms were then digitized by Struck Analog-to-Digital Converter (**ADC**)s, with 14 bit, 100 MHz sampling (1 sample every 10 ns). A copy of the analog **PMT** voltage waveforms passed through the **LUX** Field Programmable Gate Array (**FPGA**) trigger system, which sig-



Figure 33: A photo of the LUX detector installed inside the water tank. Photo credit Mark Kapust.

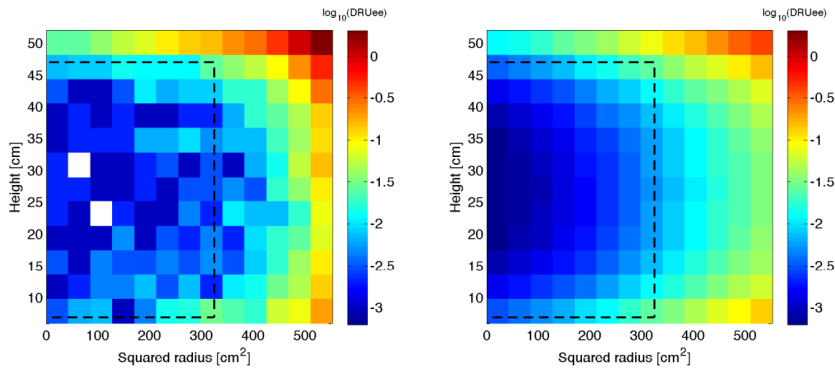


Figure 34: Backgrounds distributions in squared radius and height for expected (right) and measured (left) backgrounds in the energy range 0.9-5.3 keV<sub>ee</sub> (2-30 phe S1) for the 85.3 live-day Run03 WIMP exposure. Black lines show the 118 kg fiducial mass. Units are  $\log_{10}\text{DRU}_{ee}$ , electron equivalent differential rate units, i.e.  $\text{keV}_{ee}^{-1}\text{kg}^{-1}\text{day}^{-1}$ . Figure from [94].

#### 4.4 TRIGGER AND DATA ACQUISITION

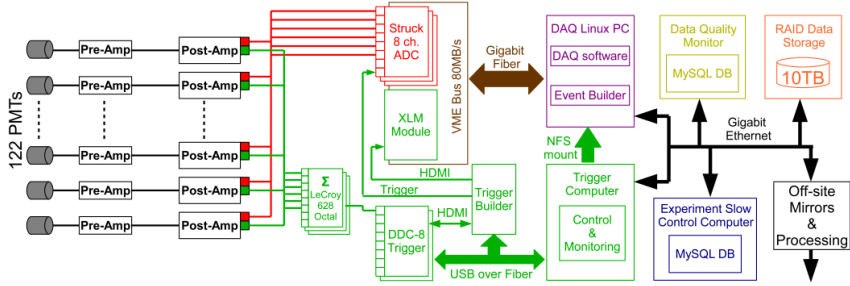


Figure 35: Overview of the [LUX](#) trigger system. Figure from [95].

naled the data acquisition computer to save the waveforms when they passed above a certain threshold, and stop when they fell below the thresh-old. Each of the 122 PMTs had its own channel in the recorded data, so recording only the channels<sup>1</sup> that passed threshold allowed for a great amount of data reduction. This technique is called Pulse Only Digitization (POD). A POD threshold of 1.5 mV was used for [LUX](#), which resulted in a single photoelectron efficiency of > 95% [67]. A figure showing the POD threshold and example waveform are shown in Figure 36. More details about the [LUX](#) data acquisition system can be found in [96].

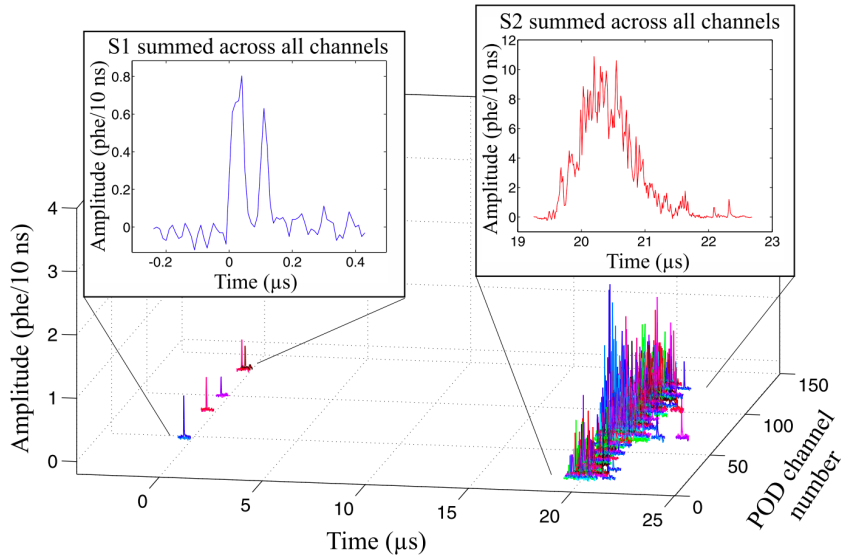


Figure 36: An example recorded event. Channels that do not pass the POD threshold are not recorded. The waveforms are summed over all channels to produce the S1 and S2. Figure from [95].

<sup>1</sup> The Struck boards actually acquired channels in pairs. Each channel had a dedicated parter, and if one of the channels exceed the POD threshold, both partner channels were acquired.

The channel-wise **POD** data was written continuously to disk as the **ADC** memory buffer fills; this is the rawest and least filtered form of **LUX** data that is saved in binary format (referred to as “**.dat**-files”). Upon receiving a trigger signal, the Event Builder takes the raw data and extracts portions located in a pre-trigger and post-trigger window. An additional hold-off time is applied after the post-trigger window to assure **PODs** are not duplicated by the subsequent event. More details about the trigger can be found in [95]. The pre- and post-trigger windows for Run03 were set to be  $500\ \mu\text{s}$ , chosen to ensure both S1 and S2 pulses were contained in the same event. The maximum electron drift time in Run03 was  $322\ \mu\text{s}$ , so a pre- and post-trigger time of  $500\ \mu\text{s}$  ensured no S2 would appear without its partner S1. Both S1 and S2 could pass the **POD** threshold and signal the Data Acquisition (**DAQ**) computer to save the waveforms, but some small S1s may not have crossed the trigger threshold and were “found” only at the event-building stage. After event-building, the waveform data was again saved in binary format. These files containing waveforms that are associated with individual events, are referred to as “**.evt**-files”.

## 4.5 DATA PROCESSING

After event-building, the waveform **.evt**-files were sent off site for additional processing. The **LUX** Data Processing Framework (**DPF**) extracts essential information from the waveforms and produces Reduced Quantity (**RQ**) files (referred to as “**RQ** files”). The **DPF** is modular, and can be applied repeatedly to the same **.evt**-files with different settings if desired. **RQ** files include event-level information (e.g. trigger timestamp), pulse-level quantities (e.g. pulse type, pulse area), and some channel-level quantities (e.g. pulse area recorded by each **PMT**). The **DPF** classifies pulses as one of five types: S1, S2, Single Photoelectron (**SPHE**), Single Electron (**SE**), and Else (for pulses that do not fit one of the previous four types). The pulse-finding and classification algorithm was designed and optimized for the **WIMP** search, and is crucial in identifying **WIMP** “golden events”, which are single-scatter interactions with only one S1 and one S2 in the event. Detector backgrounds such as gammas often scatter more than once in the active volume, producing an event with one S1 and multiple S2s. The pulse-finder and classifier also play a large role in **LIP** search, which is discussed more in Chapter 5. An example of pulse identification for a multiscatter event is shown in Figure 37.

Following identification of S1 and S2 pulses, the **DPF** position reconstruction module is run. This module uses the Mercury algorithm, originally developed for the ZEPLIN-III **LXe TPC** [97], which is based on maximum-

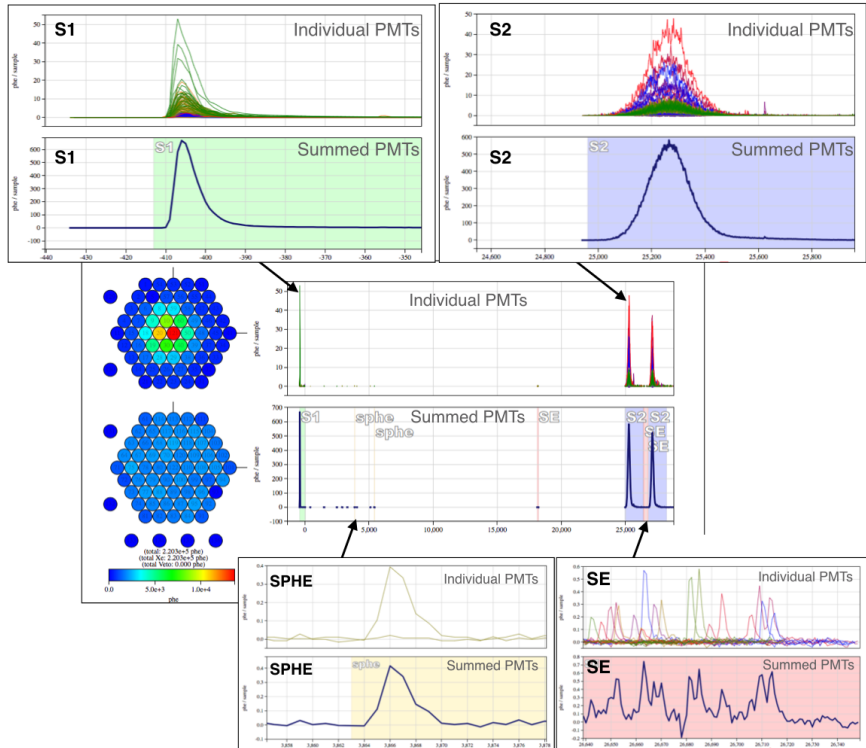


Figure 37: An example of [LUX](#) pulse classification from a multiscatter event showing detail of individual pulses of types S1, S2, SPHE, and SE. In addition to the pulse classes illustrated here, there is an Else class, for pulses that do not fit any of the definitions shown.

likelihood to find the best  $(x, y)$  position of the event. Mercury uses Light Response Function ([LRF](#))s, obtained for each [PMT](#), to predict the response of the [PMT](#) to interactions at some arbitrary distance from the [PMT](#). The [LRF](#)s were obtained using calibration data, of which  $^{83m}\text{Kr}$  was the most important for position reconstruction. The position reconstruction method and [LRF](#)s are discussed in more detail in [98].

The [DPF](#) also applies calibration constants to the data. Calibration constants, many of which change over time, are tracked and recorded in the LUX Electronic Log ([LUG](#)), which produces date-specific record files in XML format, which in turn determine the settings for some of the [DPF](#) modules. For example, the  $^{83m}\text{Kr}$  calibration (see Section 4.6.2) was used to normalize S1 pulse areas. The photon detection efficiency for S1s varies with  $z$ -position. Events occurring near the bottom [PMT](#)s were 50% more likely to be detected than those near the liquid-gas boundary. The [DPF](#) applies corrections like this to several [RQ](#)s, and both the corrected and uncorrected versions are kept in the [RQ](#) files.

## 4.6 CALIBRATIONS

Several novel calibration methods were developed by the [LUX](#) Collaboration to fully characterize the detector. The superior self-shielding ability of [LXe](#) detectors also makes them difficult to calibrate. Sources placed external to the detector cannot penetrate the fiducial volume very effectively; since high-statistics are desired for calibration data, relying on external sources becomes untenable. The solution, then, is counterintuitive: purposely introduce radioactive material into the painstakingly developed, ultra low-background, fiducial volume of the detector. For such a source to not destroy the ability to carry out a [WIMP](#) search, it must either (i) be short lived or (ii) be effectively removed by getter on a short timescale. [LUX](#) demonstrated that  $^{83m}\text{Kr}$  fit the former [99] requirement and tritiated methane ( $\text{CH}_3\text{T}$ ) fit the latter [71]. Both of these sources were used in the calibration of the [LUX](#) detector, in addition to other sources; all of the sources are discussed below.

### 4.6.1 ENERGY RECONSTRUCTION

This section covers the energy calibration of [LUX](#). Recall from Chapter 3.3 that the electron-equivalent energy of an event in a dual phase xenon [TPC](#) is reconstructed as follows:

$$E = W \left( \frac{S1}{g1} + \frac{S2}{g2} \right) \quad (39)$$

Two or more calibration line sources of different energies are required to fit for the detector gains  $g_1$  and  $g_2$ . The LUX experiment used a suite of sources to calibrate the energy response of the detector, shown in Figure 38. The  $^{83m}\text{Kr}$  is an injected source distributed in the entire internal volume (discussed in more detail below). The  $^{137}\text{Cs}$  is an external source lowered at different heights into the source tubes. The xenon lines,  $^{131}\text{Xe}$ ,  $^{129}\text{Xe}$ , and  $^{127}\text{Xe}$ , are internal sources of cosmogenic origin and were only present early in Run03; they have half lives of 11.9 days, 8.8 days, and 36.3 days, respectively.

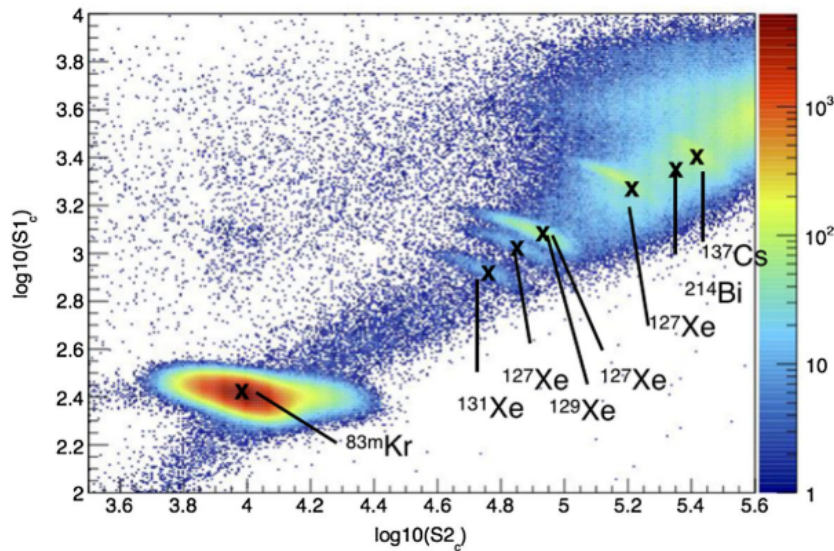


Figure 38: Plot showing calibration sources used for determination of the detector gains,  $g_1$  and  $g_2$ . The axis label subscript  $c$  denotes corrected variables with calibration for geometrical effects and electron lifetime; these corrections are discussed in Section 4.6.2. Figure from [67].

The average  $S_1$  and  $S_2$  of each calibration source is normalized to the true energy:

$$(S_1, S_2) \rightarrow \left( \frac{\langle S_1 \rangle}{E}, \frac{\langle S_2 \rangle}{E} \right) \quad (40)$$

and a line  $y = mx + b$  is fit to the transformed variables, where the slope is  $m = -g_1/g_2$  and the y-intercept is  $b = g_1/W$ . Such a plot is called a Doke plot. The sources from figure Figure 38 are shown normalized in a Doke plot in Figure 39.

From the fit in Figure 39, the LUX gains for Run03 were measured to be  $g_1 = 0.117 \pm 0.003$  phd/photon and  $g_2 = 12.1 \pm 0.8$  phd/electron.

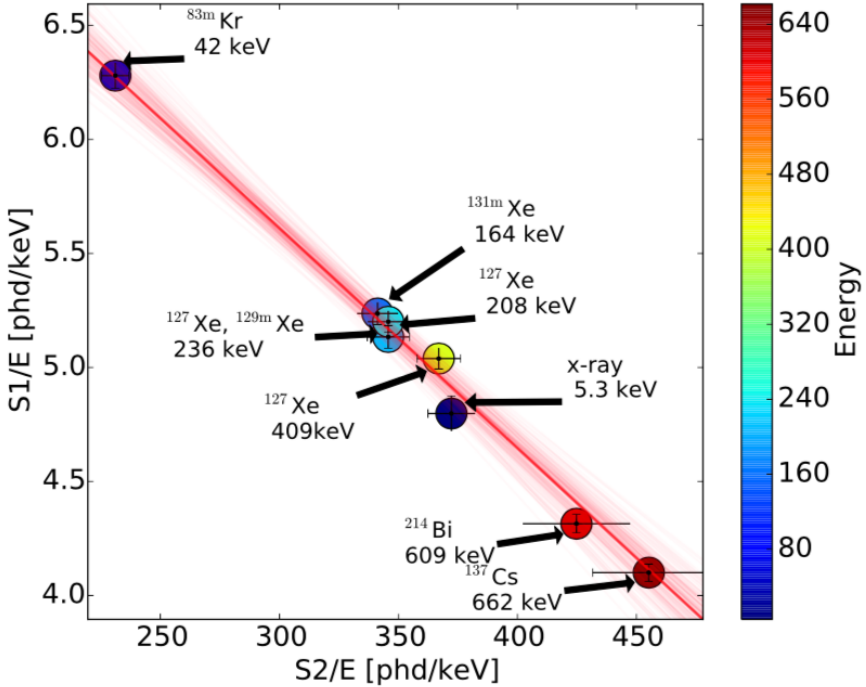


Figure 39: Doke plot used to fit for  $g_1$  and  $g_2$  in LUX Run03. Figure from [67].

$g_2$  depends on a combination of the EEE and the number of photons produced by a single extracted electron – it is useful to know both values. Single electrons are periodically emitted into the gas and undergo proportional scintillation. This phenomenon is well known in liquid xenon detectors and is discussed further in Chapter 8. A sample of pure single electrons was collected to find the average number of S2 photons produced by one electron, referred to the single electron size. The single electron size in Run03 was a skew-gaussian with mean 24.66 phd and a 1- $\sigma$  width of 5.95 phd. Combing this with  $g_2$  gives an EEE of  $49\% \pm 3\%$  [67].

#### 4.6.2 METASTABLE KRYPTON-83 ( $^{83m}\text{Kr}$ ): A MULTIFUNCTION CALIBRATION

The  $^{83m}\text{Kr}$  source used by LUX was  $^{83}\text{Rb}$  deposited on a charcoal substrate. Gaseous xenon within the circulation system was diverted over the charcoal substrate, where it could sweep  $^{83m}\text{Kr}$  on a flow path through the getter, and then into the detector.

$^{83m}\text{Kr}$  decays by two steps releasing a total energy of 41.5 keV (see Figure 40). The two branching ratios that dominate are, first, the internal conversion and subsequent Auger emission of a 32.1 keV  $\beta$  followed by

another internal conversion and Auger emission of a 9.4 keV  $\beta$ , with an intervening half-life of 154 ns. The time structure of the decay sometimes yielded two S1s, called S1a and S1b. If the second 9.4 keV  $\beta$  was prompt (i.e. within the timing resolution of the detector), then only one S1 was observed. The S2s were always merged because (1) the low energy of the decays made the energy depositions  $O(10 \mu\text{m})$  from each other, smaller than the position resolution of the detector  $O(1 \text{ mm})$  and (2) the close timing of the two decays was smaller than the typical electron diffusion distances during drift  $O(1 \text{ mm})$ , merging the two electron bunches together into one S2 [99].

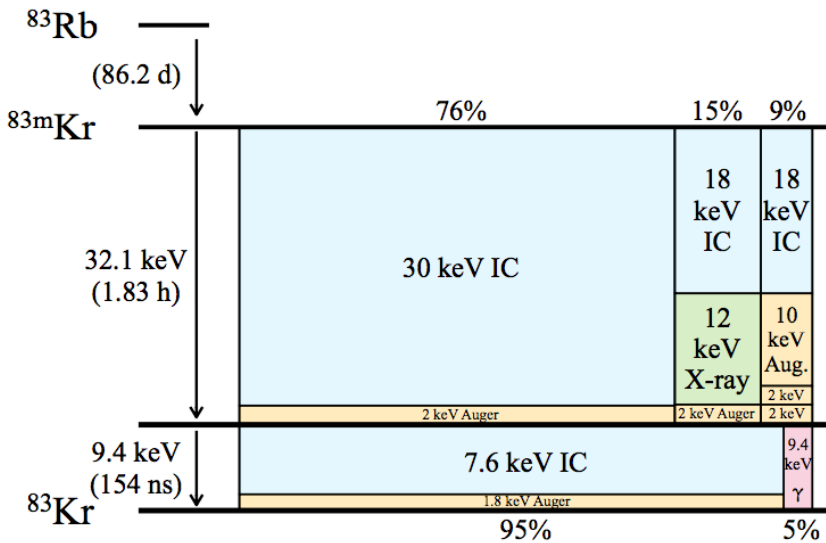


Figure 40: Decay scheme of  $^{83m}\text{Kr}$ . The width of each column is proportional to the branching fraction of that decay mode, the vertical divisions are proportional to energy partitioning among internal conversion electrons (blue), Auger electrons (yellow), x rays (green), and gamma rays (red). In the [LUX](#) detector, the S1s of the 32.1 keV  $\beta$  and the 9.4 keV  $\beta$  were sometimes separable, the S2s were always merged. If the S1s were separate they were referred to as S1a and S1b. Figure from [99].

$^{83m}\text{Kr}$  was a workhorse calibration source for [LUX](#), with  $^{83m}\text{Kr}$  injections performed weekly at activities ranging from 10 Bq to hundreds of Bq, depending on the specific calibration goal.  $^{83m}\text{Kr}$  was found to mix uniformly in the detector within 10 min of the injection, and would decay (half life 1.83 hours) back to an acceptable [WIMP](#) search background rate within a day, or few days, depending on the injected activity [99]. The combined energy of the  $^{83m}\text{Kr}$  was well out of the [WIMP](#) search energy range, so no long-term pollution, though unlikely, was risked.  $^{83m}\text{Kr}$  was used for two main calibrations, described below.

**Pulse Area Corrections:** Detector efficiencies and gains can vary over time and position within the detector.  $^{83m}\text{Kr}$  served as a “standard candle”, which produced monoenergetic signals with uniform initial light and charge yields distributed uniformly throughout the active volume. The efficiency for detecting the initial light yield as an S1 was dominated by spatially varying geometrical light detection efficiency. The areas of the S1s were binned in 3D, and the averages were found for each bin. A correction map was then constructed as the inverse of the S1 areas, normalized to the S1 amplitude at the center of the detector. The map of relative S1 amplitudes in Figure 41 (left) shows the strong z-dependence for S1 light collection. The corrections for S2 areas were more complex, as detection efficiency for the initial charge yield of an S2 depends on the presence of electronegative impurities, electron extraction efficiency, production of proportional scintillation photons, and detection of those photons in PMTs. The  $xy$ - and  $z$ -dependence for S2s are corrected in two separate maps. The electronegative impurities caused a strong z-dependence in S2 size – events originating at the bottom of the detector must drift longer and so were more likely to encounter and lose electrons to impurities. The  $z$ -dependent S2 area correction map was an exponential function of drift time, normalized to unity at the liquid surface. The  $xy$ -dependence was due to detector conditions such as pressure, liquid level, and electric field variation from the grid. The  $xy$ -correction map for S2s was normalized to (0,0) in the x-y plane. Examples of both the  $z$  and  $xy$  S2 area correction maps can be seen in Figure 41 (right). The pulse area maps were not significantly time dependent in Run03, but showed evolution over time in Run04 due to the different electric field conditions.

**Position Corrections:** 3D position reconstruction depends on a full understanding of the path electrons take from an interaction site to the position observed after extraction at the surface. The reconstructed position of the proportional scintillation signal in the  $xy$ -plane, based on the Mercury algorithm, is referred to “S2 coordinates”, often with subscripts ( $x_{S2}, y_{S2}$ ). The real coordinates may be displaced from ( $x_{S2}, y_{S2}$ ) due to, for example, a radial field pushing electrons inwards deep in the detector. In fact, there was a small radially inward component to the electric fields in LUX Run03 due to the geometry of the field cage and grids (Figure 42); there was also a small amount of PTFE charging evident as “scalloping” in the ( $x_{S2}, y_{S2}$ ) maps where one would expect straight edges. The spatial distribution of reconstructed  $^{83m}\text{Kr}$  events was used to verify a COMSOL multiphysics electric field model of the detector by drifting electrons in simulation under the electric field model conditions. This field model could then be used to transform events from S2 coordinates to real ( $x, y$ ) coordinates, however this was not done for Run03. Instead, the  $^{83m}\text{Kr}$  data itself was found to be more precise for position corrections, since it

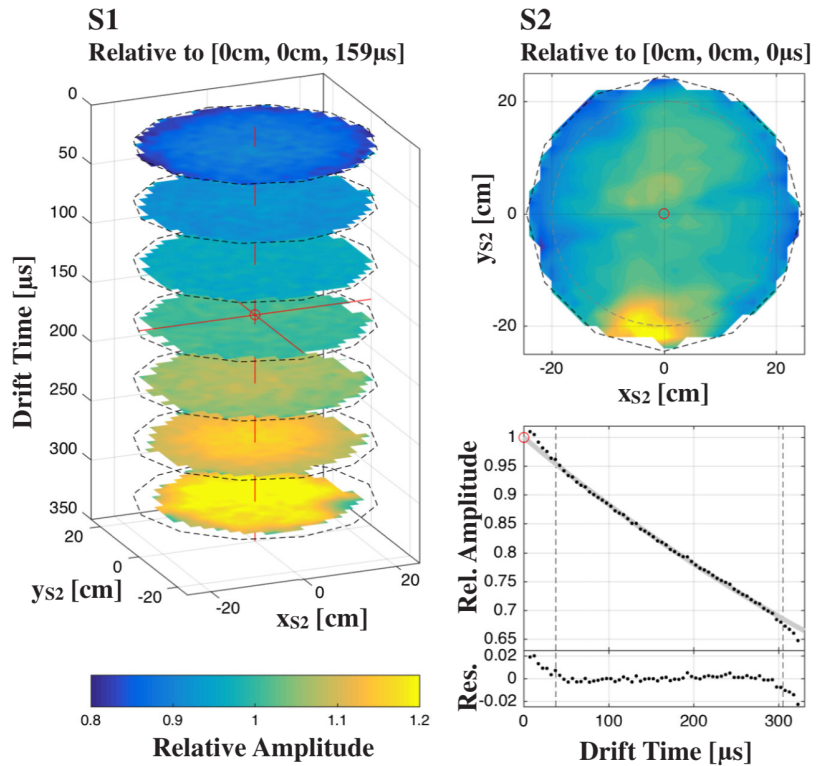


Figure 41: Spatial dependence of pulse area corrections for S1 (left) and S2 (right) from an example  $^{83m}\text{Kr}$  calibration. The red circle indicates normalization point. Figure from [99].

didn't rely on the accuracy of the field model or electron drift simulation (Figure 43). The electric field conditions were very different in Run04, and so extensive calibrations and field maps were used to map S2 coordinates to real coordinates [100].

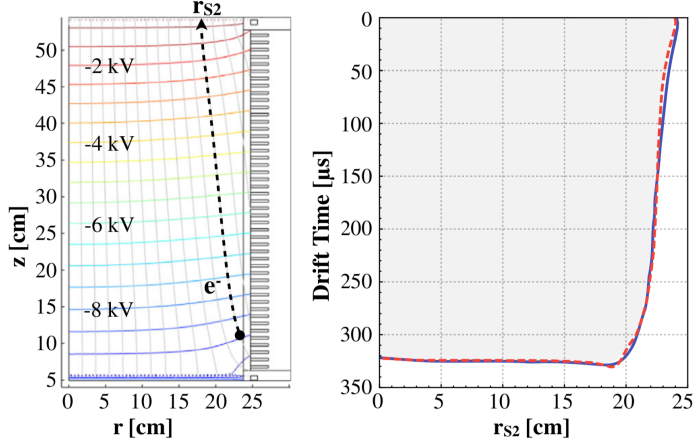


Figure 42: (left) A simplified 2D COMSOL model showing electric field lines and equipotentials for the LUX detector in Run03. A radially inward component is seen. (right) The resulting edge S2 coordinates of a uniform distribution of electrons drifted under the electric field model is shown in solid blue. The edge S2 coordinates of from  $^{83m}\text{Kr}$  data is in dashed red; it is consistent with the field model prediction. Figure from [99].

In addition to the small radial dependence, the electric fields illustrated in Figure 42 also vary in magnitude. The two decays of  $^{83m}\text{Kr}$  can be leveraged to directly probe the magnitude of the field, as they exhibit different field dependence (recall from Chapter 3.3 that signal yields depend on applied field and particle energy). The ratio of S1a to S1b increases with field, and provides a measure of the spatial dependence of the magnitude of the electric field. A highly variant electric field would affect recombination, and cause different light and charge yields at different positions in the detector, in turn affecting sensitivity. The fields measured via this method in Run03 were found to only cause corrections on the order of a percent and so no field-dependent corrections were applied [99]. However, in Run04 the ratio technique was of central importance (see [101] [100] [99] for more detail). The result of the ratio method for measuring electric field magnitude is shown in Figure 44 for Run03 fields.

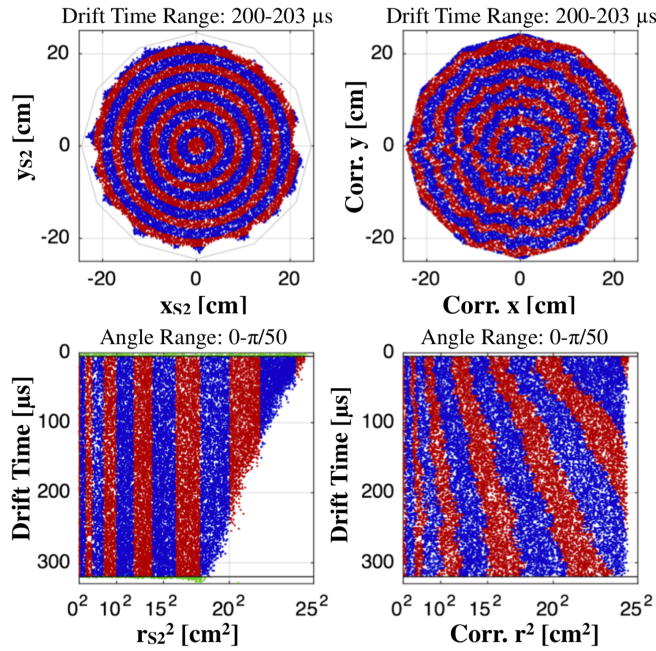


Figure 43: The effect of radial position mapping between S2 coordinates (left) and real coordinates (right). The top panels show a thin horizontal slice of the detector and the bottom panels show a thin vertical slice. The red and blue colors are used to make the effect of the mapping visible. Note that squared radius in the bottom panels exaggerates the scale of the effect. Figure from [99].

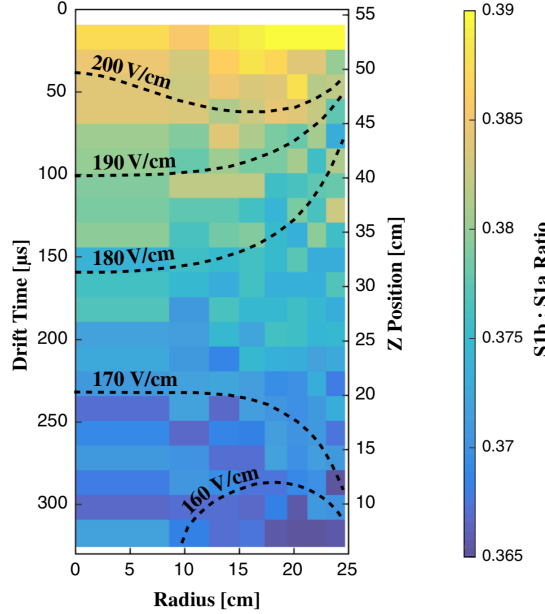


Figure 44: Field map of Run03 produced by  $^{83m}\text{Kr}$  S1a:S1b ratio. Because only a fraction of  $^{83m}\text{Kr}$  produce separate S1a and S1b, the bins are large to accomidate reduced statistics. Figure from [99]

### 4.6.3 TRITIUM BETA DECAY: CALIBRATION OF THE ER BAND AND YIELDS

In order to calibrate the **ER** band of **LUX** a  $\beta$  source in the **WIMP** energy range (1 to 8 keV $_{ee}$ ) was needed. **LUX** used a gaseous tritiated methane ( $\text{CH}_3\text{T}$ ) source to deliver tritium uniformly into the active volume. Tritiated methane was chosen over the molecular tritium ( $\text{T}_2$ ) because it does not adsorb onto surfaces like the smaller  $\text{T}_2$  molecule and it does not interfere with charge transport in **LXe** [71]. Tritium has a Q-value of 18.6 keV, but the spectrum peaks at 2.5 keV, with 64.2% of the decays occurring in the **WIMP** search energy range [71]. The half-life of tritium is 12.3 years, so efficient removal was essential. **LUX** demonstrated that once deployed,  $\text{CH}_3\text{T}$  was removed with a 6 hour time constant, returning the detector back to acceptable **WIMP** search rates.  $\text{CH}_3\text{T}$  was shipped to site in a bottle, mixed with purified xenon and released into the circulation system after the getter, to be swept into the inner volume.

The tritium energy spectrum from data is shown with the theoretical energy spectrum convoluted with the detector energy resolution in Figure 45 (left). The ratio of the two is shown in Figure 45 (right), demonstrating a 50% effective energy threshold for **ER** events at  $1.24 \pm 0.026$  keV. The agreement between data and theory shows powerful support for the energy model  $E = W(S1/g_1 + S1/g_2)$ .

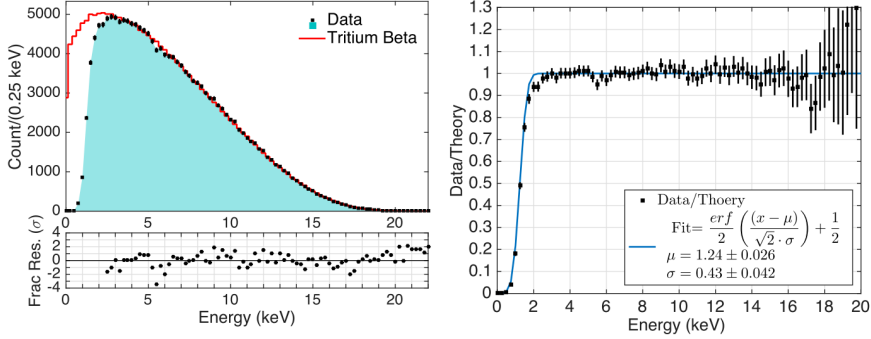


Figure 45: (left) Plot showing the theoretical tritium beta spectrum with the spectrum obtained from data, and residuals. (right) The ratio of data to theory convoluted with the detector energy resolution. Figure from [71].

Tritium was also used to measure the light and charge yields over a wide energy range. Figure 46 (left) shows the detected number of quanta,  $n_\gamma$  and  $n_e$ . Recall that this is not necessarily the number of initial quanta  $n_{ex}$  and  $n_{ion}$  that are produced, as some number of  $n_{ion}$  undergo recombination to produce additional scintillation photons. Figure 46 (right) shows the effect that event energy has on recombination. For ER events  $n_{ex}/n_{ion} = 0.2$  is assumed to be constant [68], but the observed ratio  $n_\gamma/n_e$  is clearly energy dependent.

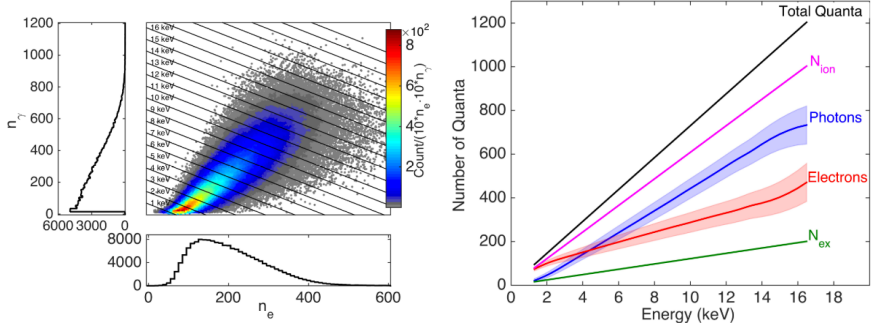


Figure 46: (left) The measured quanta yields shown with lines of equal energy. (right) A plot depicting the expected initial quanta yields,  $N_{ion}$  and  $N_{ex}$ , compared with the measured yield of photons and electrons. The difference is caused by the energy dependence of recombination. Figure from [71].

Lastly, tritium was used to construct the ER band (Figure 47 (left)), which is necessary for the WIMP search. The width of the ER band is of significant interest, as it determines the nuclear recoil discrimination of the

detector. The number of **ER** events from the tritium calibration that occur below the nuclear recoil band mean is known as the leakage fraction,  $f$ , and is shown as a function of energy in Figure 47 (right). The average **ER** discrimination efficiency ( $1 - f$ ) for Run03 was  $99.81\% \pm 0.02\%(\text{stat}) \pm 0.1\%(\text{sys})$ , where the systematic error comes from the error on  $g_1$  and  $g_2$ . This measurement of discrimination efficiency relies on knowing the mean and width of the **NR** band, which is discussed in the next section.

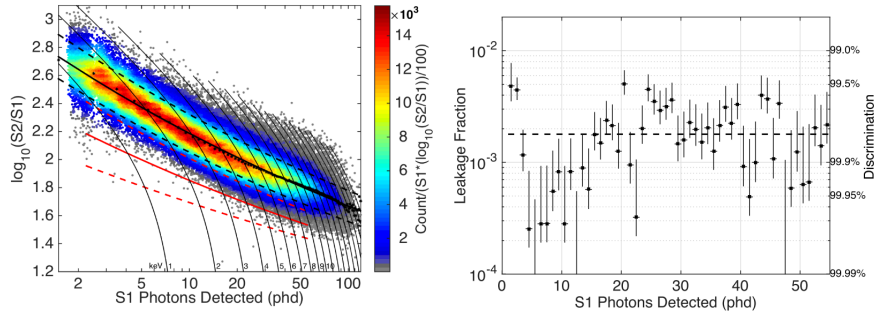


Figure 47: (left) The **ER** band for in **WIMP** search energy range obtained from the tritium calibration. (right) Leakage fraction of **ER** events below the **NR** mean in the **WIMP** search energy range. Knowledge of the **NR** band comes from the **DD** calibration detailed in Section 4.6.4. Figure from [71].

#### 4.6.4 DEUTERIUM-DEUTERIUM (DD) NEUTRONS: CALIBRATION OF THE NR BAND AND YIELDS

Neutrons from a Deuterium-Deuterium (**DD**) generator were used to calibrate the **NR** response and signal yields for **LUX** in the **WIMP** search energy range. A photo and diagram of the calibration scheme are shown in Figure 48. Following Run03, **LUX** employed the **DD** generator to deliver a collimated beam of 2.45 MeV neutrons into the **TPC**. As Figure 48 shows, the generator was positioned outside the water tank, but when aligned with the neutron conduit (a Polyvinylchloride (**PVC**) tube filled with air), deposited neutrons into the **LXe** space. The **DD** calibration leverages known kinematics of neutron scattering, the known incoming neutron energies, and the known detector gains  $g_1$  and  $g_2$  to develop a complete characterization of low-energy **NR** in **LUX**. The method is summarized here, but details are available in [76].

First, charge yield was derived from a population of multiscatter events: those with one **S1** (the **S1s** are merged due to simultaneous collection of **S1s**) and two **S2s** (separated in space and z-position/drift time). Neutron scattering kinematics allow for the reconstruction of energy at the first

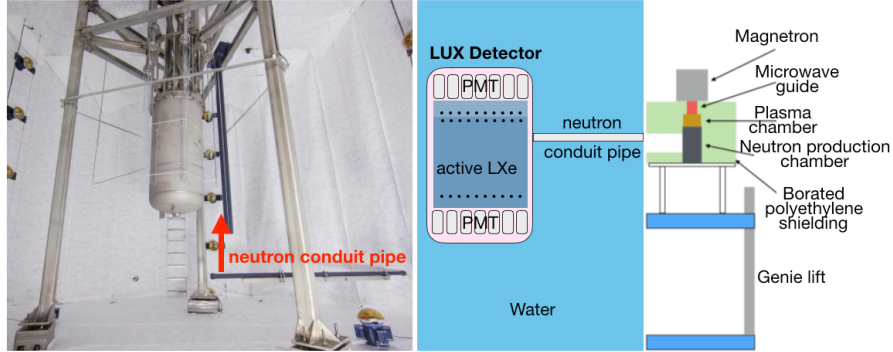


Figure 48: (left) Photo of the water tank interior showing the neutron conduit, which is raised during DD calibration. (right) Diagram of the DD generator and water tank neutron conduit during DD operation. Figure courtesy of E. Pease.

scatter site, so the unknown first S1 is not needed to ascertain the energy deposition. The charge yield is then obtained from the first S2 and the energy of the first scatter from kinematics.

Once the charge yield was obtained, a population of single scatter events was collected: one S1 and one S2. These events were from neutrons that scattered once the detector, and then exited. Here, the second scatter is not available to kinematically reconstruct energy, so instead the charge yield is employed to infer the energy of the single scatter. The light yield is then obtained from the S1 and the energy deposition inferred from charge yield.

It should be noted that though the DD generator produced monoenergetic neutrons of initial energy  $E_i$ , the energy deposited  $E_d$  by a neutron scatter is

$$E_d = E_i \frac{m_n M_{Xe}}{m_n + M_{Xe}} \sin^2 \theta_{CM} \quad (41)$$

where  $m_n$  is the neutron mass,  $M_{Xe}$  is the xenon mass, and  $\theta_{CM}$  is the scattering angle relative to the neutron conduit in the center of mass frame. The deposited energy,  $E_d$  then covers a range of energies, allowing for calibration of the NR band and yields over a range of energies. After determination of the light yield, the single scatter events were used to construct the NR band in Figure 49.

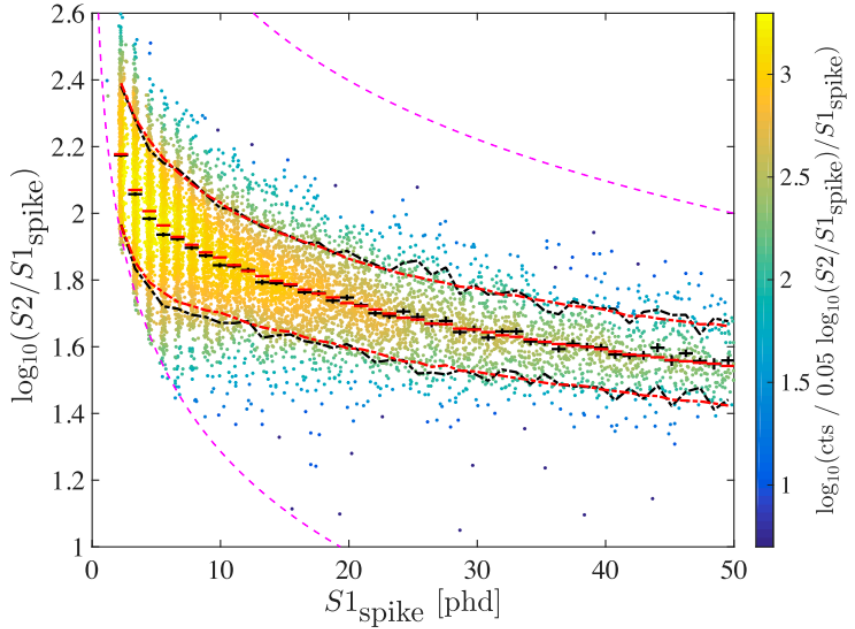


Figure 49: Calibration showing the [NR](#) band mean and width from the [DD](#) calibration. The x-axis is  $S1_{\text{spike}}$ , for which candidate single photons (“spikes”) are identified and tallied in sparse waveforms. This can be a more accurate photon count for low energies and is preferred here to the usual integrated waveform method (see [102] for more information). The black data points are the Gaussian fit centroid values for each  $S1_{\text{spike}}$  bin. The red data points are corresponding Gaussian fit mean value for the simulated nuclear recoil band produced using the model described in Sec. VII. The black and red dot-dashed lines indicate the 90% one-sided limits from data and simulation, respectively. The magenta dashed lines indicate the lower and upper  $S2$  thresholds applied to the [WIMP](#) search. Error bars are statistical only. Figure from [76].

#### 4.6.5 ENERGY RESOLUTION AND SIGNAL YIELDS OUTSIDE THE WIMP SEARCH RANGE

The extensive calibration programs outlined above focus on the [WIMP](#) search energy range of 1-8 keV<sub>ee</sub> ( $\sim$ 8-33 keV<sub>nr</sub>). The [LUX](#) detector is optimized for low-energy sensitivity, and so this is where most of the calibration effort is focused. However, [LUX](#) carried out a detailed study of the energy resolution and signal yields in an energy range complementary to the [WIMP](#) search range. The study is presented in [68], and utilized the rich spectrum of radioactive decays present during Run03 (see Figure 50), many of which were also used in the Doke plot analysis discussed earlier in this chapter. The spectrum continued above what is shown in Figure 50, but the peaks are increasingly difficult to isolate from the Compton scatter continuum and so were not used in the study. In addition to the peaks in the high energy [ER](#) spectrum, the external <sup>137</sup>Cs calibration source with energy 662 keV was used in the study. This source is the highest energy [ER](#) calibration source used in [LUX](#); the detector is not extensively characterized above 662 keV.

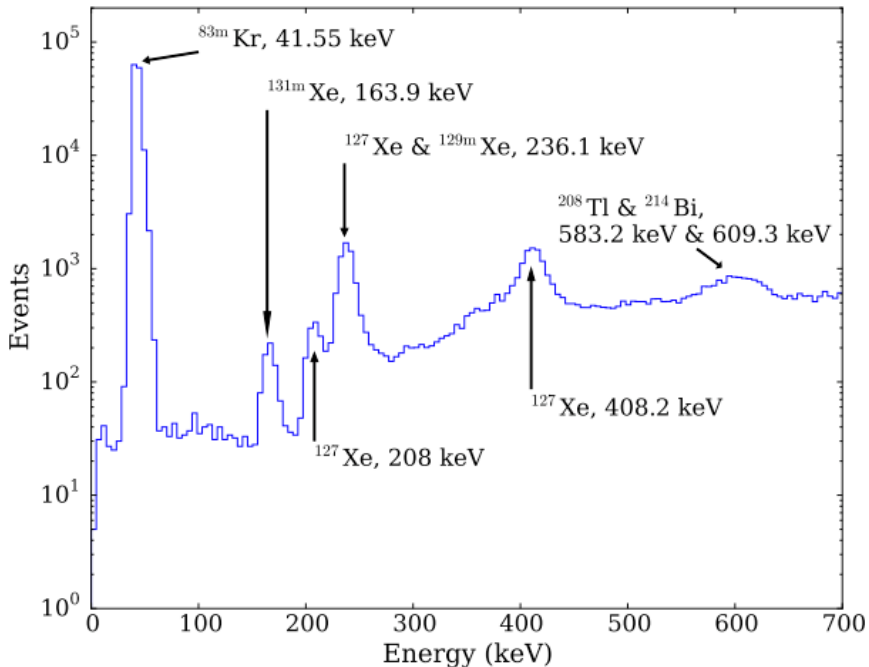


Figure 50: Single-scatter events identified in the [LUX](#) 2013 [WIMP](#)-search data. The labels indicate the source isotopes and their energies. In addition to single scatters, some of these isotopes have other decay modes that can produce multiple scatters. Figure from [68].

The signal yields of these high energy lines were found to be in consistent agreement with Noble Element Simulation Technique (**NEST**) [68]. **NEST** is a widely used simulation package for modeling noble element scintillation; more information can be found about **NEST** in [103]. The agreement between **LUX** and **NEST** demonstrates that **LUX** detector performance is understood in a wide range of energies.

The energy resolution of these high energy lines was also studied. In general, as energy increases, the resolution is expected to increase. This is because as more energy is deposited, more quanta are generated, and therefore the same detector can collect more signal. The expected behavior of the energy resolution has, naively, a underlying Poisson nature:  $\sigma/\mu \sim \sqrt{E}/E$ . In reality, the number of quanta generated cannot freely fluctuate, but depends on the stopping material, and is characterized by a factor called the Fano factor [104] [73]. The ultimate energy resolution of a **LXe** detector is given by [73]:

$$\frac{\Delta E}{E} = 2.35 \frac{\sqrt{FW_{LXe}E}}{E} \quad (42)$$

where  $\Delta E$  is the full width at half maximum of a fit to the peak,  $F$  is the Fano factor in **LXe**, and  $W_{LXe}$  is the W-value. The energy resolution of **LUX**, measured as  $\sigma/\mu$  (from Gaussian fits to the peak in the high energy ER spectrum), is presented in Figure 51. The empirical function  $a/\sqrt{E}$  is fit to the results, yielding  $a = (0.33 \pm 0.01 \text{ keV}^{1/2})$ . The energy resolution is poorer than expected at high energies, and this is due to a series of systematics that are discussed in depth in [68]. In summary, the resolution at high energy energies is limited by **DAQ** saturation, **PMT** saturation, and delayed electron noise. The latter two issues and their effects on energy resolution are discussed in depth in Chapter 8. Here we just note that with large enough energy deposits, **PMT** response becomes non-linear, and delayed electron noise contributes spurious area to pulses. **DAQ** saturation refers to an incoming **PMT** voltage signal reaching the maximum of the **ADC** range of the Struck digitizers. A method to “bypass” **PMT** saturation is used in **LUX**: **PMT** saturation from high energy events is primarily of concern in the top array due to the proximity of the S2 light and the **PMTs**. Instead, the bottom **PMT** array alone can be used in energy reconstruction. This method has been used in **LUX** to aid in reconstructing the energies to correctly identify various high energy background populations.

Some of the expected **LIP** signals discussed in the next chapter can deposit large amounts of energy; the analysis benefits from the study of yields and detector response presented in [68].

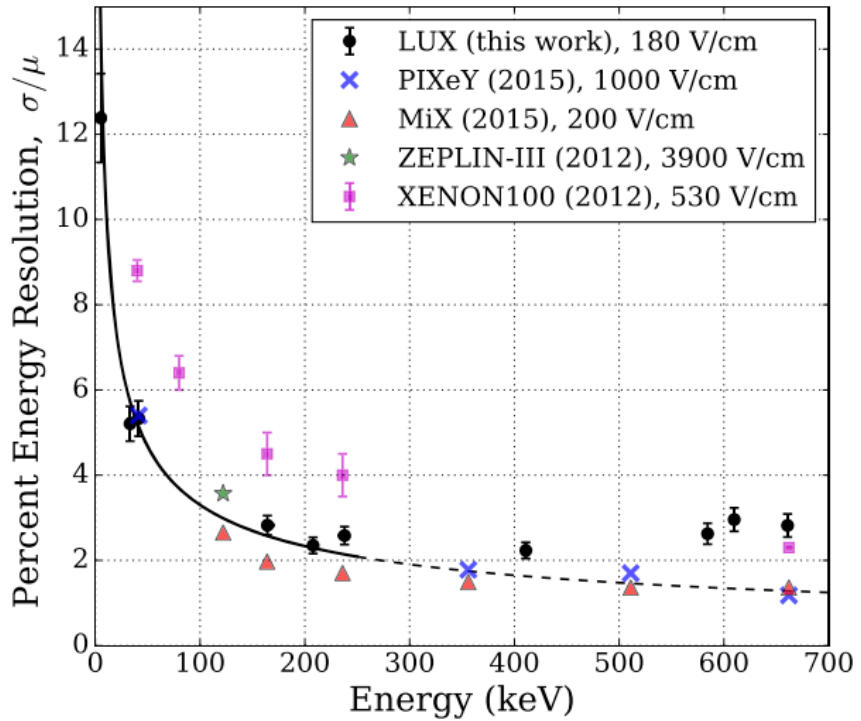


Figure 51: The measured energy resolution at known energy peaks in the LUX ER backgrounds. The detector is optimized for low-energy sensitivity, and variable amounts of PMT saturation and single-electron contributions affect S2 pulses and hamper the energy resolution at high energy. An empirical fit  $a/\sqrt{E}$  is applied. Figure from [68].

## 4.6.6 SIGNIFICANCE OF LUX CALIBRATIONS

Although this thesis is concerned mainly with a search for LIPs, it should be noted that the extensive [LUX](#) calibrations allowed for excellent understanding of the detector, resulting in a world-leading [WIMP](#) limit. In particular, the [DD](#) calibration (carried out after Run03) yielded a much better understanding of the [NR](#) band and yields, and therefore detector thresholds, than the initial AmBe neutron calibration which was carried out in the early days of [LUX](#). The power of the [DD](#) calibration can be seen in the difference between the first [LUX](#) result [81] and the Run03 re-analysis [102] shown in Figure 52. In particular, improved knowledge of the scintillation yields allowed a re-analysis threshold down to  $1.1 \text{ keV}_{nr}$ , where as the initial [WIMP](#) search adopted the more conservative threshold of  $3.0 \text{ keV}_{nr}$ . This improvement allowed [LUX](#) to exclude new spin-independent parameter space below a [WIMP](#) mass of 10 GeV.

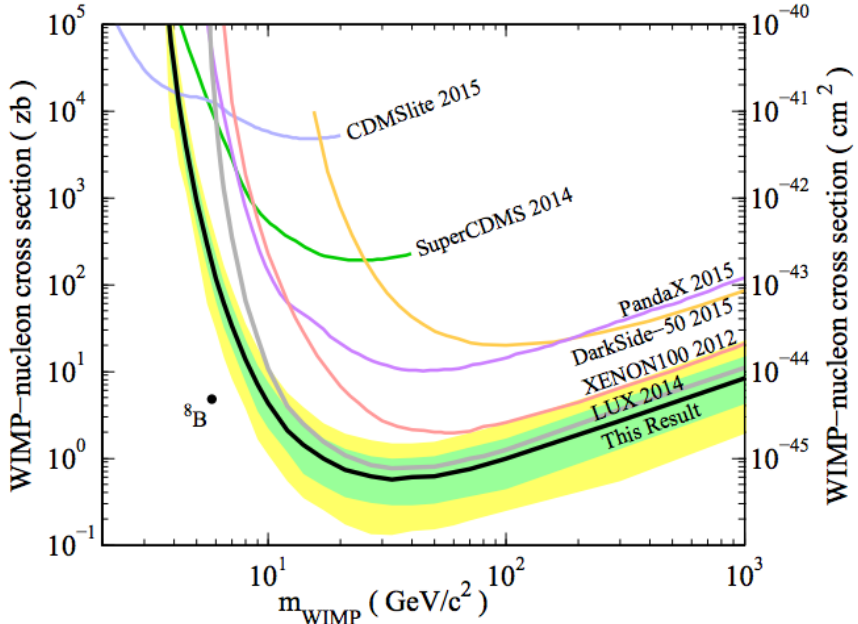


Figure 52: Improved spin-independent [WIMP](#) limit of the Run03 exposure following the [DD](#) calibration of [LUX](#). The first Run03 limit is the gray line labelled LUX 2014, the improved Run03 observed limit is the black line labelled This Result. Figure from [102].

Above the [WIMP](#) search energy range, the analysis presented in [68], and discussed above in Section 4.6.5, was used to further improve and test knowledge of the xenon microphysics responsible for signal generation. Understanding of the [LUX](#) detector response was extended over a wide range of energies.

# 5

## LIGHTLY IONIZING PARTICLE SEARCH

---

*And all this science I don't understand,  
It's just my job five days a week.*

— Elton John *Rocket Man*, 1972

### 5.1 LIP SEARCH WITH LUX

This chapter details the search for [LIPs](#) in the [LUX](#) detector during Run03. Recall from Chapter 2 that [LIPs](#) are present in some hidden sector models, and may comprise some part of the dark matter density observed today. [LIPs](#) carry an effective fractional charge,  $e/f$ , in their interactions with visible matter. Depending on the charge and mass of such a particle, it could precess along the galactic magnetic field lines and be carried out of the galactic disk [105]. This effect would make direct detection on Earth of relic [LIPs](#) over a region of mass-charge space very difficult. Therefore, we limit the [LIP](#) search to cosmogenic [LIPs](#) which can be created in the upper atmosphere or in high energy astrophysical events; such interactions are also capable of producing [LIPs](#) with masses inaccessible to collider experiments [57]. Searches for cosmogenic [LIPs](#) were carried out by Kamiokande II [51], MACRO [54] [55], and LSD [53] for a charge range between 1 and  $e/5$ . The cryogenic germanium detectors CDMS [57] and the Majorana Demonstrator [41] carried out searches in the charge range  $\leq e/6$ . Each of these searches is summarized briefly in Chapter 2.6. All of these previous searches set limits on the flux as a function of charge fraction,  $f$ ; they do not set limits on [LIP](#) mass, as the interaction cross section is independent of mass and depends very strongly on charge, scaling as  $1/f^2$  (see below in Section 5.2.2). The flux  $\Phi$  is defined as:

$$\Phi = \frac{n}{At\epsilon\Omega} \tag{43}$$

where  $A$  is the cross-sectional area of the detector,  $t$  is the time over which the search was carried out,  $\epsilon$  is the detection efficiency, and  $\Omega$  is the solid angle, or geometrical efficiency of the detector.

Previous cosmogenic LIP searches, as well as the one presented here, make the following assumptions:

- LIPs are cosmogenic.
- The incident distribution is isotropic in the upper  $2\pi$  and 0 below.
- LIPs are relativistic, and therefore do not deviate from a straight path as they pass through the detector.
- LIPs are minimum ionizing. That is, their kinetic energy is such that they deposit the minimum amount of energy in the detector.

The last assumption, that LIPs are minimum ionizing, is the most conservative assumption that can be made about LIP energy. There is no theoretical LIP energy spectrum. Any other (greater) energy loss would increase the detection efficiency, making the experiment more sensitive. Assuming minimum ionizing energy loss will generally give the least restrictive limit in the absence of a discovery. It should be noted that there is not a particular motivation that the incident spatial distribution be isotropic in the upper  $2\pi$ , but that is the practice that CDMS and MJD follow.

## 5.2 MODELING LIP INTERACTION

This section describes the steps to modeling LIP interactions for a wide range of LIP charges in the LUX detector to determine the detector response.

### 5.2.1 COLLISION CROSS SECTION

A LIP interacting in the LXe volume loses energy via interaction with electrons. To model LIPs in LUX, the expression of interest is the collision cross section Collisional Cross Section (CCS). The differential CCS describes the energy lost to electrons in a single collision for incident energy of the LIP. For particles with charge  $ze$  and mass  $M$  heavier than the electron mass  $m_e$  (“heavy” particles are those with  $M > m_e$ ), the Rutherford cross section is a familiar differential CCS [106]:

$$\frac{d\sigma_R}{dE} = \frac{2\pi r_e^2 c^2 z^2}{\beta^2} \frac{1 - \beta^2 E/T_{max}}{E^2} \quad (44)$$

where  $r_e$  is the classical electron radius,  $E$  is the energy loss of the incoming particle,  $\beta = v/c$  is the velocity of the incoming particle, and  $T_{max}$  is the maximum energy transfer possible in a single collision:

$$T_{max} = \frac{2m_2c^2\beta^2\gamma^2}{1 + 2\gamma m_e/M + (m_e/M)^2} \quad (45)$$

Often the expression  $T_{max} = 2m_e c^2 \beta^2 \gamma^2$  for  $2\gamma m_e/M \ll 1$  is used implicitly, or is referred to as the “low energy approximation” in older texts. The Rutherford cross section is a good starting point, but it describes the “hard interaction” or head-on, billiard-ball type collision of a particle interacting with free electrons. Real electrons are bound in atoms, and an incident particle can undergo “soft interactions”, in which virtual photons are exchanged. When the virtual photon matches the energy of electron orbitals of the target material, there are resonances in the CCS. The energy transfer,  $E$ , must also be finite in real atoms, where the dielectric properties modify the electromagnetic field of a moving charged particle and limit the growth of the cross section. This real-world behavior is described by a correction factor  $B(E)$ , also sometimes called an “inelastic form factor” [106]:

$$\frac{d\sigma_{CCS}}{dE} = \frac{d\sigma_R}{dE} B(E) \quad (46)$$

Various attempts spanning the 1900’s have been made to take into account the real-world behavior of electrons bound in matter. The most well-known contributions are those of Bethe and Fano. In 1930, Bethe derived a cross section doubly differential in energy loss and momentum transfer using the first Born approximation for scattering on free atoms [107]. In 1963, Fano extended the method to describe atoms in solids [108]. Combining their two methods yields the Bethe-Fano cross-section, which has undergone much study and by our current understanding has been verified to be close to reality [109]. There is another method, called the Photo Absorption Ionization (PAI) model, that is easier to calculate than the Bethe-Fano cross section, and approximates the Bethe-Fano calculation very closely [109]. This thesis uses the PAI model as a base to determine energy deposition, building the full signal model for LIPs interacting in the LUX detector.

### 5.2.2 PHOTO ABSORPTION IONIZATION MODEL FOR CHARGED PARTICLE ENERGY LOSS

The PAI model is also sometimes known as the Fermi Virtual Photon (FVP) or Weisäcker-Williams approximation. The generalized complex dielec-

tric constant  $\epsilon = \epsilon_1 + i\epsilon_2$  can be thought of encoding all the information about a medium. The real part  $\epsilon_1$  describes the polarization of the material and imaginary part  $\epsilon_2$  describes the absorptive properties. Typically both  $\epsilon_1$  and  $\epsilon_2$  are thought of as functions of  $\omega$ , or incident photon energy. In the case of inelastic collision, they are also functions of  $k$ , which denotes momentum transfer to atomic electron. So  $\epsilon(\omega) = \epsilon_1(\omega, k) + i\epsilon_2(\omega, k)$ . The generalized dielectric constant  $\epsilon(k, \omega)$  can be related to atomic matrix elements, and if desired, calculated completely and tediously. However, the PAI model allows us to avoid these tedious calculations by making specific approximations.

In particular, the PAI model approximates  $\epsilon_2(k, \omega)$  by noting that typically, the momentum  $k$  transferred to an electron is much less than the energy transfer  $\omega$ , and so the limit  $k \rightarrow 0$  can be applied below some energy, and above that energy, electrons can be treated as quasi-free. A full derivation of the relativistic PAI cross section can be found in [110], and a useful summary is in [109]. Here, we quote the result:

$$\begin{aligned} \frac{d\sigma_{PAI}(E; \beta)}{dE} &= \frac{\alpha}{\beta^2 \pi} \frac{\sigma_\gamma(E)}{EZ} \ln[(1 - \beta^2 \epsilon_1(E))^2 + \beta^4 \epsilon_2(E)^2]^{-1/2} \\ &+ \frac{\alpha}{\beta^2 \pi} \frac{1}{Nh} \left( \beta^2 - \frac{\epsilon_1(E)}{|\epsilon(E)|^2} \right) \theta \\ &+ \frac{\alpha}{\beta^2 \pi} \frac{\sigma_\gamma(E)}{EZ} \ln \left( \frac{2m_e c^2 \beta^2}{E} \right) \\ &+ \frac{\alpha}{\beta^2 \pi} \frac{1}{E^2} \int_0^E \frac{\sigma_\gamma(E')}{Z} dE' \end{aligned} \quad (47)$$

where  $N$  is the electron density in the medium ( $\text{cm}^{-3}$ ) and  $\sigma_\gamma$  is the photoabsorption cross section. Each of these terms is related to a physical phenomenon. The significance of these terms is described in detail in [110]; here we briefly summarize the salient points. The first two terms describe relativistic behavior, and the last two are the only present terms in non-relativistic theory. The natural logarithm in the first term is responsible for the relativistic rise in energy deposition. The second term describes the emission of Cherenkov radiation. The last two terms only have a  $1/\beta^2$  dependence on velocity, and become effectively constant in the relativistic region. The third term describes resonance absorption at atomic energy levels, and the fourth term is the quasi-free region of Rutherford scattering, where electrons are treated as unbound.

While Equation 47 looks complicated, the convenience of this model lies in the fact that one need only obtain  $\sigma_\gamma(E)$  or  $\epsilon_2$  to carry out the calculation. This is because  $\sigma_\gamma(E)$  is related to  $\epsilon_2$  by:

$$\sigma_\gamma(E) \sim \frac{E}{N} \epsilon_2 \quad (48)$$

and  $\epsilon_1$  and  $\epsilon_2$  are related by a Kramers-Kronig relation:

$$\epsilon_1 - 1 = \frac{2}{\pi} P \int_0^\infty \frac{x\epsilon_2(x)}{x^2 - \omega^2} dx \quad (49)$$

where  $P$  indicates the Cauchy principal value of the integral. Variable changes from  $E$  to  $\omega$  can be made the usual way:  $E = \hbar\omega$ . In practice, one does not find tabulated values of  $\epsilon_1$ ,  $\epsilon_2$ , and  $\sigma_\gamma$ , but rather a variety of databases contain a variety of different optical constants. The optical constants can be related to  $\epsilon_1$ ,  $\epsilon_2$ , and  $\sigma_\gamma$  as needed. For this thesis, the same sources for optical constants as in the [CDMS LIP](#) result [111] were used. More detail along with tabulated values for the cross section can be found in Appendix A. In general, high quality optical constants are desired because they greatly affect the result. Using the same sources as [111] for optical constants, the [PAI](#) cross section was first calculated for Si and compared to a result in the literature [109]. Then the same sources for optical constants were used to calculate the cross section for Xe. Results are shown in Figure 53.

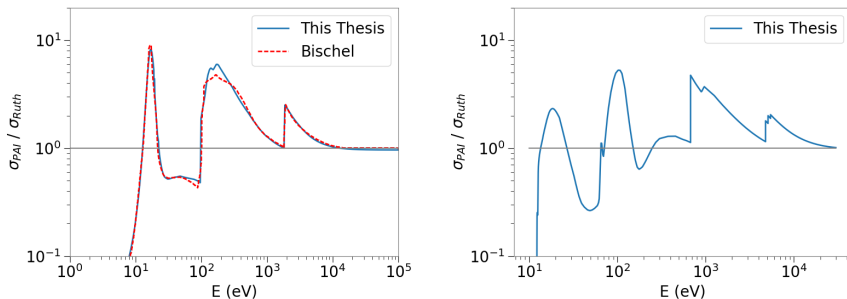


Figure 53: (left) Plot showing the deviations of the [PAI](#) cross section from the Rutherford cross section for Si. Deviations occur at energies corresponding to the M,L, and K electron shells. The result for Si is compared to [109] to check for agreement. (right) [PAI](#) cross section compared to the Rutherford cross section for xenon. In both plots, the y-axes are labeled with  $\sigma$  as a short-hand for  $d\sigma/dE$ .

To account for fractionally charged [LIPs](#), the only addition is a factor of  $(1/f)^2$ :

$$\frac{d\sigma_{PAI}(E; \beta)}{dE} \rightarrow \left(\frac{1}{f}\right)^2 \frac{d\sigma_{PAI}(E; \beta)}{dE} \quad (50)$$

This cross section represents the energy transfer  $E$  to an electron in a single collision. To get the total energy deposition in some thickness of absorber, we use the Monte Carlo method described in the following section.

### 5.2.3 STRAGGLING MONTE CARLO FOR ENERGY DEPOSITION

In most particle physics courses, the Bethe-Bloch equation, which describes the mean rate of energy loss in materials is studied. The  $\langle -dE/dx \rangle$  provided by the Bethe-Bloch equation is *not* the appropriate measure for LIP energy loss. Quoting from [106]:

Few concepts in high-energy physics are as misused as  $\langle dE/dx \rangle$ . The main problem is that the mean is weighted by very rare events with large single-collision energy deposits. Even with samples of hundreds of events a dependable value for the mean energy loss cannot be obtained. Far better and more easily measured is the most probable energy loss.... The most probable energy loss in a detector is considerably below the mean given by the Bethe equation.

This fact is particularly important for rare event detection: events are more likely to deposit energy near the peak of the probability distribution function (PDF) and not the tail, where the mean energy is skewed. The probability distribution function  $f(\Delta)$  that describes the energy deposited ( $\Delta$ ) in a medium is referred to as the straggling function. Sometimes  $f(\Delta)$  is referred to as a Landau function, but it is important to note that a Landau distribution does not always accurately describe straggling. In general,  $f$  depends on the energy of the particle  $\beta\gamma$ , and the thickness of the target  $X$ . That is,  $f = f(\Delta; \beta\gamma, X)$ . See Figure 54 for an example of a straggling PDF and how it can differ from the Landau distribution.

Reference [109] describes several methods for computing straggling functions. For this thesis the Monte Carlo method as described in [109] is employed. The PAI cross section (Equation 47) is used to calculate two quantities:  $\Sigma_t(\beta\gamma)$ , the total (macroscopic) collisional cross section, and  $\Phi(E; \beta\gamma)$ , the integrated single collision spectrum. These two quantities are useful because they lead to the physical quantities of mean free path, and energy lost in each collision, respectively. The following equations summarize the relationships. The total collisional cross section and its relationship to mean free path is:

$$\begin{aligned} \Sigma_t(\beta\gamma) &\equiv N \int \sigma(E; \beta\gamma) dE; \\ \lambda &\equiv 1/\Sigma_t \end{aligned} \tag{51}$$

where  $N$  is the number of atoms per  $\text{cm}^3$ ,  $\sigma(E; \beta\gamma)$  is the PAI cross section as in Equation 47 (the derivate notation is dropped for simplicity), and  $\lambda$

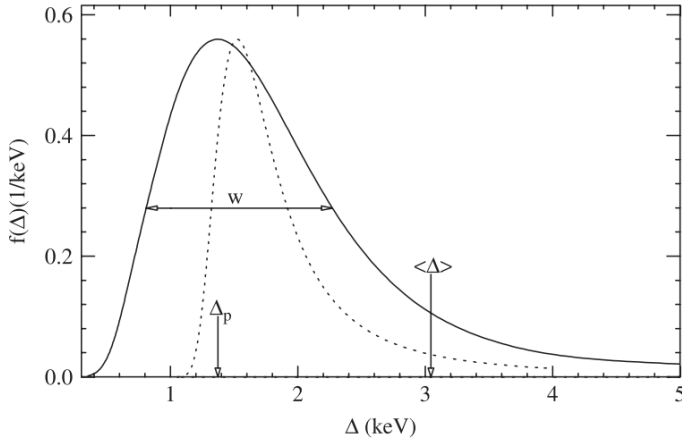


Figure 54: Solid line is the “true” straggling for particles of  $\beta\gamma = 3.6$  traversing 1.2 cm of Ar gas.  $\Delta_p$  denotes the most probable energy deposition, and  $\langle \Delta \rangle$  is the average energy deposition. Note that the average energy deposition is skewed to the high tail. The dotted line shows the Landau function approximation to straggling, which is offset from the true straggling. The physical origin of the high energy tail are the rare, “hard” scatters with electrons. Figure from [109].

is the mean free path. The integrated single collision spectrum and its relationship to energy loss is:

$$\Phi(E; \beta\gamma) = \int_0^E \sigma(E'; \beta\gamma) dE' / \int_0^\infty \sigma(E'; \beta\gamma) dE'; \quad (52)$$

$$E_{loss}(r) = \Phi^{-1}(E; \beta\gamma)$$

$\Phi(E; \beta\gamma)$ , the integrated single collision spectrum, is by definition the cumulative probability distribution function (**CDF**) of the energy loss for single collisions.  $E_{loss}$  refers to the energy loss of a single collision. A common method used in Monte Carlo to draw a random value from a specific **PDF** is to calculate the **CDF** and then invert it. As for all **CDFs**, the values of  $\Phi$  range from [0,1]. When  $\Phi$  is inverted, the resulting function  $\Phi^{-1}(E; \beta\gamma)$  is defined over the range [0,1], and the dependent variable becomes  $E_{loss}$ . Drawing a number  $r$  from a uniform random distribution between [0,1] and taking the associated y-value from an inverted **CDF** results in a the original **PDF** distribution. For unbiased sampling, the x-axis must be equally spaced. See Figure 55 for an illustration.

After obtaining  $\lambda$  and  $E_{loss}(r)$ , the Monte Carlo for a single particle traveling through a segment length  $X$  and depositing energy  $\Delta$  is carried out as follows:

1. Get the distance travelled in step  $i$ ,  $dx_i$ . Accomplish this by drawing a uniform random number  $s$ , define  $dx_i = -\log(s)\lambda$ .

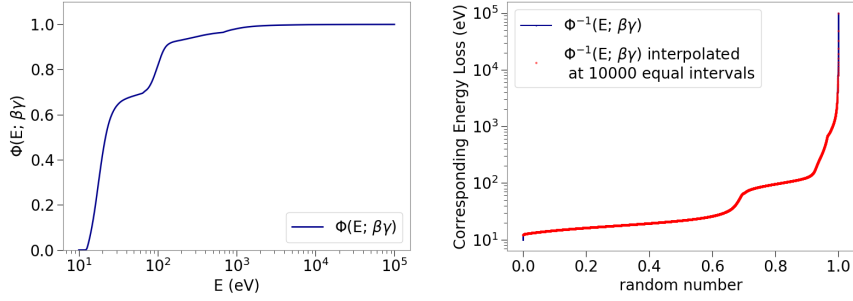


Figure 55: (left) Plot showing  $\Phi(E; \beta\gamma)$ , the integrated single collision spectrum for xenon. (right) Plot showing the inverted integrated single collision spectrum for xenon,  $\Phi^{-1}(E; \beta\gamma)$ . In order to assure unbiased sampling of the distribution, the x-axis must be equally spaced. This can be accomplished by interpolating  $\Phi^{-1}$  over an x-axis of equally spaced points from  $[0, 1]$ . Interpolating with e.g. 10 points will result in a coarse sampling of the PDF and interpolating with e.g. 10000 points will result in a smooth sampling. Drawing a random number  $r$  gives the associated  $E_{loss}(r)$ .

2. Get the energy deposited in step  $i$ ,  $dE_i$ . Accomplish this by drawing a uniform random number  $r$ , find  $dE_i = E_{loss}(r)$ .
3. Update the total distance travelled after step  $i$ :  $x+ = dx_i$
4. Update the total energy deposition after step  $i$ :  $\Delta+ = dE_i$
5. If the total distance travelled  $x$  is greater than or equal to  $X$ , exit.

The output of the Monte Carlo can be thought of as a collection of  $dx_i$  and  $dE_i$  (Figure 56). The result of this straggling Monte Carlo is referred to herein as the “base” Monte Carlo or “1D” Monte Carlo.



Figure 56: A diagrammatic representation of the output of the Monte Carlo. The output for one event is a collection of  $dE_i$  (blue circles) and the space between them  $dx_i$ . The Monte Carlo is run many times, resulting in an accumulation of segments like these. Results of this type are referred to as the “base 1D” Monte Carlo.

Repeating this procedure for many particles and histogramming the resulting  $\Delta$ s gives the straggling  $f(\Delta; \beta\gamma, X)$  in segment length  $X$ . The

$\beta\gamma$  energy dependence of the straggling is accounted for in the original PAI cross section calculation (Equation 47). The analysis assumes all LIPs are minimum ionizing. That is, they have the energy to impart the least possible amount of energy to the medium, which occurs at  $\beta\gamma \approx 4$ . An example showing the results of this Monte Carlo method for a few different LIP charge fractions is shown in Figure 57.

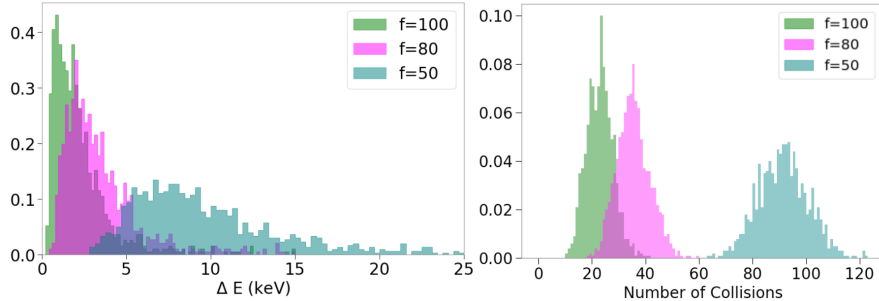


Figure 57: (left) Plot showing the straggling for different charge fractions  $f$  in 10 cm of LXe. To generate these straggling PDFs, the Monte Carlo described above was carried out 1000 times. (right) Plot showing the number of collisions for each charge fraction  $f$ .

A summary of all combinations of  $f$  and path length can be seen in Figure 58. It is useful to note that  $\Phi^{-1}(E; \beta\gamma)$  is the same for all charge fractions, but  $\lambda$  is a function of  $f$ . For high  $f$ ,  $\lambda$  is large and there are few interactions. For low  $f$ ,  $\lambda$  is small and there are many interactions. At each interaction, the same distribution of energies is sampled but for low  $f$  there are far more interactions and therefore more energy deposition total.

To better illustrate the stochastic nature of straggling, the energy deposition per unit length for different path lengths was found for each charge fraction (see Figure 59). For higher  $f$ , there are fewer expected depositions total and so one may expect a lower value for energy deposition per unit length in, say, 10.0 cm than 80.0 cm, but that is not what happens. While most events of  $f = 1000$  won't interact at all in 10.0 cm of LXe, there are a few, rare events that bias the result. The effect of these rare events is washed out over a longer path length of 80.0 cm. This is why an 80.0 cm “measure” of  $dE/dx$  results in a lower value than a 10.0 cm measure. Since low  $f$  have many millions of interactions in a few centimeters, the effect of a few additional interactions will not change the result very much. Therefore, the stochastic straggling is less visible for low  $f$ . To validate the accuracy of this Monte Carlo method, the average energy deposition for LIPs of different  $f$  is compared to  $\langle dE/dx \rangle_0 f^{-2}$ , where  $\langle dE/dx \rangle_0$  represents the average energy loss per unit length for a muon at minimum ionization from reference [106]. As expected, LIP en-

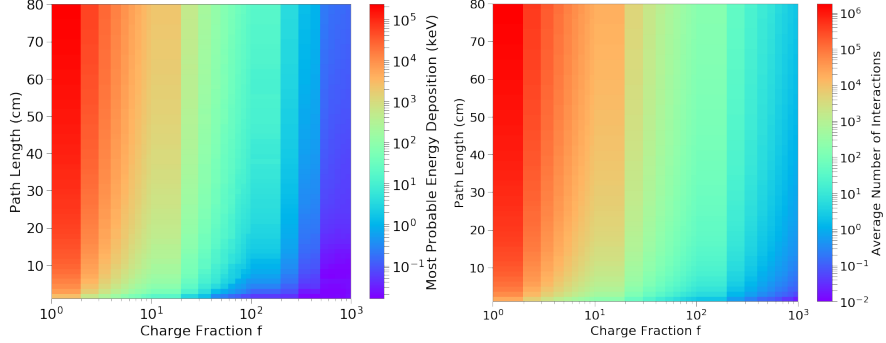


Figure 58: (left) The most probable energy deposition for a given charge fraction traveling though a path length of [LXe](#). The plot was generated by carrying out the Monte Carlo described above, histogramming the results, and finding the peak of the distribution. (right) The average number of interactions for a [LIP](#) of charge fraction  $f$  traveling though a path length of [LXe](#).

ergy depositions also fall off as  $f^{-2}$ , but the [LIP](#) values were found to be 13% lower than the value stated in [106]. This offset is treated as a systematic uncertainty, see Section 5.5.3 below.

#### 5.2.4 DOWNSAMPLING FOR 3D DISTRIBUTION

This section describes how a 1D Monte Carlo segment as in Figure 56 is used to generate 3D events in the [LUX](#) geometry; the scheme is represented in Figure 60. The incoming [LIP](#) distribution is assumed to be isotropic from above. In order to simulate this, a generator was written for LUXSim, the [LUX](#) Collaboration’s Geant4-based simulation. More details can be found about LUXSim in [112]. The generator created primary particles on a hemisphere centered at  $(0, 0, h)$  where  $h$  refers to the height of the [LUX](#) detector in the LUXSim geometry. The particle positions were uniform random on the hemisphere and the particle momenta were a uniform random direction on the unit sphere. Such an initial distribution will result in the majority of particles not entering the [LUX](#) detector, so a downsampling method was used. Instead of simulating [LIPs](#) with this hemispherical generator, geantinos were used. Geantinos are artificial, non-interacting particles from Geant4 that only generate a step action when crossing geometry boundaries. If a geantino was observed to enter the [LXe](#) volume of the detector, its initial position, momentum, and [LXe](#) entrance and exit positions were saved to a file. Drawing from this file provided an initial position and momentum (direction) for a [LIP](#) to enter the [LXe](#) volume of the [LUX](#) detector. The [LIP](#) was then propagated according to its base 1D Monte Carlo until it left the [LXe](#) volume (see Figure 60).

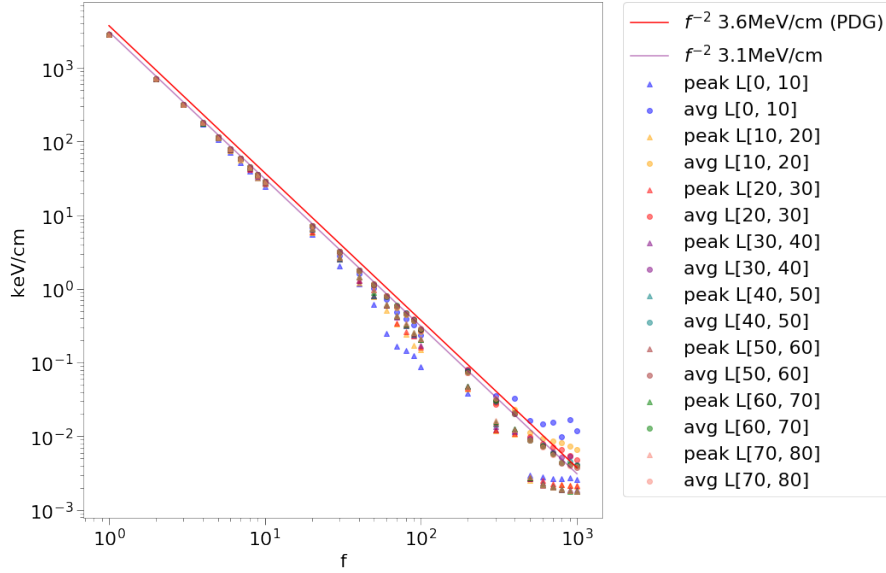


Figure 59: Plot showing the peak (triangle) and the average (circle) of energy deposition in different path lengths. At high charge fraction, interactions are less likely, and so are greatly affected by statistical deviations. The line is  $f^{-2} 3.1 \text{ MeV/cm}$ , as energy deposition for LIPs falls off as  $f^{-2}$ . The value expected at  $f = 1 (\langle dE/dx \rangle$  for a muon) is 3.6 MeV/cm [106] (red line); our result is 13% lower than this. Reference [106] gives the energy loss in units of  $\text{MeV g}^{-1} \text{ cm}^2$ , a LXe density of  $2.94 \text{ g/cm}^3$  is used to translate to MeV/cm. This is the same value for LXe density used in the straggling Monte Carlo.

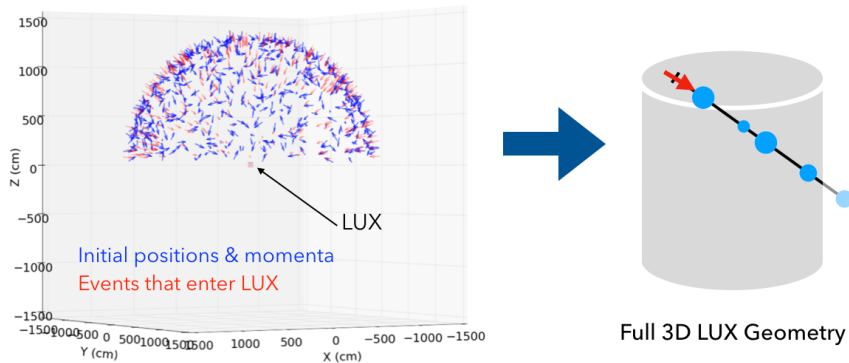


Figure 60: Diagram illustrating the downsampling method for LIPs. Geantinos were generated with uniform random position and momentum on a hemisphere. If a geantino entered the LXe volume of the detector, the position where it entered the LXe was saved along with its momentum. The base 1D Monte Carlo was then “injected” into the LXe with this position and momentum and propagated until it left the LXe volume.

### 5.2.4.1 SOLID ANGLE CALCULATION

The solid angle  $\Omega$  was calculated from the geantino simulation output. As described above, the positions and momenta of the events that entered the  $\text{LXe}$  space of the  $\text{LUX}$  detector were saved. The initial positions of these events were histogrammed, as in Figure 61. The acceptance for events coming from near vertical polar angles is small, because only a few initial momenta will allow the particle to enter  $\text{LUX}$ . For large polar angles, the acceptance grows because many initial momenta will result in success.

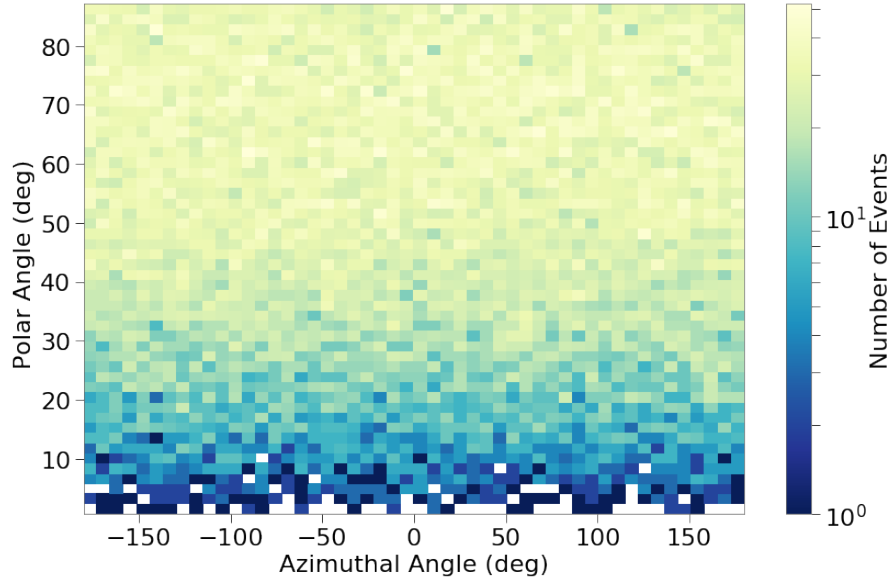


Figure 61: A 2D histogram of the initial positions for geantinos that entered the xenon space of  $\text{LUX}$ . Polar angle indicates deviation from the vertical.

Since the map of initial positions in the  $(\theta, \phi)$  plane is azimuthally symmetric, the  $\theta$ -projection was taken, counts were normalized to one, and bin density was normalized to  $2\pi$  str. Then the integral was taken to give the solid angle. This procedure was done for several different bin sizes (26 trials of integer bins from  $25 \times 25$  bins up to  $50 \times 50$  bins) and the average was taken to reduce the effect of binning. The result is  $\Omega_{\text{LUX}} = 3.78 \pm 0.04$ , where the error is the standard deviation of the results for the different bin sizes. The effect of normalizing to  $4\pi$  str was tested, and it did not change the results.

### 5.2.5 GENERATING PMT WAVEFORMS

This section describes how the 3D straggling Monte Carlo is used to generate  $\text{PMT}$  waveforms, so the full  $\text{LUX}$  detector response can be assessed. Recall that an energy deposition in  $\text{LXe}$  produces scintillation photons

and ionization electrons. One method is to generate the photons as secondary particles and do a full optical simulation following their paths until they end in a [PMT](#) and generate a photoelectron. The electrons would be drifted under the influence of the electric field, extracted into the gas region, where they would then generate more photons from their proportional scintillation in the gas, and these photons would be similarly propagated through the detector until they end in a [PMT](#) and generate a photoelectron. This method, with full tracking and optical simulation of the secondaries, is prohibitively slow and computationally intensive for [LIPs](#), which can have  $O(100)$  primary interactions in the detector.

The method used for generating photoelectrons in the [PMTs](#) was a [LUX](#) Collaboration internal piece of software called fastSim. Instead of calculating the trajectory and reflection(s) of every photon, fastSim uses the position and numbers of initial quanta to “directly transport” photons to their statistically-determined final destinations. The number of initial quanta (scintillation photons and ionization electrons) are determined by G4S1Light.cc, which includes a clustering of any energy depositions within 0.04 cm of each other. This merges nearby hits of energies  $E_1$  and  $E_2$  to a single hit of  $E = E_1 + E_2$ , with the requisite number of quanta. The choice of clustering radius is based on [113], and is related to how far electrons travel before thermalizing. The resulting output is an [.evt](#)-file which contains [PMT](#) waveforms of [LIP](#) events (see Chapter 4.5 for details about [.evt](#)-files). An example of an  $f = 100$  [LIP](#) is shown in Figure 62.

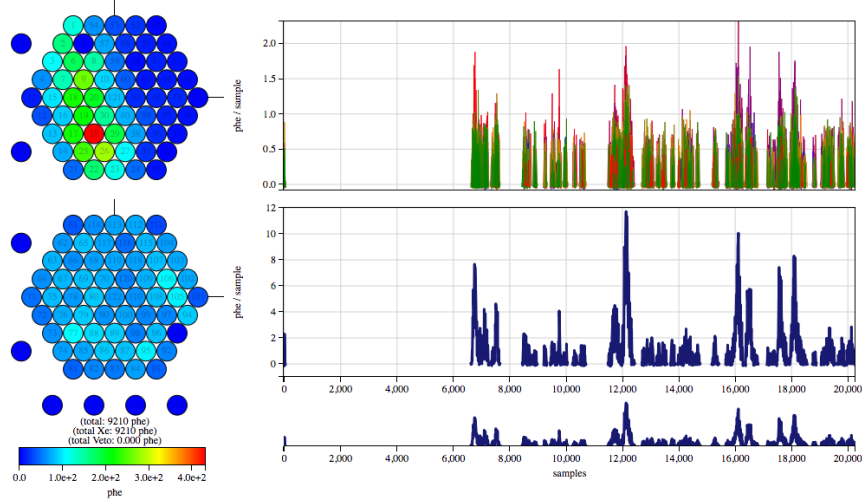


Figure 62: The simulated detector response to a LIP of charge fraction  $f = 100$ . The hexagonal maps filled with circles represent the top and bottom PMT arrays. The color scale indicates how many photons were observed in each PMT. The top graph shows each PMT voltage trace in a different color, and the bottom graph shows the summed PMT waveforms.

### 5.2.6 PMT WAVEFORM PROCESSING

The PMT waveforms were processed with the default LUX DPF, except that the number of pulses was increased from 10 to 100. That is, up to 100 pulses could be found in an event. No changes were made to the pulse finder or the definitions of the five types of pulses: S1, S2, SE, SPHE, and Else. The LUX data processing was intended for use on single-scatter events with only one S1 and one S2. Thus, its performance for LIP events, which have many pulses, is not expected to be ideal. An example of the DPF run on an  $f = 100$  event is shown in Figure 63. This is the same event shown above in Figure 62. Visible in the data processing are examples of two S2s being merged into one (pink dotted lines). Issues like these have repercussions for the position reconstruction and energy reconstruction.

The data processing plays a large role in the LIP analysis. A few merged pulses like those in Figure 63 do not greatly limit the capability to do track reconstruction, but with lower  $f$ , where more energy is deposited, the pulse finder effects are magnified. Two examples of an  $f = 10$  LIP with the DPF results are shown in Figure 64 and Figure 65.

The pulse finder often failed to isolate individual pulses for low  $f$  and the entire event would be classified as an Else pulse (Figure 64). Sometimes, the pulse finder successfully broke the ionization trail into successive S2 and/or Else pulses (Figure 65). However, these pulses often failed

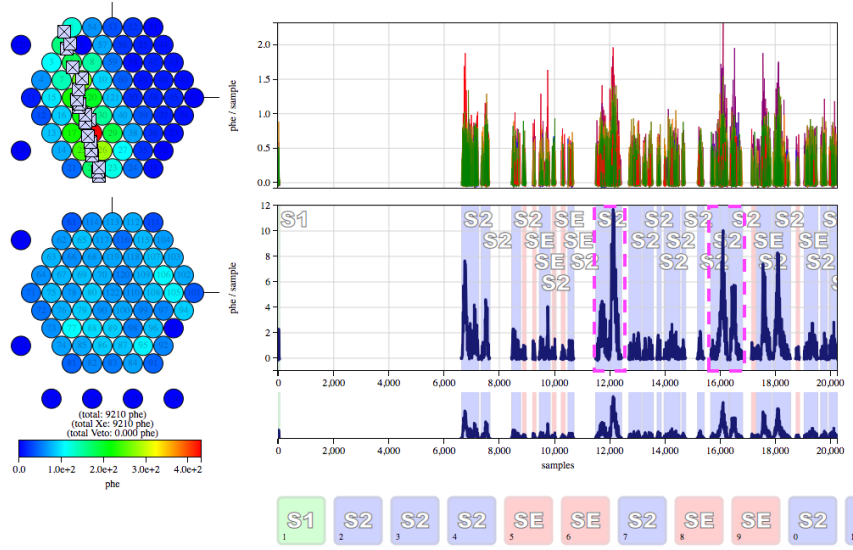


Figure 63: The result of the LUX DPF on a LIP of charge fraction  $f = 100$ . The pink dashed lines highlight energy depositions that were merged by the pulse finder. The “x” markers on the PMT map indicate the Mercury reconstructed positions, which have position corrections applied.

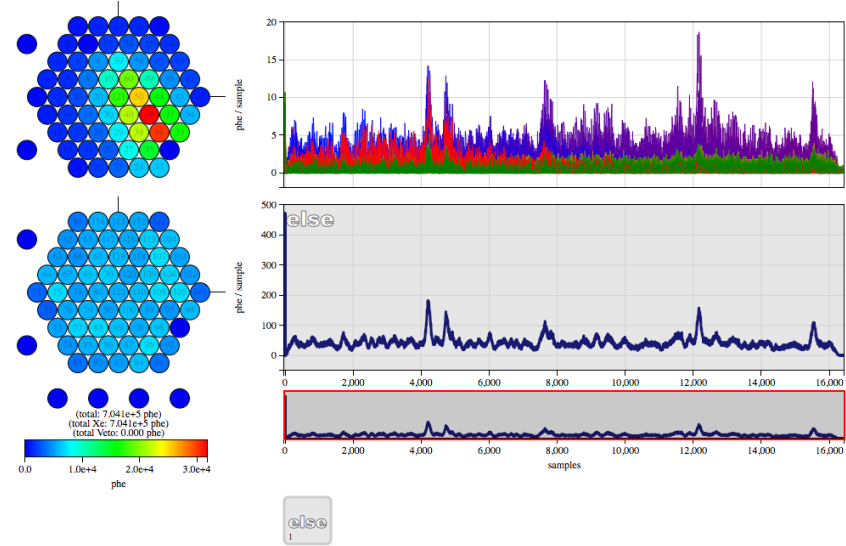


Figure 64: The result of the LUX DPF on a LIP of charge fraction  $f = 10$ . The pulse finding capability was seen to fall dramatically with decreasing  $f$ . This event traversed the detector starting near PMTs 53 and 52, and proceeded across to PMTs 23 and 24.

the Mercury position reconstruction and correction algorithms. These types of pulse finder effects have consequences especially for track reconstruction and they decrease the detection efficiency for LIPs for low  $f$ . This turnover in efficiency for low  $f$  is somewhat counter-intuitive: typically we think of detection efficiency in LXe TPCs as a function of energy deposition; if the energy deposition is large enough, we see a signal. Low  $f$  LIPs certainly deposit enough energy to produce a signal, but ability to reconstruct a track is a major factor in the detection efficiency for LIPs. It was found that the efficiency for finding corrected S2 pulses dropped off sharply below  $f = 10$ ; therefore, this analysis employs an  $f = 10$  cut off, and does not carry out a search for any lower charge fractions.

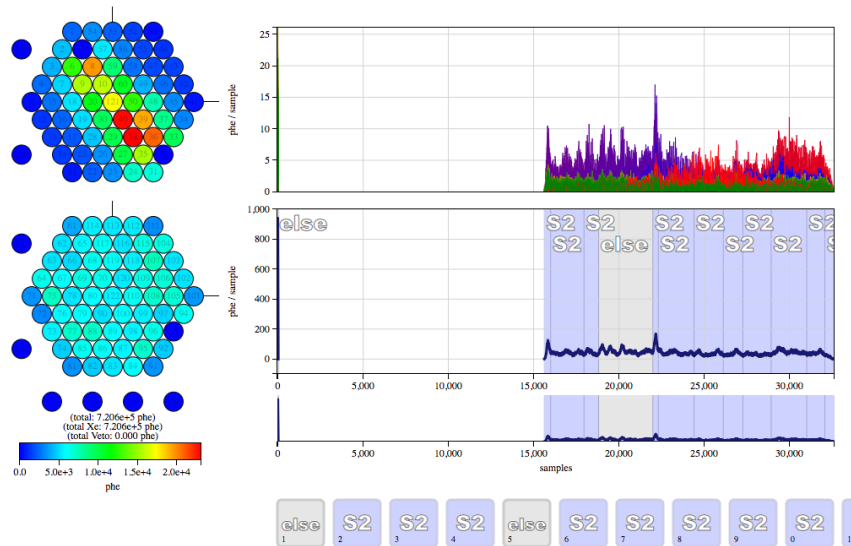


Figure 65: The result of the LUX DPF on a LIP of charge fraction  $f = 10$ . The pulse finding capability was seen to fall dramatically with decreasing  $f$ . The pulse finder was sometimes able to isolate individual S2s for low  $f$  events, but the Mercury reconstruction of these events often failed. There are no positions marked on the PMT hit map for this event, indicating that position reconstruction failed.

The energy reconstruction is also affected by the pulse finder identifying area as Else instead of S2. Figure 66 contains the reconstructed energy deposition for charge fractions in the range  $f = [10, 1000]$ . The energy is reconstructed the usual way:  $E = W(S1/g1 + S2/g2)$  and the per-event track length  $L$  reconstruction is discussed further below in Section 5.3. The factor  $E/L$  was reconstructed for several events and charge fractions, and the results were histogrammed. Plotted is the average of such histograms for each charge fraction  $f$ . For low  $f$ , the corrected energy is systematically lower due to the pulse finder. Only corrected S2 area is used in the reconstruction, so any area going into Else pulses is

“lost”. At high  $f$ , the result for reconstructed  $dE/dx$  is higher than the expected trend line due to the bias discussed earlier: for high  $f$ , only very few high-energy events are above threshold, which biases the measure to the high energy tail. Compare Figure 66 to Figure 59.

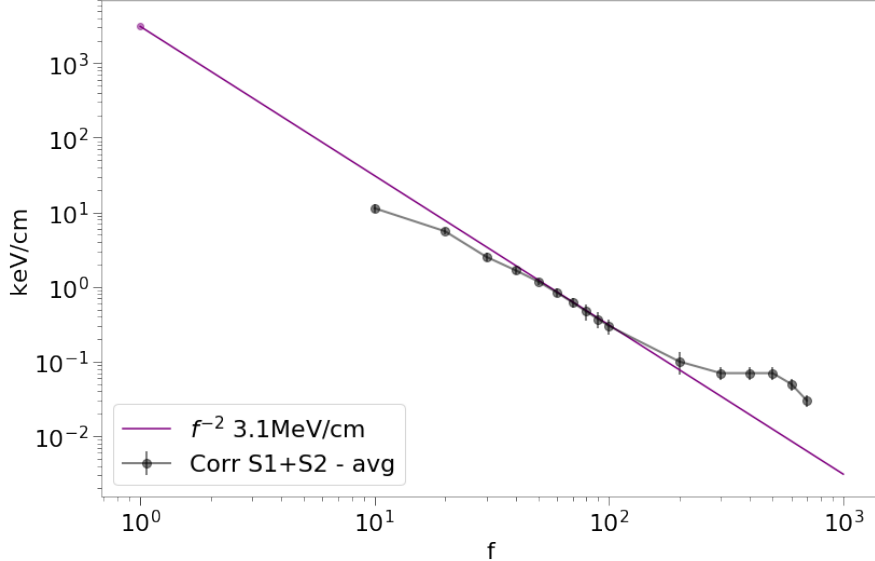


Figure 66: The reconstructed  $dE/dx$  for several charge fractions. The plot was generated by reconstructing the energies  $E$  and track lengths  $L$  from LIP waveforms that were processed with the [LUX DPF](#). The  $E/L$  from each event was added to a histogram, and the averages of the histograms for each simulated  $f$  were found. The detector response matches expectations from the [PAI](#) cross section in the charge range  $f = [50, 200]$  (compare to Figure 59). Below this range, the pulse finder yields a “loss” of any non-S2 area. Above the range, only the highest energy fluctuations are detected; and the detector response levels off due to low statistics (most events are in the first bin, but there are many events which did not deposit enough energy to be “measured”, i.e. to make it into the histogram).

### 5.3 LIP FILTER

After the waveform data is processed into [RQ](#) files, there is another step of processing referred to as the Filter Code. For the [WIMP](#) analysis, all multi-scatter events are rejected. So-called [WIMP](#) “golden events” with one S1 and one S2 are filtered from the months of live data. Once selected, the [WIMP](#) golden events were further paired down based on reconstructed position, energy, and whether they were [ER](#) or [NR](#). Thus any remaining events in the fiducial volume with an energy in the [WIMP](#) search range

below the [NR](#) mean are [WIMP](#) candidates. In the same vein, a [LIP](#) Filter was developed. The [LIP](#) Filter was designed to read in [RQ](#) files, and *keep* the multi-scatter events, as these are the potential [LIP](#) candidates. The [LIP](#) filter code also produces additional [RQs](#) that are useful in identifying a [LIP](#). Every new [LIP RQ](#) was produced three times with a different definition of “multi-scatter”. That is, each event was filtered for (1) Corrected S2s (2) Raw S2s and (3) Raw S2-like pulses, which refers to S2, Else, and SE pulses following an S1. In each case, a [LIP RQ](#) was calculated. For example, one [LIP RQ](#) is the sum of all the S2 area. For case (1) the S2 pulses with position-corrected areas were summed (see Chapter [4.6.2](#) for a description of the pulse area corrections applied with the  $^{83m}\text{Kr}$  calibration). For case (2) the raw S2 area (with no corrections) were summed. For case (3) the raw S2 and raw Else and raw SE area were summed. It should be noted that by default the [LUX DPF](#) does not apply pulse area or position corrections to Else and SE pulses. Three different pulse filters were used because at the time of the [LIP](#) Filter development, it wasn’t clear which case, (1), (2), or (3) would result in the most useful and robust [RQs](#) for identifying [LIP](#) candidates. This section summarizes the [RQs](#) calculated by the [LIP](#) Filter, and the following section discusses which [RQs](#) were ultimately used in the [LIP](#) analysis. A list of all the [RQs](#) contained in the [LIP](#) Filter output is given in Appendix [B](#).

### 5.3.1 TRACK RECONSTRUCTION AND RQS

One of the assumptions made in the [LIP](#) search is that [LIPs](#) are cosmogenic and relativistic. They are expected to enter the detector isotropic in the upper  $2\pi$  and proceed through the detector without any deviation. Thus, the [LIP](#) search requires track reconstruction. Two track reconstruction algorithms were developed, and since each event was split into 3 cases ( (1) Corrected S2, (2) Raw S2, and (3) Raw S2-like), an event could be fit up to six times. The time spent on track fitting was the most time consuming part of the [LIP](#) filter. The first track fit minimizes the following expression:

$$\chi^2 = \sum_i^n \left( \frac{d_i}{\sigma_{t_i}} \right)^2 \quad (53)$$

where  $n$  is the number of pulses for case (1), (2), or (3), as defined above,  $d_i$  is the perpendicular distance from point  $i$  to the fit line, and  $\sigma_{t_i}$  is the “total error” for point  $i$  from the Mercury position reconstruction. The error from position reconstruction is parametrized in this manner because by default, Mercury returns the reconstruction errors in the cylindrical coordinates,  $(r, \phi)$  (see [\[98\]](#)). However, positions are stored and position

corrections are applied in [RQ](#) files in cartesian coordinates  $(x, y)$ . The entire covariance matrix of the position errors is not kept, so any attempt to translate the  $(r, \phi)$  errors into errors on  $(x, y)$  would lose any underlying correlation. Therefore, the errors were added in quadrature to yield  $\sigma_t$  for each point, which can be thought of as sphere parametrizing the error in all directions, instead of separately in the  $x$  and  $y$  directions. An error of 1.0 cm was applied for the  $z$ -direction, to help account for the fact that [LIP](#) interactions are spread out along their tracks instead of being point-like. The  $\chi^2$  in Equation 53 is the minimization variable<sup>1</sup>, and each iteration of the fit tries new parameters for a line in 3D (see Figure 67). The parameters that minimize  $\chi^2$  define the [LIP](#) track.

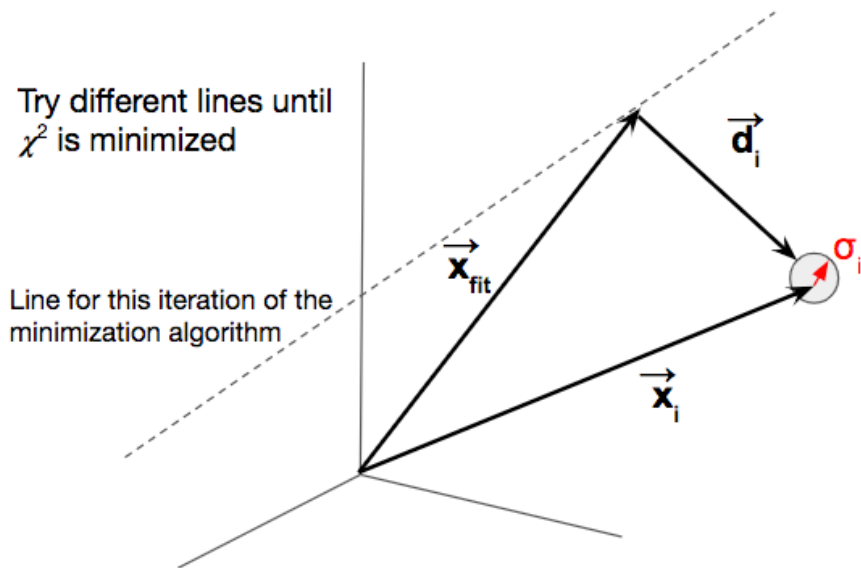


Figure 67: A diagram of the  $\chi^2$  minimization variable for track reconstruction.

The figure shows the example of one point, e.g. the corrected reconstructed position of one S2 pulse. A minimum of three points was required by the [LIP](#) Filter for track reconstruction, so that a  $\chi^2$  may be defined.

---

<sup>1</sup> This variable is actually more of a likelihood than a true  $\chi^2$ , since there is no reason to believe the  $\sigma_t$  errors are gaussian. However, the [LIP](#) filter code refers to the track minimization as  $\chi^2$  and to avoid confusion for anyone using the [LIP](#) filter in the future, we try to refer to variables here with the same names.

Another  $\chi^2$  is also defined in the LIP filter, to penalize irregular deflections and spacing between the points. The minimization variable is defined as follows:

$$\chi_{anglePen}^2 = \sum_i^n \left( \frac{d_i}{\sigma_{t_i}} \right)^2 + \sum_{i,j=i+1}^{n-1} \left( \frac{\theta_{i,j} - \bar{\theta}_{i,j}}{\Delta\theta_{i,j}} \right)^2 + \left( \frac{d_{i,j} - \bar{d}_{i,j}}{\Delta d_{i,j}} \right)^2 \quad (54)$$

where the  $d_{i,j}$  is the distance between consecutive points and  $\theta_{i,j}$  is the angle from dot product between the vector  $\vec{d}_{i,j}$  and the direction vector of the line. The bar notation (e.g.  $\bar{\theta}_{i,j}$ ) represents the average of the variable and the  $\Delta$  notation (e.g.  $\Delta\theta_{i,j}$ ) represents the standard deviation of the variable.

A number of track-related RQs are calculated and saved to the LIP Filter output. Both  $\chi^2$  values described above are saved, along with the number of degrees of freedom for each event and fit. The reconstructed track length  $L_{fit}$  is also saved by using the fit result to determine where the LIP entered and exited the detector. The polar and azimuthal angles of the track, and the parameters that define the line are also saved. Another useful track RQ was found to be the standard deviation of the distances between points.

Examples of track reconstruction using position corrected S2s are shown in Figure 68 for  $f = 100$ . The colors indicate different events and the markers are scaled by S2 pulse area.

### 5.3.2 ENERGY CONSISTENCY RQS

One of the guiding principles from the LIP straggling discussed above is that LIPs passing through the LUX detector are expected to deposit their energy around some most probable value. If one divided up a LIP track into, e.g. 10 cm segments, each segment will contain a deposition drawn from the related straggling PDF  $f(\Delta; (\beta\gamma)_{min}, X = 10 \text{ cm})$ . Most of these “random draws” from the straggling PDF will be at the peak of the distribution, since the first 10 cm of LXe are no different from the next; by assumption the LIP does not lose enough energy to change its energy deposition behavior over the height or width of the LUX detector. Therefore, the energy-related RQs are mainly developed to test whether the energy deposition along the track adheres to this expected behavior, and are not concerned with accurately measuring the total energy deposition itself.

Some examples of useful RQs that test the energy consistency of events are: the standard deviation of the pulse areas and the ratio of the first two pulse areas to the last two pulse areas. Another energy consistency RQ that was utilized was the Anderson-Darling test statistic. The Anderson-Darling test belongs to a class of test statistics that determine if a collec-

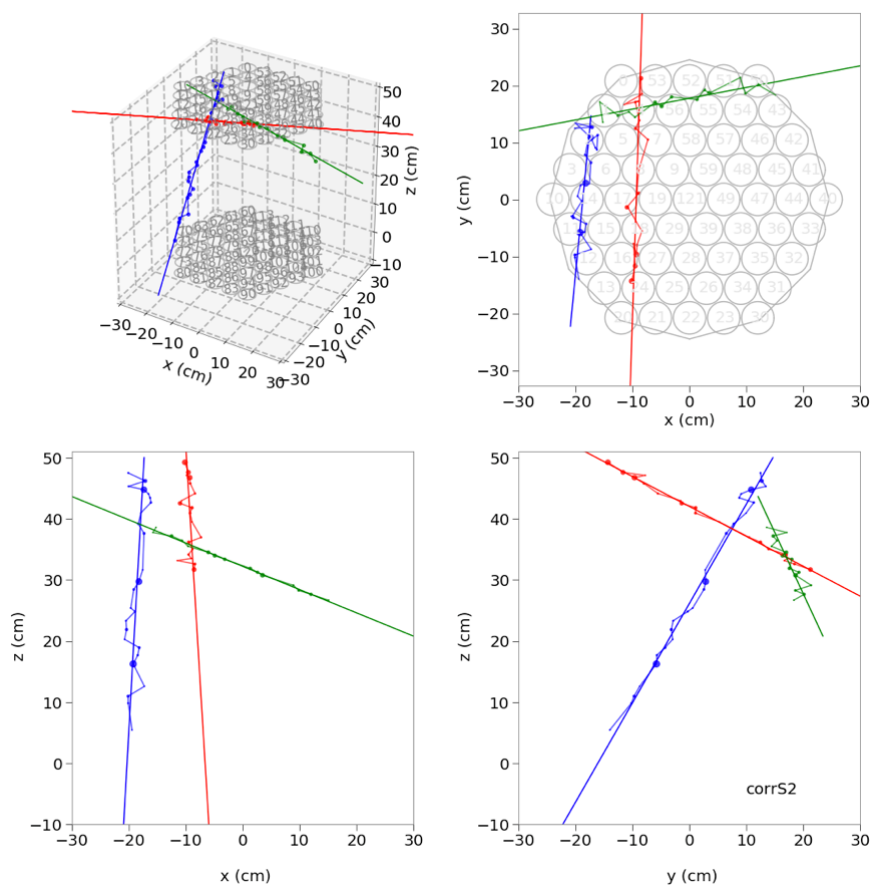


Figure 68: The result of track reconstruction for  $f = 100$  LIPs using the  $\chi^2$  in Equation 53 as the minimization variable. Each color represents a different LIP event. The panels show the full 3D view (top left), the top-down view in  $(x, y)$  (top right), and two side views  $(x, z)$  and  $(y, z)$  (bottom left and right, respectively.)

tion of observations are drawn from a given PDF. Other such test statistics are the Kolmogorov-Smirnov and Cramer von Mises test statistics. All of these tests were tried, and it was found that the Anderson-Darling test had the best performance for rejecting background. The test is a measure of the weighted quadratic difference between the hypothetical distribution  $F$  and the sample distribution  $F_n$ :

$$A^2 = n \int_{-\infty}^{\infty} \frac{(F_n(x) - F(x))^2}{F(x)(1 - F(x))} dF(x) \quad (55)$$

where  $A$  is the Anderson-Darling test statistic. Figure 69 illustrates the differences between LIP and background straggling (the backgrounds are discussed in the following section). Each event with a reconstructed track was binned into 10 equal-sample bins<sup>2</sup>, and the pulse area in the bin was divided by the number of samples to yield 10 “measurements” of phd/sample. These 10 values were hisogrammed to build up a straggling PDF. Figure 69 shows several events hisogrammed on the same axis; each color represents a separate event. The events are overlapped like this to show that each event for a given charge fraction lies roughly in the same straggling PDF, even though the bin size for each event may not be the same (there are always 10 bins, but they vary in size event to event). Recall from above that for different path lengths, the average (or peak) energy deposition is not expected to be the same due to the stochastic nature of straggling (Figure 59). However, different events for LIP tracks of the same charge fraction are similar enough that they could be drawn from the same distribution, and certainly the same class of distributions, and so the Anderson-Darling test is appropriate. This is especially true when compared to background events, which have many bins of very low phd/sample and one or two bins of very high phd/sample.

For each event, the 10 measurements of phd/sample are treated as coming from a Moyal distribution. The Moyal distribution describes the energy loss of a charged relativistic particle due to ionization [114], and it provides a convenient closed-form approximation to the Landau distribution [115]. In fact, the Anderson-Darling test was fairly robust at separating LIPs from background even if a normal distribution was used as the test distribution, but it was found that the right-skewed tail of the

---

<sup>2</sup> The number of bins was chosen by testing 6, 10, and 50 bins. A choice of 50 bins slowed down the calculation appreciably, and resulted in poorer background rejection. A choice of 10 bins did not take significantly more time than 6 bins, and showed better background rejection than 6 bins.

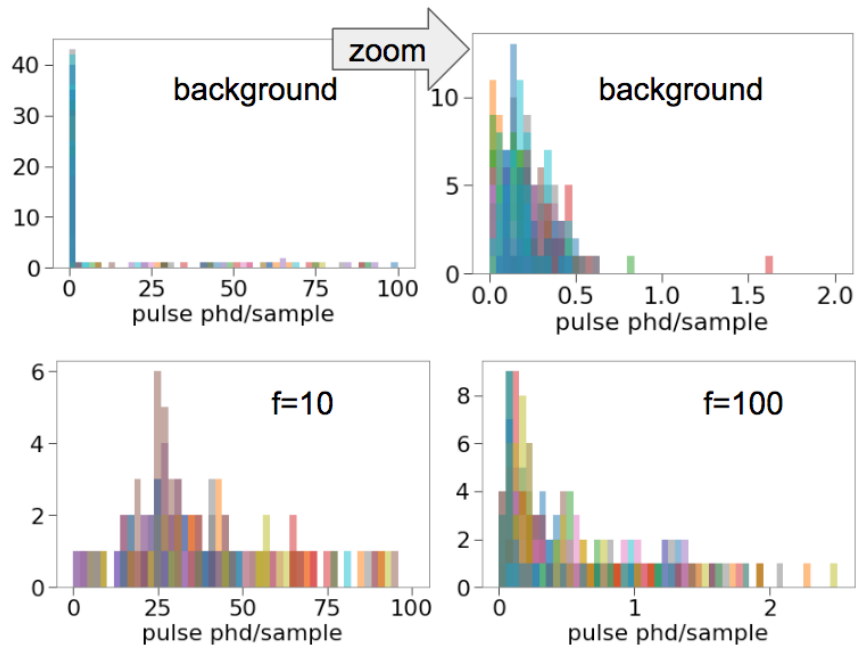


Figure 69: The binned phd/sample straggling histograms for several events displayed on the same axes. Each color represents a different event; the top shows the straggling of background events and the bottom shows the straggling of  $f = 10$  and  $f = 100$  events. The two background panels show the same events, but the top right plot is a zoomed-in and re-binned version of the top left plot.

Moyal distribution was helpful in keeping LIPs. The functional form for the Moyal distribution is:

$$f(x) = \frac{1}{\sqrt{2\pi}s} \exp\left(-1\left(\frac{x-\mu}{s} + \exp(-1\frac{x-\mu}{s})/2\right)\right) \quad (56)$$

where  $\mu$  is the mean and  $s$  is a scale variable. Each event was “fit” with distribution, following the `scipy.stats.rv_continuous` method, which doesn’t do any minimization, but simply uses the mean of the observations as  $\mu$  and standard deviation as  $s$  and carries out the Anderson-Darling test with the observations against this “fit” result. An example of a Moyal and normal distribution with the same  $\mu$  and  $s$  are shown in Figure 70 for reference.

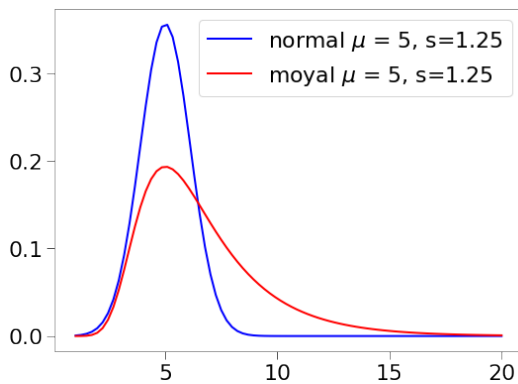


Figure 70: The Moyal and normal distributions shown for the same  $\mu$  and  $s$  variable. For the normal distribution  $s$  is usually called  $\sigma$ . The Anderson-Darling test was employed for LIPs with the Moyal as the test distribution.

## 5.4 LIP BACKGROUNDS

In contrast to the WIMP search, which throws away all multi-scatter events as background, the LIP search must keep these events as possible signal. One origin of such events are radioactive gamma backgrounds that can multiply scatter in the detector. A detailed study of the radioactive backgrounds was completed by B. Tennyson [116] for the Run03 detector conditions. Prior to Run03, each detector component, including the xenon itself, was counted to assess the contamination from radioactive materials. A simulation was carried out by B. Tennyson using LUXSim with initial input from the counting campaign, and subsequently adjusted to match the observed backgrounds during Run03. The output from this

simulation was studied, and it was determined that the maximum number of scatters that a gamma underwent in the detector was 3. Therefore, setting a requirement of 4 pulses for the [LIP](#) search reduces the gamma background from radioactive detector components to zero.

The other source of backgrounds for [LIPs](#) are the so-called “electron trains” that are present in dual phase [TPCs](#). The causes of electron trains are discussed in-depth in Chapter 8. Here, we just note electron trains are proportional scintillation signals the size of one or a few electrons that are observed to follow large energy depositions for  $O(100)$  ms. Note that the observed time persistence is orders of magnitude longer than the typical event window in [LUX](#), which is  $400\ \mu\text{s}$ . Another phenomenon associated with electron trains in [LUX](#) is colloquially referred to as an “electron burp”. Electron burps are the sudden emission of  $O(100 - 1000)$  electrons over the course of one or two event windows. In [LUX](#), electron burps have been observed to be constituents in the much longer electron trains [117]. These electron noise phenomena are the main background for the [LIP](#) analysis; they can result in similar numbers of pulses being found as for [LIPs](#) and must be rejected with both track and energy-consistency [RQs](#). There is an example of an electron train in Figure 71 and an electron burp in Figure 72.

Some electron background events have good track reconstruction (see Figure 73 and Figure 74). Although the track requirement is powerful in rejecting a lot of background events, other identifiers are needed to cut remaining electron backgrounds. The events are displayed with the marker sizes proportional to the pulse areas to highlight how energy consistency [RQs](#) are useful in rejecting electron train backgrounds. Compare the electron train tracks in Figure 73 and Figure 74 to the  $f = 100$  track reconstruction examples in Figure 68.

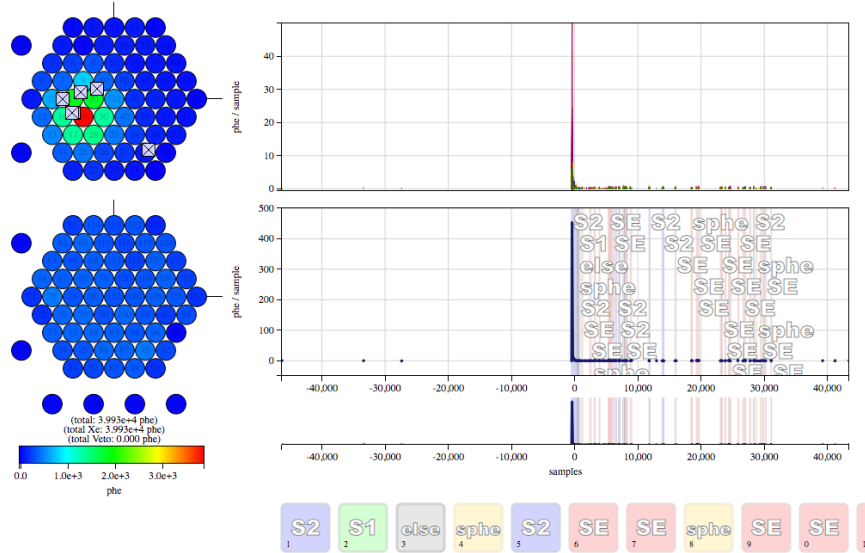


Figure 71: An example of an electron train following a large S2. In this particular example, there is no S1 found before the large S2. S1s are required to provide a drift time for S2 pulses, and events with no drift time have no pulse area or position corrections applied. If only the corrected pulse areas were used, they would appear to be approximately uniform and could be confused for a LIP. In this case, the corrected positions (displayed as “*x*” markers on the PMT array) are not aligned in a track, so a track cut could reject this particular event. Sometimes, electron trains do happen to lie along a track, and RQs using raw S2 areas and positions must be employed.

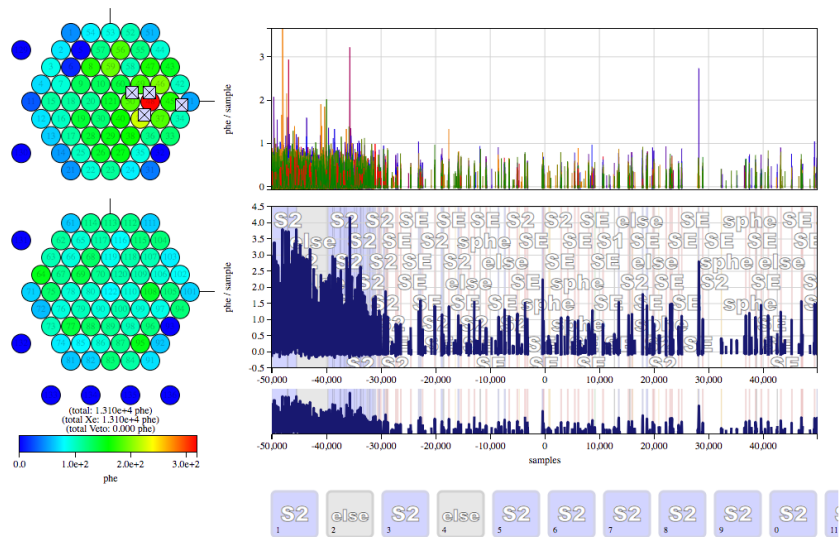


Figure 72: An example of an electron burp, which happens to straddle two event windows. The S2s in electron burps are often similarly sized, and though there is no true S1, the pulse finder sometimes identifies an S1 in the midst of the electron burp. A robust method to cut these events is to limit the amount of area appearing before the S1.

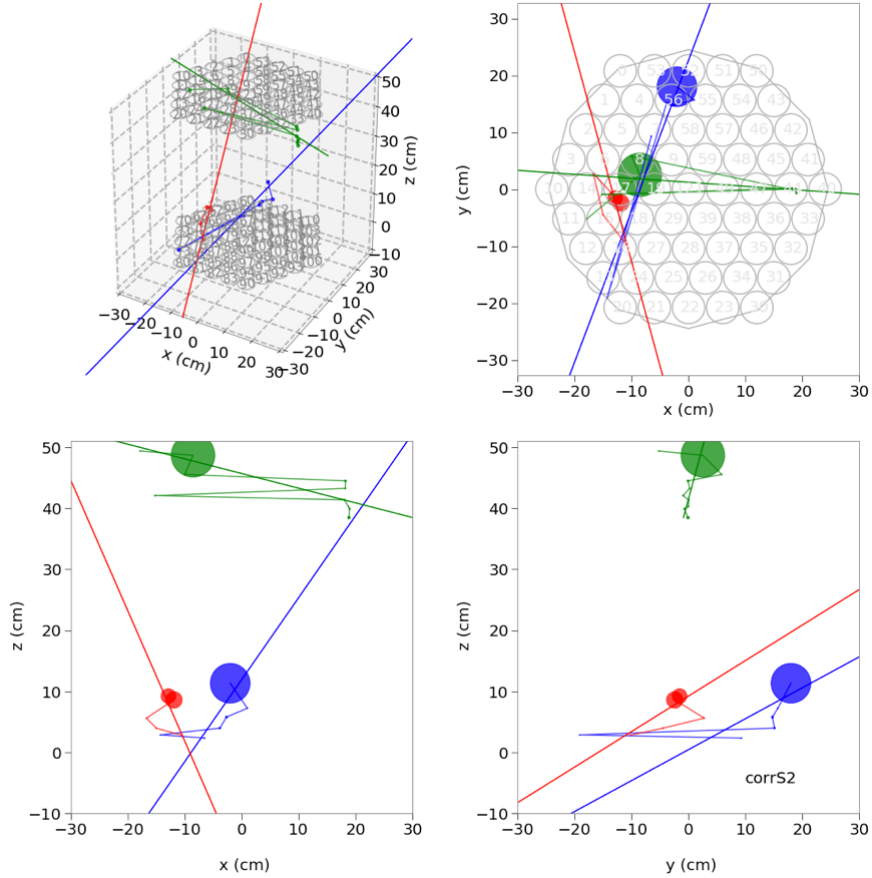


Figure 73: An example of a few electron train events that led to reconstructed tracks. Different colors indicate different events. All of the 2D plots are displayed with the marker sizes scaled as pulse area. All of these events had a  $\chi^2$  between 1.2 and 2.0. An eventual cut was applied that required  $0 < \chi^2 < 1$ , so these particular events would not have made the track reconstruction cut.

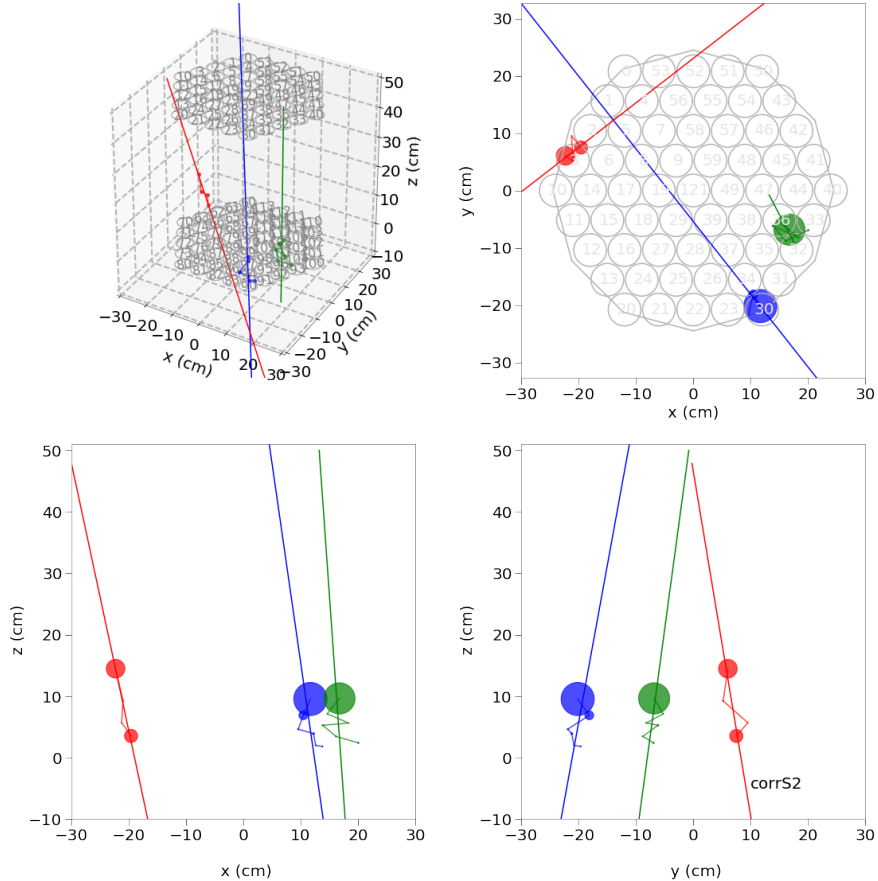


Figure 74: An example of a few electron train events that led to reconstructed tracks. Different colors indicate different events. All of the 2D plots are displayed with the marker sizes scaled as pulse area. All of these events had a  $\chi^2 < 1.0$ . An eventual cut was applied that required  $0 < \chi^2 < 1$ , so these particular events would pass the track reconstruction cut. However, they do not subtend the entire detector, which we require of LIPs.

## 5.5 LIP SEARCH ANALYSIS

This section describes the analysis steps to yield a limit on the vertical flux of [LIPs](#) observed by [LUX](#) detector. The main [LIP](#) background comes from delayed electron noise phenomena. Chapter 8 summarizes the current understanding these electron noise phenomena and describes a recent study that found two distinct time scales present in electron trains. While we are getting closer to understanding the sources of electron noise, it was not extensively characterized or modeled in simulation by the [LUX](#) collaboration. Therefore, the [LIP](#) search lacks a background model, although a background is known to exist. The approach taken in the analysis is to develop a signal region, i.e. develop cuts with [LIP Filter RQs](#) that select [LIPs](#) while rejecting electron noise, by looking at real [LUX](#) data. In order to avoid biasing in the cuts, only a limited amount of live data is used during cut development. This test data was not used in the final limit analysis.

### 5.5.1 RUN03 DATASET

The analysis carried out in this section only uses about 1 month of Run03 data, with acquisitions dated from 2013-05-15 to 2013-05-31. Acquisitions within this timeframe were reprocessed using the default [LUX DPF](#) settings, but the number of pulses that could be found in an event was increased from 10 to 100. The total available livetime is 341.03 hours. The first 13 acquisitions, amounting to 62.56 hours, or approximately 20% of the available data was used to develop cuts. The cuts were then carried out on the remaining approximately 80% of the data to produce a limit on the vertical flux of [LIPs](#).

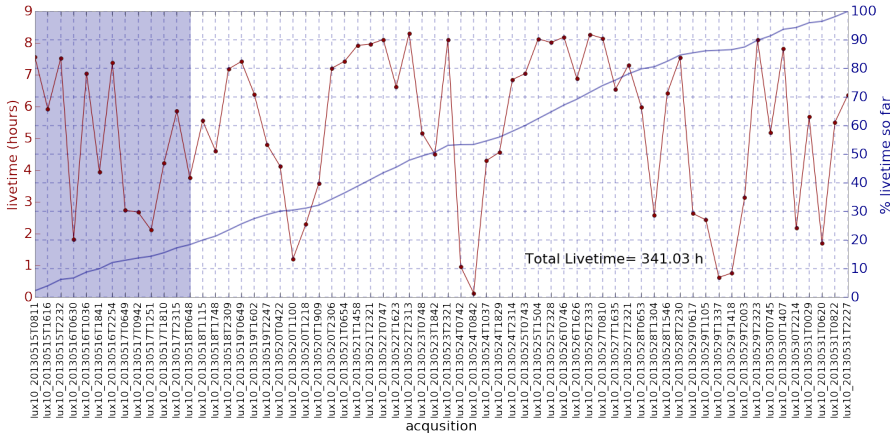


**Figure 75:** Acquisitions from Run03 that were reprocessed, allowing 100 pulses to be found instead of the usual 10. The livetime of each acquisition is indicated in red, while the cumulative percentage of the available livetime is in blue.

### 5.5.2 LIP SIGNAL REGION

The strategy for developing the **LIP** signal region cuts was to run both the **LIP** simulation and 20% of the available **LUX** data through the filter. **RQs** produced by the filter were plotted side by side for **LIPs** and data. If the **LIP** plot displayed a somewhat compact region of signal, a loose cut was defined by the region of signal, and the cut was applied to both **LIP** and data. Subsequent cuts on another **RQs** were developed similarly, and additional **RQs** were developed and tested similarly. Before applying a new cut, data events remaining in the **LIP** signal regional were investigated to both assure they were not in fact **LIPs** and to assess what additional cuts could be applied to eliminate the data event. Cuts were applied to both **LIP** simulations and the 20% subset of the data until no data events remained in the signal region. The efficiency for each charge fraction after all the cuts were applied to the **LIP** simulation is taken to be the detection efficiency. Systematic factors affecting the efficiency are discussed in the next section, the remainder of this section shows the cuts. Each cut is illustrated with **LIP** simulation on the left and data on the right.

The first cut applied is the requirement that there are more than 4 corrected S2 pulses found in the event. That is, there are 4 S2s which had successful Mercury position reconstruction, and both pulse area and position corrections were applied. The number of corrected S2 pulses is shown against the sum of all (raw) pulse area in Figure 77. This cut yields one of the largest losses in efficiency because there was no restriction placed on the **LIP** tracks that were injected into LUXSim; there are a number of events that clip the corners of the detector, and do not have

a long enough path length to produce the required number of S2 pulses. Had such a cut been placed on the injected LIP tracks, it would have been accounted for in the calculation of  $\Omega$ ; instead it is accounted for at this step. See Figure 76 for the expected rate of good S2 pulses as a function of charge fraction. For this plot, the flux is assumed to be  $\Phi = 1/\text{LUX}/\text{day}$  for all charge fractions and an overall drop from, e.g. corner clipping events is visible.

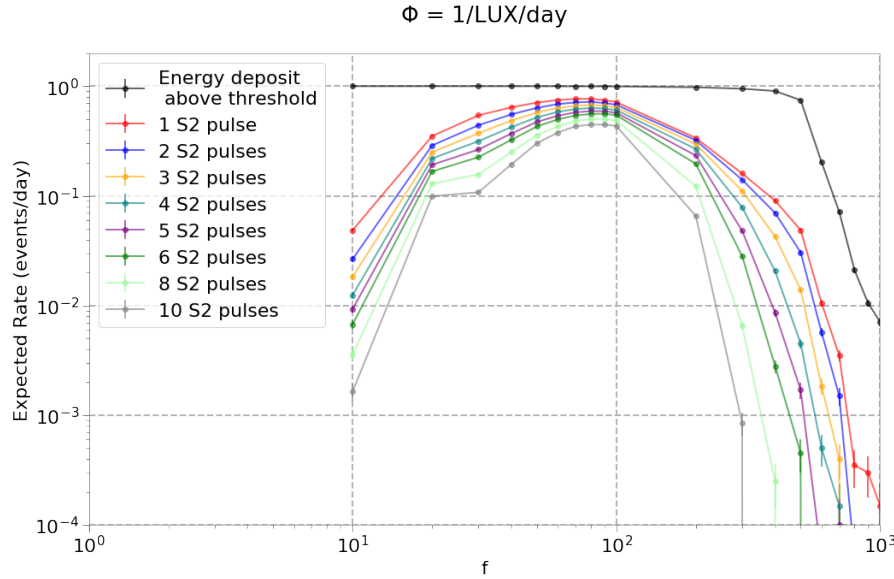


Figure 76: A plot of the expected rate of number of S2 pulses as a function of charge fraction. The flux for all charge fractions is assumed to be  $\Phi = 1/\text{LUX}/\text{day}$ . As the charge fraction increases, the expected rate of events (black) decreases because only some events will deposit enough energy to be above threshold to trigger the detector. The fall-off is more severe when a certain number of well-reconstructed S2 pulses is required.

The second cut applied is the requirement that  $0 < \chi^2/\text{dof} < 1$ . The  $\chi^2$  used for the track fit is shown in Equation 53, and only S2s with successful Mercury reconstruction and position corrections are used in the track fit. This cut is shown in Figure 78. The third cut is a measure of whether the track subtends the entire data. The distance from the first corrected S2 position to the last corrected S2 position ( $L_{\text{data}}$ ) is compared to the reconstructed track length from the fit ( $L_{\text{fit}}$ ). We require  $L_{\text{fit}}/L_{\text{data}} \approx 1$ . Since there is no guarantee that the LIP deposits enough energy immediately upon entering the xenon space to produce an S2,  $L_{\text{data}}$  is likely always less than  $L_{\text{fit}}$ ; this is why the cut is shifted to the right instead of being centered around 1.0. This cut is shown in Figure 79. The fourth cut is a requirement that the energy depositions not vary widely as the over-

all energy deposition increases. The logarithm of the standard deviation in corrected S2 area is plotted versus the reconstructed S2 energy deposition per fit track length. This cut is shown in Figure 80. The fifth cut, shown in Figure 81, plots the logarithm of the standard deviation of the S2 areas versus the first two S2 pulse areas divided by the last two S2 pulse areas. For LIPs, it is expected that the first two S2 areas are nearly identical in size to the last two S2 areas; background events show much bigger or smaller ratios, along with larger or smaller standard deviation of the S2 pulse areas. The sixth cut, shown in Figure 82, requires that the incident polar angle be greater than 20 degrees. A common background pathology is an event with a raised baseline in one or a small clustered group of PMTs, along with an electron train. This background reconstructs as a vertical-going LIP track. Since the acceptance of LUX for vertical-going LIPs is small, we can place a cut on incident polar angle without losing a large fraction of LIP events. The seventh cut, shown in Figure 83, is similar to the LUX “bad area cut.” The usual LUX bad area cut is a limit on the amount of pulse area in an event that is not in S2 pulses – this cuts events with a lot of electron noise. In the LIP analysis, an S1-normalized bad area cut is placed, by plotting the raw S2 area divided by S1 area versus the corrected S2 area divided by S1 area. The ratio should be approximately 1:1 for good LIP events; however, an efficiency loss for  $f$  from about 10-50 is observed, as these events have a fair amount of area partitioned in raw S2 pulses which failed Mercury reconstruction. The efficiency is already poor for this range of charge fraction, so the loss of these events is not dramatic. Note that this cut doesn’t place a requirement on the number of Else or SE in the event, which the usual LUX bad area cut does. The eighth cut, shown in Figure 84, is a cut on the standard deviation between successive points on the LIP track. The stochastic straggling and the pulse finder cause variation in the distances between the LIP energy depositions, so some spread is expected. A common background pathology was an S2 on one side of the detector, and some electron noise occurring on the other side of the detector. Placing a cut on standard deviation of the point distances was robust in eliminating these backgrounds. The ninth and tenth cuts are both shown in Figure 85. A restriction is placed on the Anderson-Darling test statistic and also on the amount of area allowed in the event before the first S1. The former requires an Landau-like energy straggling and the latter is effective in cutting electron noise events.

The efficiency for each cut applied subsequently is shown in Figure 86, as a function of  $f$ . The same cut was applied to each charge fraction, but efficiencies were calculated separately. The error bars shown are the statistical Poisson errors of how many events were within the cut region.

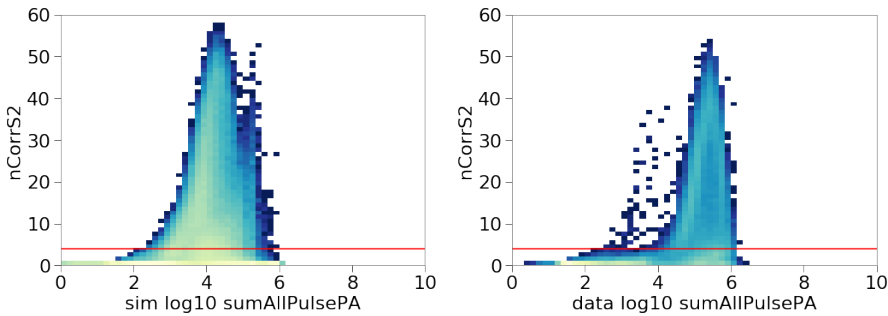


Figure 77: A 2D histogram of number of corrected S2 pulses versus the sum of all pulse area in the event. A cut is placed requiring the number of S2 pulses to be greater than 4. Only the first acquisition, lux10\_20130515T0811\_cp26812, is plotted for the demonstration.

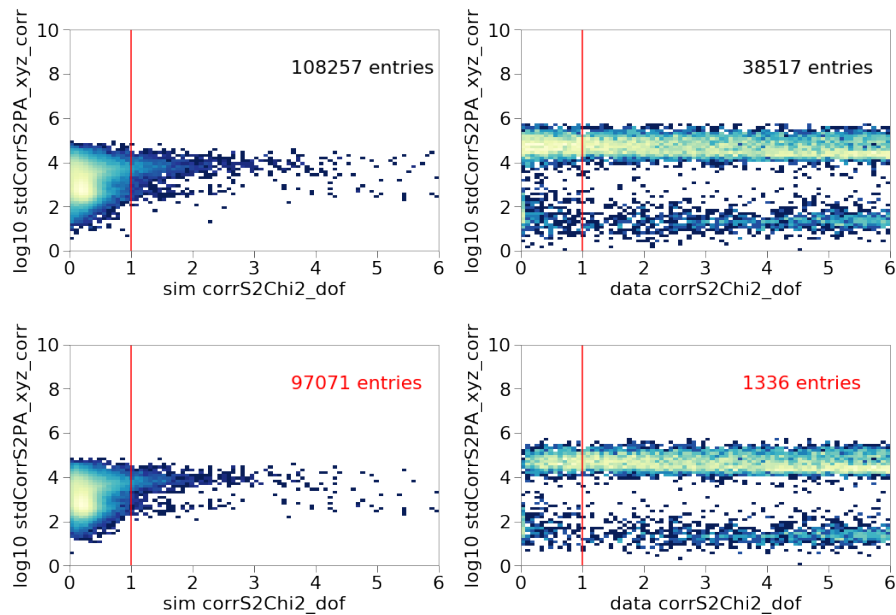


Figure 78: A 2D histogram of the standard deviation of the corrected S2 pulse area versus the  $\chi^2/dof$  from the track fit. A cut is placed requiring  $0 < \chi^2/dof < 1$ . The top plots are shown with no cuts, the bottom plots are shown with the previous cut applied, the counts in red indicate how many events will be left after this cut. Only the first acquisition is plotted for the demonstration, all LIP charge fractions are shown.

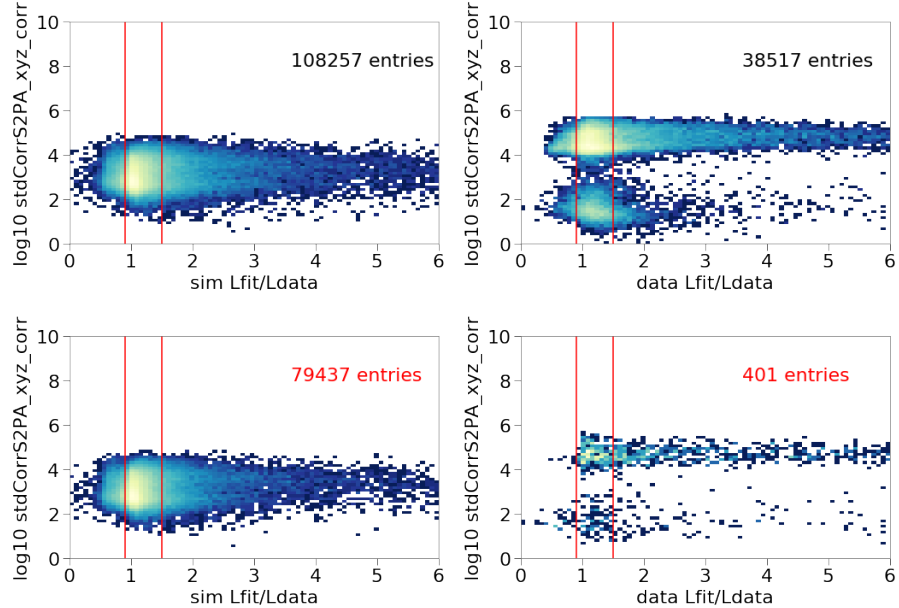


Figure 79: A 2D histogram of the standard deviation of the corrected S2 pulse area versus the fit length divided by the “data length”. The fit length  $L_{fit}$  is the reconstructed track length. The data length  $L_{data}$  is defined as the distance between the first and last (corrected) S2 positions. The factor  $L_{fit}/L_{data}$  is a measure of whether the event subtends the detector. A cut is placed requiring  $0.9 < L_{fit}/L_{data} < 1.5$ . In general  $L_{fit}$  is expected to be larger than  $L_{data}$ , as the LIP may travel some distance into the LXe before depositing energy. The top plots are shown with no cuts, the bottom plots are shown with the previous cut applied, the counts in red indicate how many events will be left after this cut. Only the first acquisition is plotted for the demonstration, all LIP charge fractions are shown.

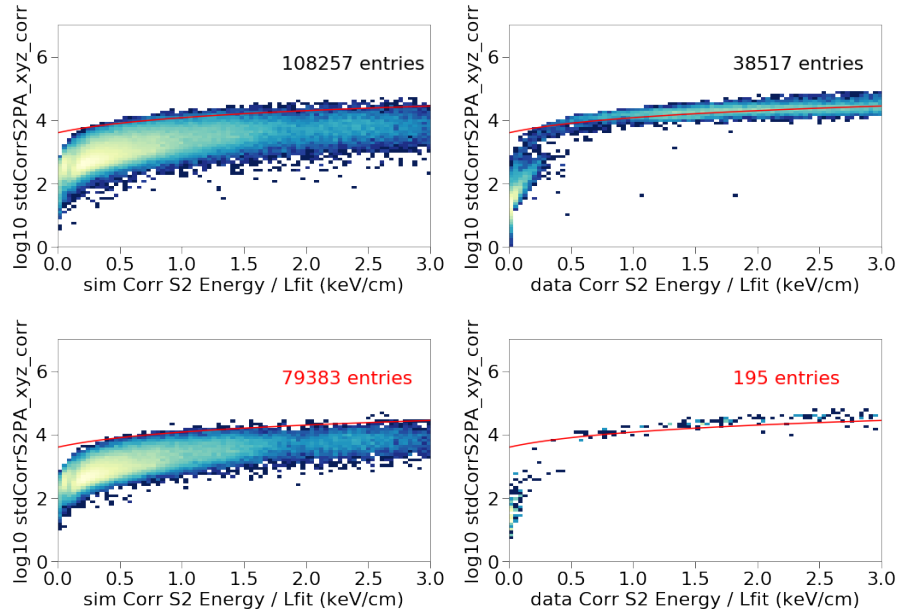


Figure 80: A 2D histogram of the standard deviation of the corrected S2 pulse area versus the corrected S2 energy divided by  $L_{fit}$ . The S2 energy is reconstructed using  $E_{S2} = W(S2/g2)$ . The top plots are shown with no cuts, the bottom plots are shown with the previous cut applied, the counts in red indicate how many events will be left after this cut. Only the first acquisition is plotted for the demonstration, all LIP charge fractions are shown.

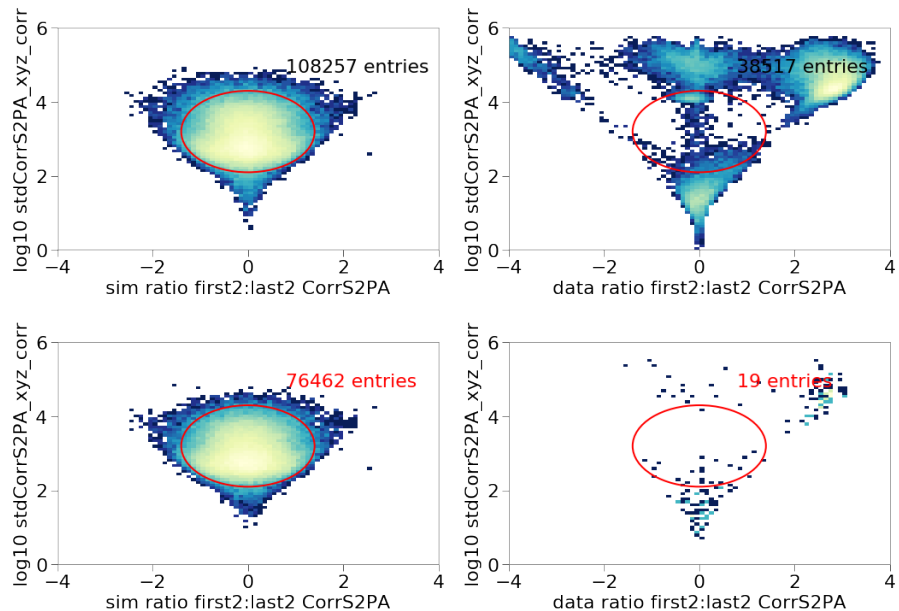


Figure 81: A 2D histogram of the standard deviation of the corrected S2 pulse area versus the ratio of the first 2 to the last 2 area corrected S2 pulses. A cut using the ellipse shown is applied. The top plots are shown with no cuts, the bottom plots are shown with the previous cut applied, the counts in red indicate how many events will be left after this cut. Only the first acquisition is plotted for the demonstration, all LIP charge fractions are shown.

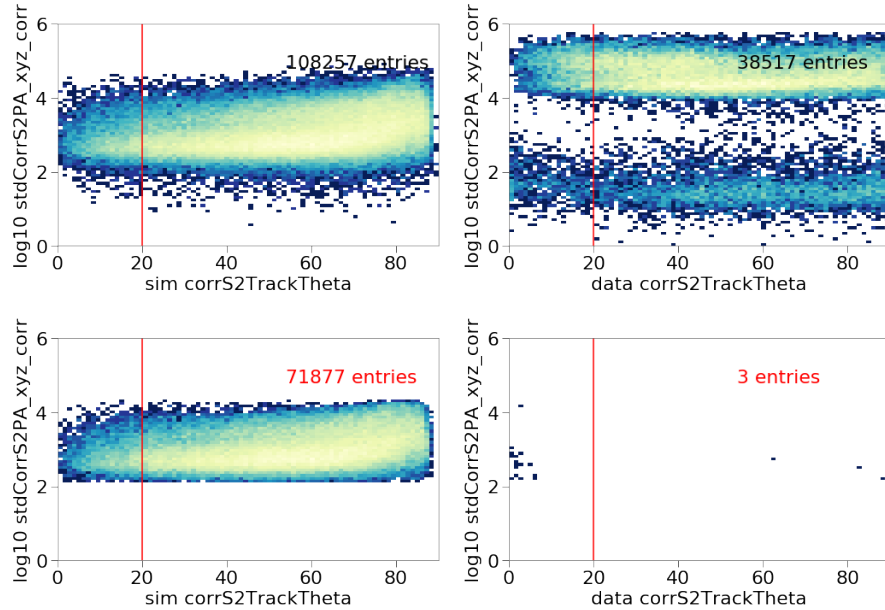


Figure 82: A 2D histogram of the standard deviation of the corrected S2 pulse area versus the reconstructed polar angle of the track. A cut requiring  $\theta > 20$  deg is placed because a disproportionate number of the background electron train events appear as vertical-going LIPs. The true acceptance for LIPs is very limited at small polar angles, so a cut on the entry angle does not result on a large loss of signal efficiency (see Figure 61). The top plots are shown with no cuts, the bottom plots are shown with the previous cut applied, the counts in red indicate how many events will be left after this cut. Only the first acquisition is plotted for the demonstration, all LIP charge fractions are shown.

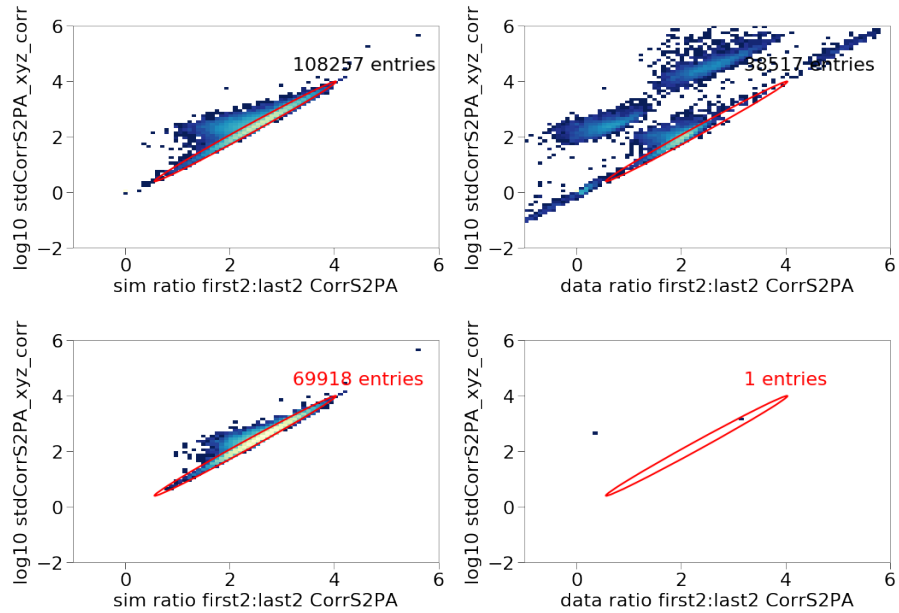


Figure 83: A 2D histogram of the raw S2 pulse area normalized to the first S1 area versus corrected S2 pulse area normalized to the first S1 area. A cut requiring events to be inside the indicated ellipse is applied. This is essentially an “S1-normalized” bad area cut, requiring that the pulse area in the event mostly goes into S2 area that has successful position reconstruction. The area that is being cut in the [LIP](#) plot is loss in lower  $f$ , where some area is partitioned into raw S2. The top plots are shown with no cuts, the bottom plots are shown with the previous cut applied, the counts in red indicate how many events will be left after this cut. Only the first acquisition is plotted for the demonstration, all [LIP](#) charge fractions are shown.

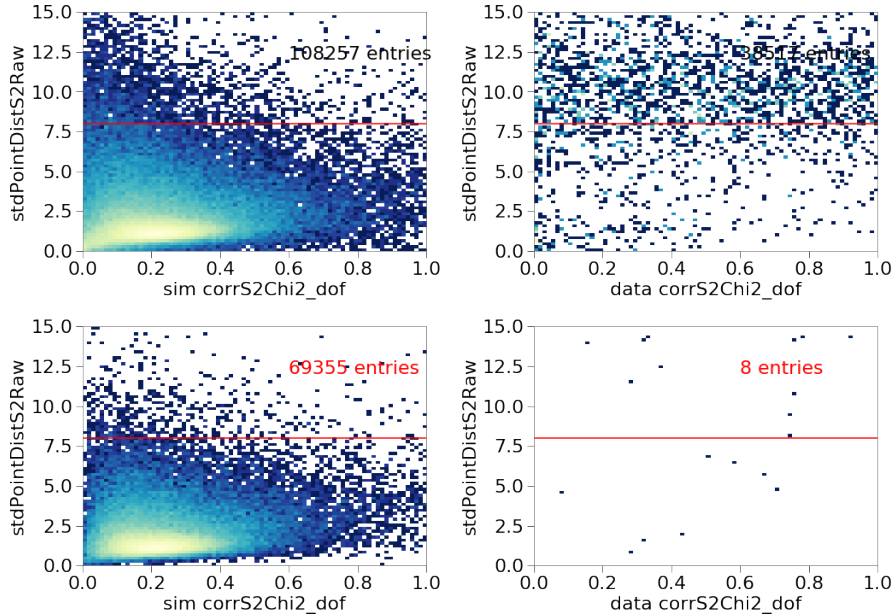


Figure 84: A 2D histogram of the standard deviation of distances between the raw positions of S2s in an event versus the  $\chi^2/dof$ . A cut requiring the standard deviation between points to be less than 8 cm is applied. The top plots are shown with no cuts, the bottom plots are shown with the previous cut applied, the counts in red indicate how many events will be left after this cut. The top data plot shows only the first acquisition. The bottom data plot shows the remaining events in the first 13 acquisitions after previous cuts were applied. All LIP charge fractions are shown.

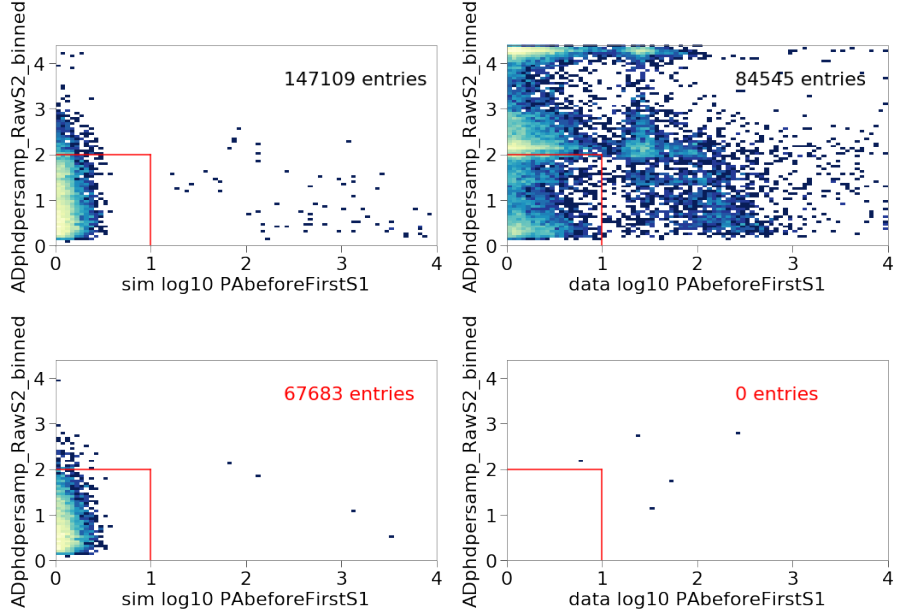


Figure 85: A 2D histogram of the Anderson-Darling test statistic versus the sum of the area before the first S1. A cut is placed requiring the Anderson-Darling test statistic to be less than 2 and the area before the first S1 to fall between 0 phd and 10 phd, inclusive. The x-axis actually shows  $\log_{10}$  of the pre-S1 area, so all events with zero area before the S1 are not shown on the plot; however, these events are retained in the cut. The top plots are shown with no cuts, the bottom plots are shown with the previous cut applied, the counts in red indicate how many events will be left after this cut. The top data plot shows only the first acquisition. The bottom data plot shows the remaining events in the first 13 acquisitions after previous cuts were applied. All LIP charge fractions are shown.

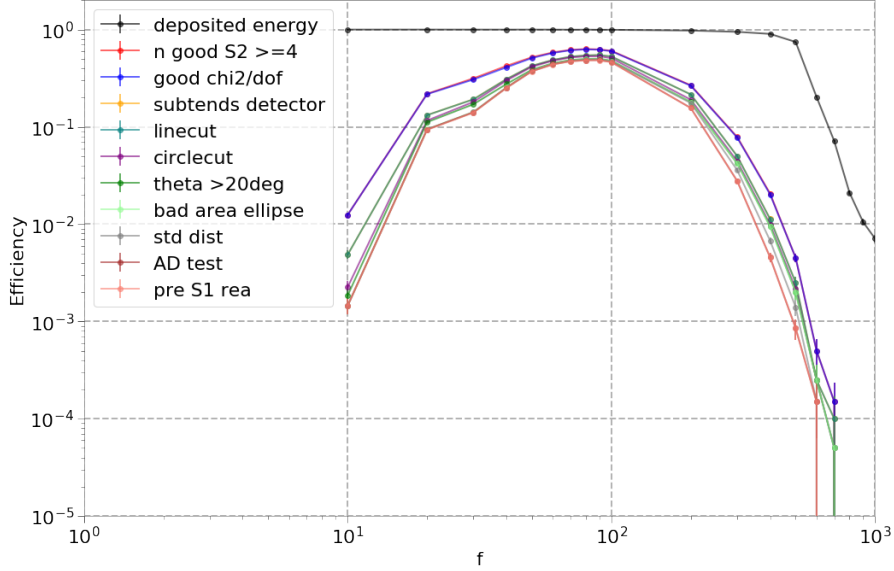


Figure 86: The efficiencies for each subsequent cut as a function of charge fraction. The detection efficiency is taken to be the logical and of all the cuts.

### 5.5.3 SYSTEMATIC ERRORS

The base 1D straggling Monte Carlo was found to result in a measure of average energy deposition  $\langle dE/dx \rangle$  13% less for charge fraction  $f = 1$  than the value given for the muon in [106] (see Figure 59). Since the detection efficiency depends heavily on track properties and not total energy deposition, the effect is expected to be small. The difference in energy deposition between two neighboring charge fractions far outweighs a 13% increase to  $\langle dE/dx \rangle$ . However, the underestimation of energy deposition is a known issue, and so it was investigated.

In order to assess the effect of the 13% underestimation of  $\langle dE/dx \rangle$  on the detection (cut) efficiency, all of the cut variables were histogrammed as a function of reconstructed energy per reconstructed path length,  $E/L$ . Corrected areas were used in the energy reconstruction, and path length was obtained from a fit to the corrected position variables. Any cuts in two dimensions were translated into a one dimensional cut variable. For example, the ellipse regions in Figure 81 and Figure 80, were translated into the ellipse coordinates and normalized to the ellipse radius. In this manner, the cut becomes a simple one dimensional  $r \leq 1$  cut instead of a 2D cut depending on two variables. An example of the  $\chi^2$  variable versus  $E/L$  (the stand-in for  $dE/dx$ ) is shown in Figure 87.

Histograms were constructed for each charge fraction and for all cuts discussed in the previous section, with the cut variable on the y-axis and

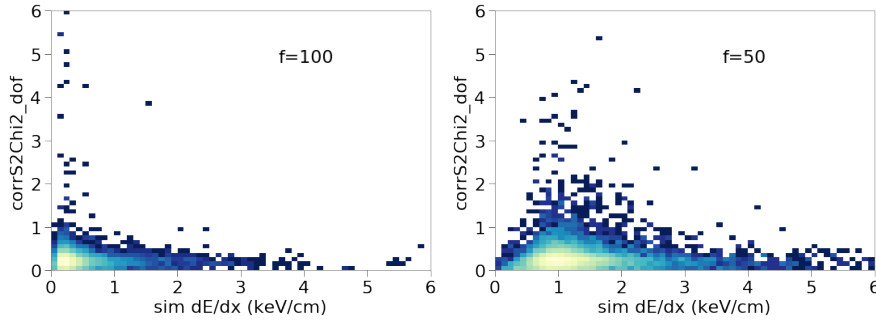


Figure 87: Two examples of the  $\chi^2/dof$  dependence on  $dE/dx$ . The plots show the  $\chi^2/dof$  versus the reconstructed  $E/L$  for two different charge fractions.

$E/L$  on the x-axis. The  $E/L$  for each event was multiplied by a factor of 1.13, and the corresponding x-bin for this new shifted value was identified. The x-bins were not actually the equal bins shown in Figure 87, rather they were determined on the requirement that 5% of the  $E/L$  values were in each x-bin (see Figure 88). Then, the y-values of the cut variable for the shifted  $E/L$  bin were sampled without replacement to construct a new histogram of the cut variable versus the shifted  $E/L$  (see Figure 89 for an example of the original and  $E/L$ -shifted distributions for  $f = 100$ ). The cut was applied to the new cut variable versus  $E/L$ -shifted distribution, and the efficiency was calculated. This procedure was done 100 times for each charge fraction. The resulting efficiencies for each cut are shown in Figure 90, where the central value is mean efficiency of the 100 trials, and the error bars are the standard deviation of efficiencies obtained from the 100 trials. This procedure was a good way to get a sense of the scale of the systematic error from placing hand-drawn cuts on populations with a known underestimation of energy, but its physical accuracy is questionable. It is unreliable to set our actual efficiency measurements to the mean of the 100 trials, but the systematic errors from this procedure is used in the limit setting.

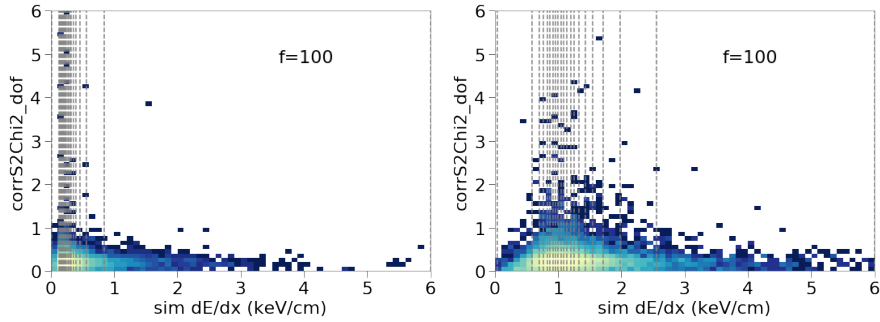


Figure 88: Examples of the 5% bins used in the sampling procedure to asses the systematic error are overlaid (gray dotted lines) on histograms of  $\chi^2/dof$  versus the reconstructed  $E/L$  for two different charge fractions.

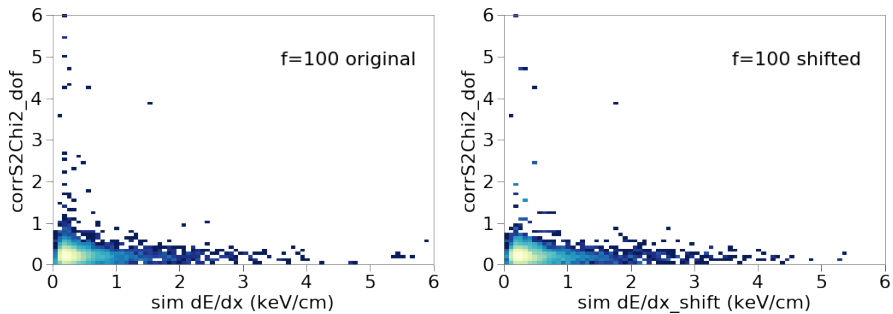


Figure 89: (left)  $\chi^2/dof$  versus  $E/L$  for  $f = 100$ . (right) The resampled  $\chi^2/dof$  distribution versus  $E/L$  after shifting the original  $E/L$  by a factor of 1.13.

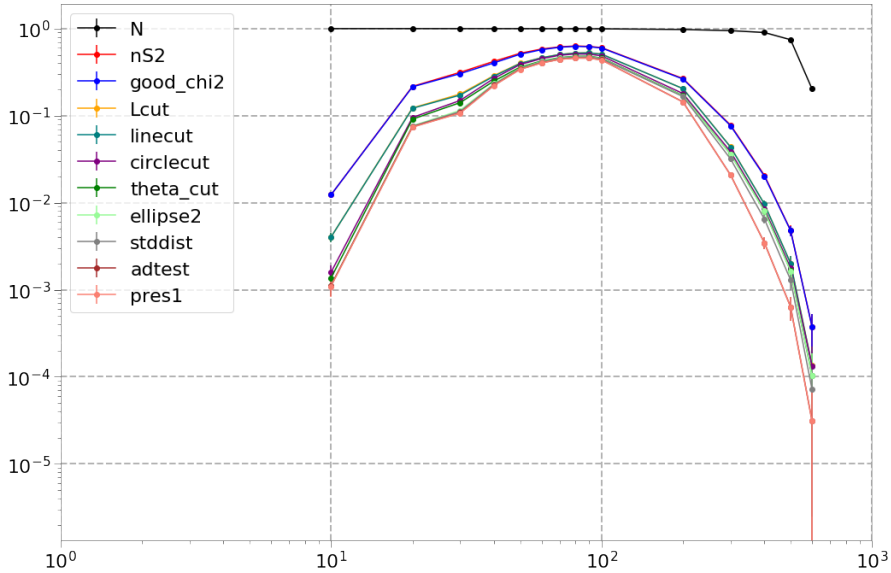


Figure 90: The systematic efficiencies of each subsequent fit.

## 5.6 RESULT: VERTICAL FLUX LIMIT

The detection efficiency is taken to be the efficiency after all cuts as in Figure 86. The procedure described in the previous section was used to obtain systematic errors. The systematic and statistical errors are added in quadrature. The first 13 acquisitions listed in Figure 75 (approximately 20% of the available data) were used for cut development. Cuts were added until there are no data events in the [LIP](#) signal region. The cuts were then carried out on the remaining 80% of the data, with an expectation of zero background. After cuts were complete, there were zero events remaining in the signal region. Therefore, we apply the Feldman-Cousins procedure for a zero signal, zero background outcome [118]. The vertical flux limit is shown in Figure 91.

## 5.7 DISCUSSION

The flux limit presented in Figure 91 is the first of its kind from an [LXe TPC](#). The range of charges probed is similar to that investigated by modern low-background cryogenic Ge detectors, but the challenges of the analysis are very different due to the phenomenon of delayed electron noise, which is the dominant background for this search. Delayed electron noise along with small energy depositions decreased the efficiency for high  $f$ . Charge fractions  $f > 700$  deposited so little energy in the [TPC](#), that the ionization signals were not S2, but single electrons. Since

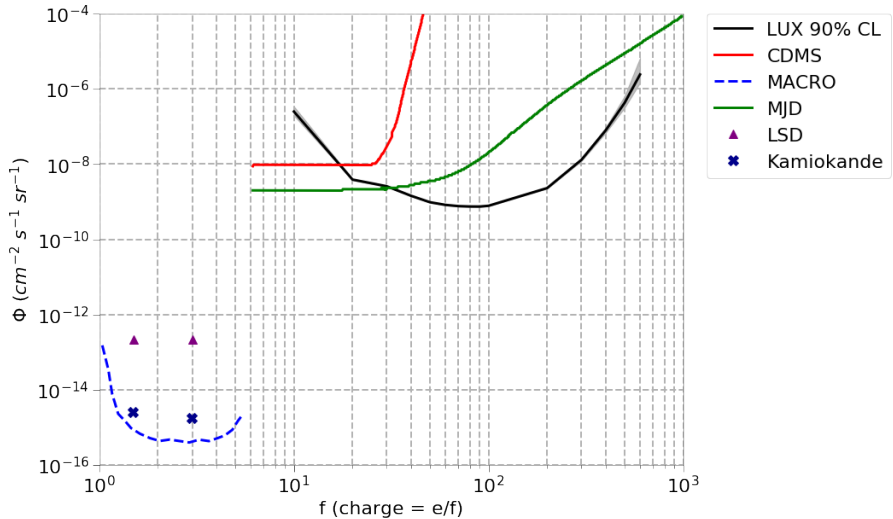


Figure 91: The vertical flux limit from 278.47 hours of livetime during [LUX](#) Run03 compared to other recent flux limits. The result of this analysis is shown in black, with grey bands indicating the combined statistical and systematic error on detection efficiency.

delayed electron noise is known to continue for  $O(100)$  ms, polluting subsequent events, the choice was made to require an ionization signal analysis threshold of 4 S2 pulses in an event, and reject the event if only SE ionization signals were present. Future searches could leverage better understanding of delayed electron noise and dedicated modeling and simulation of these backgrounds to extend the range of [LIP](#) searches to higher  $f$ . On the other side, low  $f$  events were found to deposit so much energy, creating ionization trails, that the standard data processing failed to isolate individual pulses. A modified version of data processing that, instead of attempting to find pulses, chops ionization trails into a fixed number of segments and performs the usual position and energy reconstruction on the enforced segments, would open up lower  $f$  parameter space to [LXe](#) detectors.

### PART III

## LITTLE SCIENCE

This section describes research with a small test bed at Lawrence Berkeley National Lab. The details of test bed construction and operation are discussed, with particular attention to construction of high voltage feed throughs. Two studies affecting the sensitivity of future LXe TPCs are described. One study investigates the solubility of radon daughters, and another furthers understanding of delayed electron noise phenomena.

# 6

## RESEARCH AND DEVELOPMENT TESTBED FOR FUTURE LIQUID XENON TPCS

---

*All systems go, are you sure?*

— Peter Schilling *Major Tom, 1969*

A small test bed was built at Lawrence Berkeley National Laboratory to study various detector effects facing large [LXe TPCs](#). The test bed was built and instrumented over the course of about two years, from 2015 through 2016. This chapter describes some of the details of that instrumentation.

### 6.1 TEST BED APPARATUS OVERVIEW

A large-scale overview of the testbed is shown in Figure 92, and a diagram of the inner experimental vessel is shown in Figure 93. The experimental apparatus consisted of an inner vessel, a vacuum outer vessel, and a xenon circulation system. The inner vessel was a Stainless Steel ([SS](#)) canister, topped with a 2.75 in Conflat-adaptable tower that allowed space for instrumentation cabling and [HV](#) feedthroughs. The inner vessel was offset below a 7.09 in ISO K flange, which held the (removable) vacuum outer vessel in place. Several Mini-CF ports were welded to the ISO K flange for instrumentation cabling. A Liquid Nitrogen ([LN](#)) reservoir was thermally connected to the cold-head. A half-inch pipe opened into the bottom of the reservoir, which was offset above the ISO-K flange; this allowed [LN](#) to flow into the pipe. The bottom of the pipe was connected to the cold-head via braided copper wire. A Swagelock vacuum fitting sealed the lower-half of the pipe into the outer vacuum space.

The inner vessel contained the [TPC](#). A [PTFE](#) housing cylinder fastened a [PMT](#) in place. Above the [PTFE](#) housing, a series of interlocking [PTFE](#) rings held strung wire grids and a segmented anode in place. During data taking, the entire [PMT](#) and housing were immersed in [LXe](#). The liquid level was chosen depending on the experiment being performed, and was approximated by the S2 width. In some cases, the [TPC](#) was “overfilled” by allowing the liquid level to rise above the anode. The segmented anode was instrumented with charge amplifiers for direct charge readout. When

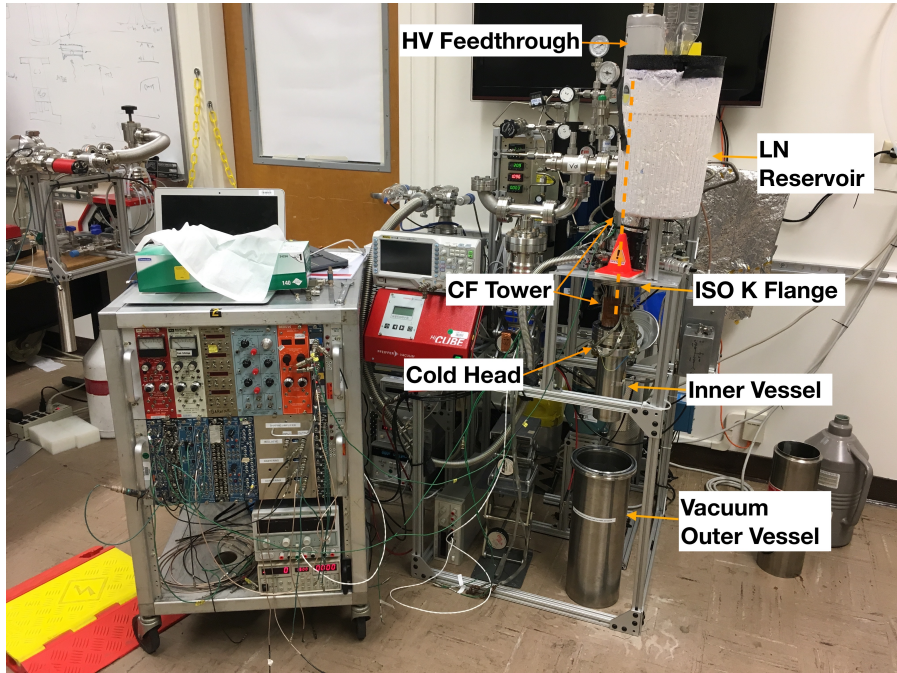


Figure 92: Large scale view of the experimental apparatus showing key parts.  
The **CF** tower extent is indicated with a dotted line; this whole tower  
is also part of the inner xenon space.

the **TPC** was overfilled, the charge amplifiers detected the ionization electrons directly from the liquid. During typical dual phase **TPC** operation, the charge amplifiers provided a secondary measurement of the ionization electrons in addition to S2. Two typical arrangements of the inner vessel are shown in Figure 93.

## 6.2 CIRCULATION SYSTEM

The xenon circulation system is shown in Figure 94. A stainless steel capillary extending into the liquid drew xenon from the inner vessel during operation to be purified. Purified xenon that was returned to the vessel was directed into the liquid via a **PTFE** tube so it could condense quickly. A gas purge from a Conflat (**CF**) tower above the inner vessel could be opened to continually renew the gas column.

## 6.3 SLOW CONTROL

The slow control for the test bed consists of a few monitoring variables such as temperature and pressure and a voltage supply that switches re-

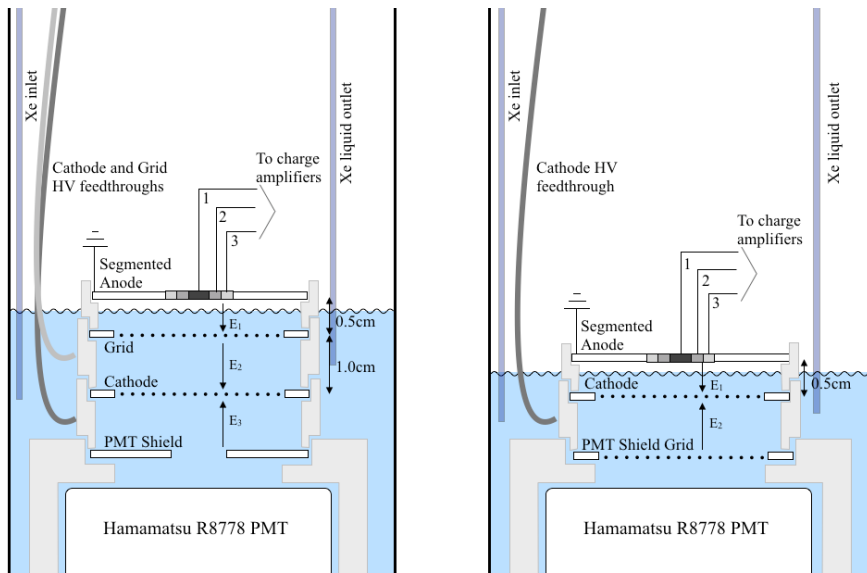


Figure 93: Diagrams of two often used internal arrangements. The configuration (left) has both a drift and extraction region. The configuration (right) is “extraction region only”. The blue region with the wavy line indicates the liquid level.

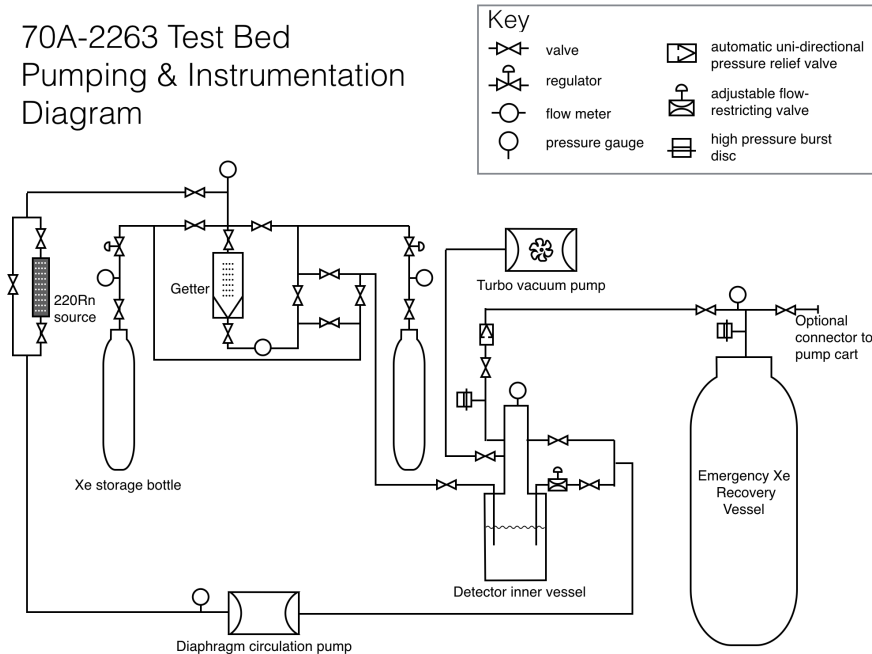


Figure 94: Pumping and instrumentation diagram of the test bed. Special symbols are labelled in the diagram, see key for other symbols. For readability, all gauges are not shown.

sistive heaters on/off. The inner experimental vessel was instrumented with two platinum Resistance Temperature Detector (RTD)s to monitor temperature and a capacitance manometer to monitor pressure. A flow meter in the circulation line determined the flow rate of xenon as it passed through the getter and returned to the inner vessel. These four variables were read using Omega i-series digital panel meters to provide a real-time display; two points of calibration were provided to the digital panel meters to translate voltage to human-readable pressure, temperature, etc. In addition, two  $25\ \Omega$  resistors are mounted, in parallel, on the cold-head. Supplying voltage to these resistors raised the temperature of the cold-head and decreased the cooling power delivered by the liquid nitrogen bath; the voltage supplied to the heaters was also recorded, but not shown with digital panel meters. The voltages for the monitoring variables and the heater voltages were fed into a USB Device from Measurement Computing, which interfaces with a computer. A slow control script on a lab computer recorded the monitoring variables and heater voltages. The script also determined if power should be supplied to the heaters and if text message and e-mail alarms should be sent for a variable out of expected range. A basic schematic of the slow control is shown in Figure 95.

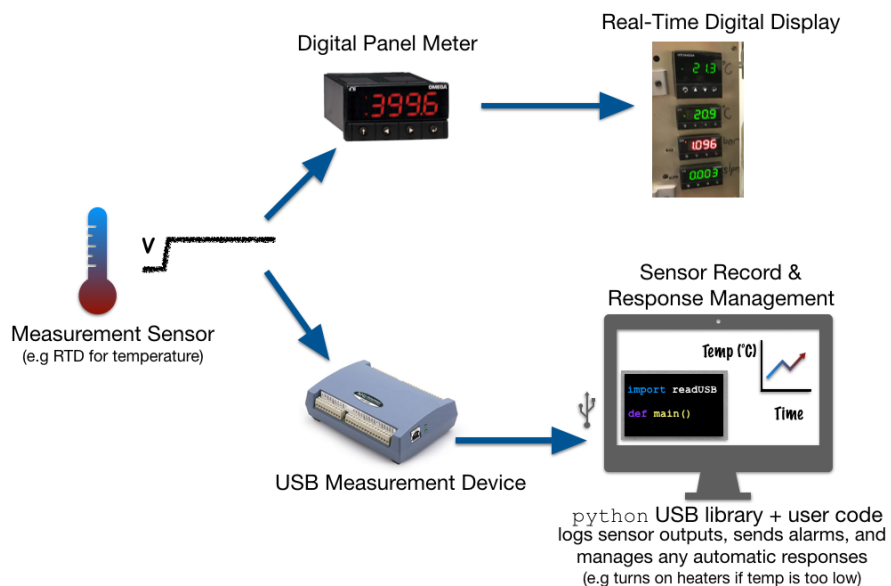


Figure 95: A diagram showing components of the slow control.

## 6.4 PMT

The test bed was instrumented with a Hammamatsu R8778 PMT, the same model of PMT used in LUX. A LUX PMT base was used and an LZ PMT base

was tested. The radon daughters study presented in Chapter 7 exclusively used the LUX PMT base; the electron trains studies presented in Chapter 8 first used the LUX base, and later used the LZ base. Various shaping amplifiers were used when digitizing the PMT over the course of these studies because the 8 ns sampling interval of the data acquisition was subject to aliasing the fast-rising alpha S1 signals.

## 6.5 CHARGE AMPLIFIERS

The TPC diagram in Figure 93 includes a segmented anode, the largest segment of which is held at ground. The anode is pictured in Figure 96 and relevant dimensions are included in Table 3.



Figure 96: (left) Segmented anode showing the xenon-facing anode segments.

The innermost segment is referred to as the “bullseye”, the next is called the “inner ring” and the last is called the “outer ring”. The largest segment on the anode was not instrumented with charge amplifiers and was held at ground. (right) The wires on the top of the anode which lead to the charge amplifiers.

Anode Segments	1	2	3	Full
Radius (mm)	3	6	9	24
Cumulative Area (mm <sup>2</sup> )	28	113	255	1810

Table 3: Dimensions of the of the anode segments. 1 refers to the inner-most segment or “bullseye”, 2 refers to the inner ring, 3 to the outer ring and full to the entire anode, which includes inactive area that is not instrumented with charge amplifiers.

The segmented anode was instrumented with three CR-110 charge amplifiers from Cremat (Figure 97). The raw charge amplifier signals were

each fed into a CR-160-R7 shaper evaluation board, also from Cremat. The evaluation board houses two more modules: one CR-200-X shaping amplifier and one CR-110 baseline restorer. The CR-200-X shaping amplifier is an  $X-\mu\text{s}$  gaussian shaping amplifier; it was determined that  $1 \mu\text{s}$  was most appropriate for the test bed signals, based on the size of the gas gap and the expected event rate.

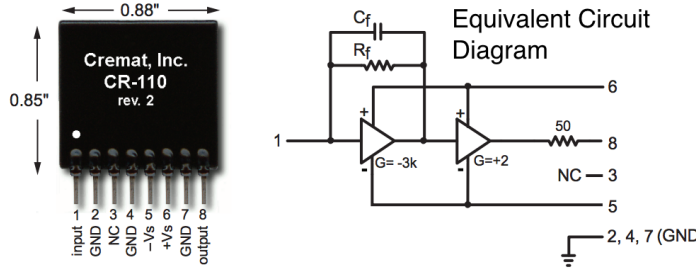


Figure 97: A picture of the CR-110 charge amplifier from the manufacturer's data sheet, shown with an equivalent circuit diagram.

The shaper evaluation board produced gaussian pulses from raw charge signals as shown in Figure 98.

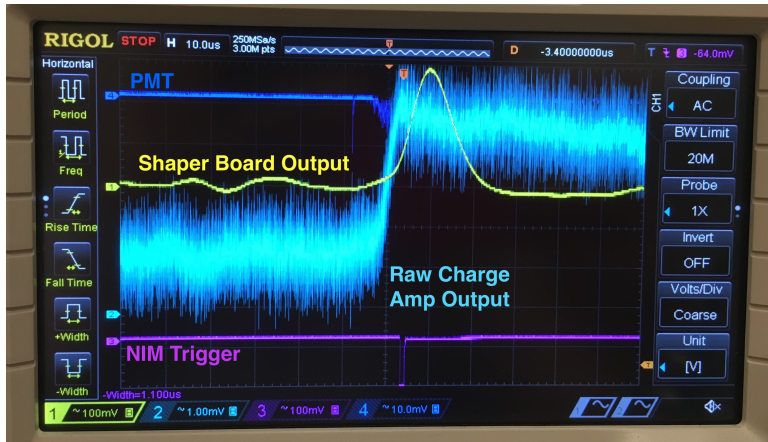


Figure 98: A raw (cyan) and shaped (yellow) charge amp signal taken in  $-100\text{C}$  gaseous xenon, with the radon source plumbed in. The PMT signal is visible in blue and the NIM trigger signal is in magenta.

The charge amplifiers were originally placed inside the experimental vessel, mounted directly on the segmented anode. The functionality of the CR-110 units in LXe conditions did not deviate from manufacturer's

specifications<sup>1</sup>, however it was found that the units generated enough heat to create a perpetual gas layer under the anode. In general this is not an issue, but for the purpose of the intended absolute electron extraction efficiency measurement, overfilling the TPC and using the charge amplifiers as a direct read-out of electrons in the liquid was required. The charge amplifiers were moved to the outer vessel space, surrounded by a small Faraday cage made of copper mesh. See Figure 99 for the charge amplifier mounting configurations.

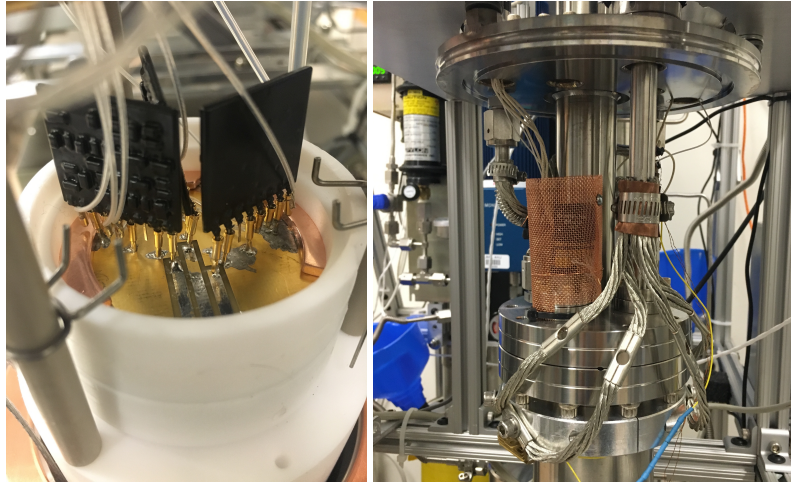


Figure 99: (left) original mounting of CR-110 charge amplifiers inside the experimental vessel. (right) Mounting in the outer vacuum reduced heat load on the TPC. In the outer vessel, the charge amplifiers were surrounded by a Faraday cage constructed from copper mesh to reduce noise.

### 6.5.1 CHARGE AMPLIFIER NOISE BEHAVIOR

Charge amplifiers have baseline RMS noise proportional to the attached capacitance. Figure 100 shows the RMS noise of a CR-110 unit attached to different lengths of BNC cable. The longer the cable, the higher the RMS noise. TPCs are essentially capacitors, and when filled with LXe have a higher capacitance than when the detector is at vacuum. The capacitance of large LXe TPCs like LUX prohibit the use of charge amplifiers for

---

<sup>1</sup> A test was done in a cryogenic fridge to ensure the behavior of the charge amps did not deviate when they were kept at -100 C. There was no change in pulse height (for a fixed input charge), or rise and decay times of the raw signals. This test was not possible in-situ, and so excludes the noise behavior described below, because the manufacturer's test board (CR-150-R5 evaluation board) was necessary to inject charge (via a square wave to an on-board 1 pF capacitor) into the amplifiers.

direct readout of the S2 electrons because the RMS noise would swamp the signal.

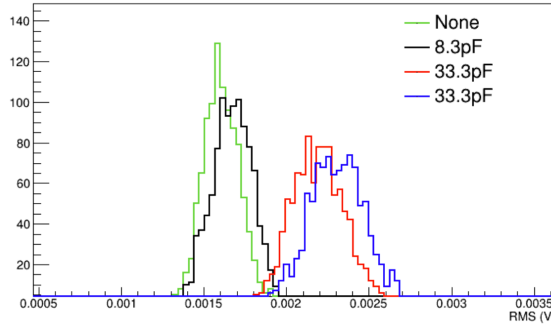


Figure 100: Different lengths of BNC cable attached to a CR-110 test board to show the RMS noise relationship to input capacitance. Two equal length segments (calculated to be 33.3 pF) were observed to have slightly different properties.

Charge amplifiers also respond to acoustics; that is, they are susceptible to microphonic noise. Tapping a finger near a charge amplifier will show as a baseline-jumping response on an oscilloscope. This additional source of noise makes [LXe TPCs](#) challenging places to use charge amplifiers for signal readout because any bubbles in the [LXe](#) create microphonic signals which the charge amplifiers pick up. By design, dual phase [LXe TPCs](#) are operated near the xenon liquid-gas boundary so the formation and dissipation of gas bubbles in the liquid is likely. Additional sources of acoustic noise like circulation of xenon into the experimental vessel also produce visible responses in charge amplifiers. The difference in micro-acoustic noise environments (gas phase but with/without the circulation pump) is illustrated in Figure 101. The baseline restorer can be seen functioning on the gaussian shaped and amplified signals, but the raw charge signals are subject to baseline wandering (Figure 102). Figure 102 was taken in a liquid environment during filling, so the effect of bubbles, pressure changes, and other vibrations are visible.

As [TPCs](#) are effectively large parallel plate capacitors, any transients coupling to the “[TPC](#) capacitor” may be picked up by the charge amplifiers. In particular, instabilities in the [HV](#) chain induce a current in the [TPC](#) capacitor that is picked up by the charge amps. Instabilities in [HV](#) can come from many places. It was observed that for the characteristic capacitance and impedance of the the test bed, partial breakdowns in a length of coaxial [HV](#) cabling caused a disruption in the functionality of the charge amplifiers. It was also found that a standard laboratory [HV](#) supply, a Glassman 20 kV negative polarity unit, created pick-up in the charge amplifiers (see Figure 103).



Figure 101: left) Event showing charge amp with detector -100 C, 1.5 bar, gas only (time scale 1.00 ms/div). (middle) Effect of circulation pump on charge amp is to cause 500 Hz oscillation noise (-100 C, 1.5 bar, gas only (time scale 1.00 ms/div)). (right) Same event as (middle), but zoomed-in time scale (10.0  $\mu$ s/div). In all figures, cyan is the raw charge signal (1 mV/div), yellow is the shaped charge (100 mV/div), blue is the PMT (10 mV/div) and magenta is the NIM trigger (100 mV/-div).

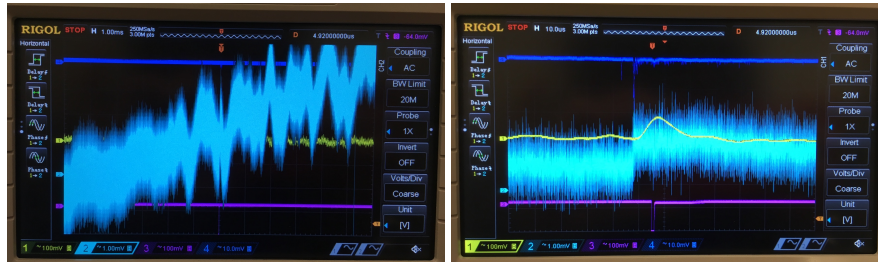


Figure 102: An event with the detector at -100 C, 1.5 bar, with liquid condensed to a level between extraction grid and anode. In both figures, cyan is the raw charge signal (1 mV/div), yellow is the shaped charge (100 mV/div), blue is the PMT (10 mV/div) and magenta is the NIM trigger (100 mV/div). (left) Scope trace showing a long time view the raw and shaped charge amplifier signals (time scale 1.0 ms/-div). (right) Scope trace showing the same event, but zoomed in (10.0  $\mu$ s/div). The baseline restorer on the shaped charge signal allowed it to be used as a trigger.

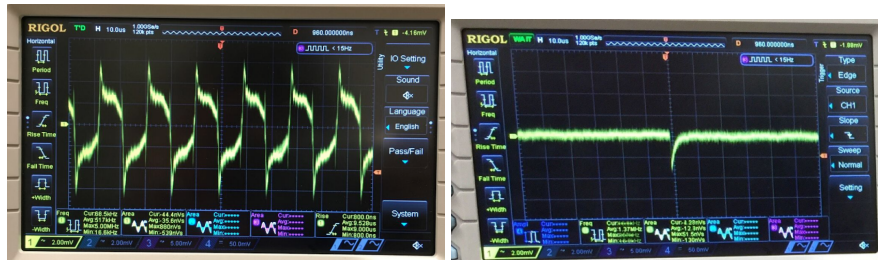


Figure 103: (left) 50 kHz periodic noise from the Glassman 20 kV negative polarity voltage supply. (right) Partial breakdown in coaxial HV cable as picked up by charge amplifiers. In both figures, the time scale is 10.0  $\mu$ s/div and the voltage scale is 2.00 mV/div.

## 6.6 DATA ACQUISITION AND PROCESSING

Data were acquired with a Picoscope 5000a, a USB-compatible “oscilloscope.” The open source pico-python Python library was used to write voltage records of [PMT](#) and charge signals to ROOT files, which were opened later for reprocessing into reduced quantities such as pulse area or pulse height. The Picoscope was run as a 14 bit ADC with 125 MHz (8 ns) sampling. For special cases, when only one channel was desired, it was possible to increase the sampling rate to 500 MHZ (2 ns). The manufacturer guide states that the Picoscope can operate in block mode, which uses on-board memory to store events and transfers them to disk only when the on-board memory buffer is full. Block mode is generally preferable to writing each event to disk as it is acquired because the overhead time for USB communication between the Picoscope and write time is only executed once, and so the dead time per event is smaller. However, the block mode capabilities were found to not function and so single event acquisition was used.

### 6.6.1 ESTIMATING PICOSCOPE DEAD TIME

Each event was written to disk as it was acquired, which led to a large dead time percentage. The manufacturer provided no information about dead time, but in general, dead times can be estimated in lab using the following method. Trigger the DAQ externally with, e.g., a square wave. Vary the rate of the external trigger, counting how many events are actually recorded by the DAQ in 1 minute. The number of events actually recorded gives the record rate. The record rate will level off at high external trigger rates because it is limited by transfer speed, write time, etc. Subtracting the actual event length from the real total time it takes to record an event gives the dead time per event. When estimating dead times, use the same conditions in data taking, e.g. if 4 channels are used for real data taking, use 4 channels when measuring the record rate. The dead time per acquisition is then the number of events in the acquisition multiplied by the dead time per event. This method is illustrated in Figure 104. Such a dead time estimate is used in Chapter 7 to calculate the rate in Bq of radon daughters observed.

### 6.6.2 PMT SIGNAL PROCESSING

A simple pulse finder was written in Python. Instead of searching for pulses left-to-right along a signal trace, the algorithm found the maximum of the trace, and then searched left and right until the trace went

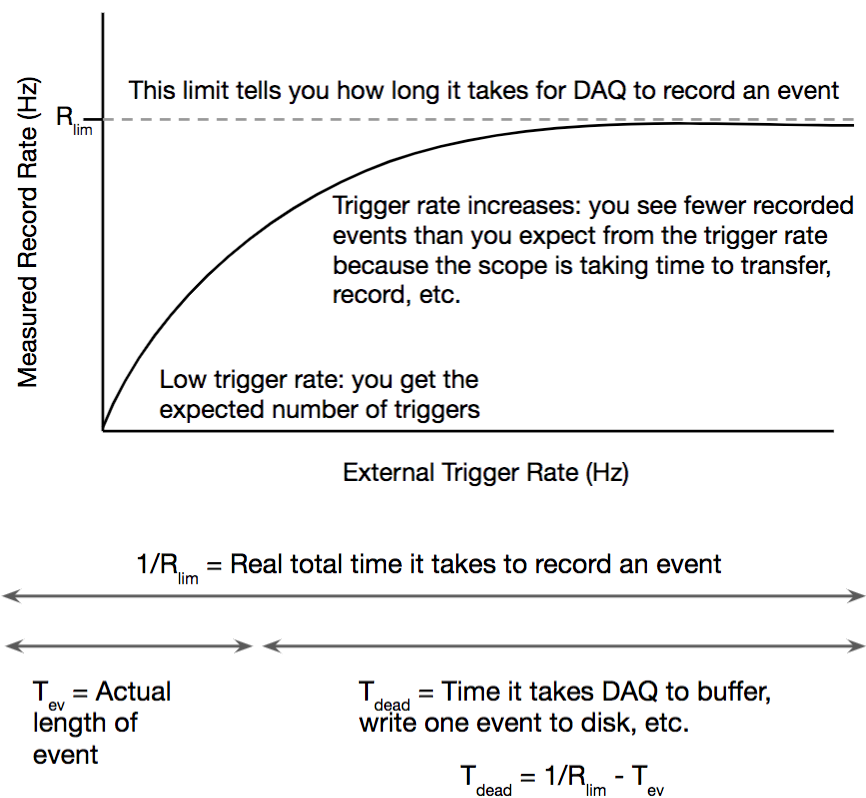


Figure 104: (top) Laboratory method to find the maximum DAQ record time time.  
 (bottom) Calculating dead time from maximum record rate.

below a threshold. After these edges were identified, the trace was set to zero for the duration of the pulse, and then the next-tallest pulse was sought. Pulses were found until there were no more, or the number found was equal to some user-defined number of pulses. Thus, pulse starts and stops were acquired for each PMT trace. These pulse starts and stops were then used to calculate useful RQs such as pulse area, width, prompt fraction, etc. S1 and S2 identification was done later, based on these RQs. The definitions of S1, S2, and other high-level PMT RQs were specific to the state of the test bed hardware, which was typically changed on a weekly basis during development. A stable data processing framework was not maintained.

### 6.6.3 CHARGE AMPLIFIER SIGNAL PROCESSING

The shaped charge amplifier signals were used primarily as a trigger throughout the studies in Chapter 7 and Chapter 8. They were originally acquired and implemented because the raw charge signals were small and difficult to process. This was due to field strength, purity, and grid transparency; these issues are described in more detail in Chapter 8, but were all essentially solved by removing the grid to produce an “extraction region only” configuration (Figure 93 (right)). Various methods were explored to process the raw signals into the relevant charge RQ: step height (mV), which could then be translated to charge (Coulombs, then number of electrons) per the manufacturer’s specifications. For small, raw charge signals a fit function was found to out-perform a simple step algorithm; for larger raw signals the step algorithm was fast and robust. Both methods are illustrated below, the fit function in Figure 105 and the step algorithm in Figure 107.

The fit function was a piece-wise defined linear function plus a falling exponential. The linear function was defined to be zero before some offset time  $t_o$ , and after the offset time plus rise time of the charge trace ( $t_o + t_r$ ). The exponential was zero before  $t_o + t_r$ , and the two functions had equal values at  $t_o + t_r$ .

The step algorithm produces a new trace with peak instead of a step by averaging a user-defined number of samples,  $n_s$ , of the original charge amp voltage trace from  $[i + n_s, i + 2n_s]$  and subtracting the average of the waveform from a previous section,  $[i, i + n_s]$ . If  $n_s$  is chosen to be exactly the rise time of the trace, then the maximum of the new trace is equal to the step height. See Figure 106 for examples of two different choices of  $n_s$ . In practice, it is difficult to choose  $n_s$  perfectly because noise plays a large role; it was easier instead to find the peak of the new trace to locate the approximate step position of the original trace based on  $n_s$ , and take the average of several samples as the step height (Figure 107). That is, if  $n_p$  is

the location of the peak after the step-finding algorithm, the approximate location of the step is  $n_p + 2n_s$ .

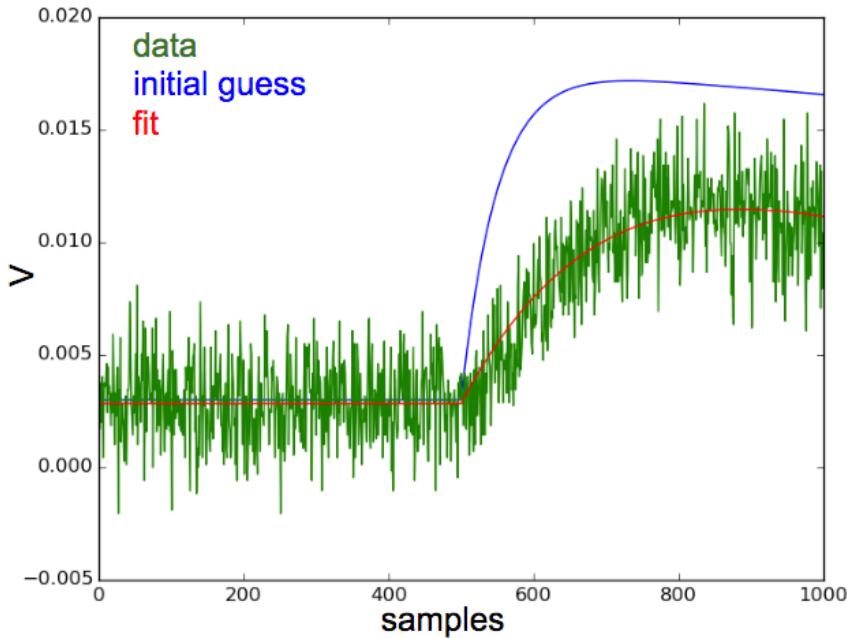


Figure 105: Fitting the charge traces with a piece-wise defined linear rise and exponential fall. 1 sample is 8 ns.

Another source of charge amplifier noise is the Shockley-Ramo effect. The Shockley-Ramo effect refers to the Shockley-Ramo theorem, which says that the instantaneous current  $i$  and charge  $Q$  induced on a given electrode due to the motion of a charge is [119]:

$$\begin{aligned} i &= q\vec{v} \cdot \vec{E}_0(\vec{x}) \\ Q &= -qV_0(\vec{x}) \end{aligned} \tag{57}$$

where  $q$  is the charge,  $\vec{v}$  is the instantaneous velocity of the charge, and  $\vec{E}_0(\vec{x})$  and  $V_0(\vec{x})$  are the electric field and potential that would exist at  $q$ 's instantaneous position  $\vec{x}$  under the following circumstances: the electrode of interest is at 1 V, all others are at 0 V, and all charges are removed. A helpful review of Shockley-Ramo and a discussion about its effect on charge sensing techniques can be found in [119]. The charge amplifiers are an integrator circuit, and the Shockley-Ramo theorem implies that even if a charge isn't directly underneath a given anode segment, that anode segment has field lines terminating on it as a result of the motion of the charge, and therefore an induced current. When an electron terminates on an anode segment, the other segments "see" the field reduction

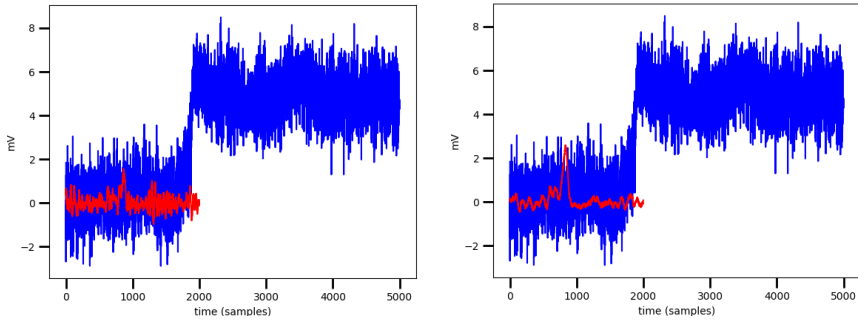


Figure 106: The step-finding algorithm shown with a choice of 20 samples averaged (left) and with 50 samples averaged (right). If  $n_s$  is chosen to be the rise time of the pulse, the height of the output waveform is the height of the step. These step algorithms actually include an offset,  $n_o = 1000$ , so the averages are taken from  $[i + n_o + n_s, i + n_o + 2n_s]$  and  $[i + n_o, i + n_o + n_s]$ . Alternatively, a smaller number can be chosen for  $n_s$ , and the location of the maximum of the output waveform can be used to find the location of the top of the step (shown in Figure 107). 1 sample is 8 ns.

and register it as a positive charge, or an electron moving in the opposite direction; the response is a dip in the trace. For the gaussian shaping amplifiers, the Shockley-Ramo effect was more evident, and can be corrected for by adjusting the maximum for any following dip; on the raw traces, it is more difficult to account for. The dips are present in the raw traces, but in general much less visible and aren't corrected for. In the amplified and gaussian-shaped traces, the dip is more visible, as in Figure 108.

The gains of the gaussian shaping amplifiers were not extensively characterized because they were never used to reconstruct a physical quantity. The shaping amplifiers were used primarily as a trigger because the unit had a baseline restorer, which the raw charge amplifiers did not (see Figure 101 and Figure 102 for the noise conditions on shaped and raw charge amplifiers).

## 6.7 HIGH VOLTAGE FEEDTHROUGH DESIGN

A significant amount of time was spent developing and testing HV feedthroughs for the test bed. This section describes a few of the feedthroughs that were unsuccessful, leading to the final design, which is capable of delivering -11 kV to the cathode with no observable breakdown or other effects. Extensive detail of the tests and procedures are not provided. Instead, the following vignettes are intended as an overview to be useful to a student tasked with designing a HV feedthrough.

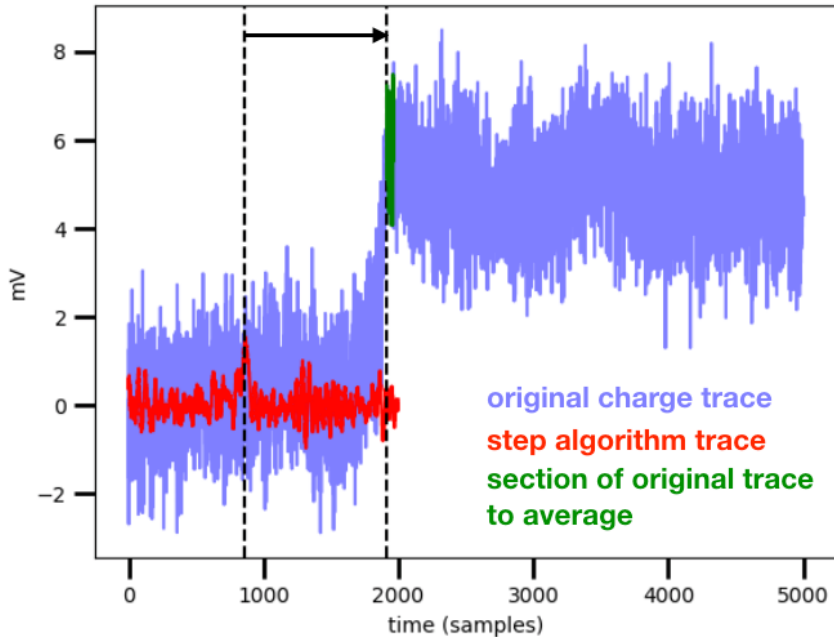


Figure 107: The location of the top of the step can be robustly found from the location of maximum of the step-finding algorithm. Some number of samples at the top of the step can be averaged to give the step height. 1 sample is 8 ns. This particular example uses  $n_s = 20$ . The step-finding algorithm is calculated with an offset,  $n_o = 1000$ , so the averages are taken from  $[i + n_o + n_s, i + n_o + 2n_s]$  and  $[i + n_o, i + n_o + n_s]$ . If the peak location (red peak) is  $n_p$ , then the approximate location of the step is  $n_p + n_o + 2n_s$ , and some number of samples of the original trace (50 samples shown in green) can be averaged to give the step height.

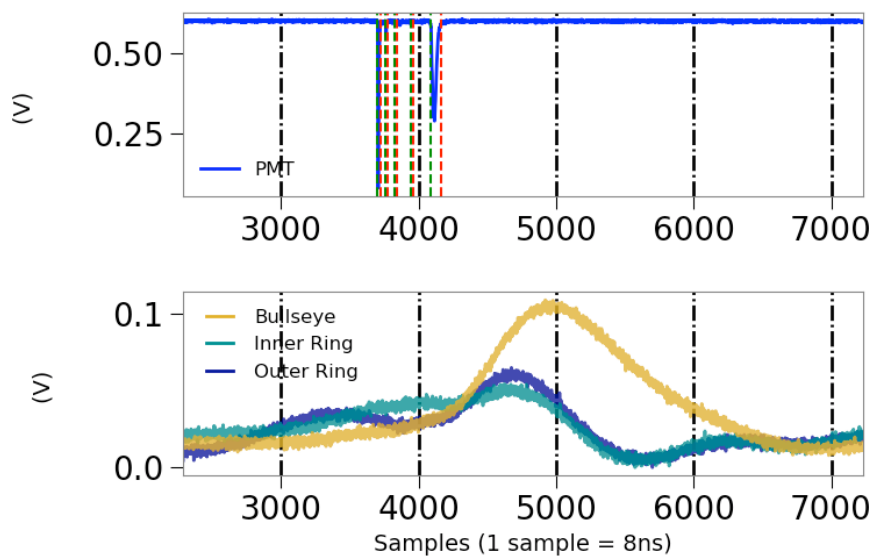


Figure 108: An alpha event showing the Shockley-Ramo effect on the inner and outer ring segments of the anode. The top plot shows the PMT trace and the bottom plot shows the shaped response of the anode segments. The Shockley-Ramo effect is the rise (around 4700 samples) and subsequent dip (around 5500 samples) of the inner and outer ring traces. The event happened under the bullseye segment, but the other traces see the field line density increase and then disappear, producing both an increase and decrease in the shaped anode signal.

## 6.7.1 OFF THE SHELF FEEDTHROUGHS

The first attempts at building feedthroughs were to use off-the-shelf products from typical vacuum supply vendors such as MDC Vacuum and Kurt J. Lesker. Vacuum HV feedthroughs are intended for use from air to vacuum, not air to LXe; we were attempting to operate them outside of their intended usage parameters. Additionally, by combining ceramic and metal (typically aluminum, stainless steel, nickel, copper) they are especially prone to breakdown at the meeting of these different materials, known colloquially as “triple points”. When there are interfaces between materials with different permittivities (dielectric constants), the electric fields are distorted. Electric field is “pushed” out of the higher dielectric material into the lower dielectric material. This creates a field enhancement where peak fields can be much higher than average fields in the system. The field enhancement from triple points where there is an interface between a conductor and two different dielectrics (e.g conductor, ceramic insulator, and gaseous Xe) is a common source of breakdown along insulator surfaces. Good design practices, namely choices of geometry, reduce the field enhancements in these regions. With commercial feedthroughs, the geometry choice is set and may not be sufficient for the task.

Note that ceramic feedthroughs are not appropriate for low background experiments due to their high radioactivity. For test beds, where low radioactivity is not a priority, ceramic feedthroughs may be used.

The first few feedthroughs used a 12 kV Safe High Voltage (SHV) weldable feedthrough as shown in Figure 109. If used as intended, the side indicated by A is used on the vacuum-side and B connects to the voltage supply. Instead, we trimmed the long B side and attached a copper, screw-port connector to make the 90 degree connection from vertical feedthrough to horizontal grid. This was done to avoid placing a conducting surface at high voltage (the cap on the ceramic on side A) in gaseous xenon, thereby increasing the risk of breakdown to the walls of the detector. The feedthrough’s vertical placement is designed such that the copper connector is fully submerged in LXe (Figure 110).

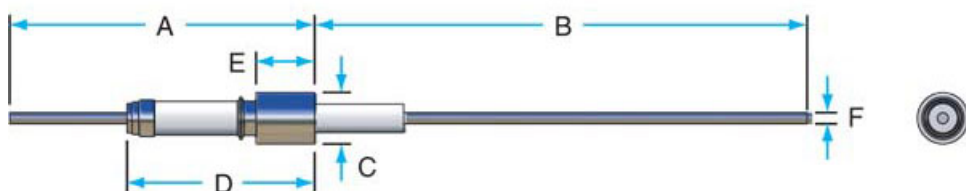


Figure 109: A 12kV SHV weldable connector from vacuum supplier Kurt Lesker.

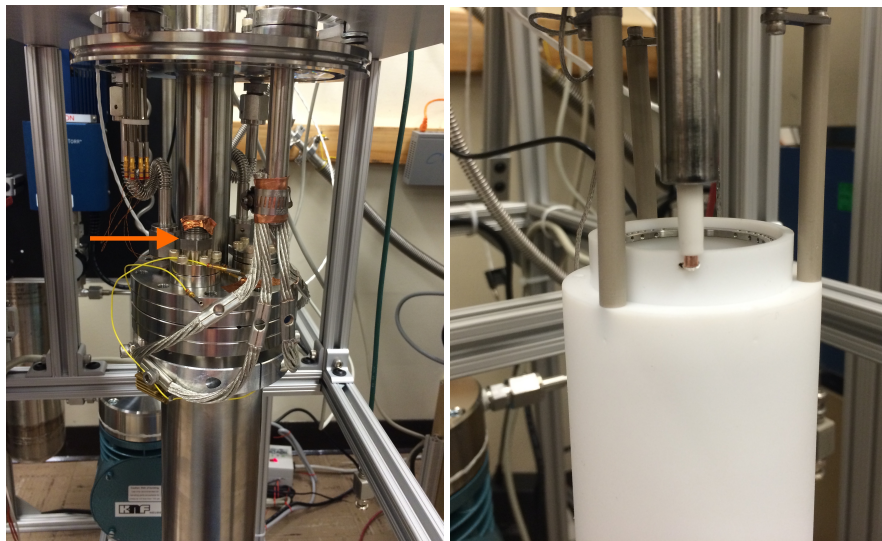


Figure 110: (left) The copper tape in this picture is sitting on top of a 1/2 inch swage connector (indicated by the arrow). The swage connector captures a 1/2 in pipe, which has the 12 kV SHV feedthrough welded to the end. (right) 12 kV SHV weldable connector, inverted, clipped, and attached with a machined copper connector. The connector uses a screw to capture the SHV feed though, and the same screw to capture a stranded wire, visible in this picture as the silver strands on the copper tip, which is then fed through a hole drilled in the PTFE to connect to the wire grid frames. The wire was wrapped around the grid frame.

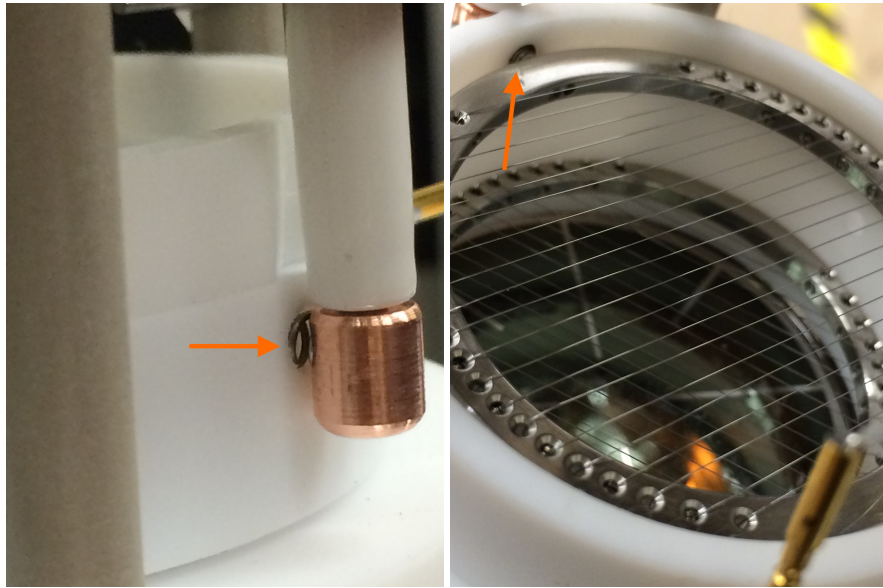


Figure 111: (left) The same 12 kV SHV feedthrough as in Figure 110, now with a modified spring connection connecting the feedthrough to the grid frame. (right) A close-up of the cathode grid showing the spring connection.

Feedthroughs were tested by performing a cool down, ramping the HV supply slowly, and watching an oscilloscope for a higher than baseline photon rate (Figure 112) or a full xenon breakdown (Figure 113). The effect of raising the voltage on the HV supply at a specific rate was also tested, and it was determined that the extremely slow and steady rate of a computer program was not necessarily superior to the imperfect method of the human experimenter. That is, the construction of the feedthrough, itself, outweighed any gains from computer-supervised voltage ramping.

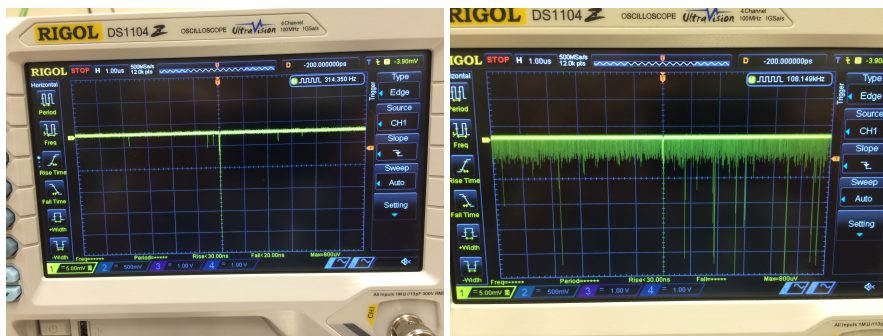


Figure 112: Oscilloscope showing baseline rate of single photons (left) compared to a high rate of single photons (right) caused by the high voltage feedthrough.

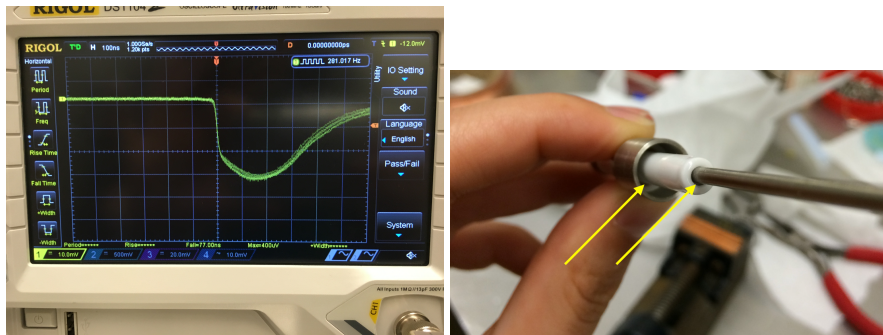


Figure 113: (left) Full xenon breakdown as visible on the [PMT](#) trace. The large, saturated pulse is caused by the high intensity of light. This type of breakdown was often accompanied by an audible buzz, and a rise in current that would initiate a trip of the high voltage supply. (right) a close up of the xenon-facing side of the feedthrough. The arrows indicate visible gaps where xenon gas is exposed to high fields. These areas are particularly problematic for breakdowns.

Iterations of the 12 kV [SHV](#) feed though were not able to reach and sustain more than about 7 kV for extended periods of time like those that would be required for data acquisition.

We also tried a stock 20 kV [SHV](#) feedthrough with a custom end cap designed by [HV](#) engineer Will Waldron, meant to smooth out typical triple point issues. This feedthrough was mounted on a CF flange far from the active region. A length of cable was stripped of grounding sheath for its entire length. A small section on one end was stripped of dielectric, this end was tied to the SHV feed though with copper wire, and the custom end cap was placed over this. The side of the cable making the connection to the cathode grid was drilled out for a short length on the bottom, leaving only a tube of dielectric with no conductor. A threaded rod was inserted into the cable, such that the rod made contact with the conductor. The cathode grid frame was screwed onto the threaded rod. The SHV-20 feed though is summarized in pictures in Figure 114, and was found to hold sufficient voltage (10 kV) for extended periods of time. It was also tested whether holding the feedthrough in place with Polyether ether ketone ([PEEK](#)) zip ties would increase voltage capabilities Figure 115; no change in voltage capability was observed. This feedthrough was in use for a few months, and during that time it was found that the voltage capability decreased over time; this is discussed in the next section.

## 6.7 HIGH VOLTAGE FEEDTHROUGH DESIGN

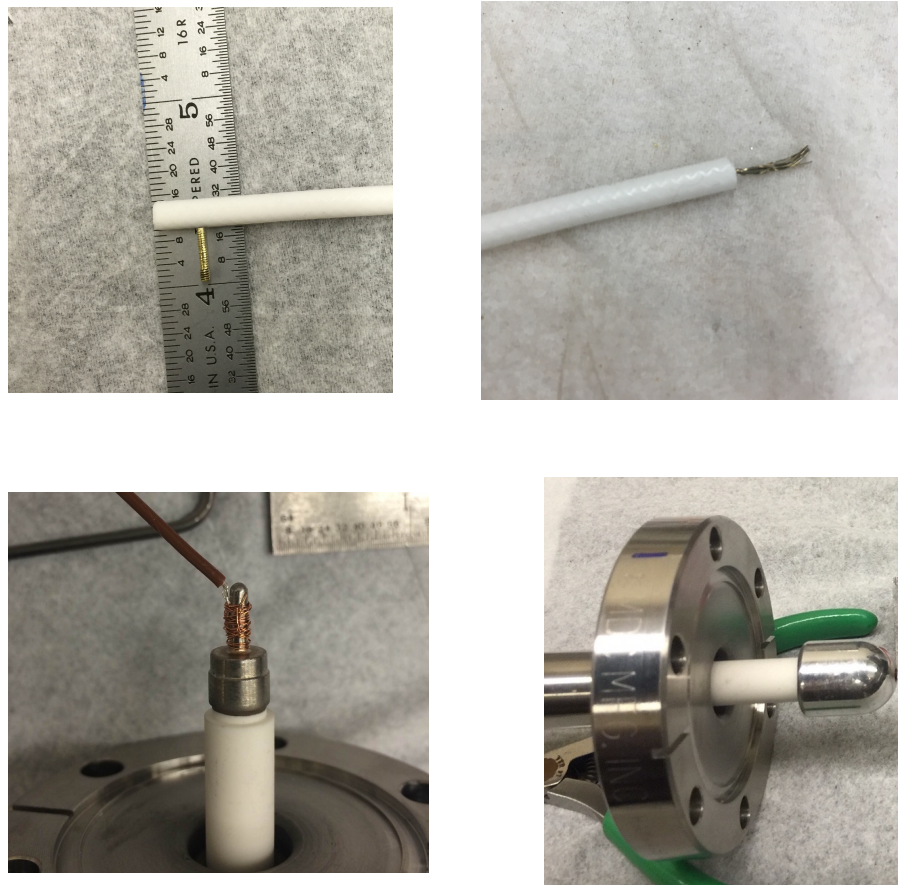


Figure 114: Design of high voltage delivery system based on an [SHV-20](#) feedthrough. (top left) cathode connection side (top right) [SHV-20](#) connection side. (bottom left) an example showing how the cable was attached to the stock [SHV-20](#) feed though end (bottom right) a custom cap fit over the connection, smoothing out triple points. The cap had a hole at the tip to allow the cable to pass through.



Figure 115: Effect of holding the feedthrough in place with [PEEK](#) zip ties was explored. The voltage properties were not found to improve, but neither did they degrade.

### 6.7.1.1 FEEDTHROUGH AGING

It was noticed during subsequent operation that the SHV-20 feedthrough was subject to aging (black line in Figure 116). A month of use resulted in noticeably lower voltage capabilities. The issue could have been at any point along the entire voltage chain: feedthrough - custom cap - connection to cable - cable - connection to grid - grid. Tests focusing on different parts of the voltage chain did not reveal any weak points. Instead, it was found that the SHV-20 feed though, itself, was subject to aging (red line in Figure 116).

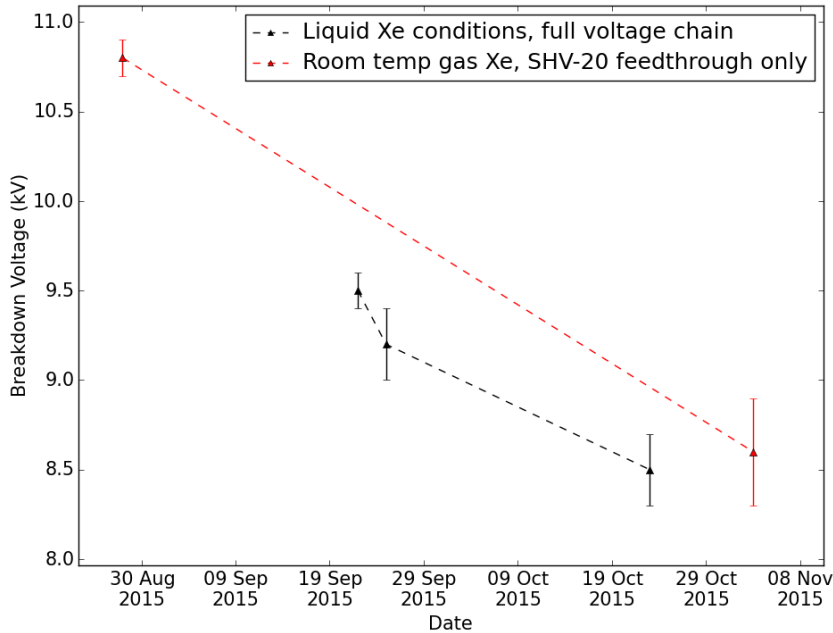


Figure 116: The black line shows the aging observed in the course of normal operations. The red line shows breakdown tests of the SHV-20 feed through in gas, illustrating that the aging observed during operation was due to aging of the feed though.

Feedthrough aging can be the result of arcing and discharges which cause local heating and carbonization of an insulator surface. Once there is a carbon path, the insulator is considered “tracked” and then holds a much lower voltage than before. Sophisticated HV systems keep peak currents and fault energies to a minimum using series resistors. In this way, a breakdown event does not degrade system performance in the future. In addition to carbon tracks, there can also be insulator degradation from exposure to Ultra Violet (UV) light if there is ionization in the region. Xenon ionization is in this region of the spectrum, and so any ionization near a feed through insulator may degrade the feedthrough performance. In the

case of this particular feed though, the high field which caused the breakdowns or ionization was likely a result of poor triple-point geometry.

### 6.7.2 CUSTOM FEEDTHROUGHS

To achieve better voltage performance, we moved away from typical, stock feedthroughs composed of ceramic and metal. Figure 117 shows a feedthrough made with a Swagelock reducing union. This blue and white PTFE piece connects 1/4 in SS pipe to an 1/8 in PTFE tube, which then houses a SS rod. The rod is screwed onto a connector, which holds a wire to connect to the grid. This feedthrough had stable voltage performance, but could not achieve sustained voltages higher than about 9 kV. A woven SS shield was added to the feed though to reach higher voltages (Figure 117 (left)) but this actually decreased the voltage performance to a maximum of about 5 kV.

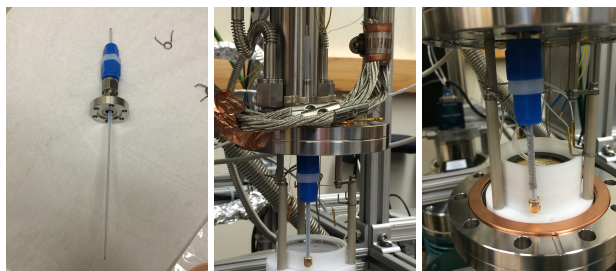


Figure 117: First attempt at a custom feedthrough built out of Swagelock parts combined with basic materials like PTFE and stainless steel rods. The orientation shown (left) was later inverted due to concerns of temperature stress and pressure stress on the PTFE ferrules. The feedthrough as assembled (center) was functional, but higher voltage capability was desired. The effect of adding a grounding braid (right) was found to decrease the voltage capability instead of increasing it.

There are two issues with the approach of adding a grounding braid in this method: (1) the braid is not held in place tightly along the dielectric, which introduces peak fields between the dielectric and the braid (Figure 118) (2) at the braid termination, a small effective radius creates an enhanced radial field through the dielectric and an enhanced field along the cable dielectric facing the high voltage. Peak fields can occur in unexpected places, greatly decreasing the voltage capability of a feedthrough that seems, naively, robust. The breakdown field of xenon gas depends on a variety of factors such as temperature (i.e density), purity, electrode shape, etc. Peak fields arising in gas regions in or around HV feedthroughs are sources of unwanted light and, in the worst case, complete breakdown and eventual degradation of the feedthrough.

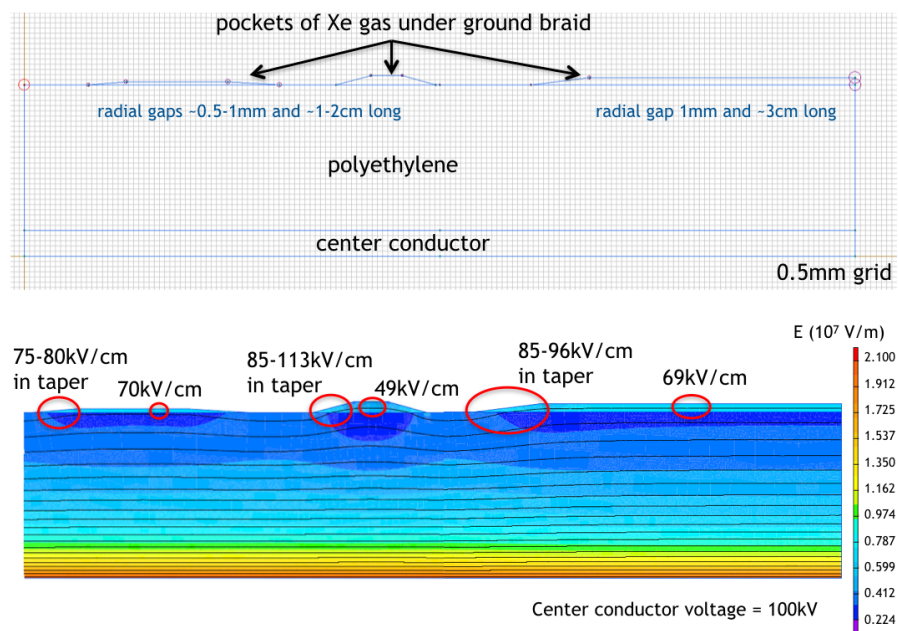


Figure 118: (top) Input to a COMSOL model simulating gaps between the grounding braid and dielectric of a high voltage feedthrough. (bottom) COMSOL output of the model, showing that peak fields arise when gaps exist between dielectric and grounding braid. Both images provided by W. Waldron.

Due to the poor performance of the Swagelock PTFE custom feedthrough (Figure 117) and concerns about the cold connection, another feedthrough was built out of a SS rod with PTFE dielectric and no shield braid (Figure 119). The rod was inserted into the PTFE tube while warm (the tube was snug on the rod, and no temperature contraction or expansion of the PTFE tube was done). The PTFE ferrules formed a vacuum-tight seal on the PTFE tube, but some epoxy at the top where the rod exits the tube is necessary (see Figure 119 (top left and right)); helium leak rates during testing were around  $10^{-10} - 10^{-9}$  mbar l/s. The vacuum test was done by creating a test piece from a short piece of SS rod and PTFE tube; the test piece was sealed with the PTFE ferrules with epoxy where the rod exited the PTFE tube (no epoxy at the ferrules) and tested with a helium leak checker over the course of several hours. A pressure test was also done where the test piece was placed on a small SS vessel which was then filled with N<sub>2</sub> gas until the total pressure was 3 bar. The test piece was left overnight at 3 bar of pressure and no drop in pressure was observed the next day. The total pressure was then increased to 4 bar, and left for approximately 10 hours. Again, no drop in pressure was observed. When the feedthrough was installed on the experimental vessel, more epoxy was added inside the swage nut near the ferrules for extra assurance. This feedthrough entered the inner vessel at the top of the tall CF tower, where the connection is warm. The xenon-facing side was a copper rod bent into a U-shape which connected to the SS conductor rod via a pin, and the other end, which was threaded, screwed into the cathode grid frame. The bare copper section was only exposed under the liquid level, and elsewhere the PTFE dielectric helped contain the electric field and prevent breakdown to the inner vessel wall. This feedthrough had good voltage performance, and there was no sign of aging. It was decided, however, that the charge amplifiers were more susceptible to detecting transients from an unshielded feedthrough, so another feedthrough with shielding was constructed.

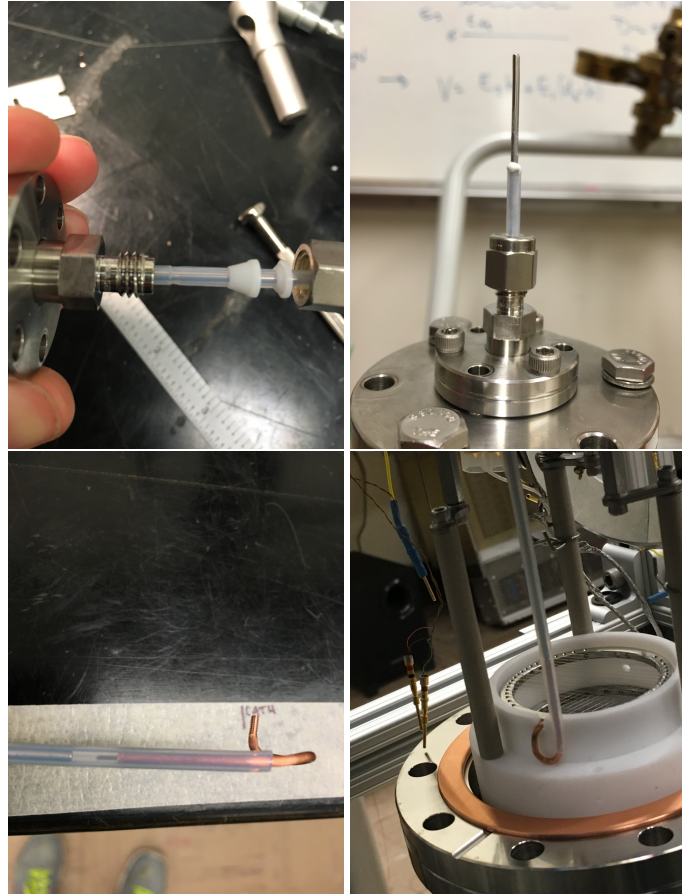


Figure 119: Top: (left) Close up showing the **PTFE** ferrules and notch. (right) Close-up of the sealed top connection. Although the **PTFE** ferrules and some epoxy where the rod exited the **PTFE** tube kept an acceptable vacuum and pressure seal, more epoxy was added during installation on the experimental vessel inside the swage nut near the ferrules. Bottom: (left) Threaded U-bend cathode connector (right) Feedthrough assembled and installed.

## 6.7.3 FINAL FEEDTHROUGH DESIGN

The final feedthrough design is shown in Figure 120. The number of different materials and components used were kept to a minimum in order to avoid unnecessary high voltage triple points and complicated geometries. The feedthrough is constructed from a cable with a stranded inner **SS** conductor, **PTFE** dielectric, an outer **SS** grounding braid, and an outer **PTFE** sheath. The outer **PTFE** sheath functions to keep the shielding tight against the inner dielectric, to avoid gaps where peak fields can develop. The feedthrough has a warm connection, entering the experimental vessel at the top of the **CF** tower. The cable is held in place with a Swagelok connection and **PTFE** ferrules. Although the feedthrough held vacuum with only the **PTFE** ferrules and Swagelok connection, epoxy was placed inside the swage nut around the ferrules before tightening the nut for extra assurance in the case of high pressure. Epoxy was also applied where the inner dielectric was cut back to expose the conductor, otherwise air could travel in the space between the dielectric and the conductor into the inner vessel. Inside the **CF** tower, the grounding braid was connected to ground via a screw on the underside of the **CF** flange. When the cable reached the xenon experimental space, the outer sheath and shielding braid were cut back in such a way to only leave unshielded dielectric below the **LXe** liquid level. The inner dielectric was cut back to expose approximately 0.5 inches of conductor, but the cable was routed through the interlocking **PTFE** rings such that the point where the conductor was exposed was imbedded in **PTFE**. Inside the **PTFE** ring, the exposed conductor was wrapped around the wire grid. This final feedthrough design has been extremely successful, and has been in use for 2 years at the time of writing this thesis.

The cathode feedthrough design for **LZ** also uses a similar, but much more sophisticated, “cable pass through” design where the **HV**-supplying cable goes from air into xenon space without being terminated at the xenon vessel, e.g. termination in a connector, which then connects to a different cable on the inside of the vessel. The **LZ** technical design report shows the scheme [120].



Figure 120: Top: (left) Sealed top connection with liberal epoxy use. A male Bendix pin was soldered to the cable conductor. (middle) SHV connector with female Bendix to mate with feedthrough (right) Grounded safety housing with SHV connector. Bottom: (left) Ends of the feedthrough were held in the Teflon stack. (middle) Close up showing cable conductor, PTFE dielectric, and grounding sheath pulled back. The calipers are measuring the length of exposed conductor. (right) Grounding scheme for feedthrough cables at the top of the CF tower.

## 6.8 ELECTRIC FIELDS IN TEST BED

Both peak fields, which occur on the grid wires, and fields at the liquid-gas boundary are important to understand. Peak fields are often at a “weak link” in the voltage chain where breakdown is most likely to occur. The field in the liquid near the gas boundary extracts electrons, making it important for TPC function. The electric field changes as a function of liquid height, and can be calculated analytically following the McDonald lecture notes [121]. A COMSOL model with the test bed geometry and materials was also developed by E. Mizrachi. The COMSOL model and the analytic calculation were found to agree. Figure 121 provides a summary of the electric fields on the grids wires for a case where there is only a cathode and anode, separated by 5 cm. The color scale on the COMSOL is misleading: the peak fields, which occur on the cathode wires, are  $\sim 130$  kV/cm, which appears the same color as 20 kV/cm.

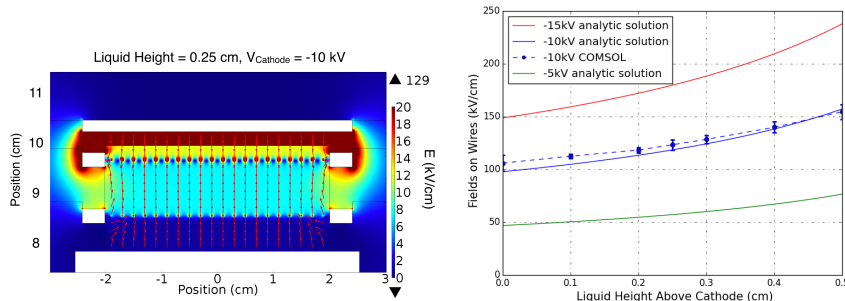


Figure 121: (left) COMSOL model with specific cathode voltage and liquid level.

The peak fields of  $\sim 130$  kV/cm occur on the wires, and the gas fields are  $\sim 20$  kV/cm. These two values are both dark red on the color scale, which can be misleading. (right) Analytic calculation following the McDonald notes [121], which shows how the peak fields vary with change in liquid level and cathode voltage. The voltages in the legend refer to the cathode voltage; the anode is held at ground.

The COMSOL model shows that the fields in the liquid and gas do not vary very much with position, once there is sufficient distance from the wires. The fields do, however, vary with liquid level. Figure 122 shows how the liquid and gas electric fields vary with liquid level and cathode voltage; the TPC configuration “extraction region only” with cathode and anode separated by 0.5 cm. The calculation is straightforward: the TPC is essentially a capacitor with a dielectric. Cathode and anode provide boundary conditions on the voltage, and continuity of the derivatives at the liquid-gas boundary is the remaining boundary condition to solve Poisson’s equation.

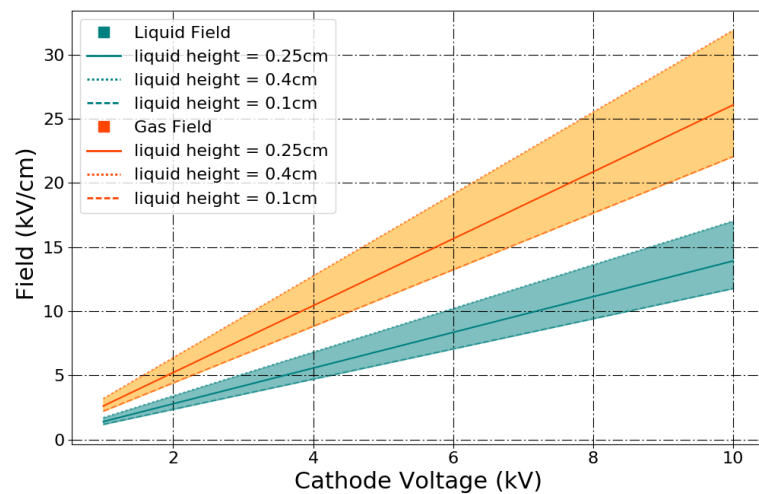


Figure 122: Ranges for the electric fields in gas and liquid for different cathode voltages and liquid levels.

# 7

## SOLUBILITY OF RADON DAUGHTERS IN LIQUID XENON

---

Rare-event searches are very sensitive to backgrounds from radioactivity in and on detector materials. Some of the most omnipresent and troublesome are  $^{222}\text{Rn}$  and its daughters. Decay products from  $^{222}\text{Rn}$  plate out on detector surfaces and have typically been assumed to be fixed there (plate out is further defined in Section 7.1.1). In this chapter, a series of experiments is described; the results provide evidence that radon daughters are mobile in liquid xenon after having been fixed to a surface.

### 7.1 MOTIVATION

Radon and radon daughters produce problematic backgrounds for rare-event searches [81]. Of particular concern for liquid xenon dark matter detectors are “naked” beta decays. These ground-state to ground-state decays have no accompanying gammas and cannot be rejected via coincidence tagging. Rejection of these backgrounds in WIMP search experiments relies solely on being able to discriminate electron recoils from nuclear recoils. For example, the ER leakage fraction from the LUX Run03 tritium calibration is on the order of 2/1000 over the WIMP search region [71] (See Chapter 4 for more details about tritium calibration). The  $^{222}\text{Rn}$  chain contains  $^{210}\text{Pb}$  ( $T_{1/2} = 22.23\text{ y}$ ), effectively splitting the decay chain into a “fast chain” and “slow chain” (Figure 123). Radon can be introduced via two pathways: (1) during detector construction and (2) during detector operation (see Figure 124). Great care is taken to ensure minimal contamination via pathway 2 because the fast chain naked betas,  $^{214}\text{Pb}$  and  $^{214}\text{Bi}$ , may decay in the fiducial volume before the purification system can remove them or before they can plate out on detector surfaces. In pathway 1,  $^{222}\text{Rn}$  and daughters plate out onto detector surfaces during construction of parts, and construction of the detector itself. Models for the plate out process can be found in [122] and [123]. Typically it is assumed that once  $^{222}\text{Rn}$  and daughters plate out, they remain fixed at that position, and can be rejected by a fiducial volume cut. This means that the slow chain naked betas of  $^{210}\text{Pb}$  and  $^{210}\text{Bi}$  from initial exposure dur-

ing construction are assumed to occur outside the fiducial volume. However, evidence of  $^{210}\text{Bi}$  mobility has been observed in the liquid scintillator environment of KamLAND [124], [125] and Borexino [126]. If radon daughters are soluble in liquid xenon, the late chain naked betas (from both pathway 1 and 2) pose a serious background distributed throughout the fiducial volume.

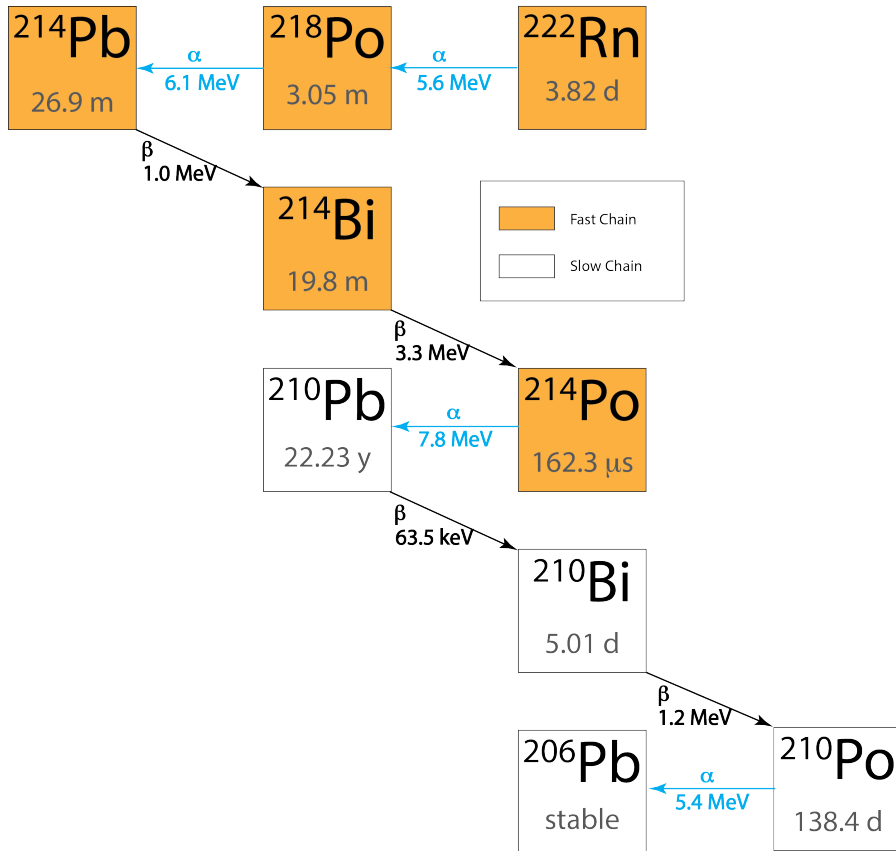


Figure 123: The  $^{222}\text{Rn}$  decay scheme. The fast and slow chains are indicated.  
Data from [127], image provided by K. Lesko and modified for this thesis.

In order to investigate the mobility of radon daughters in liquid xenon, a  $^{220}\text{Rn}$  source was employed instead of  $^{222}\text{Rn}$  (see Figure 127). The analogous long lived daughter in the  $^{220}\text{Rn}$  chain,  $^{212}\text{Pb}$ , has a half-life of 10.6 h, making it appropriate for a laboratory test. Investigating pathway 2 in the laboratory by introducing radon in a  $\text{LXe}$  environment will necessarily yield inconclusive results, because it is impossible to tell if the daughter decay of interest plated out before decaying. Therefore, we required the radon daughters to be on a surface.

Xenon gas was circulated through the  $^{220}\text{Rn}$  source and detector components for a period of >24 h. The detector was then evacuated, thereby assuring the initial position of radon daughters on a detector surface. The

## Pathways to Radon and Radon Daughters Contamination

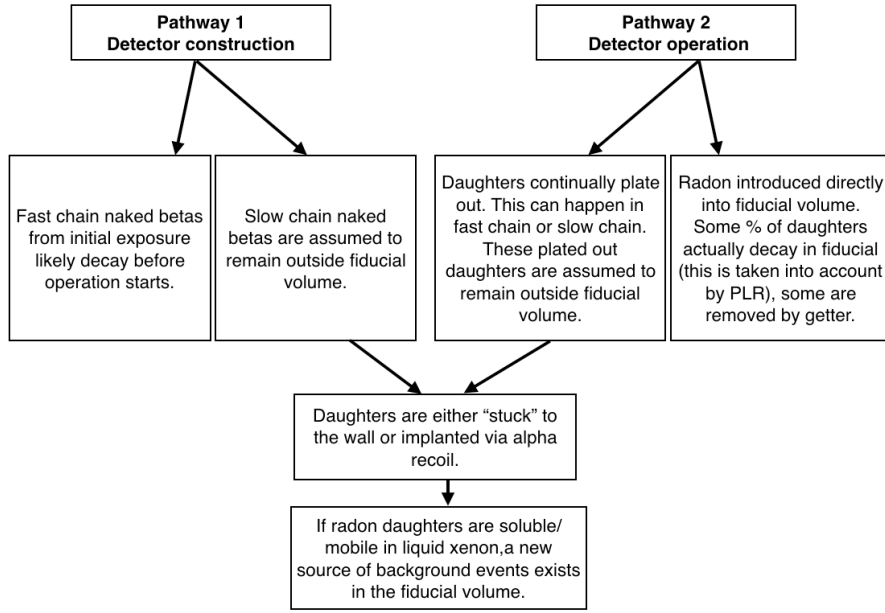


Figure 124: Pathways to radon and radon daughter contamination.

study makes the assumption that any radon daughters subsequently observed in the bulk region after condensing liquid xenon must therefore have dissolved.

### 7.1.1 PLATE OUT

The term “plate out” is used above but not defined. The literature indicates that there two known types of radon daughter plate out [128]. The following terms are used in [128] to identify each type.

1. *implantation*: Alpha recoil implantation of a daughter nucleus.
2. *sticking*: Daughters are sitting on the surface of a material; it is possible to wash a percentage of these off with various surface cleaning methods.

The percentages of daughters plated out in these different modes are not indicated, but [128] relates a story of researchers being unable to remove  $^{214}\text{Po}$  from glass samples, whereas  $^{218}\text{Po}$  was easily removed with surface cleaning methods. This is explained by the fact that further down the  $^{222}\text{Rn}$  chain, more alpha decays have occurred, so a late-stage daughter has had more chances to be implanted. It is also noted that the durability of the implanted activity is subject to change under different conditions, as is the implant integrity. The author cites factors such as humidity

and temperature affecting whether daughters implant, and whether they remain implanted; since the conditions for plate out are different in pathways 1 and 2 it logical to infer that implantation functions differently in these two environments for [LXe TPCs](#).

The chemistry of radon has been studied as well, and may provide some context to the plate-out discussion. Radon is frequently regarded as a totally inert element. It is, however, classified as a “metalloid”, and exhibits some of the characteristics of both true metals and nonmetals [129]. For example, it is known to react chemically with fluorine, halogen fluorides, dioxygenyl salts, fluoro-nitrogen salts, and halogen fluoride-metal fluoride complexes to form ionic compounds [130]. It is also known to co-crystallize with hydrogen chloride, hydrogen sulfide, sulfur dioxide and carbon dioxide [129]. In the latter case, the author notes that the radon is not forming true chemical bonds, but rather is held in place by weak Van der Waals forces. These chemical experiments found radon to be readily reactive at “room temperature and lower”, but the low temperate range is not stated. It is clear that chemical / Van der Waals bonds formed by radon belong in the ‘sticking’ class of radon plate out, as opposed to implantation.

If we look to surface physics, the plate-out term ‘sticking’ is well defined by the terms physisorption and chemisorption. Physisorption is distinct from chemisorption in that it is a general phenomenon occurring between the adsorbed atom and surface, while chemisorption involves a chemical reaction between surface and adsorbate, and is characterized by higher bond strengths. Chemisorption potentials have been calculated for many atoms and surfaces [131] and are generally greater than 1 eV. Physisorption potentials, such as the well-known Van der Waals potential, are less than 1 eV and as low as 10 meV.

Plate out occurs with different rates on different materials [132], and can be an order of magnitude larger on [PTFE](#) than stainless steel, likely due to [PTFE](#) tendency to accumulate negative static charge [133]. Plate out of radon daughters can be reduced by employing a nitrogen gas purge or an electric field (approximately 90% of radon daughters are charged) [134]. However, [132], [133], and [134] do not distinguish between implantation and sticking, and only use the term “plate out”.

## 7.2 EXPERIMENTAL CONFIGURATION AND METHOD

A diagram of the [TPC](#) for this work is shown in Figure 125. A 50 mm diameter cathode wire grid, extraction wire grid, and a planar, segmented anode were held in Teflon [PTFE](#) housing. The anode was instrumented with charge-sensitive preamplifiers. Both grids were constructed from

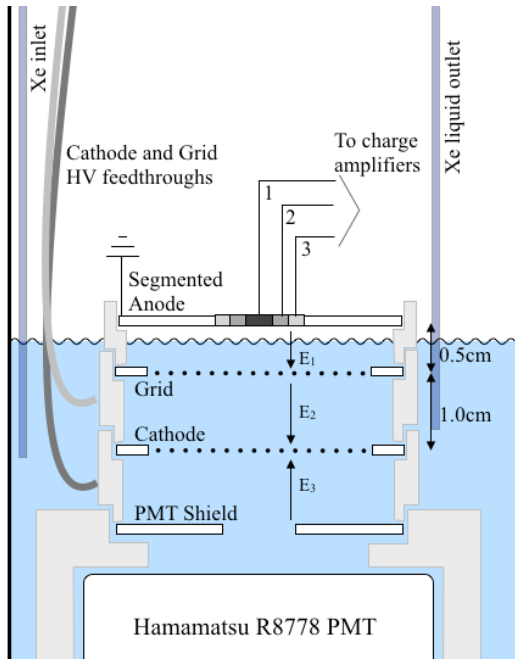


Figure 125: Diagram of the test bed. For this study, the cathode is held at -6.0 kV, and the grid is held at -4.0 kV.  $E_1^{liq} \approx 5.0 \text{ kV/cm}$ ,  $E_1^{gas} \approx 10.0 \text{ kV/cm}$   $E_2 = 1.0 \text{ kV/cm}$ .  $E_3 = 2.7 \text{ kV/cm}$ . The large gray regions represent the structural rings of PTFE. The line between the grid and anode represents the liquid xenon level. The xenon inlet pipes incoming gas directly into the liquid region, and the liquid outlet pulls from the level of the active region. A gas outlet (not pictured) also draws xenon gas into the circulation system to be purified.

a stainless steel frame strung with  $4 \mu\text{m}$  diameter stainless steel wire on a 2 mm pitch. The xenon inlet was a PTFE tube which introduced xenon gas into the liquid region where it was condensed. The xenon liquid outlet was a thin stainless steel capillary that drew liquid from the TPC into the purification system. Both inlet and outlet tubes were placed near holes drilled in the PTFE to aid circulation into the active volume.

Recall from Chapter 3 that a particle interaction in liquid xenon produces primary scintillation photons (S1) and ionization electrons. The ionization electrons are drifted with an electric field into the gas phase, where they produce secondary scintillation light (S2). A single Hamamatsu R8778 VUV-sensitive PMT was installed in Teflon PTFE housing, facing upward to view the active region. Directly above the PMT was a copper shield mask, held at the same voltage as the PMT bias of -1250 V. Recall from Chapter 6 that this test bed has a segmented anode instrumented with charge amplifiers installed at the top of the gas region. The segments are concentric rings, and provide a way to localize events in  $(x, y)$ . The charge amplifiers produce raw and amplified signals. The

amplified signals are shaped by a gaussian amplifier with a module to restore the baseline; the shaped shaped signals can be used as a trigger to select events in a specific ( $x, y$ ) region.

The TPC was filled with 1.5 bar of xenon gas at room temperature. The gas was circulated continuously through the TPC and a heated zirconium getter for at least 24 hours to remove contaminants. The TPC was then cooled to  $-100^{\circ}\text{C}$  while circulating xenon gas. Circulation was stopped, and xenon was condensed into the TPC until the liquid level rose to between the extraction grid and anode. The process of filling the TPC took 4 to 5 hours. The liquid level was kept stable by keeping the temperature and pressure constant in the TPC. During data collection, xenon from the TPC was continually circulated through a getter and re-condensed into the TPC to remove impurities.

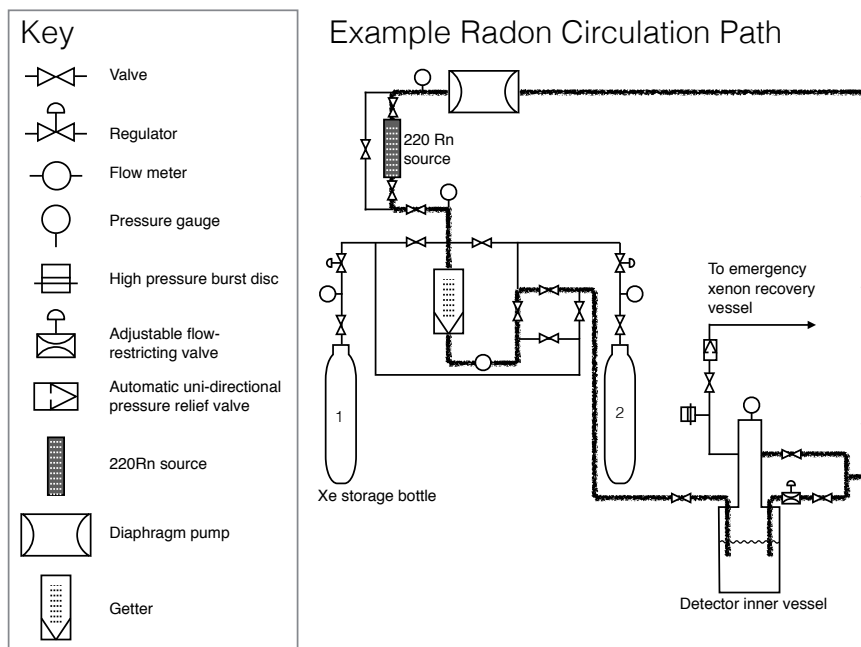


Figure 126: An example a circulation path used for plate out is shown on the pumping and instrumentation diagram. During data-taking the radon source was bypassed. The typical liquid level is indicated on the diagram to show that the outlet drew from the liquid via a capillary, ensuring purification of the liquid xenon. A gas purge also purified the gas column in the detector.

### 7.2.1 PLATE OUT OF $^{220}\text{Rn}$ DAUGHTERS

The procedure to plate out  $^{220}\text{Rn}$  daughters on the inner surfaces of the detector was the same as described above, except that the circulation path

was directed through a 2 kBq  $^{220}\text{Rn}$  source. The  $^{220}\text{Rn}$  decay scheme is shown in Figure 127. The rate of radon activity in the TPC was measured to be  $4.5 \pm 0.5$  Hz during plate out. The total alpha rate was measured by taking repeated 1200 ms traces on an oscilloscope of the PMT with a falling edge trigger and counting the alpha decays. This rate was then halved to get the rate of radon decays. The half factor was necessary because the  $^{216}\text{Po}$  alpha decay followed  $^{220}\text{Rn}$  decay within the time window on the oscilloscope. The  $4.5 \pm 0.5$  Hz rate of radon activity represents activity for all of the space internal to the PTFE support structure. Decay daughters diffused until they contacted a wall or other surface, where they could plate out. Some percentage of decay daughters are expected to be positively charged ions. If the cathode grid was biased, charged decay daughters drifted preferentially to the cathode grid. The cathode voltage during plate outs is noted in Table 4.

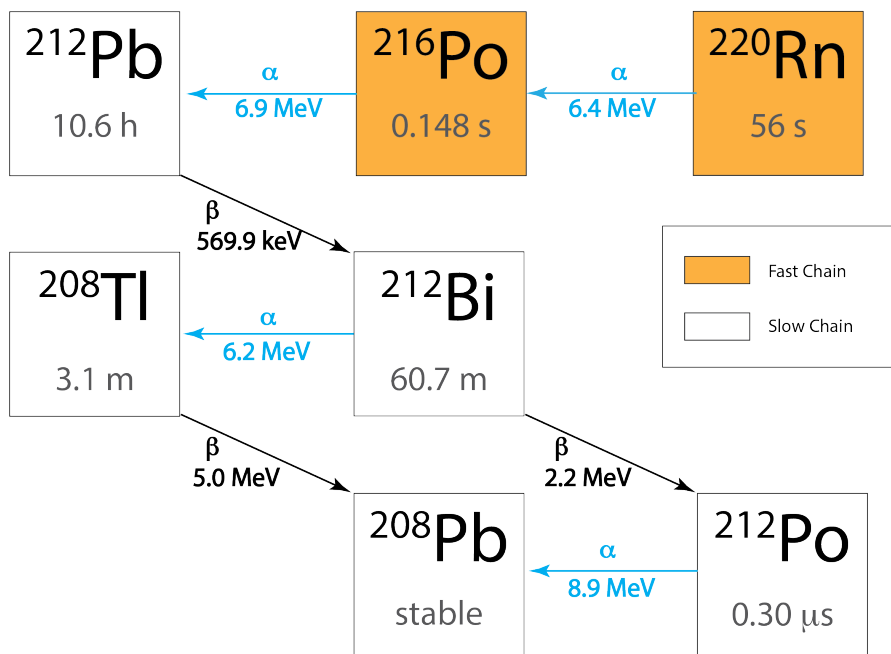


Figure 127: The  $^{220}\text{Rn}$  decay scheme. The fast and slow chains are indicated. Events in the plate out data sets are from the slow chain. Data from [127], image provided by K. Lesko and modified for this thesis.

Prior to filling the TPC with liquid xenon, the circulation was stopped and the xenon gas removed from the TPC and the circulation lines. A vacuum pressure of a few  $10^{-4}$  Torr was achieved in a period of ten minutes. This step ensured removal of  $^{220}\text{Rn}$  and decay daughters which are dissolved in the gas, leaving only those daughters which had plated out on a detector surface. Since the fill time of the TPC is 4 to 5 hours, there were no fast chain alpha decays of  $^{220}\text{Rn}$  and  $^{216}\text{Po}$  in the plate out data. Additional details are summarized in Table 4.

---

Dataset ID	A	B	C	D
<b>Plate-Out</b>				
Circ thru $^{220}\text{Rn}$	yes	yes	no	-
Circ time (h)	24	48	24	-
Cathode (kV)	-1	0	0	-
<b>Data-Taking</b>				
Circ thru $^{220}\text{Rn}$	no	no	no	yes
Cathode (kV)	-6	-6	-6	-6
Grid (kV)	-4	-4	-4	-4
Livetime (h)	$12.02 \pm 0.5$	$23.93 \pm 0.5$	$25.02 \pm 0.2$	$4.15 \pm 0.2$

---

Table 4: Summary of plate out and data-taking conditions. Data sets A and B were taken after circulating radon gas and data set C, background, had no radon circulation. Data set D was taken following dataset A, and radon was circulated in a liquid xenon environment, purposefully introducing radon into the detector bulk to calibrate the detector response. The errors in livetime come from the fact that it is not recorded when datasets ended, only when they started. The error accounts for a new data set not beginning promptly after another dataset finishes.

## 7.2.2 DATA COLLECTION

Voltage records from [PMT](#) and charge channels were collected with a 14-bit ADC with 125 MHz sampling and a 20 MHz low-pass filter. The trigger was a coincidence between the [PMT](#) and the central anode segment, used to select events in the central ( $r < 3$  mm) column of xenon. This avoids any electric field fringing effects.

## 7.2.3 CALIBRATION

In order to identify a signal region for bulk radon daughters, the flow though  $^{220}\text{Rn}$  source was employed directly following dataset A, allowing  $^{220}\text{Rn}$  to flow into the liquid bulk of the [TPC](#). The bulk daughter decay of interest,  $^{212}\text{Bi}$  alpha, has an energy approximately equal to the  $^{220}\text{Rn}$  alpha decay. The alpha signals were sufficient to saturate the biasing circuit of the [PMT](#), so alpha decays within 1 MeV of each other were indistinguishable. Therefore, the region in S1 area vs. S2 area where the bulk

$^{220}\text{Rn}$  alphas appeared was also where bulk  $^{212}\text{Bi}$  alphas were expected (Figure 132).

#### 7.2.4 POSITION RECONSTRUCTION

The central anode segment was assumed to select events from the central column with 100% efficiency. Events occurring under one of the outer concentric segments can produce a signal on the central anode, but the signal was largest at the anode segment nearest the charge. It was not required that there be zero signal on the outer segments, so the (x,y) position of the event is treated as a source of uncertainty, which is taken into account in the calculation of fiducial volume. The drift time of the events was calculated from the time difference between the S1 and S2 pulses, and a linear scaling of 2 mm/us was applied using the electron drift velocity in LXe measurements in [73].

#### 7.2.5 FIDUCIAL VOLUME

Different values for the fiducial volume are presented below. Since there was no calibration to determine the efficiency at which the central anode segment responds to selected events from the central column, it is unclear what the true fiducial volume is. In the future, a calibration scheme could be devised with the  $^{210}\text{Po}$  source discussed in the next chapter. The  $^{210}\text{Po}$  can be deposited on small segments of the grid wire. Depositions could be made at desired locations, i.e. radial distances from the central anode segment, and the response of the anode to a source at different locations could be characterized. For this study measurement, we fold in the uncertainty by calculating several possible fiducial volumes. If the central anode segment only detects events directly underneath it and nowhere else, then the fiducial volume is  $0.39 \pm 0.03$  mL. However, if the central anode segment reacted to events near the walls, the fiducial volume is the entire active region,  $25.3 \pm 1.8$  mL.

### 7.3 ANALYSIS

#### 7.3.1 NUMBER OF $^{220}\text{Rn}$ DAUGHTERS IN THE TPC

As described in Section 7.2.1, the rate of  $^{220}\text{Rn}$  in the TPC was measured to be  $4.5 \pm 0.5$  Hz during plate out. From this, the number of daughter atoms  $^{212}\text{Pb}$  and  $^{212}\text{Bi}$  present in the TPC just prior to filling the liquid xenon were calculated. The number of daughter atoms as a function of the plate out time is shown in Figure 128 along with the data acquisition

---

Anode Segments	1	2	3	Full
Radius (mm)	3	6	9	24
Area (mm <sup>2</sup> )	28	113	255	1810
Volume (mL)	0.39 ± 0.03	1.6 ± 0.1	3.6 ± 0.3	25.3 ± 1.8
Mass (g)	1.1 ± 0.1	4.6 ± 0.3	10 ± 1	73.4 ± 5.2

Table 5: Calculations of fiducial volume. The liquid level is taken to be 14 ± 1 mm. The density of  $\text{LXe}$  near its boiling point is taken to be 2.9 g/mL.

periods for each dataset. This calculation assumes that the diffusion time in the  $\text{PTFE}$  walls was less than the removal time via the capillary, so the daughter of any decay that occurs in the  $\text{TPC}$  remains in the  $\text{TPC}$ .

### 7.3.2 DATA SELECTION

The trigger described in Section 7.2.2 captured the slow chain decays as shown in Figure 127. The  $^{212}\text{Bi}$  beta decay is followed by the 300 ns alpha decay of  $^{212}\text{Po}$ ; these decays are referred to herein as “Bi-Po”.

The aim of this analysis was to reconstruct the z-position of radon daughter alpha decays via the timing difference between the S1 and S2 of an event. Therefore, Bi-Po events were rejected, as the two S2s presented a timing ambiguity. The focus was instead on identifying  $^{212}\text{Bi}$  alpha decays. All events were expected to take place on detector surfaces, so  $^{212}\text{Bi}$  alpha decays in the drift region indicate mobility of plated-out daughters  $^{212}\text{Pb}$  and/or  $^{212}\text{Bi}$ ; it was not possible to determine whether the original position was on the cathode wires,  $\text{PTFE}$  walls, or other detector surface.

The software cuts used to select  $^{212}\text{Bi}$  alphas and reject all other  $^{220}\text{Rn}$  slow chain decays are described below:

1. **Data Cleaning** Remove events with any railed charge channel.
2. **Fiducialization** Require more signal in the central anode segment than the other two concentric anode segments.
3. **Select Alpha Events** The tallest pulse in an event was required to be an S1. Alphas are higher energy than the other decays in the  $^{220}\text{Rn}$  chain, and have a characteristically high light yield, so this cut is generous in keeping all alpha events. S1s were distinguished from S2s by requiring a high percentage of the total pulse area to lie in the first 10 samples of the pulse. This is referred to as a prompt fraction cut.

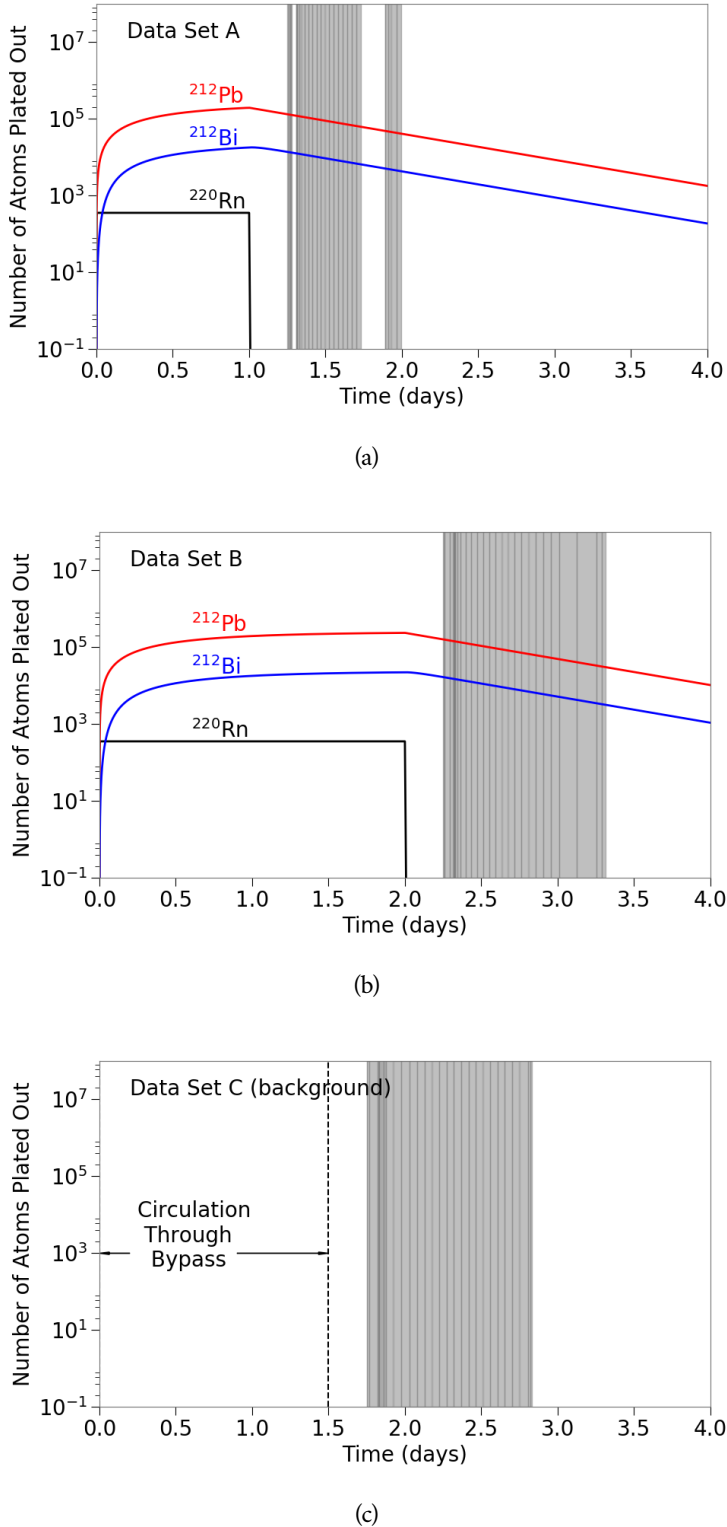


Figure 128: (a) and (b) and (c) show the plate out conditions of datasets A, B, and C, respectively. The gray bands indicate time when data was being acquired. Dataset D (calibration) was taken following dataset A and consisted of a few hours.

4. **Reject Bi-Po Topology** Of the alpha events, those with one S1 and one S2 (single-scatter) were classified as  $^{212}\text{Bi}$  alpha. Events with two S1s (one of which is alpha-like), and one or two S2s were classified as Bi-Po.
5. **Reject Bi-Po Energy** There are two ways a Bi-Po event can mimic the topology of  $^{212}\text{Bi}$  alpha: (i) alpha decay was prompt and so the scintillation signals from the beta and alpha were combined into one large S1 (ii) the beta was ejected into the cathode wire and therefore there was no signal detectable from the beta. To robustly identify  $^{212}\text{Bi}$ , the alpha S1 areas of  $^{212}\text{Bi}$  alpha and Bi-Po events from Step 2 were histogrammed and fit with Gaussian functions.  $^{212}\text{Bi}$  alpha events were tightly selected with a high and low S1 area cut placed on single-scatter alpha events: anything above  $(\mu - 3\sigma)_{\text{Bi-Po}}$  was considered a Bi-Po event and anything below  $(\mu + 3\sigma)_{\text{Bi-alpha}}$  was considered a beta or gamma, and discarded (Figure 129). It should be noted that this cut doesn't affect the signal region for  $^{212}\text{Bi}$  alpha in bulk; it affects the region for  $^{212}\text{Bi}$  alpha on the cathode. This cut is conservative in discarding Bi-Po events, and this leads to a more conservative result for dissolved fraction of  $^{212}\text{Bi}$  alphas.
6. **Z-position Cut** Events in the cathode region were separated from events in the bulk region with a z-position cut (discussed further below).
7. **Bulk Signal Area Cut** Only  $^{212}\text{Bi}$  alpha tagged events which also fell in a signal region expected from calibration with the  $^{220}\text{Rn}$  flow though source (Figure 132) were considered to be daughters which have dissolved.

In order to choose the value for the z-position cut in Step 4, a Monte Carlo approach was used. A Bi-Po decay with a prompt alpha (appears as single-scatter) where the beta penetrates into the bulk region, could mimic a  $^{212}\text{Bi}$  alpha bulk event. To better understand Bi-Po cathode events and the danger of mis-identifying them as  $^{212}\text{Bi}$  alphas in bulk, a Monte Carlo study was done with the  $^{212}\text{Bi}$  beta spectrum (the highest energy beta in the  $^{220}\text{Rn}$  chain) to determine the maximum distance a beta could penetrate into the bulk region. The study yielded a maximum beta penetration of  $z_{\max MC} = 0.12$  cm, see Fig. 130. The z position cut separating cathode from bulk was then defined to be  $z_{\text{cut}} = z_{\max MC} + 3\sigma_{\text{fit}}$ , where  $\sigma_{\text{fit}}$  is just the width of a Gaussian fit for the position of the cathode. Figures 131a and 131c show the cathode position fits as well the the location of  $z_{\text{cut}}$ . The cathode position fit error,  $\sigma_{\text{fit}}$ , was the same for both datasets

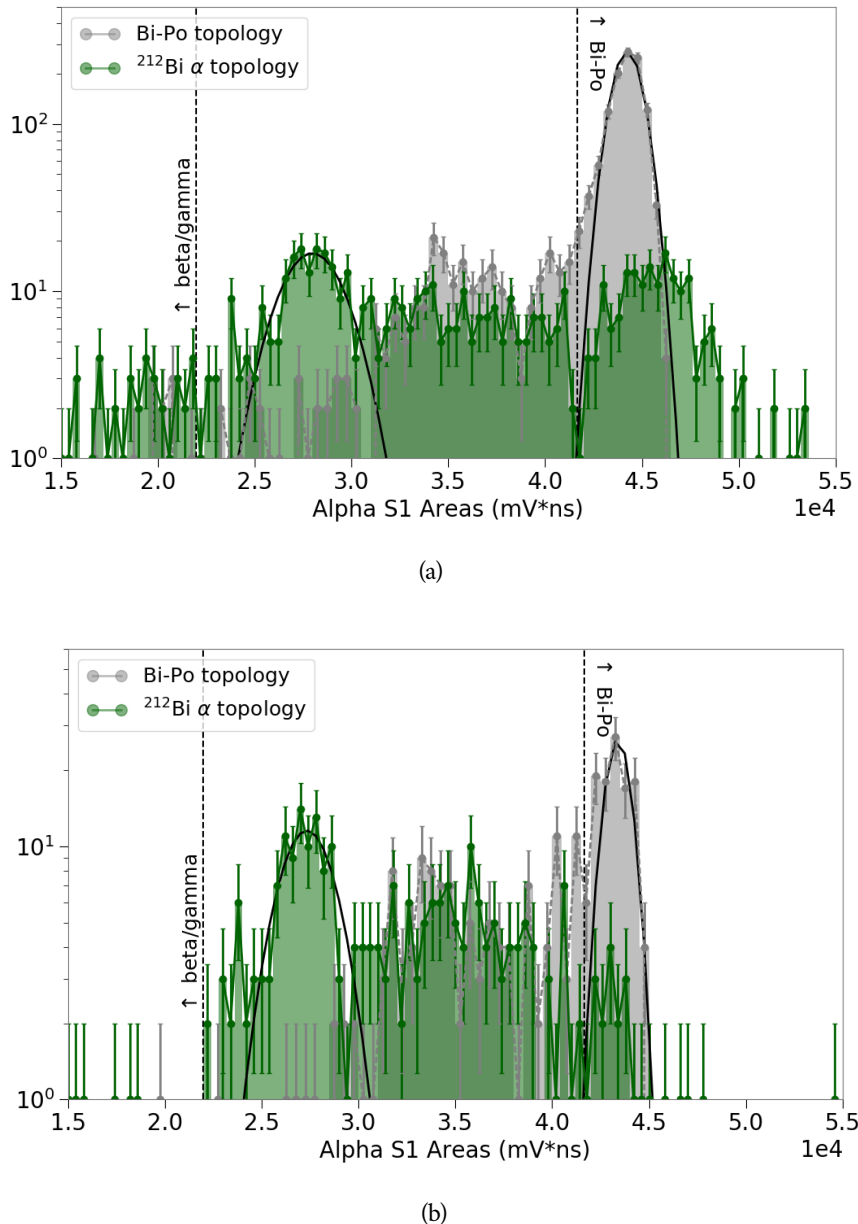


Figure 129: The S1 areas of events that were tagged using topological features.

These distributions were then used to employ the cuts in Step 3. The branching ratio for  $^{212}\text{Bi}$  is 36:64 for  $\alpha:\text{Bi-Po}$ . Dataset (a) showed 10:90 and dataset (b) showed 35:65. It is unclear why the branching ratios for dataset (a) deviate so much from expectation. The trigger is more efficient for Bi-Po events because those decays produce a larger charge signal. It's possible that the cathode being left on during the plate out procedure had some effect on the geometrical distribution of daughters on the cathode wires, which further biased the trigger in the case of dataset (a).

A and B, and was also used to determine  $z_{cut}$  for the background and calibration sets.

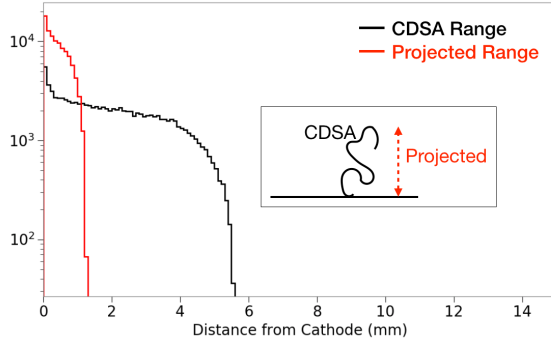


Figure 130: Monte Carlo study to find the maximum distance a  $^{212}\text{Bi}$  beta (2.2 MeV) on the cathode could penetrate into the drift region. The projected range (red) is the relevant curve for this analysis; it shows a beta is not expected to travel more than 1.2mm from the cathode. The plot inset describes the difference between the two ranges: the CDSA range is a measure of the entire path length travelled, the projected range is the one-dimensional maximum range.

One feature that merits further discussion from Figure 131 and Figure 132 is the strong anti-correlation in S1 Pulse Area vs. S2 Pulse Area apparent in cathode events. The cathode region was subject to very high, non-uniform fields due to the thin wires that comprised the cathode grid. Events that occurred on the wires encountered different fields depending on their position on the surface of the wire. Additionally, two events that occurred at exactly the same spot encountered different fields depending on which direction the decay particle (alpha, beta, etc.) traveled. The amount of scintillation and ionization from an interaction in liquid xenon depends on the field at the interaction site. Higher fields result in more ionization electrons being separated from the interaction site and therefore more S2. Mono-energetic events occurring in a uniform field have small anti-correlated fluctuations in S1 and S2 size. Non-uniform fields greatly exaggerate the typical variation in S1 and S2 size resulting in the spread out cathode region (blue) observed in Figures 131 and 132 (right). Events in the bulk region encounter a relatively low, uniform field resulting in a compact signal region in S1 vs. S2 (visible in red region of calibration data, Dataset D).

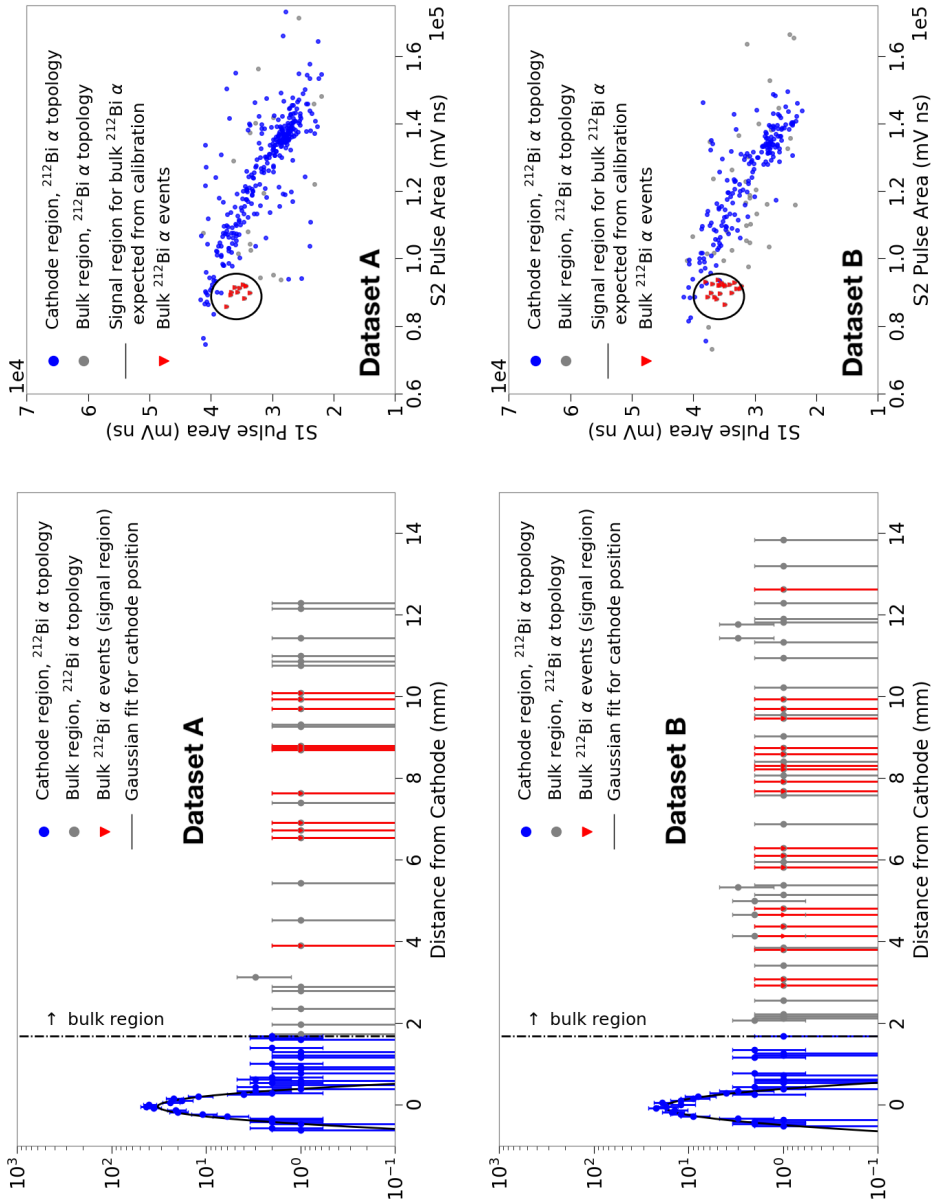


Figure 131: For datasets A and B: (left) Distribution of events in z. (right) The same events distributed in the S1-S2 plane, showing selection criteria for candidate  $^{212}\text{Bi}$  alpha events in the bulk liquid xenon.

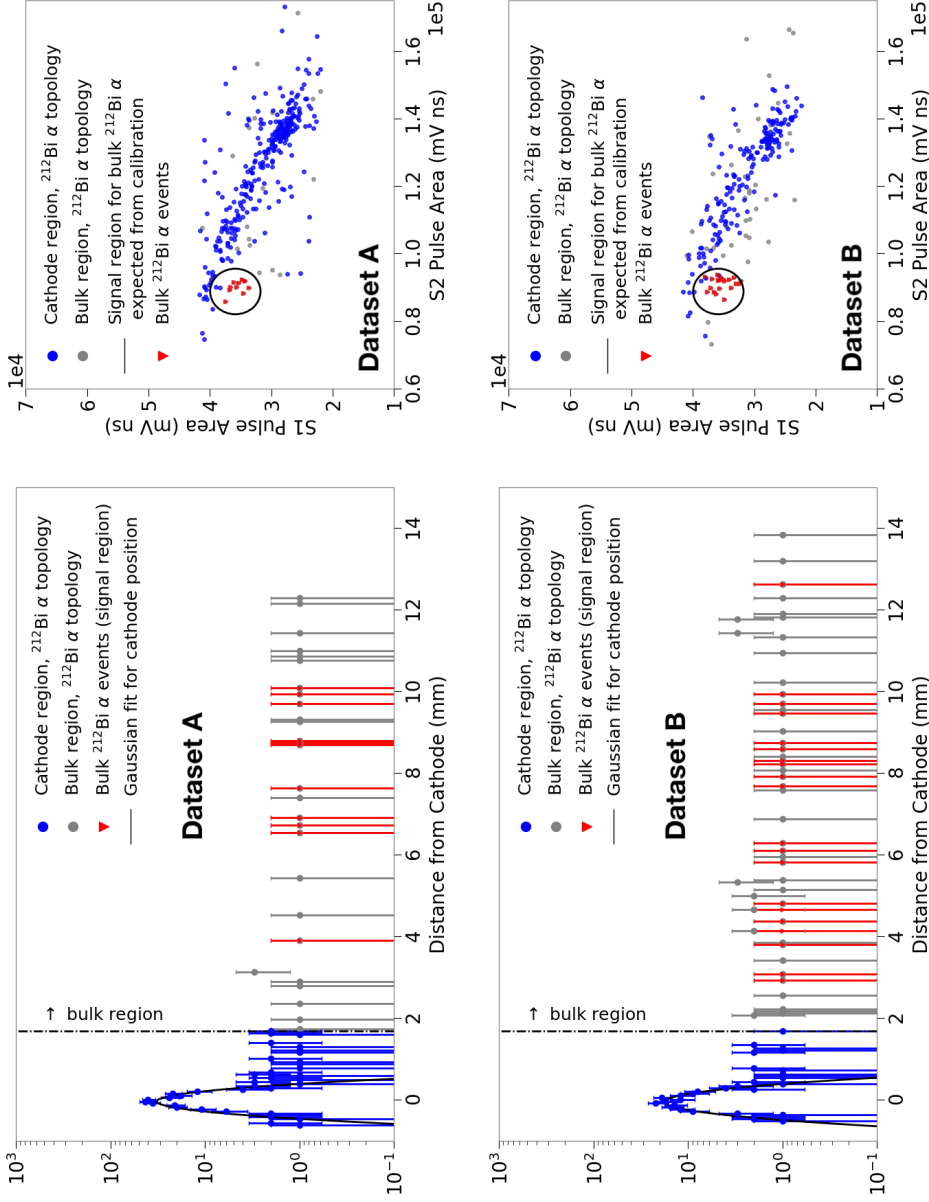


Figure 132: For datasets C and D: (left) Distribution of events in  $z$ . (right) The same events distributed in the S1-S2 plane, showing selection criteria for candidate  $^{212}\text{Bi}$  alpha events in the bulk liquid xenon. The calibration cut shown for dataset D (bottom right) selected events within the region indicated at 98% efficiency. That is, all the gray points passed the [topology] cuts to identify a bulk  $^{220}\text{Rn}$  alpha decay, and the circle restricts the signal region further, keeping 98% of the gray points.

## 7.4 RESULTS

We observed 11 bulk  $^{212}\text{Bi}$  alphas for dataset A, 20 for dataset B, and 1 background event in the signal region from dataset C. The counts of cathode region  $^{212}\text{Bi}$  alphas are presented in Table 6. There was only one background event observed in the signal region, so with 95% confidence the true background count is at most 4.74. The observed counts for dataset A and B lie far above the 95% confidence limit for background, indicating they are true observations of  $^{212}\text{Bi}$  alphas in bulk. Defining the dissolved fraction as  $N_{bulk} / N_{cath}$ , the dissolved fraction of  $^{212}\text{Bi}$  alphas for dataset A ( $\approx 13$  h livetime) is  $0.035 \pm 0.010$ , and for data set B ( $\approx 25$  h livetime) is  $0.099 \pm 0.020$ .

These results indicate that either  $^{212}\text{Pb}$  or  $^{212}\text{Bi}$  itself is soluble (i.e. mobile once plated out) to a small degree in liquid xenon.

Table 6: Number of detected alpha particle events whose energy determination was consistent with  $^{212}\text{Bi}$  decay to  $^{208}\text{Tl}$ . Live times are quoted in Table 4

dataset ID:	A	B	C
Bulk Events	11	20	1
Cathode Events	300	183	4

The solubility is presented in the following units:

$$\frac{\text{Bq (dissolved)}/\text{kg LXe}}{\text{Bq (plated out)}/\text{cm}^2 \text{ (detector surface)}} \quad (58)$$

The solubility calculation is subject to errors from the following factors. Where appropriate, it is noted how the error taken into account in the calculation; otherwise, the assumption is stated.

1. Liquid height (folded into fiducial volume)
2. Area over which charge amps are sensitive (calculation using different fiducial volumes)
3. Area over which daughters are plated out (varying area over which  $^{212}\text{Bi}$  is distributed; a 10% error is assumed in the area calculation due to PTFE contraction with temperature)
4. Initial activity of plated out daughters (assume circulation time for gas to leave inner PTFE stack > decay time of  $^{216}\text{Po}$ )

### 5. Live time calculation (uncertainty included)

Folding in all of these assumptions and errors, we find a best and worst case for datasets A and B. The solubility found in dataset A is at worst  $84 \pm 26$  Bq/kg/Bq/cm<sup>2</sup> and at best  $0.091 \pm 0.030$  Bq/kg/Bq/cm<sup>2</sup>. For dataset B, the worst case is  $58 \pm 18$  Bq/kg/Bq/cm<sup>2</sup> and the best case is  $0.064 \pm 0.021$  Bq/kg/Bq/cm<sup>2</sup>. The largest factor in the best versus worst case is what volume to identify as the fiducial volume. The worst case assumes the central anode segment only selects events directly beneath it, this leads to the highest solubility. The best case assumes the central anode segment may pick up events anywhere in the active region so the fiducial volume is much larger; this leads to the lowest solubility.

## 7.5 DISCUSSION

These results are first evidence that the  $^{220}\text{Rn}$  daughters  $^{212}\text{Pb}$  and/or  $^{212}\text{Bi}$  are soluble in liquid xenon (i.e. mobile once plated-out). The dissolved events are a small fraction of events that are plated-out on detector surfaces. These daughters are proxies for the isotopes  $^{210}\text{Pb}$  and/or  $^{210}\text{Bi}$ , which undergo naked beta decays in the  $^{222}\text{Rn}$  chain and pose a problem for liquid xenon dark matter detectors. Our study counts dissolved  $^{212}\text{Bi}$  alpha events as well as  $^{212}\text{Bi}$  alphas plated out on the cathode. We found 11 counts in dataset A and 20 counts in dataset B consistent with  $^{212}\text{Bi}$  decay in the bulk region; these counts are significantly above a background count of 1. The experimental apparatus is not characterized extensively. Regardless, we carried through the solubility calculation, taking into account uncertainties to arrive at a ‘best case’ and ‘worst case’ result. After carrying out the calculations, the range of solubility observed by our method is 0.1 to 84 Bq/kg/Bq/cm<sup>2</sup>

The limit derived from [LUX](#) observations, stated in the [LZ](#) projected sensitivity paper [135], is  $0.1 \mu\text{Bq}/\text{kg}/\text{Bq}/\text{cm}^2$  for  $^{212}\text{Bi}$  mobility, given  $50 \text{nBq}/\text{cm}^2$  on [PTFE](#) panels. Our observed solubility is much greater than this. One explanation (the “chemistry explanation”) is that we are sensitive to the ‘stuck’ radon daughters that wash off easily in the first few days of an experiment due to the introduction of [LXe](#). Our experiment only tests the initial introduction of [LXe](#). Large [TPCs](#) may then expect an increased rate of radon daughter decays in the fiducial volume at the beginning of a search, but a decreasing rate as these are removed by the getter or are implanted in detector materials.

Another, testable, explanation that would reconcile the different solubilities in the  $^{220}\text{Rn}$  and  $^{222}\text{Rn}$  chain is beta ejection (the “particle physics explanation”). Referring to Figure 127 and Figure 123, both bottleneck decays,  $^{XXX}\text{Pb}$ , are beta decays. However,  $^{212}\text{Pb}$  in the  $^{220}\text{Rn}$  chain has

a beta decay endpoint of 570 keV, which is about 10 times the endpoint energy for  $^{210}\text{Pb}$  in the  $^{222}\text{Rn}$  chain. Daughter recoils from beta decay are indeed small; the endpoints are approximately 0.6 eV for the recoil from  $^{212}\text{Pb}$  decay in the  $^{220}\text{Rn}$  chain and 0.006 eV for the recoil from  $^{210}\text{Pb}$  decay in the  $^{222}\text{Rn}$  chain. As discussed in Section 7.1.1, the physisorption potential for both cases is expected to be below 1 eV. Depending on the exact value, which is unavailable, the  $^{212}\text{Pb}$  decay could provide enough energy to liberate the daughter  $^{212}\text{Bi}$  most of the time, whereas  $^{210}\text{Pb}$  decay produces a maximum recoil value below the potential depth.

Although typically the chemistry-style solubility units ( $\text{Bq}/\text{kg}/\text{Bq}/\text{cm}^2$ ) are utilized, it should be noted that these units imply that larger experiments gain an advantage from the volume/surface area ratio. The term “solubility” implies a chemical equilibrium between dissolved bulk Bi and surface Bi, but it is reasonable that a Bi atom, once ejected into the bulk, will likely not come into contact with a surface again. If this is the case, it may be useful to employ probability-style mobility units: the ratio of activity in the bulk to activity on the surface. Unfortunately, our test bed is not sensitive to its walls; that is, we cannot accurately hope to measure the  $^{212}\text{Bi}$  activity on the walls of the detector like LUX can. However, utilizing the fact that  $\approx 90\%$  of radon daughters are charged [136], we can use dataset A to make an estimate of mobility in probability-style units. Since the cathode voltage was at -1 kV during the plate-out procedure, we can make the assumption the 90% of the radon daughters were collected on the cathode. Using the number of counts observed on the cathode and the livetime from dataset A, we arrive at a plated-out activity of  $^{212}\text{Bi}$  alpha decays of approximately 8 mBq. For dataset B, where the cathode voltage was off during plate out, the number of observed cathode events does not relate easily to the total plated-out rate because daughters can collect on any surface. Continuing with dataset A, we can arrive at an observed bulk rate for  $^{212}\text{Bi}$  alpha decays of approximately  $250 \mu\text{Bq}$ , which gives a mobility probability of  $\approx 0.03$ . The LUX preliminary result<sup>1</sup> gives a mobility probability of  $\approx 0.0026$ . In probability-style units, the laboratory measurement ( $^{220}\text{Rn}$  chain) is a factor of 10 greater than the LUX preliminary result ( $^{222}\text{Rn}$  chain). To explain the discrepancy, the same “chemistry explanation” and “particle physics explanation” cited above apply.

Further study, where a known amount of  $^{220}\text{Rn}$  daughters are plated out on a known area is necessary to measure dissolution rates. Additional studies that compare the solubility of radon daughters adsorbed on different materials, and under different conditions (e.g. temperature) would

---

<sup>1</sup> The measurements were obtained from K. Oliver-Mallory’s presentation at IDM 2018 titled “Latest Analyses and Results from the LUX Experiment.” The activity of  $^{210}\text{Pb}$  on the wall in the fiducial volume drift range for WS-2014/16 is  $> 9.6 \pm 0.6 \text{ mBq}$ . The activity of  $^{210}\text{Pb}$  in the fiducial volume is  $< 0.099 \mu\text{Bq}/\text{kg}$ .

also be useful. The effect of cleaning these surfaces before searching for dissolved daughters should also be investigated.

If beta recoil, not ‘washing’ by the LXe, is the cause of radon daughter solubility, then the high rate seen by this study of  $^{220}\text{Rn}$  can be reconciled with the low rate of  $^{222}\text{Rn}$  daughter dissolution seen in LUX.

Table 7: Using observations from Table 6, proceed through solubility calculation.

Dataset ID:	A	B
Total Inferred Bi decays	$20 \pm 6$	$36 \pm 11$
Livetime (hours)	$12.02 \pm 0.5$	$23.93 \pm 0.5$
$\mu\text{Bq}$ Bi in bulk	$460 \pm 140$	$420 \pm 130$
Bq (dissolved) / kg LXe (smallest fiducial)	$0.42 \pm 0.13$	$0.38 \pm 0.12$
Bq (dissolved) / kg LXe (largest fiducial)	$0.0063 \pm 0.0020$	$0.0057 \pm 0.0018$

Plate-Out Areas		
	Area	
Total Internal Area Including PMT	$496 \text{ cm}^2$	
Active Region PTFE	$36 \text{ cm}^2$	

Dataset ID:	A	B
Number of $^{212}\text{Bi}$ Plated-Out	13191	17280
Bq (plated-out)	2.5	3.2
Bq (plated) / $\text{cm}^2$ min	$0.0050 \pm 0.0005$	$0.0065 \pm 0.0007$
Bq (plated) / $\text{cm}^2$ max	$0.069 \pm 0.007$	$0.089 \pm 0.009$
Solubility min	$0.091 \pm 0.030$	$0.064 \pm 0.021$
Solubility max	$84 \pm 26$	$58 \pm 18$

# 8

## STUDIES OF DELAYED SINGLE ELECTRON SIGNALS

---

### 8.1 MOTIVATION FOR STUDYING DELAYED SINGLE ELECTRON SIGNALS

Delayed single electron signals, known colloquially as “electron trains”, are a generic single electron background in dual-phase [LXe TPCs](#). Proportional scintillation signals consistent with those of single electrons, emitted regularly over time, are known to follow high energy depositions. These electron trains can last  $O(10 - 100)$  ms, which is the equivalent of several event windows for most [LXe TPCs](#). Single electron signals were observed and investigated by ZEPLIN [137] [138], Xenon100 [139], and [LUX](#) [117].

[LUX](#) collaborator J. Xu investigated delayed electron signals in [LUX](#) [117]. A plot of an electron train from [LUX](#) is shown in Figure 133. Note that the time window is orders of magnitude greater than the [LUX](#) event window of 400  $\mu$ s, and the maximum drift time for Run03 of 300  $\mu$ s. In addition to electron trains, the [LUX](#) collaboration colloquially refers to one type of delayed electron signal as “electron burps” or “e-burps”. They are characterized by the sudden emission of  $O(100 - 1000)$  electrons. Xu noted that e-burps can be part of an electron train, but unlike electron trains in general, he found e-burps to be uncorrelated with the size of the previous event (see inset of Figure 133).

In Section 3.4.2, we discussed several dark matter searches that differ from the standard [WIMP](#) search and how they can be completed with dual-phase [LXe TPCs](#). In particular, recall the Xenon10 search for low-mass [WIMPs](#) [86]. The S2-sensitive trigger threshold was set to the level of a single electron, but an analysis threshold of 4 electrons was required for S2 size. The reason behind this is illustrated in Figure 134. Although single electrons following a high-energy event can be positively identified as belonging to an electron train, electron trains can last  $O(10 - 100)$  ms. In any event window following the start of electron train, it is unknown whether the single electron is truly a small energy deposition from a low-mass dark matter event or if it belongs to an electron train. Moreover, sin-

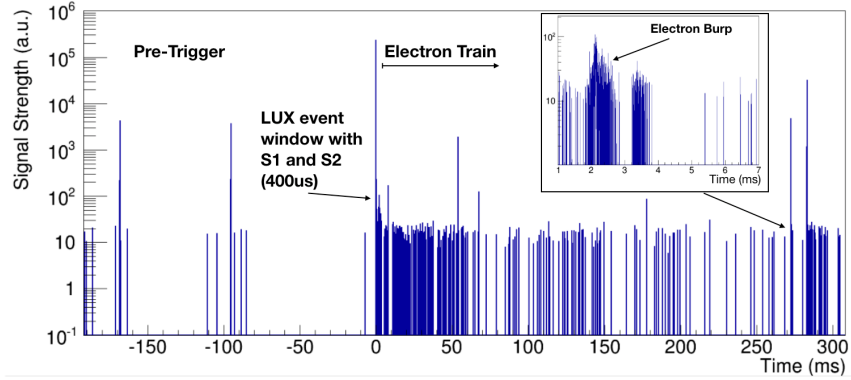


Figure 133: An electron train spanning several ms. Pre-trigger and electron train regions are indicated along with the LUX event that originated the electron train. The inset shows the shorter time structure of e-burps. The y-axis is a proxy for phd/sample. Figure courtesy of J. Xu.

gle electrons from a train can pile up in time, creating energy depositions the size of 2 and more electrons – so an analysis threshold of 2 electrons is not sufficient to cut out electron train backgrounds. In general, electron trains are irritating for WIMP searches because some percentage of the detector livetime is taken up by electron train pile-up; but they greatly limit the discovery potential for low-mass searches, as the expected signal size (S2 of 2 or 3 electrons) is possibly electron train pile-up, and therefore must be considered as such.

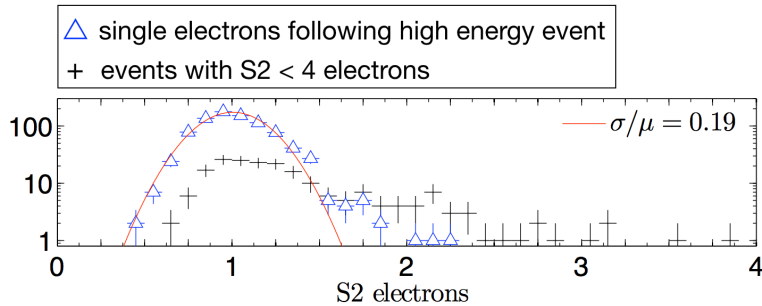


Figure 134: A histogram of the small electron signals in the Xenon10 low-mass dark matter search. The significance of the plot is that single/few-electron pulses immediately following an S2 can be positively identified as belonging to an electron train. In subsequent event windows, single electrons can appear alone or in coincidence as a small S2, which can be mistaken for the S2 produced by a low-mass dark matter interaction. Figure adapted from [86].

Xenon100 measured the rates of 1-, 2-, and 3-electron signals following an S2 [139]. They saw a relation of the time constants  $\tau_3 \approx \tau_1/3$  for 3-electron signals compared to 1-electron signals, and  $\tau_2 \approx \tau_1/2$  for 2-electron signals. They note that if multi-electron signal results arise from accidental time coincidences of single electrons, these time relations can be explained. Quoting from [139] :

Indeed if  $R_1$  is the rate of single electrons, the accidental time coincidence of  $n$  single electrons is  $R_n = R_1^n \cdot \Delta t^{n-1}$ , where  $\Delta t$  is the time coincidence window, which corresponds to the mean S2 width ( $\sim 1 \mu\text{s}$ ).... [T]he electron rates decrease with time by following the expression  $R_n(t) = R_n(0) \cdot \exp(-t/\tau_n)$ . By substituting this equation in the previous formula we obtain the final relation  $\tau_n = \tau_1/n$ .

## 8.2 ORIGIN OF DELAYED SINGLE ELECTRON SIGNALS

While the origin of delayed single electron signals is still an area of active research, some behavior of electron trains are fairly well understood. An electron train can be split into two time regions: the primary event window ( $O(100) \mu\text{s}$ , e.g.  $400 \mu\text{s}$  in LUX), and the following train, which continues for  $O(10 - 100) \text{ ms}$ . A few features are typically evident in the primary event window, which have origin in physical phenomena. These phenomena and what is found in the literature are discussed in the following subsections. The testbed study and its result, which shed more light on the origin of delayed single electron signals, are presented later in the chapter.

### 8.2.1 PHOTOIONIZATION ON GRIDS

The large number of VUV photons in big S2s are capable of liberating electrons from metallic electrodes. Electrons can be photoionized on any grid in the TPC, but the effect is largest on the grids closest to the gas gap where the S2 is generated. Photoionized electrons from the anode aren't detected because they have essentially no space in which to proportionally scintillate. Photoionized electrons from extraction grid are directed toward the gas gap, extracted and then undergo proportional scintillation. These electrons join the S2 signal at a delay approximately equal to the distance between the extraction grid and the liquid-gas interface. Large S2s have tails that are composed of electrons photoionized from

the extraction grid. An average of many high-energy S2s, clearly shows the photoionization feature (Figure 135).

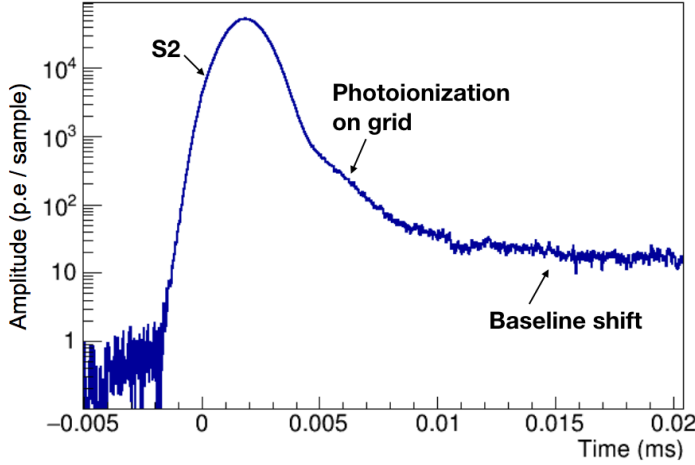


Figure 135: The average of many high energy S2s from LUX, plotted with logarithmic y-scale, showing a prominent photoionization feature. After the photoionization, an instrumental effect is visible: for the highest-energy events, one to a few PMTs often do not return to baseline quickly, which gives the single electrons in the following train artificially higher areas. Figure from J. Xu.

## 8.2.2 PHOTOIONIZATION OF IMPURITIES

Electronegative impurities in the liquid (e.g. O<sub>2</sub>) capture ionization electrons from events as they are drifted to the gas region (e.g. O<sub>2</sub> binds an electron at 0.45 eV to become O<sub>2</sub><sup>-</sup>). Just as the VUV photons can ionize electrons from grids, they can also ionize electrons attached to impurities. Xenon100 found that the rate of single electrons in the primary event window scaled with S2 size, as well as the concentration of impurities [139] (see Figure 136). Some of the electrons in the primary event window of an electron train are now believed to come from photoionized impurities. This is supported by Xenon100 data which showed that the rate of single electrons has a sharp cut off corresponding to the maximum drift time, and the the PMT hit pattern of the multi-electron signals are not localized around one PMT but rather spread over the PMT array [139].

## 8.2.3 DELAYED EXTRACTION OF TRAPPED ELECTRONS

Dual-phase LXe TPCs depend on the ability to extract electrons from liquid into gas. This is accomplished with some efficiency, called the EEE.

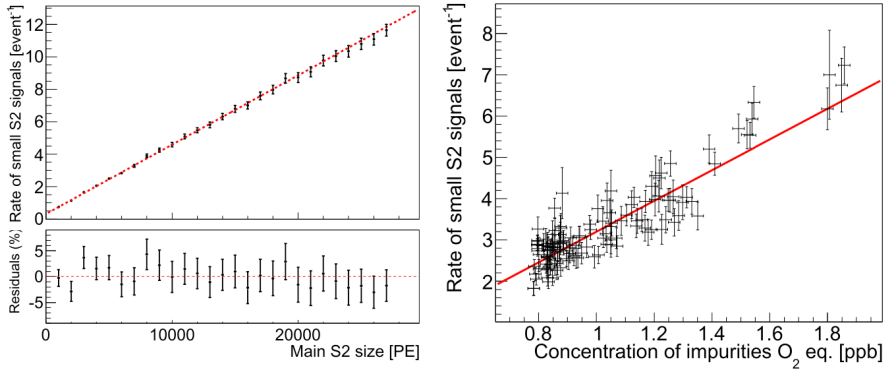


Figure 136: (left) The per-event rate of single electron signals 20 to 150  $\mu$ s after the main S2 of a single-scatter type event as a function of the main S2 size. The fit line and residuals show a good proportionality in the relation. (right) The per-event rate of single electron signals, for events with the main S2 between 5000 and 10000 phe, as a function of the O<sub>2</sub>-equivalent concentration of impurities in liquid xenon. Figures from [139].

Gushchin et al. measured the absolute EEE in xenon and argon in 1982 as function of electric field [140] (see Figure 137). Their result extends to an extraction field of 5 kV/cm in the liquid. It is common practice for modern experiments that achieve an extraction field  $\gtrsim$  5keV/cm to assume they have 100% extraction, an assumption based on the Gushchin result. Relative extraction efficiency is measured only by the size of the S2 scintillation light and inferred number of initial ionization electrons based on calibration source energy and knowledge of recombination. Relative measurements of EEE as a function of extraction field assume 100% extraction at the highest field and scale the other points accordingly. In contrast, absolute extraction efficiency measurements measure the number of electrons generated in the liquid as well as how many are extracted with no scaling.

Since there does not exist a second absolute measurement of EEE out to higher extraction fields, it is uncertain when 100% EEE is reached in LXe. However, it is well known that the number of extracted electrons depends on the extraction field. In addition to photoionization of impurities, it is thought that the unextracted electrons are liberated from the liquid surface at a later time, making up some component of electron trains [139], [141]. To understand why we must consider the energy of the electrons in the liquid, and the potential barrier they encounter in order to escape into gas.

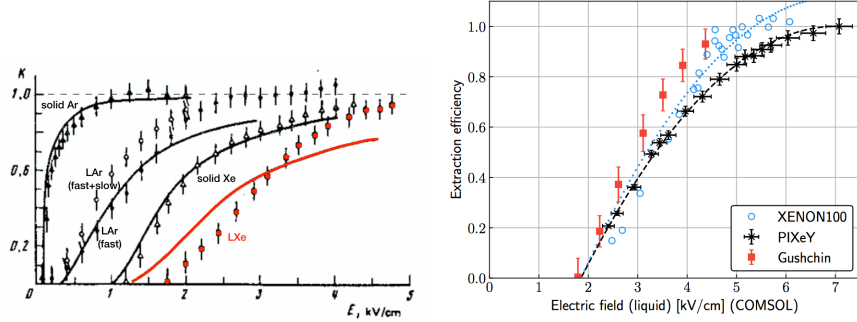


Figure 137: (left) The absolute EEE measured by Gushchin from [140]. The [LXe](#) points were re-colored red. (right) Two relative EEE measurements from modern experiments, Xenon100 and PIXEY, compared to Gushchin. The plot is from the PIXEY result [141], where the authors fit their result with a quadratic function ( $y = ax^2 + bx + c$ ). The fit to the PIXEY data (black dashed line) is scaled by a constant and applied to the Xenon100 data (blue dotted line).

When an electron approaches a dielectric boundary held at a constant potential, a potential barrier results from its image charge. This barrier, called the Schottky barrier, takes the form [142]:

$$\phi_b = \frac{e^2}{8\pi\epsilon_0 z} \frac{\epsilon - 1}{\epsilon + 1} \quad (59)$$

where  $z$  is often taken to be the lattice spacing of the medium,  $\epsilon$  is the dielectric constant of the medium, and  $\epsilon_0$  is the usual vacuum permittivity. If [LXe](#) is arranged in a simple cubic lattice,  $z \approx 4 \text{ \AA}$ , and the calculation yields  $\phi_b = 0.61 \text{ eV}$  [142]. The potential barrier of liquid xenon was measured by Tauchert to be 0.67 eV [143]. There are two modes for emission of electrons across a surface boundary: (1) “hot” electrons accelerated by an electric field gain enough energy to overcome the barrier and be extracted (2) emission of thermal electrons, where only electrons in the tail of the velocity distribution have enough energy to escape the boundary. For an external field  $E$ , the Schottky barrier is lowered by [142]:

$$\Delta\phi_b = e \left( \frac{eE}{4\pi\epsilon_0 z} \frac{\epsilon - 1}{\epsilon + 1} \right)^{1/2} \quad (60)$$

The  $E$  field also results in the aforementioned heating of the electrons. The new energy distribution  $f$  can be determined by solving the Boltzmann equation as in [144], but this is not shown here. With  $f$  and adjusted

barrier height, the EEE as a function of electric field can be calculated. It is the fraction of electrons with energy expectation value above  $\phi_b - \Delta\phi_b$ :

$$\kappa = \int_{\phi_b - \Delta\phi_b}^{\infty} K^{1/2} f(K) dK / \int_0^{\infty} K^{1/2} f(K) dK \quad (61)$$

$K = K(E)$  is the electron energy, which is implicitly a function of the electric field and  $f(K)$  is the energy distribution of the electrons under the influence of an electric field. The factor within the integral is  $K^{1/2}$  instead of the usual  $K$  in order to select only electrons that have an upward velocity component. The red LXe line in Gushchin's EEE result (Figure 137 (left)) is from this calculation with the assumption that  $\phi_b = 0.61$  eV. Bolozdynya follows a similar approach and notes that electrons which are not emitted as hot electrons are thermalized by collisions and can be emitted later as thermal electrons [145]. Others have treated the potential barrier as a free parameter and fit to data. Gushchin, seeing that the line did not fit the data for LXe, treated the value of  $\phi_b$  as free in the integral above. He found  $\phi_b = 0.85$  eV was a better fit [140], but the agreement is still not very satisfying. Sorensen implemented an  $n$ -th chance model for electrons approaching the liquid-gas boundary, where the cumulative probability of emission after  $n$  attempts is  $\kappa_n = 1(1 - \kappa)^n$ , where  $\kappa$  is as in Equation 61 [142]. This reference shows that with  $\phi_b = 0.34$  eV and  $n = 20$ , the  $n$ -th chance model fits Gushchin's original data [142]. If the  $n$ -th chance model is applied, with some assumptions about the relaxation time for electrons to be thermalized, the time constant for emission of thermal electrons is  $O(10)$  ms. Both Bolozdynya [145] and Sorensen [142] note that the relaxation time is dependent on field (strength and direction) and temperature. Sorensen adds possible diffusion effects, fluid flow, varying surface height, etc. One critique of the  $n$ -th chance model is that it is unclear how the electron lifetime near the surface could be  $O(10)$  ms, while current LXe TPCs achieve electron lifetimes much lower, e.g. the electron lifetime during LUX Run03 ranged from 600-1000  $\mu$ s. The argument here is that the electrons that aren't emitted should be absorbed by impurities, so they are not free to have  $n$  chances of emission. Although research is still on-going into how to properly model the physics of electron extraction, there is agreement that a fast component from extracted hot electrons yields the initial S2 and a thermal component from the unextracted electrons contributes in part to the electron train.

## 8.3 TEST BED STUDIES OF ELECTRON TRAINS

An initial goal of the test bed described in Chapter 6 was to complete an absolute measurement of EEE, since there has been so such measurement

since Guschin's 1982 result. Unlike typical TPCs, the testbed can be "over-filled", with the liquid level above the anode, and the generation of ionization electrons in the liquid can be measured with the charge amplifiers. The liquid level can then be dropped between the anode and extraction grid for a measure of extracted electrons with S2 (and with the charge amplifiers). During the multi-year process of instrumenting and understanding the test bed, this goal changed and evolved. In particular, it became more interesting to try and probe the source of electron trains with the hope of eventually eliminating them, rather than try to measure the EEE. In order to provide a record, the remainder of this chapter briefly describes the attempts made with the radon source and configuration as in Chapter 7. Finally, the most recent results published in [146], which used the  $^{210}\text{Po}$  source described below, are summarized.

### 8.3.1 RADON SOURCE AND "FULL TPC CONFIGURATION"

Here, full TPC configuration refers to the same detector configuration as in the previous chapter (Chapter 7); specifically, there is a 1 cm drift region and an 0.5 cm extraction region. Both cathode and extraction grids are employed. The  $^{220}\text{Rn}$  flow through source was initially chosen for electron train studies because of some nice properties of alpha decays. The fast chain alphas from  $^{220}\text{Rn}$  are:

- **High Energy** The alpha events in the  $^{220}\text{Rn}$  fast chain have energies of 6.4 MeV ( $^{220}\text{Rn}$ ) and 6.9 MeV ( $^{216}\text{Po}$ ). Applying the LXe W-value, shows that these alphas generate  $\mathcal{O}(500,000)$  quanta. Although 90% of alpha energy goes into S1 [73], that still leaves  $\mathcal{O}(50,000)$  electrons to be detected. In contrast, a 662 keV  $^{137}\text{Cs}$  button source produces  $\mathcal{O}(50,000)$  quanta, but this value is ~halved by recombination. Alpha light and charge yields also do not vary greatly with applied field (Figure 22 (right)), which is convenient from an experimental standpoint of tagging a signal region and adjusting trigger conditions.
- **Uniformly Distributed with Compact Track** The  $^{220}\text{Rn}$  can be deposited directly into the LXe, yielding a uniformly distributed source which can be fiducialized to the inner-most anode segment to avoid field edge effects. Alphas do not travel far, and so a deposition could be realistically expected to deposit all its energy in the  $(x, y)$  resolution of the detector, i.e. under one and only one anode segment. This is contrast to betas, which can travel; recall the 2.2 MeV beta in the  $^{220}\text{Rn}$  chain that could travel 1.2 mm from Chapter 7).

We expected to be able to select the monoenergetic alpha signal of either  $^{220}\text{Rn}$  or  $^{216}\text{Po}$  with the **PMT** signal. However, **PMT** saturation merged the two fast chain alphas in the S1 spectrum. There are two types of **PMT** saturation effects relevant to the R8778 **PMTs** used in **LUX**: anode saturation and capacitor depletion [91]. The effects of the two types of saturation are shown in Figure 138. Quoting directly from [91] to describe these two types of saturation:

- **Anode Saturation** The repulsive field created by a large number of electrons confined to a small spatial extent (an effect known as space-charge) yields nonlinear signal production. Since the electron cloud density is exponentially larger at the latter stages of the photomultiplier, this effect is most dominant at the anode. Anode saturation is only dependent on the instantaneous (peak) current value of the output signal. Anode saturation prevents the electron signal in the anode from further increasing. When the anode is fully saturated, the output signal cannot increase in size any further. As such, anode saturation defines the maximum peak signal that the **PMT** can output. Increasing the voltage across the latter stages can provide a modest increase in anode linearity.
- **Capacitor Depletion** A **PMT** is a current source. Due to the nature of the electron multiplication process, the signal current direction is opposite to that from the bias current. When a large signal current pulse is generated at the anode, the **PMT** bias current in the last resistor decreases proportionally and the last dynode stage becomes temporarily unbiased. This effect leads to a decrease in signal size (smaller gain) and can completely turn off the multiplication process if the signal current is comparable to the bias current. A common method for mitigating the dynode voltage loss effect is to add capacitors that can provide reserve charge during a signal current pulse. These capacitors are called decoupling capacitors. Saturation effects from capacitor depletion occur when the reserve charge in the decoupling capacitors is insufficient to counteract the signal current and prevent **PMT** un-biasing. Whereas anode saturation is caused by the instantaneous current, capacitor depletion is caused by the total charge drawn for a signal

It is noted in C. Faham's thesis that any signal within  $50\ \mu\text{s}$  after a large pulse is also subject to non-linearity [91]; therefore, the S2 signals also did not yield a usable spectrum for separating  $^{220}\text{Rn}$  from  $^{216}\text{Po}$  decays. Operating the **PMT** at a bias voltage  $\lesssim 1000\text{ V}$  resulted in less visible saturation, but single photoelectron sensitivity was lost below an operating bias voltage of  $\lesssim 1200\text{ V}$ . Since single electron proportional scintillation signals

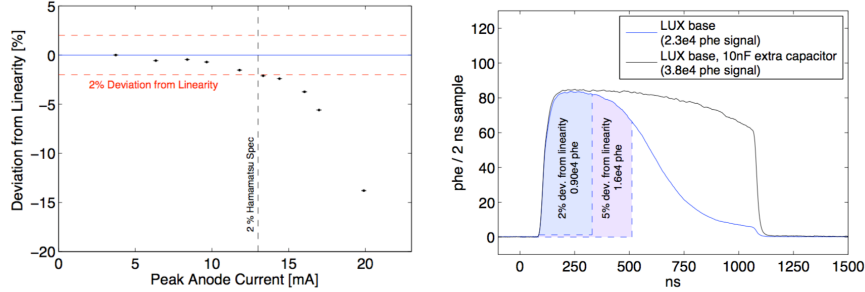


Figure 138: (left) Effect of anode saturation measured as deviation from signal linearity as a function of the peak anode current. (right) Effect of capacitor depletion on the voltage trace in the R8778. The blue trace shows the largest S2-like pulse that can be generated with a [LUX](#) voltage divider base (generated with a  $1\ \mu\text{s}$  square pulse on a blue LED); the 2% and 5% deviations from linearity are shown. The fall-off indicates the capacitor is depleted and the photomultiplication process is temporarily turned off. The black trace shows the effect of adding an extra capacitor between dynodes Dy9-Dy10. Figures are from [91], which also contains more information about the [LUX PMTs](#) and bases.

are comparatively small, single phe sensitivity was desired for electron train studies. A series of masks were implemented to try reduce the overall light collection, while still retaining single phe sensitivity. Of course, on the other side, over-masking and not collecting enough photons would also result in inability to distinguish peaks. The masks are shown in Figure 139. Initially, we started with the smallest mask and thought we had made the mistake of cutting out too many photons. However, even with the smallest mask size, which reduced the effective [PMT](#) cathode area by  $\sim 98\%$ , the anode current was estimated to be  $\sim 50\ \text{mA}$ , which from Figure 138 is far past where the effects of anode saturation cause loss in signal linearity. The anode current can be estimated using the following relations:

$$I_{\text{PMT}} \approx \frac{N_{\text{photons}} \cdot G \cdot e}{S1_{\text{width}}} \quad (62)$$

where  $G$  is the [PMT](#) gain. Note that the numerator gives the charge at the [PMT](#) anode and the  $S1_{\text{width}}$  is in units of time; thus the equation above is a simple current = charge / time relation. For the 2% mask, the highest voltage without visual saturation was 1250 mV. The single phe peak was

at 35 mV/ns for that bias voltage, which corresponds to a gain of  $8.7 \times 10^6$ . **PMT** gains can be calculated by the relation:

$$G = \frac{SPHE \cdot 1 \times 10^{-12}}{R \cdot e} \quad (63)$$

where *SPHE* is the pulse area of a single photoelectron in mV/ns, obtained from a spectrum of dark current pulses; an example of a single phe spectrum in Figure 140 shows a single phe peak at about 80 mV/ns. *R* is the effective output resistance of the **PMT** base,  $R = 25 \Omega$  for the **LUX PMT** bases [91]. The factor  $1 \times 10^{-12}$  reflects that the original photoelectron was amplified by the 12 dynodes of the R8778. The average alpha pulse area with the 2% mask and the **PMT** at 1250 mV bias was 37500 mV/ns, so combining with the single phe size,  $N_{photons} = 1070$ . Combined with a typical  $S1_{width}$  of 30 ns, this yields  $I_{PMT} \sim 50 \text{ mA}$ .

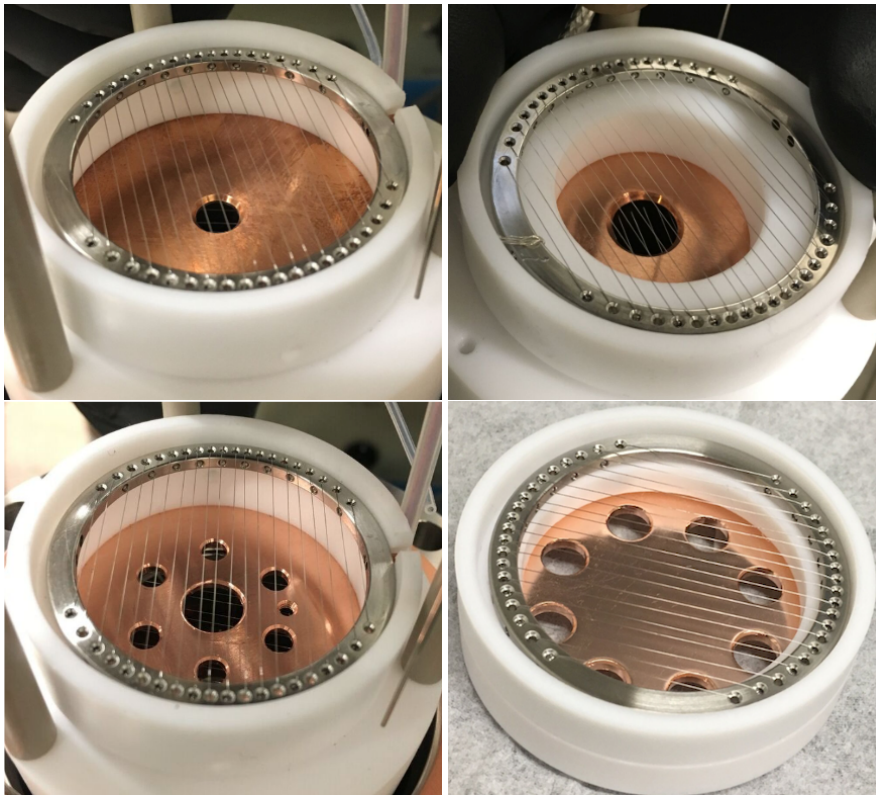


Figure 139: A series of **PMT** masks made from **CF** blanks which reduced the light collection area of the **PMT** to approximately 2%, 5%, 15%, and 10% (clock-wise from top left). The masks were installed in place of the **PMT** shield grid, and similarly to the **PMT** grid, they were kept at the same bias voltage of the **PMT**.

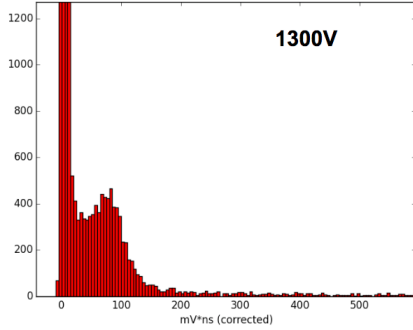


Figure 140: The single phe spectrum from the [PMT](#) with a bias voltage of 1300 V.

The spectrum was obtained by using a variable gain amplifier to 100x amplify the [PMT](#) signal (at room temperature, in vacuum). A [NIM](#) quad discriminator was used to externally trigger the picoscope. The waveforms were summed in a fixed window, and the results were histogrammed. The single photoelectron peak is appears around 80 mV/ns, and the double photoelectron peak is visible around 160 mV/ns. (See [72] for more detail on the double photoelectron emission in [VUV](#)-sensitive [PMTs](#).)

While [PMT](#) saturation was the main challenge for selecting a monoenergetic source from the  $^{220}\text{Rn}$  fast chain alphas, geometrical signal efficiency was also an issue. The central anode segment was only 1% of the total anode area, so most of the signal was not in this area. The radon could be distributed directly into the teflon stack (with a [PTFE](#) tube) for a higher rate, but this increased the noise environment for the charge amplifiers. In theory the charge spectra should have had two distinct populations for the  $^{220}\text{Rn}$  and  $^{216}\text{Po}$  alphas, but with the slow trigger rate and ambient background radiation ( $\beta$ ,  $\gamma$ ) depositing various amounts of charge across the anode segments, two peaks could not be distinguished. A large loss in charge was also observed across the extraction grid (see Figure 142), which decreased the signal to noise ratio. Bunemann's equation describes the necessary condition for grid transparency for transiting charges, i.e. it describes what relative voltages of cathode, grid, and anode result in zero electric field lines from the cathode terminating on the grid [147] [148]:

$$\frac{V_A - V_G}{V_G - V_C} \cdot \frac{D_{C-G}}{D_{G-A}} \geq \frac{1 + \rho[1 + \frac{d}{4\pi D_{G-A}}(\rho^2 - 4\ln\rho)]}{1 - \rho[1 + \frac{d}{4\pi D_{C-G}}(\rho^2 - 4\ln\rho)]} \quad (64)$$

Where C denotes cathode, G denotes grid, and A denotes anode.  $d$  is the grid pitch,  $D_{C-G}$  and  $D_{G-A}$  are respectively the distances between C-G and G-A and  $\rho$  is defined as  $\rho \equiv 2\pi \frac{r}{d}$  where  $r$  is the grid wire ra-

dius. The Left Hand Side ([LHS](#)) and Right Hand Side ([RHS](#)) of Equation 64 can be reorganized as:  $T \equiv \log_{10}(LHS - RHS)$  to give the transparency condition  $T \geq 0$ . An example result,  $T$  as a function of  $V_C$ , is shown in Figure 141 for a grid voltage of -4.0 kV. The charge-vs-drift plot in Figure 142 shows a loss of charge across the grid for voltage setting  $V_G = -4.0$  kVm,  $V_C = -6.0$  kV, and  $V_A = 0$ V. According to Bunemann's equation plotted in Figure 141, a cathode voltage of  $V_C = -6$  kV should have resulted in a transparent grid. Different voltages of  $V_C$  were also tried, but they resulted in smaller drift fields, which reduced the charge yield from alphas. It is possible the grid transparency condition was affected by the relative angle of the cathode grid wires to those of the extraction grid; this was not investigated further.

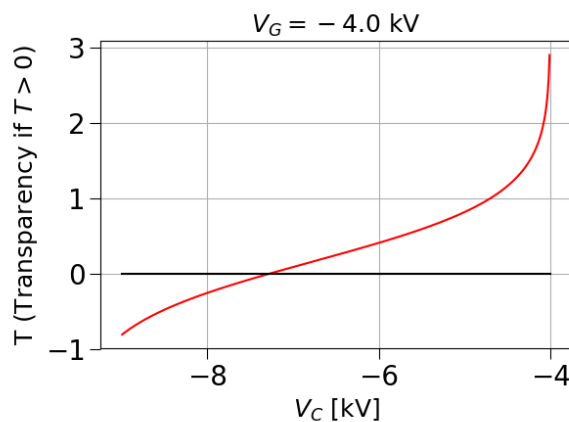


Figure 141: Bunemann's condition for grid transparency for a grid voltage of -4.0 kV. The cathode voltage must be between -7.24 kV and -4 kV to achieve grid transparency. A cathode voltage greater than -4 kV would result in a “reverse field”, with the electrons drifting downward to the [PMT](#) instead of the upward to the gas gap. For cathode voltages below -7.24 kV (more negative), field lines terminate on the grid and the charge is deposited there instead of proceeding upward to be extracted.

Recall from Chapter 7 that the late chain alphas were separable on a basis of [PMT](#) S1 signal. The possibility of using the plated out alpha decays of  $^{212}\text{Bi}$  and  $^{212}\text{Po}$  for electron train studies was also investigated, but it was difficult to reach the purity necessary to gain a robust signal from the cathode. Note that the bullseye charge amplifier signals approach threshold level for signals from the cathode (Figure 142 (right)). Again, it should in theory have been possible to distinguish two peaks in the charge spectra alone, but this time there was an additional complication of the beta spectrum (recall a  $^{212}\text{Bi}$  beta precedes the  $^{212}\text{Po}$  alpha decay, this is the Bi-Po)

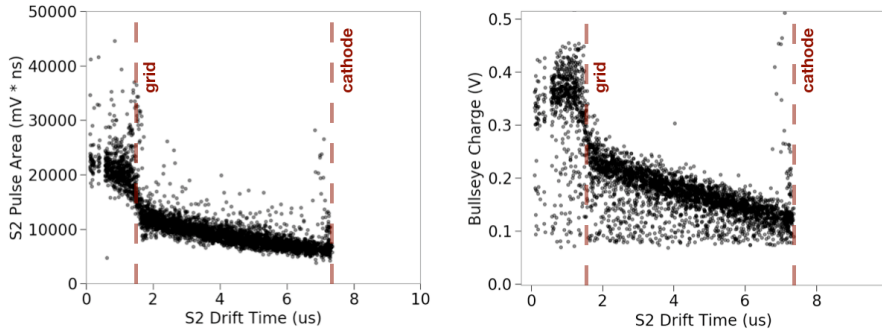


Figure 142: Ionization charge vs. drift time presented in both S2 (left) and charge amplifier voltage from the central anode segment (right). The events are  $^{220}\text{Rn}$  and  $^{216}\text{Po}$  alpha decays from the radon source. A  $\sim 50\%$  drop in signal is visible between events occurring above the grid and events occurring below the grid. The effect of purity is also visible in the fall off of the charge signal with drift time. The points under the obvious line in the charge amplifier plot are from events which share charge with other anode segments. The charge amplifier approaches its threshold at the cathode, indicated by the sharp cut-off at 0.1 V.

to the issues described above. The trigger efficiency was biased to events with more charge, which made collection of a population of  $^{212}\text{Bi}$  alphas more difficult, and the beta spectrum polluted the charge spectrum.

### 8.3.2 POLONIUM SOURCE AND "EXTRACTION REGION ONLY" CONFIGURATION

The grid was removed and the separation from cathode to anode was reduced to 0.5 cm. This configuration mimics the extraction region of a TPC; there is no separate drift region. A diagram of the configuration is shown in Figure 143. The PMT base was changed to an LZ PMT base, which has larger capacitors. However, capacitor depletion was still evident in the PMT trace for alpha decays.

Literature refers to the spontaneous deposition, an irreversible adsorption process, of polonium from an HCl solution on copper, silver, and nickel [149] [150]. A solution of aqueous  $^{210}\text{Po}$  ( $\text{PoCl}_4$ ) was obtained and the efficacy of this process on stainless steel was tested on a  $\sim 1$  mm segment of the central cathode wire. A dropper was used to immerse the wire segment in the  $^{210}\text{Po}$  solution, and the solution was allowed to evaporate. A  $\frac{1}{4}$  in blank gasket was placed under the wire to hold the drop of solution in place during evaporation (Figure 144 (left)). The grid was then placed in the TPC and xenon was condensed as normal. The  $^{210}\text{Po}$  deposition on the cathode wire was robust to dissolution in the LXe (Figure 144

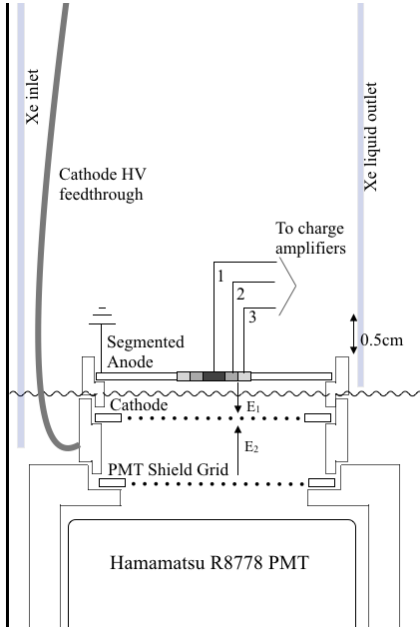


Figure 143: The testbed configuration used in [146]. There is only a cathode grid and anode, with no separate drift region. The TPC can be thought of as “extraction region only”.

(right)). The  $^{210}\text{Po}$  was also found to remain on the grid over the course of multiple fills, and the rate observed over the multiple fills ( $\sim 3$  weeks cumulative) was slightly lower than, but statistically consistent with the  $^{210}\text{Po}$  half-life. There were no background data sets acquired to investigate whether the few events in Figure 144 (right) with drift times shorter than those consistent with the cathode were consistent with background.

$^{210}\text{Po}$  is a 5.3 MeV alpha-emitter, so it has the same high energy / many quanta generated benefit as noted above (see Figure 145 for a decay scheme). The deposition location was chosen to be directly under the central anode segment, which increased detection efficiency. The effect of non-uniform recombination on the grid wires is visible in polonium source, as it was visible in the plated-out radon daughters. At longer drifts, the ratio S2/S1 decreases, indicating that the decays occurred in a lower-field region (see Figure 146).

Both  $^{210}\text{Po}$  alpha decay and, in the case the alpha went into the wire, recoils of the  $^{206}\text{Pb}$  nucleus were observable (Figure 147). The trigger used to observe these events was similar to that described in Chapter 7: a coincidence between PMT and central anode segment was required. If  $^{206}\text{Pb}$  recoil events were desired, the PMT discriminator was adjusted to selectively trigger on smaller traces. As visible in Figure 147, the  $^{210}\text{Po}$  alpha provided a much richer electron train, and so these events were used in the study described in the following section.

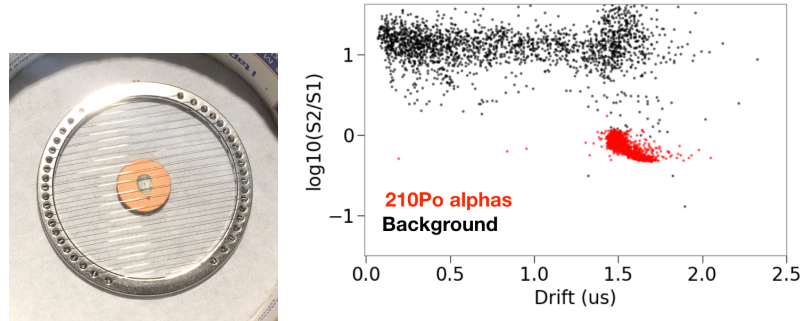


Figure 144: (left) Method for depositing  $^{210}\text{Po}$  on the cathode was to use a dropper to submerge a section of wire in polonium chloride and allowing the liquid to evaporate. (right) This method was robust for depositing  $^{210}\text{Po}$  on the cathode, as evidenced by an alpha population with drift consistent with the cathode.

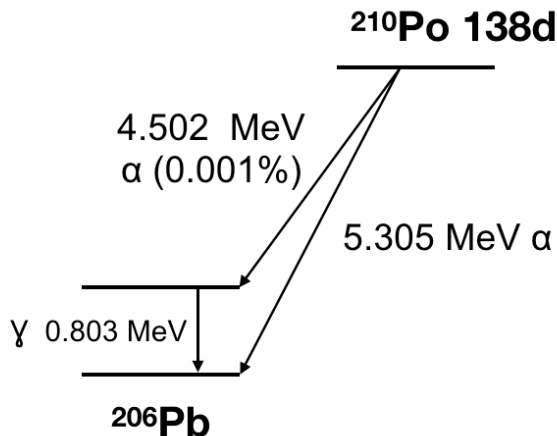


Figure 145:  $^{210}\text{Po}$  decay scheme. Data from [127].

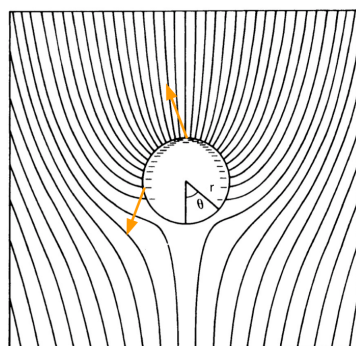


Figure 146: Decays on grid wires experience different field strength depending on particle trajectory, this results in different recombination. Adapted from [151].

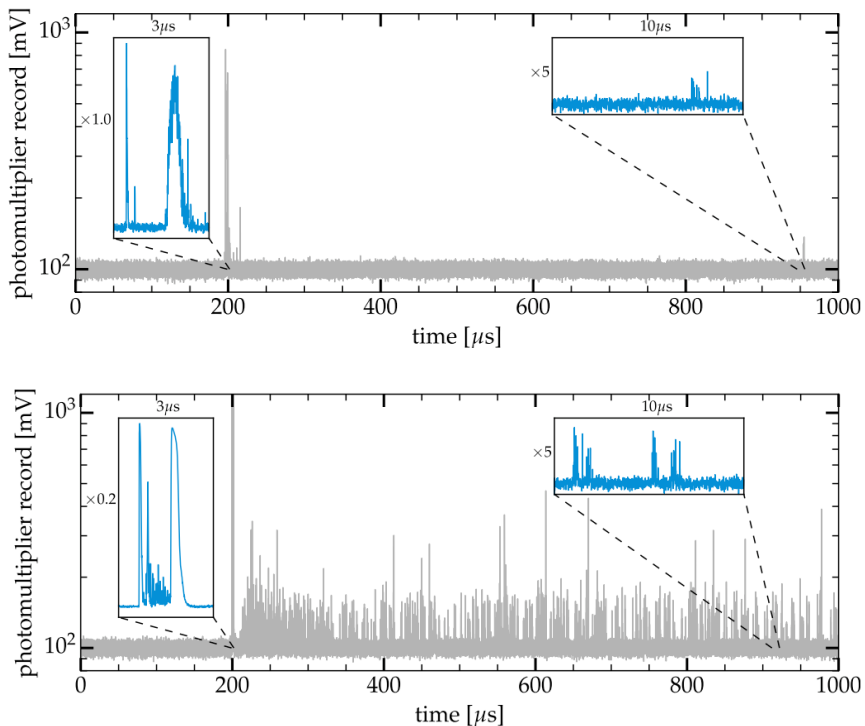


Figure 147: (top) Recoiling  $^{206}\text{Pb}$  nucleus. (bottom)  $^{210}\text{Po}$  alpha decay. Capacitor depletion is visible in the S2 shape, and  $\sim 20 \mu\text{s}$  dead time between the S2 and start of the electron train. Insets on both (top) and (bottom) show detail of the event S1 and S2, and electron train segments. Figure from [146].

## 8.4 ELECTRON TRAIN STUDY SUMMARY

The study done with the  $^{210}\text{Po}$  cathode wire source and the extraction only TPC configuration is described in detail in [146]. Here, a short summary follows. Data were taken with cathode voltages of 3 kV, 4 kV, 5 kV, and 6 kV, and  $^{210}\text{Po}$  alpha events were selected. The waveforms of the events were stacked, as in Figure 148. Two distinct time components are evident in the electron train: fast and slow. Notice the large dip in the PMT signal followed by a rise back to the electron train – this is the classic signature of capacitor depletion-type PMT saturation. Due to the PMT saturation, we were unable to observe any photoionization on grids feature following the S2.

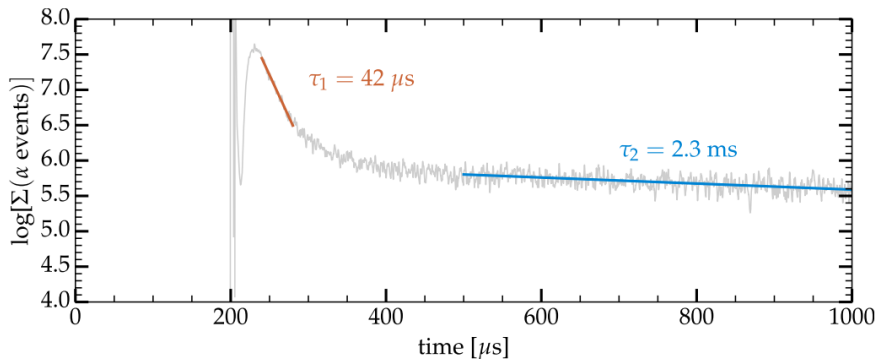


Figure 148: Stacked waveforms and fits from a dataset with cathode voltage at -4 kV. Figure from [146].

The quantity of interest is the number of electrons in each component of the electron train compared to the previous S2. Since the S2 saturates the PMT biasing circuit capacitors, the measurement of S2 electrons is done with the charge amplifiers. It was found for PMT voltages above  $\sim 1100$  V in gas or 600 V in liquid, the raw charge amplifier signal mirrored the PMT trace (see Figure 149). The effect was likely caused by the size of the generated at S1 and S2, which was in turn dependent on PMT bias voltage. Two Frisch grids (cathode and PMT shield grid) were located between the anode and the PMT so the charge amplifiers should not have been able to “see” the electron cascade in the PMT. The Outer Vessel (OV) electronics were investigated for a location where the PMT signal could have been picked up, but none was found. The effect was likely due to pickup on the charge amplifier electronics within the Inner Vessel (IV), as the charge signal output cables were unshielded; however, the PMT signal output cable was shielded, with the shield at ground, so it is unclear how the signals became coupled. To solve the issue, the PMT was merely

turned off and the charge signal was acquired separately. A trigger threshold was set for the charge amplifiers with the [PMT](#) at some low, nominal voltage (to assure we were actually selecting alpha events with the charge trigger and not background), and then the [PMT](#) was completely turned off, and raw charge data collected. The step height of the raw charge signals from the central anode segment were found using the step finding algorithm described in Section 6.6.3. Several events were histogrammed and the mean of a gaussian fit was found and converted to the number of electrons as per the manufacturer's specifications (Figure 150). The left-skewed population visible in Figure 150 is from longer drift, lower charge events that occurred in lower field regions of the cathode wires; the events were not removed before fitting the charge distribution.



Figure 149: Examples of the charge amplifier mirror effect on one anode segment. The example (left) is an event where charge is collected on the anode segment, and so the charge amplifier signal trace shows a step. The example (right) shows the charge trace mirroring the [PMT](#), but with no charge collected on the anode segment.

The number of electrons in the train were reconstructed by summing the [PMT](#) area above the rms-noise level, and dividing the result by the single electron size, which was measured at each cathode voltage. Based on the time constants of the fast and slow components, the number of electrons in each component was extrapolated forward to infinity and backward to the S2, correcting for the other time component. This method was preferred to pulse-funding and counting the single electrons because single electrons pile up in time, resulting in multi-electron pulses, which would have introduced a new source of error. The single electron peak was acquired with a similar method as the single photoelectron peak described above (see Figure 140); the obvious difference being that the [PMT](#) was immersed in liquid xenon and the  $^{210}\text{Po}$  was generating the electrons. An example of the single electron and single photoelectron peaks is shown in Figure 151.

The number of electrons in the fast and slow components found in the [PMT](#) trace, as a fraction of the number of electrons found in the S2 via the charge amplifiers is shown in Figure 152.

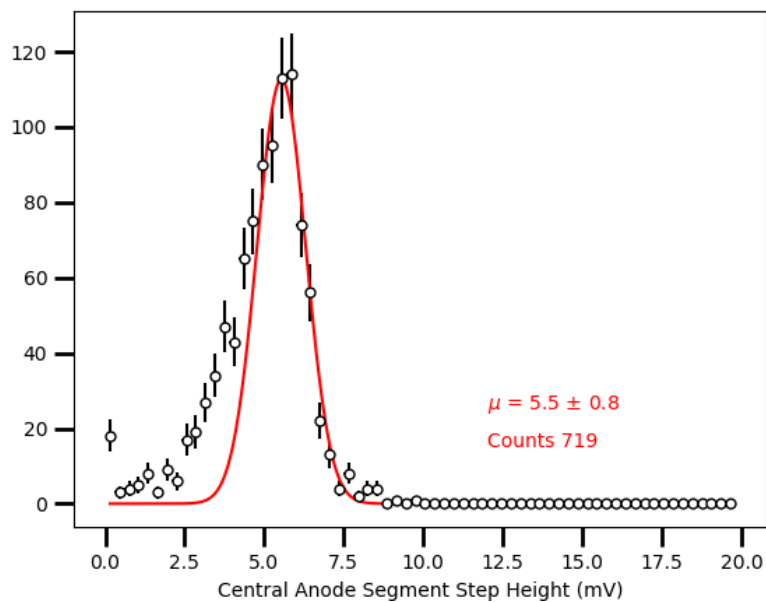


Figure 150: Histogram of charge amplifier step height for a cathode voltage of -3 kV. The histogram is skewed by wire position-dependent recombination; the same effect is visible in Figure 144 (right). This mean of the fit was converted to electrons using the manufacturer's specification of charge amplifier gain, 1.4 V/pC. 5.5mV converts to 24500 electrons.

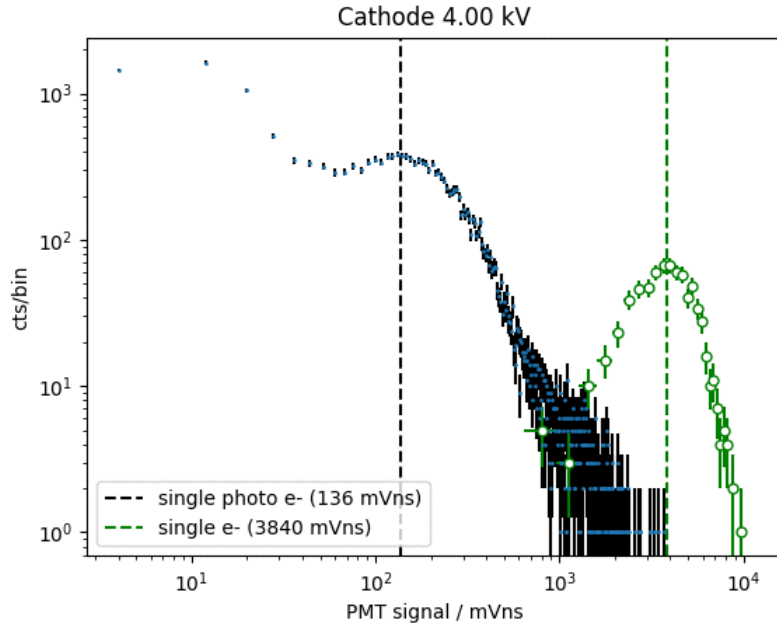


Figure 151: Single electron and photoelectron peaks obtained in liquid conditions for a [PMT](#) bias voltage of 1500 V.

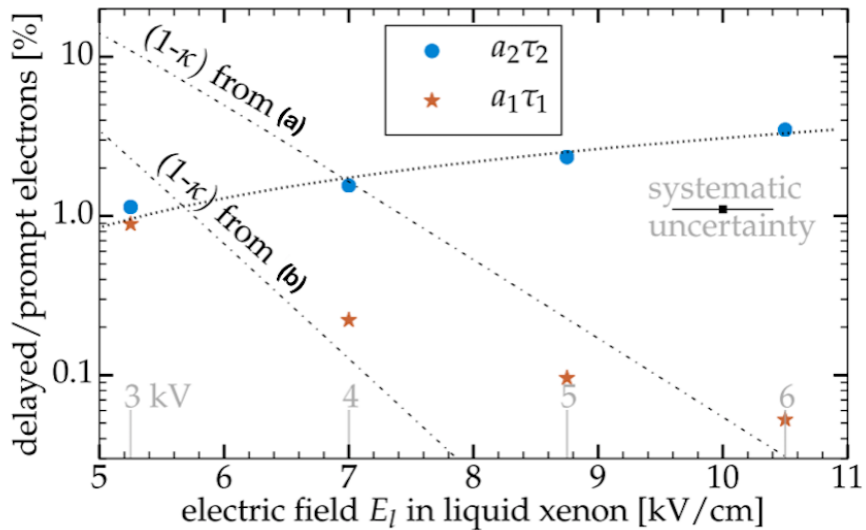


Figure 152:  $\kappa$  is the extraction efficiency as in Equation 61, so unextracted electrons should scale as  $(1 - \kappa)$ . In this thesis, (a) is reference [140], an absolute measurement of [EEE](#); (b) is reference [141], a relative measurement of [EEE](#). The methods use different methods and assumptions; they are shown to illustrate that the fast component follows the behavior trend of what is expected from unextracted electrons.

The fast component of the train decreases in amplitude relative to the prompt electrons as electric field increases. This is the behavior expected if delayed extraction is the cause of electron trains. The slow component, however, increases slightly with electric field, which does not make sense if the slow part of the train has physical origin in the delayed extraction of electrons. The TPC was left under stable operating conditions for 5 days, during which time the xenon was continuously purified through the getter. Typical flow rates were 0.2 slm, which correspond to a turn-over time of the entire liquid mass of  $\sim$ 6 hours. The same data were acquired again, and it was found the slow amplitude decreased by a half, while the fast amplitude was unchanged (Figure 153). The behavior of the fast and slow amplitudes with increased purity indicates that the slow component has physical origin in electronegative impurity content of the xenon.

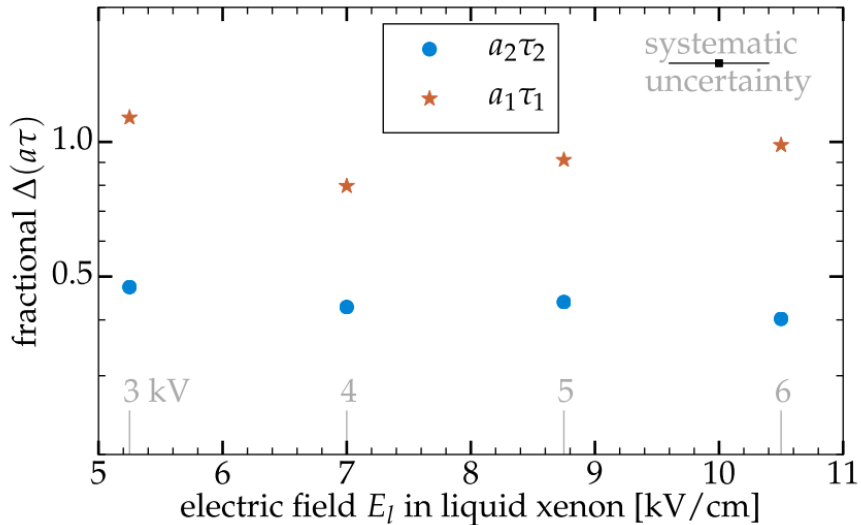


Figure 153: Figure showing the ratio of fast and slow amplitude components after purification to the amplitude components measured prior to purification (shown in Figure 152). The fast component amplitude was unaffected by the improved purity while the slow component amplitude was decreased by half with the improved purity. Note that here, as in Figure 152, amplitudes refer to the fraction of fast and slow components with respect to the previous S2.

The time constants, themselves, were also observed to be dependent on applied electric field. This behavior is not yet understood. We found that  $\tau_1 = \exp(2.62 + 0.157E_l)$  and  $\tau_2 = \exp(6.32 + 0.214E_l)$

## 8.5 DISCUSSION

The study described in the previous section revealed two distinct time components for electron trains. The fast component amplitude decreases with increased extraction field and is not affected by purity. The drift time for the configuration of the TPC during the study was only  $\sim 2 \mu\text{s}$ , so while it is possible that photoionization of impurities was a component of the fast amplitude, it was dominated by behavior that is consistent with increasing extraction efficiency. The slow component amplitude behavior is extremely interesting: it matches the observations of delayed electron noise continuing long past a drift length in large TPCs, and it is tied with xenon purity. This suggests the physical origin of the delayed single electrons is the release of electrons from electronegative impurities. Photoionization of impurities is one possible mechanism for liberating electrons; however, other mechanisms are also possible. Exploring the timescales of such mechanisms can help lead to a positive identification of the origin of delayed electrons.

Electrons can be liberated from impurities by collisional detachment, tunneling, and, as already discussed, photoionization. Collisional detachment refers to the impurity's collision with other atoms, which could provide enough energy for the electron to be released. Collisional detachment can be expected to have timescales of  $t \approx 10 \text{ s}$  [146], which is longer than the timescales observed in both the test bed and the larger TPCs discussed in the beginning of the chapter. Additionally, the late time component amplitude was observed to increase slightly with a higher applied electric field, which should have no effect on collisional detachment. On the other hand, electrons tunneling out of their binding potential (0.45 eV for oxygen) should increase with applied field. However, if tunneling were the case, one would expect the timescale  $\tau_2$  to decrease with applied field, which is counter to our observation. Photoionization of impurities by the UV xenon scintillation light has been discussed already, but other sources of light are also possible. Detector materials can fluoresce following exposure to the UV light. Fluorescence is characterized by delayed emission at a lower wavelength than was absorbed by the material. Of course, any light emitted in the visible spectrum would be seen in the PMT, but light in the infrared spectrum would not be seen by the PMT and is sufficient in energy to photoionize electrons from impurities. Teflon has been observed to fluoresce in the visible region [152] [153], but this fluorescence depends on the content and synthesis of the Teflon. Other sources of fluorescing materials could be the impurities themselves.

Further investigation that more closely characterizes the delayed single electron behavior with purity is planned; purity (electron lifetime) can be measured with the  $^{220}\text{Rn}$  source, which remains plumbed into circula-

tion system. The PTFE can also be removed to investigate if fluorescence of Teflon is a concern. Infrared LEDs were installed to investigate the feasibility of periodically flooding the TPC with photons that would not interfere with the PMT but that would be sufficient to photoionize the impurities.

PART IV

## CONCLUSIONS

# 9

## SUMMARY AND OUTLOOK

---

The nature of dark matter remains one of the most compelling mysteries of modern physics, and the [LUX](#) experiment has been noteworthy in setting limits on available [WIMP](#) dark matter parameter space. Although [WIMPs](#) are a dark matter candidate well-motivated by cosmology and particle physics, other classes of dark matter candidates, namely from the dark sector, are also excellent candidates. The search for [LIPs](#) in this thesis explored the possible parameter space available for one class of dark photon model. [LIPs](#) arise when the dark photon is massless and other dark sector particles gain an effective fractional charge in their interaction with the [SM](#). The [LIP](#) search presented in Chapter 5 was successful in putting further limits on the available parameter space for cosmogenic [LIPs](#). The analysis pioneered a new technique for [LXe TPCs](#), in which track reconstruction and energy consistency variables both play a role.

One limitation of the [LIP](#) search was in the data processing: for low charge fractions ( $f \lesssim 20$ ), [LIPs](#) were found to deposit so much energy that their signals produced ionization trails, which the default [LUX DPF](#) was unable to process into individual pulses. One way to drastically improve the [LIP](#) sensitivity at low  $f$  is to implement new data processing methods capable of dealing with continuous ionization signals. The main background for the [LIP](#) search is the well-known, troublesome phenomenon of electron trains. These delayed electron backgrounds continue for  $O(10 - 100)$  ms, taking up valuable detector livetime. Electron trains are typically considered an annoyance for [WIMP](#) searches, but they severely limit the sensitivity of [LXe TPCs](#) to some dark matter candidates such as low-mass [WIMPs](#) or massive dark photons (see Chapter 3.4.2), and even, as we saw in Chapter 5, [LIPs](#) with charge fractions sufficiently high ( $f \gtrsim 400$ ) to dominantly produce SE pulses instead of S2 pulses.

Chapter 8 of this thesis describes the current understanding of the causes of electron trains, and details a study that revealed two distinct time components in electron trains: a slow component and a fast component. This study was carried out on a laboratory test bed built over the course of this thesis, and showed that the slow component of electron trains is tied to [LXe](#) purity. It is the slow component of electron trains that extends far past a single event window, polluting future events with spurious signals.

That the slow component can be reduced with improved purity holds promise for future **LXe TPCs**, as improvements to **LXe** cleaning methods can reduce or possibly eliminate the long time component of electron trains.

Another particularly troublesome background for **LXe TPCs** comes from  $^{222}\text{Rn}$  and its daughters. In fact,  $^{222}\text{Rn}$  emanation is projected to produce the majority of the **ER** background counts in **LZ** [135]; some of these **ER** events can leak into the **NR** band, producing spurious **WIMP** signals. A new possible source of background counts in the fiducial volume is highlighted in Chapter 7 of this thesis. The practice in the field has historically been to assume the  $^{222}\text{Rn}$  late chain naked beta decays of  $^{210}\text{Pb}$  and  $^{210}\text{Bi}$  are fixed to a surface of the detector and can be rejected via a fiducial cut. The studies carried out in this thesis provide evidence that either  $^{212}\text{Pb}$  or  $^{212}\text{Bi}$  (from the  $^{220}\text{Rn}$  late chain) are mobile to a small degree in **LXe** after having been fixed on a surface. The measurement in this thesis (from  $^{220}\text{Rn}$ ) shows considerable disagreement with limits from **LUX** (from  $^{222}\text{Rn}$ ), which can be accounted for if beta recoil is the mechanism for radon daughter mobility. Further study with samples of known surface area and activity should be carried out with both  $^{222}\text{Rn}$  and  $^{220}\text{Rn}$  to better identify the mobility mechanism and make a more precise measurement.

The next decade is an exciting time for direct detection. **LZ**, the ton-scale successor to **LUX**, is currently under construction and is expected to reach a best sensitivity of  $1.6 \times 10^{-48} \text{ cm}^2$  (for a 40 GeV **WIMP**) for 1000 live days [135]. **LZ** will push further down into **WIMP** parameter space, inching closer to the “neutrino floor,” where neutrinos from solar, atmospheric, and astrophysical sources start appearing as background in direct detection experiments. In fact, **LZ** is expected to see nuclear recoil events from  $^8\text{B}$  solar neutrinos; these events appear in the low-mass **WIMP** signal region and are taken into account in the **WIMP** search analysis [135]. With new analysis techniques and technology updates, **LXe** detectors are poised to make an impact even in non-**WIMP** dark matter searches. R&D to create a **LXe TPC** that is free of delayed electron backgrounds is underway with the Low Background Electron Counting Apparatus (**LBECA**) experiment. Even a 10 kg **LXe** detector has discovery potential for massive dark photons if electron backgrounds can be mitigated [154].

New detector technology will push the direct detection boundaries to new theories and new signals. Whether or not upcoming experiments will uncover any hints of elusive dark matter remains to be seen.

PART V

APPENDIX

# A

## PAI CROSS SECTION AND OPTICAL CONSTANTS

### A.1 SOURCES FOR OPTICAL CONSTANTS

The PAI cross section in Chapter 5 uses the same sources for optical constants as were used in the CDMS result [57] [111]. The sources are outlined in Figure 154, along with the cross section for Si.

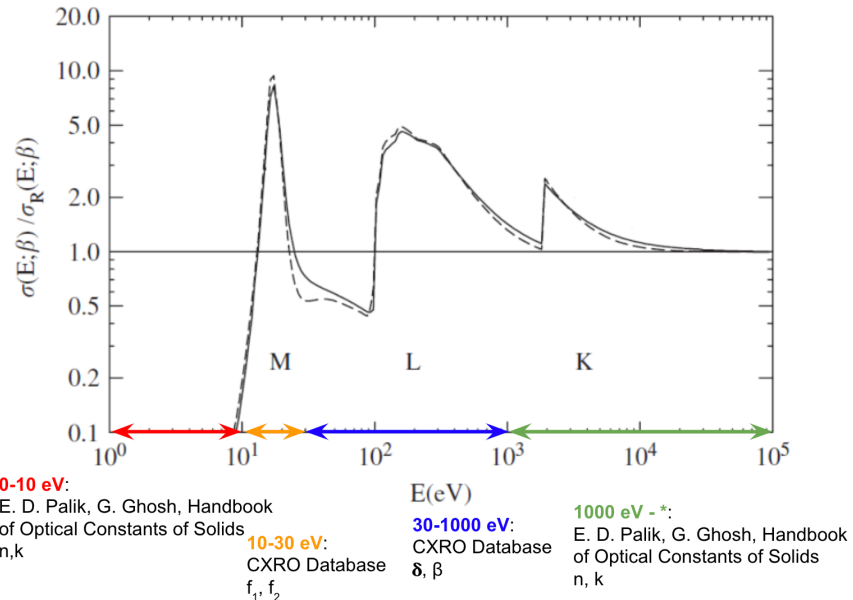


Figure 154: The sources for the different optical constants used for the CDMS LIP result and also the LIP analysis presented in Chapter 5 of this thesis.  
Figure from [109].

Dresselhaus [155] was the most helpful text in translating these various optical constants into the useful  $\epsilon_1$  and  $\epsilon_2$ .

Milhay Novak of Geant4 also provided a different set of optical constants, which originated from the EPICS database (this correspondence was over email). The two results are shown in Figure 155 for both Si and Xe. All the different combinations of constants and code match for Si, in-

dicating there is no error in my calculation of the cross section. For Xe, the EPICS constants do not appear to match the Palik and CXRO constants.

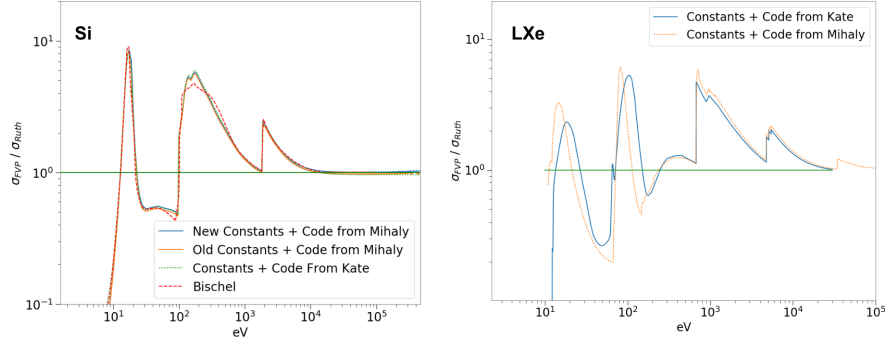


Figure 155: (left) Plot of the PAI cross section divided by the Rutherford cross section for Si. Comparing the different sources for optical constants and calculation method shows that (1) the EPICS constants and the Palik/CXRO match and (2) my code that calculates the PAI cross section does not have any obvious errors. (right) Plot of the PAI cross section divided by the Rutherford cross section, showing the EPICS and Palik/CXRO constants do not match for Xe.

The 1D base straggling Monte Carlo described in Chapter 5 was compared for both the EPICS and Palik/CXRO versions of the Xe cross section. There wasn't a measurable difference in the  $\langle dE/dx \rangle$ , and the same 13% error when compared to [106] was present.

Both the Palik/CXRO and EPICS versions of the cross section for Xe are tabulated below.

## A.2 PAI CROSS SECTION

Need to figure out if I can attach a data file to the thesis.

# B

## LIP FILTER RQS

---

The following is a summary of the LIP Filter RQSs. Several existing LUX RQSs are kept and saved as-is, along with several new RQSs.

The RQSs kept from Run03 are:

```
[fontsize=\small]
run03_rq_list_to_keep = [
file_number
luxstamp_samples
x_corrected
y_corrected
pulse_classification
z_drift_samples
x_cm
y_cm

sd_radius_inf
sd_radius_sup
sd_phiXR
n_samples_in_evt

pulse_area_phe
z_corrected_pulse_area_all_phe
z_corrected_pulse_area_bot_phe
xyz_corrected_pulse_area_all_phe
xyz_corrected_pulse_area_bot_phe
top_bottom_asymmetry

pulse_classification
full_evt_area_phe
s1s2_pairing
prompt_fraction_tlx
pulse_start_samples
pulse_end_samples
pulse_length_samples
s2filter_max_s2_area
```

```
s2filter_max_s1_area

aft_t0_samples
aft_t1_samples
aft_t2_samples
hft_t1_samples
}]}
```

The LIP RQs generated by the LIP filter are as follows. The shape of the RQ is noted, along with type. All RQs use -999 as the initialization value.

```
[fontsize=\small]
def lip_rqs(nEvents, nPulses):
dict_lip_rqs = \{

#RQs about Pulse Area
sumAllPulsePA : (nEvents,) float
#S2 Pulse Area
sumCorrS2PA : (nEvents,) float
firstCorrS2PA : (nEvents,) float
lastCorrS2PA : (nEvents,) float
maxCorrS2PA : (nEvents,) float
minCorrS2PA : (nEvents,) float
first2CorrS2PA : (nEvents,) float
last2CorrS2PA : (nEvents,) float

sumCorrS2PA_xyz_corr : (nEvents,) float
firstCorrS2PA_xyz_corr : (nEvents,) float
lastCorrS2PA_xyz_corr : (nEvents,) float
maxCorrS2PA_xyz_corr : (nEvents,) float
minCorrS2PA_xyz_corr : (nEvents,) float
first2CorrS2PA_xyz_corr : (nEvents,) float
last2CorrS2PA_xyz_corr : (nEvents,) float

sumCorrS2PA_xyz_corr_bot : (nEvents,) float
firstCorrS2PA_xyz_corr_bot : (nEvents,) float
lastCorrS2PA_xyz_corr_bot : (nEvents,) float
maxCorrS2PA_xyz_corr_bot : (nEvents,) float
minCorrS2PA_xyz_corr_bot : (nEvents,) float
first2CorrS2PA_xyz_corr_bot : (nEvents,) float
last2CorrS2PA_xyz_corr_bot : (nEvents,) float

sumRawS2likePA : (nEvents,) float
firstRawS2likePA : (nEvents,) float
```

```

lastRawS2likePA : (nEvents,) float
maxRawS2likePA : (nEvents,) float
minRawS2likePA : (nEvents,) float
first2RawS2likePA : (nEvents,) float
last2RawS2likePA : (nEvents,) float

sumRawS2PA : (nEvents,) float
firstRawS2PA : (nEvents,) float
lastRawS2PA : (nEvents,) float
maxRawS2PA : (nEvents,) float
minRawS2PA : (nEvents,) float
first2RawS2PA : (nEvents,) float
last2RawS2PA : (nEvents,) float

cumSumCorrS2PA : (nEvents,nPulses) float
cumSumCorrS2PA_xyz_corr : (nEvents,nPulses) float
cumSumCorrS2PA_xyz_corr_bot : (nEvents,nPulses) float
cumSumRawS2PA : (nEvents,nPulses) float
cumSumRawS2likePA : (nEvents,nPulses) float

stdCorrS2PA : (nEvents,) float
stdCorrS2PA_xyz_corr : (nEvents,) float
stdCorrS2PA_xyz_corr_bot : (nEvents,) float
stdRawS2PA : (nEvents,) float
stdRawS2likePA : (nEvents,) float

maxZScoreCorrS2PA : (nEvents,) float
maxZScoreCorrS2PA_xyz_corr : (nEvents,) float
maxZScoreCorrS2PA_xyz_corr_bot : (nEvents,) float
maxZScoreRawS2PA : (nEvents,) float
maxZScoreRawS2likePA : (nEvents,) float

minZScoreCorrS2PA : (nEvents,) float
minZScoreCorrS2PA_xyz_corr : (nEvents,) float
minZScoreCorrS2PA_xyz_corr_bot : (nEvents,) float
minZScoreRawS2PA : (nEvents,) float
minZScoreRawS2likePA : (nEvents,) float

#S1 Pulse Area
firstS1PA : (nEvents,) float
sumAllS1PA : (nEvents,) float
largestS1PA : (nEvents,) float

```

```

#Amount of pulse area before the first S1
PAbeforeFirstS1 : (nEvents,) float

#RQs about numbers of pulses
nCorrS2FitPoints : (nEvents,) int
nRawS2FitPoints : (nEvents,) int
nRawS2likeFitPoints : (nEvents,) int
nS1 : (nEvents,) int

#Track RQs
#from fitting
#regular "chi2" fit
corrS2Chi2 : (nEvents,) float
corrS2Chi2_dof : (nEvents,) float

rawS2Chi2 : (nEvents,) float
rawS2Chi2_dof : (nEvents,) float

rawS2likeChi2 : (nEvents,) float
rawS2likeChi2_dof : (nEvents,) float

corrS2TrackFit_params : (nEvents,6) float
rawS2TrackFit_params : (nEvents,6) float
rawS2likeTrackFit_params : (nEvents,6) float

#angle and distance penalty "chi2" fit
corrS2Chi2_anglePen : (nEvents,) float
corrS2Chi2_anglePen_dof : (nEvents,) float

rawS2Chi2_anglePen : (nEvents,) float
rawS2Chi2_anglePen_dof : (nEvents,) float

rawS2likeChi2_anglePen : (nEvents,) float
rawS2likeChi2_anglePen_dof : (nEvents,) float

corrS2TrackFit_anglePen_params : (nEvents,6) float
rawS2TrackFit_anglePen_params : (nEvents,6) float
rawS2likeTrackFit_anglePen_params : (nEvents,6) float

#Single value decomposition result
#(used to provide an initial guess to the fits)
corrS2SVD_params : (nEvents,6) float
rawS2SVD_params : (nEvents,6) float

```

```

rawS2likeSVD_params : (nEvents,6) float

#theta and phi of the track
corrS2TrackTheta : (nEvents,) float
corrS2TrackPhi : (nEvents,) float

rawS2TrackTheta : (nEvents,) float
rawS2TrackPhi : (nEvents,) float

rawS2likeTrackTheta : (nEvents,) float
rawS2likeTrackPhi : (nEvents,) float

corrS2TrackTheta_anglePen : (nEvents,) float
corrS2TrackPhi_anglePen : (nEvents,) float

rawS2TrackTheta_anglePen : (nEvents,) float
rawS2TrackPhi_anglePen : (nEvents,) float

rawS2likeTrackTheta_anglePen : (nEvents,) float
rawS2likeTrackPhi_anglePen : (nEvents,) float

#entrance and exit points of the track
corrS2TrackEnter : (nEvents,3), float
corrS2TrackExit : (nEvents,3), float
rawS2TrackEnter : (nEvents,3), float
rawS2TrackExit : (nEvents,3), float
rawS2likeTrackEnter : (nEvents,3), float
rawS2likeTrackExit : (nEvents,3), float

corrS2TrackEnter_anglePen : (nEvents,3), float
corrS2TrackExit_anglePen : (nEvents,3), float
rawS2TrackEnter_anglePen : (nEvents,3), float
rawS2TrackExit_anglePen : (nEvents,3), float
rawS2likeTrackEnter_anglePen : (nEvents,3), float
rawS2likeTrackExit_anglePen : (nEvents,3), float

#Track length of the fits
corrS2Lfit : (nEvents,) float
rawS2Lfit : (nEvents,) float
rawS2likeLfit : (nEvents,) float
corrS2Lfit_anglePen : (nEvents,) float
rawS2Lfit_anglePen : (nEvents,) float
rawS2likeLfit_anglePen : (nEvents,) float

```

```

#angle between "Data direction" and fit track direction
corrS2DataToFitAng : (nEvents,) float
rawS2DataToFitAng : (nEvents,) float
rawS2likeDataToFitAng : (nEvents,) float

corrS2DataToFitAng_anglePen : (nEvents,) float
rawS2DataToFitAng_anglePen : (nEvents,) float
rawS2likeDataToFitAng_anglePen : (nEvents,) float

#RQs about point statistics (no fits required)
avgPointDistS2Corr : (nEvents,) float
stdPointDistS2Corr : (nEvents,) float

avgPointDistS2Raw : (nEvents,) float
stdPointDistS2Raw : (nEvents,) float

avgPointDistS2likeRaw : (nEvents,) float
stdPointDistS2likeRaw : (nEvents,) float

corrS2Ldata : (nEvents,) float
rawS2Ldata : (nEvents,) float
rawS2likeLdata : (nEvents,) float

#Comb refers to all the n choose 2 combinations
#from an event with n pulses
stdCombThetaS2Corr : (nEvents,) float
stdCombPhiS2Corr : (nEvents,) float

stdPairThetaS2Corr : (nEvents,) float
stdPairPhiS2Corr : (nEvents,) float

stdCombThetaS2Raw : (nEvents,) float
stdCombPhiS2Raw : (nEvents,) float

stdPairThetaS2Raw : (nEvents,) float
stdPairPhiS2Raw : (nEvents,) float

stdCombThetaS2likeRaw : (nEvents,) float
stdCombPhiS2likeRaw : (nEvents,) float

#Pair refers to all the consecutive pulses
stdPairThetaS2likeRaw : (nEvents,) float

```

```

stdPairPhiS2likeRaw : (nEvents,) float

avgCombThetaS2Corr : (nEvents,) float
avgCombPhiS2Corr : (nEvents,) float

avgPairThetaS2Corr : (nEvents,) float
avgPairPhiS2Corr : (nEvents,) float

avgCombThetaS2Raw : (nEvents,) float
avgCombPhiS2Raw : (nEvents,) float

avgPairThetaS2Raw : (nEvents,) float
avgPairPhiS2Raw : (nEvents,) float

avgCombThetaS2likeRaw : (nEvents,) float
avgCombPhiS2likeRaw : (nEvents,) float

avgPairThetaS2likeRaw : (nEvents,) float
avgPairPhiS2likeRaw : (nEvents,) float

#Anderson-Darling test statistic for Pulse Areas
#each event is compared to a Landau (Moyal) distribution
ADPA_CorrS2_xyz_bot : (nEvents,) float
ADPA_CorrS2_xyz : (nEvents,) float
ADPA_CorrS2 : (nEvents,) float
ADPA_RawS2 : (nEvents,) float
ADPA_RawS2like : (nEvents,) float

#number of points outside (bad) and
#inside (good) different fiducial radii
nBadFiducialCorrS2_18cm : (nEvents,) float
nBadFiducialCorrS2_20cm : (nEvents,) float
nGoodFiducialCorrS2_18cm : (nEvents,) float
nGoodFiducialCorrS2_20cm : (nEvents,) float

nBadFiducialRawS2_18cm : (nEvents,) float
nBadFiducialRawS2_20cm : (nEvents,) float
nGoodFiducialRawS2_18cm : (nEvents,) float
nGoodFiducialRawS2_20cm : (nEvents,) float

nBadFiducialRawS2like_18cm : (nEvents,) float
nBadFiducialRawS2like_20cm : (nEvents,) float
nGoodFiducialRawS2like_18cm : (nEvents,) float

```

```

nGoodFiducialRawS2like_20cm : (nEvents,) float

#get the phd/sample for events
#and various statistics for each event
#for "easy", the pulse areas divided
#by the number of samples between the
#start of this pulse and start of the next pulse
#the last pulse is dropped
stdphdpersamp_CorrS2_xyz_bot_easy : (nEvents,) float
stdphdpersamp_CorrS2_xyz_easy : (nEvents,) float
stdphdpersamp_CorrS2_easy : (nEvents,) float
stdphdpersamp_RawS2_easy : (nEvents,) float
stdphdpersamp_RawS2like_easy : (nEvents,) float

minZScorephdpersamp_CorrS2_xyz_bot_easy : (nEvents,) float
minZScorephdpersamp_CorrS2_xyz_easy : (nEvents,) float
minZScorephdpersamp_CorrS2_easy : (nEvents,) float
minZScorephdpersamp_RawS2_easy : (nEvents,) float
minZScorephdpersamp_RawS2like_easy : (nEvents,) float

maxZScorephdpersamp_CorrS2_xyz_bot_easy : (nEvents,) float
maxZScorephdpersamp_CorrS2_xyz_easy : (nEvents,) float
maxZScorephdpersamp_CorrS2_easy : (nEvents,) float
maxZScorephdpersamp_RawS2_easy : (nEvents,) float
maxZScorephdpersamp_RawS2like_easy : (nEvents,) float

#Anderson-Darling test statistic for phd/sample from the "easy" method.
#each event is compared to a Landau (Moyal) distribution
ADphdpersamp_CorrS2_xyz_bot_easy : (nEvents,) float
ADphdpersamp_CorrS2_xyz_easy : (nEvents,) float
ADphdpersamp_CorrS2_easy : (nEvents,) float
ADphdpersamp_RawS2_easy : (nEvents,) float
ADphdpersamp_RawS2like_easy : (nEvents,) float

#for "binned" divide pulse area based on width percentage in bin
#each event is divided into 10 bins, but each event will not have the
#same bin size, as track lengths through the detector
#are different for different events
stdphdpersamp_CorrS2_xyz_bot_binned : (nEvents,) float
stdphdpersamp_CorrS2_xyz_binned : (nEvents,) float
stdphdpersamp_CorrS2_binned : (nEvents,) float
stdphdpersamp_RawS2_binned : (nEvents,) float
stdphdpersamp_RawS2like_binned : (nEvents,) float

```

```

minZScorephdpersamp_CorrS2_xyz_bot_binned : (nEvents,) float
minZScorephdpersamp_CorrS2_xyz_binned : (nEvents,) float
minZScorephdpersamp_CorrS2_binned : (nEvents,) float
minZScorephdpersamp_RawS2_binned : (nEvents,) float
minZScorephdpersamp_RawS2like_binned : (nEvents,) float

maxZScorephdpersamp_CorrS2_xyz_bot_binned : (nEvents,) float
maxZScorephdpersamp_CorrS2_xyz_binned : (nEvents,) float
maxZScorephdpersamp_CorrS2_binned : (nEvents,) float
maxZScorephdpersamp_RawS2_binned : (nEvents,) float
maxZScorephdpersamp_RawS2like_binned : (nEvents,) float

#Anderson-Darling test statistic for phd/sample from binning
#each event is compared to a Landau (Moyal) distribution
ADphdpersamp_CorrS2_xyz_bot_binned : (nEvents,) float
ADphdpersamp_CorrS2_xyz_binned : (nEvents,) float
ADphdpersamp_CorrS2_binned : (nEvents,) float
ADphdpersamp_RawS2_binned : (nEvents,) float
ADphdpersamp_RawS2like_binned : (nEvents,) float
}

lip_rq = collections.OrderedDict(dict_lip_rq)
return lip_rq

```

## BIBLIOGRAPHY

---

- [1] F Zwicky. “Die Rotverschiebung von extragalaktischen Nebeln”. In: *Helv. Phys. Acta* **6**: (1933), pp. 110–127. ISSN: 0018-0238. arXiv: [arXiv:1011.1669v3](https://arxiv.org/abs/1011.1669v3). URL: [http://adsabs.harvard.edu/cgi-bin/nph-data/\\_query?bibcode=1933AchPh...6.110Z&link\\_type=GIF%5Cnpapers2://publication/uuid/E29E0909-762A-4A9D-B5B6-B850822D944A](http://adsabs.harvard.edu/cgi-bin/nph-data/_query?bibcode=1933AchPh...6.110Z&link_type=GIF%5Cnpapers2://publication/uuid/E29E0909-762A-4A9D-B5B6-B850822D944A).
- [2] Gianfranco Bertone and Dan Hooper. “A History of Dark Matter”. In: (2016), pp. 1–88. arXiv: [1605.04909](https://arxiv.org/abs/1605.04909). URL: <http://arxiv.org/abs/1605.04909>.
- [3] Vera C Rubin and W Kent Ford. “Rotation of the Andromeda Nebula From a Spectroscopic Survey of Emission Regions”. In: *Astrophys. J.* **159**:February (1970).
- [4] Vera C Rubin, W Kent Ford, and Norbert Thonnard. “Rotational Properties of 21 Sc Galaxies with a Large Range of Luminoisties and Radii, from NGC 4605 (R=4kpc) to UGC 2885 (R=122kpc)”. In: *Astrophys. J.* **238**: (1980), pp. 471–487.
- [5] J.P. Ostriker and P.J.E Peebles. “A Numerical Study of the Stability of Flattened Galaxies: Or, Can Cold Galaxies Survive?” In: *Astrophys. J.* **186**: (1973), pp. 467–480.
- [6] M. Milgrom. “A Modification Of the Newtonian Dynamics as a Possible Alternative to the Hidden Mass Hypothesis”. In: *Astrophys. J.* **270**: (1983), pp. 365–370.
- [7] M. Milgrom. “A Modification of the Newtonian Dynamics: Implications for Galaxies”. In: *Astrophys. J.* **270**: (1983), pp. 371–383.
- [8] M. Milgrom. “A Modification of the Newtonian Dynamics: Implications for Galaxy Systems”. In: *Astrophys. J.* **270**: (1983), pp. 384–389.
- [9] John Huchra. *CfA Redshift Survey*. URL: <https://www.cfa.harvard.edu/~dfabricant/huchra/zcat/>.
- [10] T. S. van Albada, J. N. Bahcall, K. Begeman, and R. Sanscisi. “Distribution of Dark Matter in the Spiral Galaxy NGC 3198”. In: *Astrophys. J.* **295**: (1985), pp. 305–313.

- [11] Julio F. Navarro, Carlos S. Frenk, and Simon D. M. White. “The Structure of Cold Dark Matter Halos”. In: *Astrophys. J.* **462**: (1996), p. 563. issn: 0004-637X. arXiv: [9508025 \[astro-ph\]](#). URL: <http://adsabs.harvard.edu/doi/10.1086/177173>.
- [12] W.J. G. de Blok, Stacy S. McGaugh, Albert Bosma, and Vera C. Rubin. “Mass Density Profiles of Low Surface Brightness Galaxies”. In: *Astrophys. J.* **552**:1 (2001), pp. L23–L26. issn: 0004637X. arXiv: [0103102 \[astro-ph\]](#). URL: <http://stacks.iop.org/1538-4357/552/i=1/a=L23>.
- [13] W. J. G. de Blok, Stacy S. McGaugh, and Vera C. Rubin. “High-Resolution Rotation Curves of Low Surface Brightness Galaxies. II. Mass Models”. In: *Astron. J.* **122**:5 (2001), pp. 2396–2427. issn: 00046256. arXiv: [0107326 \[astro-ph\]](#). URL: <http://stacks.iop.org/1538-3881/122/i=5/a=2396>.
- [14] Kyle A. Oman et al. “The unexpected diversity of dwarf galaxy rotation curves”. In: *Mon. Not. R. Astron. Soc.* **452**:4 (2015), pp. 3650–3665. issn: 13652966. arXiv: [1504.01437](#).
- [15] Davide Martizzi, Romain Teyssier, and Ben Moore. “Cusp-core transformations induced by AGN feedback in the progenitors of cluster galaxies”. In: *Mon. Not. R. Astron. Soc.* **432**:3 (2013), pp. 1947–1954. issn: 00358711. arXiv: [1211.2648](#).
- [16] Jonah Herzog-Arbeitman, Mariangela Lisanti, Piero Madau, and Lina Necib. “Empirical Determination of Dark Matter Velocities Using Metal-Poor Stars”. In: *Phys. Rev. Lett.* **120**:4 (2018), p. 41102. issn: 10797114. arXiv: [1704.04499](#). URL: <https://doi.org/10.1103/PhysRevLett.120.041102>.
- [17] Lina Necib, Mariangela Lisanti, and Vasily Belokurov. “Dark Matter in Disequilibrium: The Local Velocity Distribution from SDSS-Gaia”. In: (2018), pp. 1–21. arXiv: [1807.02519](#). URL: <http://arxiv.org/abs/1807.02519>.
- [18] Denis Erkal, Sergey E. Koposov, and Vasily Belokurov. “A sharper view of Pal 5’s tails: Discovery of stream perturbations with a novel non-parametric technique”. In: *Mon. Not. R. Astron. Soc.* **470**:1 (2017), pp. 60–84. issn: 13652966. arXiv: [1609.01282](#).
- [19] Nilanjan Banik, Gianfranco Bertone, Jo Bovy, and Nassim Bozorgnia. “Probing the nature of dark matter particles with stellar streams”. In: *J. Cosmol. Astropart. Phys.* **2018**:7 (2018). issn: 14757516. arXiv: [1804.04384](#).

- [20] M. Markevitch, A. H. Gonzalez, L. David, A. Vikhlinin, S. Murray, W. Forman, C. Jones, and W. Tucker. “A Textbook Example of a Bow Shock in the Merging Galaxy Cluster 1E0657-56”. In: (2001). ISSN: 0004-637X. arXiv: [0110468 \[astro-ph\]](#). URL: <http://arxiv.org/abs/astro-ph/0110468{\%}0Ahttp://dx.doi.org/10.1086/339619>.
- [21] Douglas Clowe, Marusa Bradac, Anthony H. Gonzalez, Maxim Markevitch, Scott W. Randall, Christine Jones, and Dennis Zaritsky. “A direct empirical proof of the existence of dark matter”. In: (2006). ISSN: 0004-637X. arXiv: [0608407 \[astro-ph\]](#). URL: <http://arxiv.org/abs/astro-ph/0608407{\%}0Ahttp://dx.doi.org/10.1086/508162>.
- [22] George F. Smoot. “COBE observations and results”. In: *Conf. 3K Cosmol.* (1999), pp. 1–10. arXiv: [9902027 \[astro-ph\]](#). URL: <http://aip.scitation.org/doi/abs/10.1063/1.59326>.
- [23] Wayne Hu. “Lecture Notes on CMB Theory: From Nucleosynthesis to Recombination”. In: (2008). arXiv: [0802.3688](#). URL: <http://arxiv.org/abs/0802.3688>.
- [24] Planck Collaboration. “Planck 2018 Results VI Cosmological parameters”. In: **62**: (2018), pp. 1–71. arXiv: [arXiv:1807.06209v1](#). URL: <https://pla.esac.esa.int>.
- [25] Adam G. Riess et al. “Observational Evidence from Supernovae for an Accelerating Universe and a Cosmological Constant”. In: (1998). ISSN: 00046256. arXiv: [9805201 \[astro-ph\]](#). URL: <http://arxiv.org/abs/astro-ph/9805201{\%}0Ahttp://dx.doi.org/10.1086/300499>.
- [26] S. Perlmutter et al. “Measurements of Omega and Lambda from 42 High-Redshift Supernovae”. In: (1998), pp. 1–33. ISSN: 0004-637X. arXiv: [9812133 \[astro-ph\]](#). URL: <http://arxiv.org/abs/astro-ph/9812133{\%}0Ahttp://dx.doi.org/10.1086/307221>.
- [27] Barbara Ryden. “Introduction to Cosmology”. 2006. ISBN: 0470849096. arXiv: [9904502 \[hep-ph\]](#). URL: <http://arxiv.org/abs/hep-ph/9904502>.
- [28] Edward W. Kolb and Michael S. Turner. “The Early Universe”. In: *Front.Phys.* **69**: (1990), pp. 1–547.
- [29] Clifford Cheung, Lawrence J. Hall, David Pinner, and Joshua T. Ruderman. “Prospects and blind spots for neutralino dark matter”. In: *J. High Energy Phys.* **2013**:5 (2013). ISSN: 11266708. arXiv: [1211.4873](#).

- [30] Chris Quigg. “Cosmic Neutrinos”. In: (2008). arXiv: [0802.0013](#). URL: <http://arxiv.org/abs/0802.0013>.
- [31] Steen Hannestad. “Cosmological neutrinos”. In: (2004). arXiv: [0404239](#) [[hep-ph](#)]. URL: <http://arxiv.org/abs/hep-ph/0404239>{\%}0A<https://dx.doi.org/10.1088/1367-2630/6/1/108>.
- [32] Matteo Viel, Julien Lesgourgues, Martin G Haehnelt, Sabino Matarrese, and Antonio Riotto. “Constraining warm dark matter candidates including sterile neutrinos and light gravitinos with WMAP and the Lyman- forest”. In: *Phys. Rev. D* **71**:063534 (2005), pp. 1–10.
- [33] Jonathan L. Feng. “Dark Matter Candidates from Particle Physics and Methods of Detection”. In: (2010), pp. 495–547. ISSN: 0066-4146. arXiv: [1003.0904](#). URL: <http://arxiv.org/abs/1003.0904>{\%}0A<https://dx.doi.org/10.1146/annurev-astro-082708-101659>.
- [34] Mariangela Lisanti. “Lectures on Dark Matter Physics”. In: (2016). arXiv: [1603.03797](#). URL: <http://arxiv.org/abs/1603.03797>{\%}0A[https://dx.doi.org/10.1142/9789813149441\\\_\\\_0007](https://dx.doi.org/10.1142/9789813149441\_\_0007).
- [35] Particle Data Group. “61 . Axions and Other Similar Particles”. In: October (2017), pp. 1–27.
- [36] R. Foot and S. Vagnozzi. “Dissipative hidden sector dark matter”. In: [023512](#): (2014), pp. 1–23. ISSN: 1550-7998. arXiv: [1409.7174](#). URL: <http://arxiv.org/abs/1409.7174>{\%}0A<https://dx.doi.org/10.1103/PhysRevD.91.023512>.
- [37] R. Essig et al. “Dark Sectors and New, Light, Weakly-Coupled Particles”. In: (2013). arXiv: [1311.0029](#). URL: <http://arxiv.org/abs/1311.0029>.
- [38] Bob Holdom. “Two U(1)’s and  $\epsilon$  charge shifts”. In: *Phys. Lett. B* **166**:2 (1986), pp. 196–198. ISSN: 03702693.
- [39] S. A. Abel, M. D. Goodsell, J. Jaeckel, V. V. Khoze, and A. Ringwald. “Kinetic mixing of the photon with hidden U(1)s in string phenomenology”. In: *J. High Energy Phys.* **2008**:7 (2008). ISSN: 11266708. arXiv: [0803.1449](#).
- [40] Martin L. Perl. “Searches for Fractionally Charged Particles: What Should Be Done Next?” In: *Nucl. Phys. B - Proc. Suppl.* **189**:C (2009), pp. 5–8. ISSN: 09205632.

- [41] S I Alvis et al. “First Limit on the Direct Detection of Lightly Ionizing Particles for Electric Charge as Low as  $e = 1000$  with the M AJORANA D EMONSTRATOR”. In: *Phys. Rev. D* **120**:211804 (2018), pp. 1–7.
- [42] Jonathan L. Feng and Jason Kumar. “Dark-matter particles without weak-scale masses or weak interactions”. In: *Phys. Rev. Lett.* **101**:23 (2008). ISSN: 00319007. arXiv: [0803.4196](#).
- [43] R Foot, H Lew, and R.R. Volkas. “Electric Charge Quantization”. In: *J. Phys. G. Nucl. Part. Phys.* **12**: (1993), pp. 361–372. ISSN: 0954-3899.
- [44] K. S. Babu and Rabindra N. Mohapatra. “Quantization of electric charge from anomaly constraints and a Majorana neutrino”. In: *Phys. Rev. D* **41**:1 (1990), pp. 271–277. ISSN: 05562821.
- [45] A. N. Schellekens. “Electric charge quantization in string theory”. In: *Phys. Lett. B* **237**:3-4 (1990), pp. 363–369. ISSN: 03702693.
- [46] Xiao Gang Wen and Edward Witten. “Electric and magnetic charges in superstring models”. In: *Nucl. Physics, Sect. B* **261**:C (1985), pp. 651–677. ISSN: 05503213.
- [47] P. A. M. Dirac. “P. A. M. Dirac”. In: *Proc. R. Soc. London* **A133**:60 (1931).
- [48] Björn Penning. “The pursuit of dark matter at colliders—an overview”. In: *J. Phys. G Nucl. Part. Phys.* **45**:6 (2018), p. 063001. ISSN: 0954-3899. URL: <http://stacks.iop.org/0954-3899/45/i=6/a=063001?key=crossref.d3fb31b11773e9c891463947d7d31ee2>.
- [49] A. A. Prinz et al. “Search for Millicharged Particles at SLAC”. In: **94309**: (1998), pp. 7–10. arXiv: [9804008 \[hep-ex\]](#). URL: <http://arxiv.org/abs/hep-ex/9804008{\%}0Ahttp://dx.doi.org/10.1103/PhysRevLett.81.1175>.
- [50] Sacha Davidson, Steen Hannestad, and Georg Raffelt. “Updated Bounds on Milli-Charged Particles”. In: (2000). ISSN: 1029-8479. arXiv: [0001179 \[hep-ph\]](#). URL: <http://arxiv.org/abs/hep-ph/0001179{\%}0Ahttp://dx.doi.org/10.1088/1126-6708/2000/05/003>.
- [51] M. Mori et al. “Search for fractionally charged particles in Kamiokande II”. In: *Phys. Rev. D* **43**:9 (1991), pp. 2843–2846.
- [52] K.S Hirata, M Nakahata, N Sato, M Yamada, W Beier, and W Frati. “Observation in the Kamiokande-II detector of the neutrino burst from supernova SN1987A”. In: **38**:2 (1988), pp. 448–458.

- [53] M. Aglietta et al. “Search for fractionally charged particles in the Mont Blanc LSD scintillation detector”. In: *Astropart. Phys.* **2**:1 (1994), pp. 29–34. issn: 09276505.
- [54] M. Ambrosio et al. “Search for lightly ionizing particles with the MACRO detector”. In: *Phys. Rev. D - Part. Fields, Gravit. Cosmol.* **62**:5 (2000), p. 9. issn: 15502368. arXiv: [0002029v2 \[arXiv:hep-ex\]](#).
- [55] M Ambrosio et al. “Final Search for Lightly Ionizing Particles with the MACRO detector”. In: (2004). arXiv: [0402006v1 \[arXiv:hep-ex\]](#).
- [56] M. Ambrosio et al. “The MACRO detector at Gran Sasso”. In: *Nucl. Instruments Methods Phys. Res. Sect. A Accel. Spectrometers, Detect. Assoc. Equip.* **486**:3 (2002), pp. 663–707. issn: 01689002.
- [57] R. Agnese et al. “First direct limits on lightly ionizing particles with electric charge less than  $e/6$ ”. In: *Phys. Rev. Lett.* **114**:11 (2015), p. 111302. issn: 10797114. arXiv: [1409.3270](#). URL: <https://doi.org/10.1103/PhysRevLett.114.111302>.
- [58] Carl Eric Dahl. “The physics of background discrimination in liquid xenon, and first results from Xenon10 in the hunt for WIMP dark matter.” In: PhD Thesis (2009).
- [59] D. S. Akerib et al. “Chromatographic separation of radioactive noble gases from xenon”. In: *Astropart. Phys.* **97**: (2018), pp. 80–87. issn: 09276505. arXiv: [1605.03844](#).
- [60] E. Aprile et al. “Removing krypton from xenon by cryogenic distillation to the ppq level”. In: *Eur. Phys. J. C* **77**:5 (2017). issn: 14346052. arXiv: [1612.04284](#).
- [61] J. Mock, N. Barry, K. Kazkaz, D. Stolp, M. Szydagis, M. Tripathi, S. Uvarov, M. Woods, and N. Walsh. “Modeling pulse characteristics in Xenon with NEST”. In: *J. Instrum.* **9**:4 (2014). issn: 17480221. arXiv: [arXiv:1310.1117v2](#).
- [62] K. Abe et al. “XMASS detector”. In: *Nucl. Instruments Methods Phys. Res. Sect. A Accel. Spectrometers, Detect. Assoc. Equip.* **716**: (2013), pp. 78–85. issn: 01689002. arXiv: [1301.2815](#).
- [63] V. Chepel and H. Araújo. “Liquid noble gas detectors for low energy particle physics”. In: *J. Instrum.* **8**:4 (2013). issn: 17480221. arXiv: [1207.2292](#).
- [64] XMASS Collaboration. “A direct dark matter search in XMASS-I”. In: (2018), pp. 1–23. arXiv: [1804.02180](#). URL: <http://arxiv.org/abs/1804.02180>.
- [65] M. Auger et al. “The EXO-200 detector, part I: Detector design and construction”. In: *J. Instrum.* **7**:5 (2012). issn: 17480221. arXiv: [1202.2192](#).

- [66] F. Neves, A. Lindote, A. Morozov, V. Solovov, C. Silva, P. Bras, J. P. Rodrigues, and M. I. Lopes. “Measurement of the absolute reflectance of polytetrafluoroethylene (PTFE) immersed in liquid xenon”. In: *J. Instrum.* **12**:1 (2017). issn: 17480221. arXiv: [1612.07965](#).
- [67] D. S. Akerib et al. “Calibration, event reconstruction, data analysis and limits calculation for the LUX dark matter experiment”. In: *Phys. Rev. D* **97**:10 (2017), p. 102008. issn: 24700029. arXiv: [1712.05696](#). URL: <http://arxiv.org/abs/1712.05696>.
- [68] D. S. Akerib et al. “Signal yields, energy resolution, and recombination fluctuations in liquid xenon”. In: *Phys. Rev. D* **95**:1 (2017), pp. 1–12. issn: 24700029. arXiv: [1610.02076](#).
- [69] Tadayoshi Doke, Akira Hitachi, Jun Kikuchi, Kimiaki Masuda, Hiroyuki Okada, and Eido Shibamura. “Absolute scintillation yields in liquid argon and xenon for various particles”. In: *Japanese J. Appl. Physics, Part 1 Regul. Pap. Short Notes Rev. Pap.* **41**:3 A (2002), pp. 1538–1545. issn: 00214922.
- [70] E. Aprile, K. L. Giboni, P. Majewski, K. Ni, and M. Yamashita. “Observation of anticorrelation between scintillation and ionization for MeV gamma rays in liquid xenon”. In: *Phys. Rev. B - Condens. Matter Mater. Phys.* **76**:1 (2007), pp. 1–7. issn: 10980121. arXiv: [0704.1118](#).
- [71] D. S. Akerib et al. “Tritium calibration of the LUX dark matter experiment”. In: *Phys. Rev. D* **93**:7 (2016). issn: 24700029. arXiv: [1512.03133](#).
- [72] C. H. Faham, V. M. Gehman, A. Currie, A. Dobi, P. Sorensen, and R. J. Gaitskell. “Measurements of wavelength-dependent double photoelectron emission from single photons in VUV-sensitive photomultiplier tubes”. In: *J. Instrum.* **10**:9 (2015). issn: 17480221. arXiv: [1506.08748](#).
- [73] E. Aprile and T. Doke. “Liquid xenon detectors for particle physics and astrophysics”. In: *Rev. Mod. Phys.* **82**:3 (2010), pp. 2053–2097. issn: 00346861. arXiv: [0910.4956](#).
- [74] J Lindhard, V Nielsen, M Scharff, and P V Thomsen. “Integral equations governing radiation effects”. In: *Det Kgl. Danske Videnskabernes Selskabs Matematisk-fysiske Meddelelser* **33**:10 (1963). URL: <http://www.sdu.dk/bibliotek/materiale+efter+type/hostede+ressourcer/matfys>.
- [75] Peter Sorensen and Carl Eric Dahl. “Nuclear recoil energy scale in liquid xenon with application to the direct detection of dark matter”. In: *Phys. Rev. D - Part. Fields, Gravit. Cosmol.* **83**:6 (2011), pp. 1–6. issn: 15507998. arXiv: [1101.6080](#).

- [76] LUX Collaboration et al. “Low-energy (0.7-74 keV) nuclear recoil calibration of the LUX dark matter experiment using D-D neutron scattering kinematics”. In: (2016), pp. 1–24. issn: 15502368. arXiv: [1608 . 05381](https://arxiv.org/abs/1608.05381). URL: [http : / / arxiv . org / abs / 1608 . 05381](http://arxiv.org/abs/1608.05381).
- [77] J. D. Lewin and P. F. Smith. “Review of mathematics, numerical factors, and corrections for dark matter experiments based on elastic nuclear recoil”. In: *Astropart. Phys.* **6**:1 (1996), pp. 87–112. issn: 09276505. arXiv: [1410 . 6160](https://arxiv.org/abs/1410.6160).
- [78] Laura Baudis. “WIMP dark matter direct-detection searches in noble gases”. In: *Phys. Dark Universe* **4**: (2014), pp. 50–59. issn: 22126864. arXiv: [1408 . 4371](https://arxiv.org/abs/1408.4371). URL: [http : / / dx . doi . org / 10 . 1016 / j . dark . 2014 . 07 . 001](http://dx.doi.org/10.1016/j.dark.2014.07.001).
- [79] P. Cushman, C. Galbiati, D.N. McKinsey, H. Robertson, T.M.P. Tait, and Others. “Working Group Report: WIMP Dark Matter Direct Detection”. In: (2013). arXiv: [1310 . 8327 \[hep-ex\]](https://arxiv.org/abs/1310.8327). URL: [http : / / inspirehep . net / record / 1262767 ? ln = en](http://inspirehep.net/record/1262767?ln=en).
- [80] U Oberlack. “First limits on WIMP dark matter from the XENON10 experiment”. In: *J. Phys. Conf. Ser.* **110**:6 (2008), p. 062020. issn: 1742-6596. URL: [http : / / stacks . iop . org / 1742 - 6596 / 110 / i = 6 / a = 062020 ? key = crossref . bfd78c6898a820849cdc54a2974555a3](http://stacks.iop.org/1742-6596/110/i=6/a=062020?key=crossref.bfd78c6898a820849cdc54a2974555a3).
- [81] D. S. Akerib et al. “First results from the LUX dark matter experiment at the Sanford Underground Research Facility”. In: *Phys. Rev. Lett.* **112**: (2014). issn: 0031-9007, 1079-7114. arXiv: [arXiv : 1310 . 8214v2](https://arxiv.org/abs/1310.8214). URL: [http : / / arxiv . org / abs / 1310 . 8214](http://arxiv.org/abs/1310.8214).
- [82] E. Aprile et al. “First dark matter results from the XENON100 experiment”. In: *Phys. Rev. Lett.* **105**:13 (2010), pp. 9–13. issn: 00319007. arXiv: [1005 . 0380](https://arxiv.org/abs/1005.0380).
- [83] P. Sorensen et al. “Lowering the low-energy threshold of xenon detectors”. In: *Proc. Sci.* (2010). issn: 18248039. arXiv: [arXiv : 1011 . 6439v1](https://arxiv.org/abs/1011.6439v1).
- [84] Peter Sorensen. “Anisotropic diffusion of electrons in liquid xenon with application to improving the sensitivity of direct dark matter searches”. In: *Nucl. Instruments Methods Phys. Res. Sect. A Accel. Spectrometers, Detect. Assoc. Equip.* **635**:1 (2011), pp. 41–43. issn: 01689002. arXiv: [1102 . 2865 \[astro-ph . IM\]](https://arxiv.org/abs/1102.2865).
- [85] E. Aprile et al. “Low-mass dark matter search using ionization signals in XENON100”. In: *Phys. Rev. D* **94**:9 (2016), pp. 8–13. issn: 24700029. arXiv: [1605 . 06262](https://arxiv.org/abs/1605.06262).

- [86] J. Angle et al. “Search for light dark matter in XENON10 data”. In: *Phys. Rev. Lett.* **107**:5 (2011), pp. 1–6. ISSN: 10797114. arXiv: [1104.3088](https://arxiv.org/abs/1104.3088).
- [87] Rouven Essig, Aaron Manalaysay, Jeremy Mardon, Peter Sorensen, and Tomer Volansky. “First direct detection limits on Sub-GeV dark matter from XENON10”. In: *Phys. Rev. Lett.* **109**:2 (2012), pp. 1–5. ISSN: 00319007. arXiv: [1206.2644](https://arxiv.org/abs/1206.2644).
- [88] D. S. Akerib et al. “A search for annual and diurnal rate modulations in the LUX experiment”. In: (2018), pp. 1–12. arXiv: [1807.07113](https://arxiv.org/abs/1807.07113). URL: <http://arxiv.org/abs/1807.07113>.
- [89] D. S. Akerib et al. “First Searches for Axions and Axionlike Particles with the LUX Experiment”. In: *Phys. Rev. Lett.* **118**:26 (2017), pp. 1–7. ISSN: 10797114. arXiv: [1704.02297](https://arxiv.org/abs/1704.02297).
- [90] D. S. Akerib et al. “The Large Underground Xenon (LUX) experiment”. In: *Nucl. Instruments Methods Phys. Res. Sect. A Accel. Spectrometers, Detect. Assoc. Equip.* **704**: (2013), pp. 111–126. ISSN: 01689002. arXiv: [1211.3788](https://arxiv.org/abs/1211.3788).
- [91] C Faham. “Prototype, Surface Commissioning and Photomultiplier Tube Characterization for the Large Underground Xenon (LUX) Direct Dark Matter Search Experiment”. In: PhD Thesis (2014).
- [92] Nicole A Larsen. “An Effective Field Theory Analysis of the First LUX Dark Matter Search”. In: PhD Thesis (2016).
- [93] A. Dobi, C. Davis, C. Hall, T. Langford, S. Slutsky, and Y. R. Yen. “Detection of krypton in xenon for dark matter applications”. In: *Nucl. Instruments Methods Phys. Res. Sect. A Accel. Spectrometers, Detect. Assoc. Equip.* **665**: (2011), pp. 1–6. ISSN: 01689002. arXiv: [1103.2714](https://arxiv.org/abs/1103.2714) [astro-ph]. URL: <http://dx.doi.org/10.1016/j.nima.2011.11.043>.
- [94] D.S. Akerib et al. “Radiogenic and muon-induced backgrounds in the LUX dark matter detector”. In: *Astropart. Phys.* **62**: (2015), pp. 33–46. ISSN: 09276505. arXiv: [1403.1299](https://arxiv.org/abs/1403.1299). URL: <http://dx.doi.org/10.1016/j.astropartphys.2014.07.009><http://linkinghub.elsevier.com/retrieve/pii/S0927650514001054>.
- [95] D. S. Akerib et al. “FPGA-based trigger system for the LUX dark matter experiment”. In: *Nucl. Instruments Methods Phys. Res. Sect. A Accel. Spectrometers, Detect. Assoc. Equip.* **818**: (2016), pp. 57–67. ISSN: 01689002. arXiv: [1511.03541](https://arxiv.org/abs/1511.03541).

- [96] D. S. Akerib et al. “Data acquisition and readout system for the LUX dark matter experiment”. In: *Nucl. Instruments Methods Phys. Res. Sect. A Accel. Spectrometers, Detect. Assoc. Equip.* **668**: (2012), pp. 1–8. ISSN: 01689002. arXiv: [1108.1836](https://arxiv.org/abs/1108.1836).
- [97] A Currie et al. “Position Reconstruction in a Dual Phase Xenon Scintillation Detector”. In: *IEEE* **59**:6 (2012), pp. 3286–3293.
- [98] D. S. Akerib et al. “Position reconstruction in LUX”. In: *J. Instrum.* **13**:2 (2018). ISSN: 17480221. arXiv: [1710.02752](https://arxiv.org/abs/1710.02752).
- [99] D. S. Akerib et al. “83m-Kr calibration of the 2013 LUX dark matter search”. In: *Phys. Rev. D* **96**:11 (2017), p. 112009. ISSN: 2470-0010. arXiv: [arXiv:1708.02566v1](https://arxiv.org/abs/1708.02566v1). URL: <https://link.aps.org/doi/10.1103/PhysRevD.96.112009>.
- [100] D. S. Akerib et al. “3D modeling of electric fields in the LUX detector”. In: *J. Instrum.* **12**: (2017), P11022.
- [101] D. S. Akerib et al. “Results from a Search for Dark Matter in the Complete LUX Exposure”. In: *Phys. Rev. Lett.* **118**:2 (2017), pp. 1–8. ISSN: 10797114. arXiv: [1608.07648](https://arxiv.org/abs/1608.07648).
- [102] D. S. Akerib et al. “Improved Limits on Scattering of Weakly Interacting Massive Particles from Reanalysis of 2013 LUX Data”. In: *Phys. Rev. Lett.* **116**:16 (2016), pp. 1–7. ISSN: 10797114. arXiv: [1512.03506](https://arxiv.org/abs/1512.03506).
- [103] M. Szydagis, N. Barry, K. Kazkaz, J. Mock, D. Stolp, M. Sweany, M. Tripathi, S. Uvarov, N. Walsh, and M. Woods. “NEST: A comprehensive model for scintillation yield in liquid xenon”. In: *J. Instrum.* **6**:10 (2011). ISSN: 17480221. arXiv: [1106.1613](https://arxiv.org/abs/1106.1613).
- [104] U. Fano. “Ionization yield of radiations. II. the fluctuations of the number of ions”. In: *Phys. Rev.* **72**:1 (1947), pp. 26–29. ISSN: 0031899X.
- [105] Samuel D. McDermott, Hai Bo Yu, and Kathryn M. Zurek. “Turning off the lights: How dark is dark matter?” In: *Phys. Rev. D - Part. Fields, Gravit. Cosmol.* **83**:6 (2011), pp. 1–9. ISSN: 15507998. arXiv: [1011.2907](https://arxiv.org/abs/1011.2907).
- [106] C. et al. Patrignani. “Passage of Particles Through Matter”. In: *PDG (Particle Data Group)* (2017). ISSN: 1434-6044. URL: <http://dbcompas.ihep.su/2006/reviews/passagerpp.pdf>.
- [107] H. Bethe. “Zur Theorie des Durchgangs schneller Korpuskularstrahlen durch Materie”. In: *Ann. Phys.* **5**: (1930), pp. 325–400. ISSN: 15213889.

- [108] U Fano. "Penetration of Protons, Alpha Particles, and Mesons12". In: *Ann. Rev Nucl. Scei* **123**: (1963), pp. 1–66. URL: [https://www.google.com/books?hl=tr&lr={\&}id=I6wrAAAAYAAJ{\&}oi=fnd{\&}pg=PA287{\&}dq=Fano,%20U.%20+\(1964\)%20.+Penetrations+of+protons,%20+alpha+particles,%20+and+mesons.+Studies+in+Penetra--tion+of+Charged+Particles+in+Matter,%20+1133%3A287.%20+\(cited+on+pages+15,%20+16,%20+and+17\){\&}ots=PYmM1cE](https://www.google.com/books?hl=tr&lr={\&}id=I6wrAAAAYAAJ{\&}oi=fnd{\&}pg=PA287{\&}dq=Fano,%20U.%20+(1964)%20.+Penetrations+of+protons,%20+alpha+particles,%20+and+mesons.+Studies+in+Penetra--tion+of+Charged+Particles+in+Matter,%20+1133%3A287.%20+(cited+on+pages+15,%20+16,%20+and+17){\&}ots=PYmM1cE)
- [109] Hans Bichsel. "A method to improve tracking and particle identification in TPCs and silicon detectors". In: *Nucl. Instruments Methods Phys. Res. Sect. A Accel. Spectrometers, Detect. Assoc. Equip.* **562**:1 (2006), pp. 154–197. ISSN: 01689002.
- [110] J.H. Allison, W. W. M ; Cobb. "Relativistic Charged Particle Identification By Energy Loss". In: *Ann. Rev. Nucl. Part. Sci.* **30**: (1980), pp. 253–298.
- [111] K. Prasad. "Search For Lightly Ionizing Particles Using CDMS-II Data and Fabrication of CDMS Detectors With Improved Homogeneity in Properties". Tech. rep. PhD Thesis. 2013.
- [112] D. S. Akerib et al. "LUXSim: A component-centric approach to low-background simulations". In: *Nucl. Instruments Methods Phys. Res. Sect. A Accel. Spectrometers, Detect. Assoc. Equip.* **675**: (2012), pp. 63–77. ISSN: 01689002. arXiv: [1111.2074](https://arxiv.org/abs/1111.2074). URL: <http://dx.doi.org/10.1016/j.nima.2012.02.010>.
- [113] A Mozumder. "CHEMICAL PHYSICS Free-ion yield and electron-ion recombination rate in liquid xenon". In: *Chem. Phys. Lett.* **245**: (1995), pp. 359–363.
- [114] JE Moyal. "Theory of ionization fluctuations". In: *Philos. Mag.* **46**: June 2013 (1955), pp. 263–280. ISSN: 1941-5982. URL: <http://www.tandfonline.com/doi/full/10.1080/14786440308521076>.
- [115] Gauss M Cordeiro, Juvêncio S Nobre, Rodrigo R Pescim, and Edwin M M Ortega. "The beta moyal: a useful-skew distribution". In: *International Journal of Research and Reviews in Applied Sciences* **10**:2 (2012), pp. 1–22. URL: [www.arpapress.com/Volumes/Vol10Issue2/IJRAS{\\\_}10{\\\_}2{\\\_}02.pdf](http://www.arpapress.com/Volumes/Vol10Issue2/IJRAS{\_}10{\_}2{\_}02.pdf).
- [116] B. Tennyson. "Two-Phase Liquid-Gas Xenon Time Projection Chambers: Theory, Applications, and Analysis". PhD thesis. Yale, 2017.
- [117] J. Xu and Et al. "An investigation of the background electron emissions in the LUX detector". Tech. rep. Salt Lake City, UT: 16-19 April Meeting APS, 2016.

- [118] Gary J Feldman. "FeldmanCousins.pdf". In: *57:7* (1998), pp. 3873–3889.
- [119] Zhong He. "Review of the Shockley-Ramo theorem and its application in semiconductor gamma-ray detectors". In: *Nucl. Instruments Methods Phys. Res. Sect. A Accel. Spectrometers, Detect. Assoc. Equip.* **463**:1-2 (2001), pp. 250–267. issn: 01689002.
- [120] B. J. Mount et al. "LUX-ZEPLIN (LZ) Technical Design Report". In: (2017). arXiv: [1703.09144](https://arxiv.org/abs/1703.09144). URL: <http://arxiv.org/abs/1703.09144>.
- [121] KT McDonald. "Notes on electrostatic wire grids". In: *Notes Electrostat. wire grids*. 2003. URL: <http://www.hep.princeton.edu/~mcdonald/examples/grids.pdf>.
- [122] V. E. Guiseppe, S. R. Elliott, A. Hime, K. Rielage, and S. Westerdale. "A Radon Progeny Deposition Model". In: 2011, pp. 95–100. URL: <http://aip.scitation.org/doi/abs/10.1063/1.3579565>.
- [123] E. O. Knutson. "Radon and Its Decay Products in Indoor Air". Wiley, 1988.
- [124] Yasuhiro Takemoto. "7Be solar neutrino observation with KamLAND". In: *Nucl. Part. Phys. Proc.* **265-266**: (2015), pp. 139–142. issn: 24056014. URL: <http://linkinghub.elsevier.com/retrieve/pii/S2405601415003788>.
- [125] A. Gando et al. "Be 7 solar neutrino measurement with KamLAND". In: *Phys. Rev. C* **92**:5 (2015), p. 055808. issn: 0556-2813. URL: <https://link.aps.org/doi/10.1103/PhysRevC.92.055808>.
- [126] G. Bellini et al. "Final results of Borexino Phase-I on low-energy solar neutrino spectroscopy". In: *Phys. Rev. D* **89**:11 (2014), p. 112007. issn: 1550-7998. URL: <https://link.aps.org/doi/10.1103/PhysRevD.89.112007>.
- [127] Laboratoire National Henri Becquerel. 2017. URL: [http://www.nucleide.org/DDEP{\\\_}WG/DDEPdata.htm](http://www.nucleide.org/DDEP{\_}WG/DDEPdata.htm).
- [128] Christer Samuelsson. "Plate-out and Implantation of 222Rn Decay Products in Dwellings". In: *Environ. Int. Vol.* **22**:Suppl. 1 (1996), pp. 839–843.
- [129] Lawrence Stein. "Chapter 18 Chemical Properties of Radon". In: *Radon Its Decay Prod.* 1987, pp. 240–251.
- [130] Lawrence Stein. "The Chemistry of Radon". In: *Radiochim. Acta* **32**: (1982), pp. 163–171. issn: 0036-8075.
- [131] J.K. Hammer, B; Norskov. "Theory of adsorption and surface reactions". In: (1997), pp. 285–351.

- [132] J . Bigu. "Plate-Out of Radon and Thoron Progeny on Large Surfaces". In: *Radon Its Decay Prod.* 1987. Chap. 21, pp. 272–284.
- [133] E S Morrison, T Frels, E H Miller, R W Schnee, and J Street. "Radon daughter plate-out onto Teflon." In: *arXiv.org, e-Print Arch. Phys.* **090002**: (2017), pp. 1–4. ISSN: 15517616. URL: <http://arxiv.org/pdf/1708.08534.pdf>.
- [134] M. Bruemmer, M. Nakib, R. Calkins, J. Cooley, and S. Sekula. "Studies on the reduction of radon plate-out". In: *AIP Conf. Proc.* **1672**: (2015). ISSN: 15517616. arXiv: [1506.04050](https://arxiv.org/abs/1506.04050).
- [135] D. S. Akerib et al. "Projected WIMP sensitivity of the LUX-ZEPLIN (LZ) dark matter experiment". In: (2018), pp. 1–16. arXiv: [1802.06039](https://arxiv.org/abs/1802.06039). URL: <http://arxiv.org/abs/1802.06039>.
- [136] J B Albert et al. "Measurements of the ion fraction and mobility of  $\alpha$ - and  $\beta$ -decay products in liquid xenon using the EXO-200 detector". In: *Phys. Rev. C* **92**:045504 (2015), pp. 1–10.
- [137] B. Edwards et al. "Measurement of single electron emission in two-phase xenon". In: *Astropart. Phys.* **30**:2 (2008), pp. 54–57. ISSN: 09276505.
- [138] E. Santos et al. "Single electron emission in two-phase xenon with application to the detection of coherent neutrino-nucleus scattering". In: *J. High Energy Phys.* **2011**:12 (2011). ISSN: 11266708. arXiv: [1110.3056 \[physics.ins-det\]](https://arxiv.org/abs/1110.3056).
- [139] E. Aprile et al. "Observation and applications of single-electron charge signals in the XENON100 experiment". In: *J. Phys. G Nucl. Part. Phys.* **41**:3 (2014). ISSN: 09543899. arXiv: [1311.1088](https://arxiv.org/abs/1311.1088).
- [140] E. M. Gushchin, A. A. Kruglov, and I. M. Obodovskii. "Emission of "hot" electrons from liquid and solid argon and xenon". In: *Sov. Phys. JETP* **55**:5 (1982).
- [141] B. N.V. Edwards et al. "Extraction efficiency of drifting electrons in a two-phase xenon time projection chamber". In: *J. Instrum.* **13**:1 (2018). ISSN: 17480221. arXiv: [1710.11032](https://arxiv.org/abs/1710.11032).
- [142] Peter Sorensen. "Electron train backgrounds in liquid xenon dark matter search detectors are indeed due to thermalization and trapping". In: (2017), pp. 1–5. arXiv: [1702.04805](https://arxiv.org/abs/1702.04805). URL: <http://arxiv.org/abs/1702.04805>.
- [143] W. Tauchert and Werner F. Schmidt. "Energy of the Quasi-free Electron State in Liquid Argon, Krypton, and Xenon". In: *Zeitschrift für Naturforsch. A* **30a**: (1975), pp. 1085–1086.

- [144] Morrel Cohen and J. Lekner. "Theory of Hot Electrons in Gases, Liquids, and Solids". In: *Phys. Rev.* **158**:1935 (1967), pp. 305–309. ISSN: 0031-899X.
- [145] A I Bolozdynya. "Two-phase emission detectors and their applications". In: *Nucl. Instruments Methods Phys. Res. A* **422**: (1999), pp. 314–320.
- [146] P. Sorensen and K. Kamdin. "Two distinct components of the delayed single electron noise in liquid xenon emission detectors". In: *J. Instrum.* **13**:2 (2018). ISSN: 17480221. arXiv: [1711.07025](https://arxiv.org/abs/1711.07025).
- [147] O. Bunemann, T.E. Cranshaw, and J.A. Harvey. "Design of Grid Ionization Chambers". In: *Candian J. Res.* **27**:A (1949), pp. 191–206.
- [148] R. Bevilacqua, A. Göök, F. J. Hambach, N. Jovančević, and M. Vidić. "A procedure for the characterization of electron transmission through Frisch grids". In: *Nucl. Instruments Methods Phys. Res. Sect. A Accel. Spectrometers, Detect. Assoc. Equip.* **770**: (2015), pp. 64–67. ISSN: 01689002.
- [149] T. Hashimoto, A. Habiro, M. Noguchi, and T. Kubota. "Spontaneous deposition behavior of polonium on several kinds of metallic wires and its utilization as a conventional alpha-source". In: *Radioisotopes* **39**:7 (1990), pp. 291–297.
- [150] P.E. Figgins. "The Radiochemistry of Polonium". Tech. rep. 1961.
- [151] Luigi Blum, Walter; Riebler, Werner; Rolandi. "Particle Detection with Drift Chambers Particle Acceleration and Detection". 2008. ISBN: 9783540766834.
- [152] V. F. Gachkovskii, T. A. Kudryavtseva, and N. M. Chirkov. "Dependence of the fluorescence intensity of polytetrafluoroethylene on the conditions of synthesis and molecular weight". In: *Bull. Acad. Sci. USSR Div. Chem. Sci.* **18**:11 (1969), pp. 2297–2299. ISSN: 05685230.
- [153] S. A. Khatipov, R. N. Nurmukhametov, Yu E. Sakhno, V. G. Klimenko, D. I. Seliverstov, S. T. Sychkova, and T. V. Sakhno. "Color and fluorescence of polytetrafluoroethylene treated by  $\gamma$ -irradiation near the melting point". In: *Nucl. Instruments Methods Phys. Res. Sect. B Beam Interact. with Mater. Atoms* **269**:21 (2011), pp. 2600–2604. ISSN: 0168583X. URL: <http://dx.doi.org/10.1016/j.nimb.2011.07.017>.
- [154] Marco Battaglieri et al. "US Cosmic Visions : New Ideas in Dark Matter 2017 : Community Report". Tech. rep. 2017. arXiv: [arXiv: 1707.04591v1](https://arxiv.org/abs/1707.04591v1).

- [155] M S Dresselhaus. “Solid State Physics Part II: Optical Properties of Solids”. In: *Proceedings Int. Sch. Phys.* (1966), p. 198. ISSN: 978-981-4405-94-2. URL: <http://web.mit.edu/course/6/6.732/www/6.732-pt2.pdf>.